UNIVERSITY OF SOUTHAMPTON

FACULTY OF ENGINEERING, SCIENCE & MATHEMATICS

OPTOELECTRONICS RESEARCH CENTRE

Development and characterisation of phosphate glasses for athermalisation

by

Eric Tong Yih Lee

Thesis submitted for the degree of Doctor of Philosophy

June 2004

DECLARATION OF AUTHORSHIP

I declare that the thesis entitled

"Development and characterisation of phosphate glasses for athermalisation."

and the work presented in it are my own. I confirm that:

- this work was done wholly while in candidature for a research degree at this University;
- where I have consulted the published work of others, this is always clearly attributed;
- where I have quoted from the work of others, the source is always given. With the exception of such quotations, this thesis is entirely my own work;
- I have acknowledged all main sources of help;
- where the thesis is based on work done by myself jointly with others, I have made clear exactly what was done by others and what I have contributed myself;
- parts of this work have been published, as given under the section of 'Publications'.

Eric Tong Yih, Lee

June 2004

UNIVERSITY OF SOUTHAMPTON

ABSTRACT

FACULTY OF ENGINEERING, SCIENCE AND MATHEMATICS

OPTOELECTRONICS RESEARCH CENTRE

Doctor of Philosophy

DEVELOPMENT AND CHARACTERISATION OF PHOSPHATE GLASSES FOR ATHERMALISATION

by Eric Tong Yih Lee

Lightwave devices such as gratings have a drawback where the central wavelength of the devices is sensitive to changes in temperature, which compromises their performance. This problem is particularly acute in systems that employ Wavelength Division Multiplexing (WDM), where the stability of wavelength with regards to temperature is essential. An athermal waveguide, which is inherently insensitive to temperature, is an ideal choice to solve this problem instead of using a passive temperature control unit, which could limit the optimum performance of a WDM system.

Generally, athermal glasses must exhibit negative refractive index change with temperature (*dn/dT*) to counter the effect of thermal expansion. Phosphate glasses are ideal candidates for athermalisation as they exhibit negative *dn/dT*. An interferometer set-up has been constructed to specifically measure *dn/dT* of the glasses.

Three different phosphate glass families were prepared and characterised in terms of their optical and thermal properties. The properties of the potassium aluminophosphate glasses were strongly influenced by the strengthening effect of Al^{3+}, the trend observed for the binary phosphate glasses depended on the availability of terminal oxygens to coordinate the cations while the change in the properties of borophosphate glasses depended on the effect and coordination number of B^{3+}.

Glasses with negative *dn/dT* have been achieved from the various compositions of glasses studied. The results showed that there was a minimum thermal expansion coefficient (α) for each glass system, beyond which α would overcome the effect of polarisability change with temperature so that the glasses exhibited negative *dn/dT*. Semi-empirical equations linking *dn/dT* and α have been defined, enabling the estimation of *dn/dT* of any glass within the same system. This research work represents the first comprehensive measurement of *dn/dT* of phosphate glasses.

Both fibre and planar waveguides were fabricated. Extrusion was used to prepare the preform for fibre drawing. The extrusion process used a two-die assembly to extrude dissimilar glasses, and is the first demonstration of its kind. The spin-coating process was used to deposit layers of glass on glass substrates to produce planar structures. The success of the extrusion and spin-coating work showed that these processes could be used for combinations of glasses with dissimilar thermal properties. Femtosecond writing was investigated on the phosphate glasses and channel waveguides have been successfully defined.

TABLE OF CONTENTS

	Content	***Page***
	Abstract	I
	Table of Contents	III
	List of Figures	VIII
	List of Photographs	XII
	List of Tables	XIII
	Acknowledgements	XV
	Nomenclature	XVI
	Glossary of Terms	XVIII
Chapter 1	**Introduction**	1
1.1	Objectives and Scope of the Research	1
1.2	Motivation	2
1.3	Concept of Athermalisation	5
1.3.1	Bulk Glass	5
1.3.2	Bragg Grating	6
1.3.3	Optical Waveguides and Fibres	7
1.4	*dn/dT* of Glasses	9
1.5	Contribution of the Research	11
1.6	Layout of Thesis	12
	References	13
Chapter 2	**Literature Review**	16
2.1	Phosphate Glasses	16
2.1.1	Properties	16
2.1.2	Structures	19
2.1.2.1	Binary Phosphate	21
2.1.2.2	Aluminophosphate	24
2.1.2.3	Borophosphate	26

2.1.3 Applications 27
2.2 *dn/dT* Measurement 28
2.3 Athermalisation 32
References 41

Chapter 3 Experimental Work 50
3.1 Glass Preparation 50
3.1.1 Glass Melting 50
3.1.2 Glass Polishing 55
3.2 Thermal Properties 56
3.2.1 Glass Transition Temperature, T_g 56
3.2.2 Thermal Expansion Coefficient, α 58
3.3 Optical Properties 60
3.3.1 Refractive Index, *n* 60
3.3.2 Thermo-optic Coefficient, *dn/dT* 61
3.3.3 UV Spectrum 62
3.3.4 OH Content, r_{OH} 64
3.4 Study of *dn/dT* 66
3.4.1 Theory of Interference 66
3.4.2 Interferometer Set-up 67
3.4.3 Analysis of Fringe Pattern 69
3.4.4 *dn/dT* Measurements 71
3.4.4.1 Effect of Sample Thickness on *dn/dT* 72
3.5 Fibre Fabrication 74
3.5.1 Extrusion 74
3.5.2 Fibre Drawing 77
3.6 Waveguide Fabrication 79
3.6.1 Hot-dip Spin-coating 79
3.6.2 UV Writing 80
3.6.3 Femtosecond Writing 81
References 83

Chapter 4 Potassium Aluminophosphate Glasses 87
4.1 Introduction 87
4.2 Glass Preparation 87
4.3 Property Measurements 89
4.4 Results and Discussion 90
4.4.1 OH Content and UV Spectrum 92
4.4.2 Refractive Index 95
4.4.3 Glass Transition Temperature and Thermal Expansion Coefficient 98
4.4.4 Thermo-optic Coefficient 101
4.4.5 Athermalisation 107
4.5 Device Fabrication 109
4.6 Summary 109
References 110

Chapter 5 Binary Phosphate Glasses 113
5.1 Introduction 113
5.2 Glass Preparation 113
5.3 Property Measurements 114
5.4 Results and Discussion 115
5.4.1 OH Content and UV Spectrum 117
5.4.2 Refractive Index and Glass Transition Temperature 120
5.4.3 Thermal Expansion Coefficient and Thermo-optic Coefficient 124
5.4.4 Athermalisation 130
5.5 Device Fabrication 131
5.5.1 Fibre Fabrication 133
5.5.1.1 Fabrication Requirements 133
5.5.1.2 Extrusion 135
5.5.2 Planar Waveguide Fabrication 139
5.6 Channel Definition 144
5.6.1 UV Writing 144
5.6.2 Femtosecond Writing 145
5.7 Summary 148

References 151

Chapter 6 Borophosphate Glasses 154

6.1 Introduction 154

6.2 Glass Preparation 154

6.3 Property Measurements 156

6.4 Results and Discussion 157

6.4.1 Refractive Index and Glass Transition Temperature 159

6.4.2 Thermal Expansion Coefficient and Thermo-optic Coefficient 162

6.4.3 OH Content and UV Spectrum 166

6.4.4 Athermalisation 169

6.5 Device Fabrication 171

6.5.1 Fibre Fabrication 173

6.5.1.1 Extrusion 173

6.5.1.2 Fibre Drawing 177

6.5.1.3 Fibre Characterisation 178

6.5.2 Planar Waveguide Fabrication 180

6.6 Channel Definition 181

6.6.1 UV Writing 181

6.6.2 Femtosecond Writing 182

6.7 Summary 184

References 186

Chapter 7 Conclusions 188

7.1 Conclusions 188

7.2 Future Work 195

References 197

Appendices 199

A Derivation of *dn/dT* from Lorentz-Lorenz equation 200

B Raw Material Calculation for Glass Synthesis 203

C EDAX Analysis of Glasses 207

D Commercial Schott Glasses 209

E Bismuthate Glass 212

Publications 234

LIST OF FIGURES

Figure	***Title***	***Page***
1.1	Relationship between g and z/a^2	10
2.1	UV edges for different glass formers	17
2.2	Relationship between dn/dT and (z/a^2-r_k) in metaphosphate glasses	18
2.3	Phosphate tetrahedral sites	19
2.4	Phosphate structural network	21
2.5	Q^i fractions in binary phosphate glasses	22
2.6	Binary phosphate structure when (a) $M_{TO} > CN_{Me}$ and (b) $M_{TO} < CN_{Me}$	23
2.7	Binary lithium and sodium phosphate density	24
2.8	Glass transition temperature of sodium aluminophosphate glasses as a function of the O/P ratio	25
2.9	Sodium aluminophosphate structure : (a) Metaphosphate, (b) Pyrophosphate and (c) Orthophosphate	25
2.10	Borophosphate and borate groups in borophosphate glass network	26
2.11	Glass transition temperature of calcium borophosphate glasses	27
2.12	Example of an interferometer set-up for dn/dT measurement	28
2.13	Interferometer for fast-Fourier-transform-based fringe analysis	30
2.14	Ridge-loaded silica-based athermal waveguide	35
2.15	Transmission spectrum of an athermal FBG in a boron co-doped germanosilicate core fibre	36
2.16	Relationship between P_2O_5:GeO_2 ratio and $d\lambda/dT$	36
2.17	Bent LPFG for temperature compensation	37
2.18	Athermalisation with a hybrid substrate	38
2.19	Cross-section of silica waveguide with polymer layer	38
2.20	Athermal silica-based waveguides (a) without and (b) with a grating layer	39
3.1	Glass synthesis procedures	53
3.2	Timeline for glass synthesis	54
3.3	Differential thermal analyser (DTA)	57

3.4	Typical T_g measurement data	58
3.5	Thermomechanical analyser (TMA)	59
3.6	Typical α measurement data	59
3.7	Abbe '60' refractometer	60
3.8	Total internal reflection in a prism	61
3.9	Typical UV transmission spectrum	63
3.10	Typical UV absorption spectrum	64
3.11	Typical FTIR spectrum	65
3.12	Interferometer set-up	68
3.13	Sinusoidal interference pattern	71
3.14	ΔT values for barium metaphosphate sample at different thickness	73
3.15	Extrusion process	76
3.16	Fibre drawing tower	77
3.17	Fibre drawing furnace	78
3.18	Spin-coating rig	80
3.19	Direct UV writing	81
3.20	Femtosecond writing	82
4.1	KAP glass-forming region	89
4.2	Infrared transmission spectra through xK$_2$O-(35-x)Al$_2$O$_3$-65P$_2$O$_5$ glasses	93
4.3	Ultraviolet transmission spectra through 20K$_2$O-yAl$_2$O$_3$-(80-y)P$_2$O$_5$ glasses	94
4.4	Ultraviolet absorption spectra through 20K$_2$O-yAl$_2$O$_3$-(80-y)P$_2$O$_5$ glasses	94
4.5a	Refractive index (n) of series 1 (metaphosphate), 2 (65 mol% P$_2$O$_5$) and 3 (20 mol% K$_2$O) KAP glasses	95
4.5b	Refractive index (n) of series 4 (15 mol% Al$_2$O$_3$) KAP glasses	96
4.6	Potassium aluminophosphate structure	97
4.7a	Glass transition temperature (T_g) of series 1 (metaphosphate), 2 (65 mol% P$_2$O$_5$) and 3 (20 mol% K$_2$O) KAP glasses	99
4.7b	Glass transition temperature (T_g) of series 4 (15 mol% Al$_2$O$_3$) KAP glasses	99
4.8a	Thermal expansion coefficient (α) of series 1 (metaphosphate), 2 (65 mol% P$_2$O$_5$) and 3 (20 mol% K$_2$O) KAP glasses	100
4.8b	Thermal expansion coefficient (α) of series 4 (15 mol% Al$_2$O$_3$) KAP glasses	100
4.9a	Thermo-optic coefficient (dn/dT) of series 1 (metaphosphate),	101

	2 (65 mol% P_2O_5) and 3 (20 mol% K_2O) KAP glasses	
4.9b	Thermo-optic coefficient (*dn/dT*) of series 4 (15 mol% Al_2O_3) KAP glasses	102
4.10	α and *dn/dT* of KAP glasses as a function of $Al(PO_3)_3$ mole fraction	103
4.11	Comparison of measured and estimated *dn/dT* of KAP glasses	104
4.12	*dn/dT* of KAP glasses as a function of α	105
4.13	*A* of KAP glasses as a function of *n*	105
4.14	γ of KAP glasses as a function of $Al(PO_3)_3$ mole fraction	106
5.1	Infrared transmission spectra through xMO-(100-x)P_2O_5 glasses	118
5.2	Ultraviolet transmission spectra through xMO-(100-x)P_2O_5 glasses	119
5.3	Ultraviolet absorption spectra through xMO-(100-x)P_2O_5 glasses	120
5.4	Refractive index (*n*) of CaP and BaP glasses	121
5.5a	Glass transition temperature (T_g) of CaP and BaP glasses	121
5.5b	Glass transition temperature (T_g) of NaP glasses	124
5.6a	Thermal expansion coefficient (α) of CaP and BaP glasses	125
5.6b	Thermal expansion coefficient (α) of NaP glasses	125
5.7	Thermo-optic coefficient (*dn/dT*) of CaP and BaP glasses	126
5.8	α and *dn/dT* of CaP and BaP glasses as a function of MeO mol%	127
5.9	Comparison of measured and estimated *dn/dT* of BaP glasses	128
5.10	*dn/dT* of CaP and BaP glasses as a function of α	129
5.11	γ of CaP and BaP glasses as a function of MeO mol%	130
5.12	Total internal reflection in a fibre	134
5.13	Axial stress in a fibre	135
5.14	Cladding stress as a function of (core/clad) ratio for different (α_{co}-α_{cl}) values	136
5.15	Viscosity ranges for extrusion	137
5.16	DTA plots for *BaP-1c* (core) and *KAP-1d* (clad) glasses	137
5.17	Cane cut-back attenuation measurement set-up	139
5.18	DTA plots of *KaP-1d* sample under oxidising and reducing conditions	141
5.19	Cross-section of *BaP-1c* : *KaP-1d* planar sample : (a) optical microscope and (b) SEM	142
5.20	UV written channels in *BaP-1c* bulk glass : (a) top view and (b) cross-section	144
5.21	Cross-section of femtosecond written channels at 50 mW in *KAP-1d* bulk glass with a (a) 10X objective and (b) 50X objective	145

5.22	NA measurement set up	146
5.23	Estimation of NA	147
5.24	Modal output of the waveguide written at 150 mW and 80 μm/s with a 50X objective	147
5.25	(a) Cross-section and (b) modal output of the waveguide written at 270 mW and 80 μm/s with a 50X objective	148
6.1	BaBP and NaBP glass-forming region	156
6.2a	Refractive index (n) of BaBP glasses	159
6.2b	Refractive index (n) of NaBP glasses	160
6.3a	Glass transition temperature (T_g) of BaBP glasses	161
6.3b	Glass transition temperature (T_g) of NaBP glasses	161
6.4a	α and dn/dT of BaBP glasses as a function of B/(B+P) ratio	163
6.4b	α and dn/dT of NaBP glasses as a function of B/(B+P) ratio	163
6.5	Comparison of measured and estimated dn/dT of BaBP and NaBP glasses	164
6.6a	dn/dT of BaBP glasses as a function of α	165
6.6b	dn/dT of NaBP glasses as a function of α	165
6.7	γ of BaBP and NaBP glasses as a function of B/(B+P) ratio	166
6.8	Infrared transmission spectra through (100-x)$Ba(PO_3)_2$-xB_2O_3 glasses	167
6.9	Ultraviolet transmission spectra through (100-x)$Ba(PO_3)_2$-xB_2O_3 glasses	168
6.10	Ultraviolet absorption spectra through (100-x)$Ba(PO_3)_2$-xB_2O_3 glasses	169
6.11	Transmission spectra through *BaBP-1b* (core) and *BaBP-2c* (clad) glasses	172
6.12	DTA plots for *BaBP-1b* (core) and *BaBP-2c* (clad) glasses	174
6.13	*BaBP-1b* : *BaBP-2c* extruded cane : (a) side view and (b) cross-section	175
6.14	(Core/clad) ratio at different cane lengths	176
6.15	Cross-section of 150 μm OD *BaBP-1b* : *BaBP-2c* fibre	178
6.16	Loss measurement set-up	178
6.17	*BaBP-1b* : *BaBP-2c* fibre cladding loss	179
6.18	*BaBP-1b* : *BaBP-2c* fibre core loss	180
6.19	Cross-section of UV written channels in *BaBP-1b* bulk glass	182
6.20	Cross-section of femtosecond written channels at 20 mW in *BaBP-1b* bulk glass with a (a) 10X objective and (b) 50X objective	183
7.1	Flow diagram summarising the main stages in the research	189

LIST OF PHOTOGRAPHS

Photograph	***Title***	***Page***
3.1	Glass melting	54
3.2	Glass casting	55
3.3	Interferometer set-up	68
3.4	Sample holder	69
3.5	Fringe pattern	69
3.6	Body parts for extrusion	75
3.7	Extrusion rig	76
3.8	Fibre neck down	78
5.1	*BaP-1c* : *KaP-1d* planar sample	140
6.1	*BaBP-1b* : *BaBP-2c* preform	177

LIST OF TABLES

Table	***Title***	***Page***
1.1	Properties of pure network formers	4
1.2	Relationship between g and dn/dT	10
2.1	Properties of metaphosphate glasses	18
2.2	Relationship between the phosphate glass networks and the O/P ratio	20
2.3	Q^i fractions in binary phosphate glasses	21
2.4	j_i of various oxides in silicate and phosphate laser glasses	32
2.5	Properties of optical materials for ridge-loaded silica-based athermal waveguide	35
2.6	Summary of the research work on lower temperature sensitivity	40
3.1	Raw materials for glass melting	51
3.2	Casting material	51
3.3	Sample thickness for property measurements	56
3.4	dn/dT of trial glasses	72
3.5	dn/dT values for barium metaphosphate sample at different thickness	73
4.1	Compositions of KAP glasses	88
4.2	Thermal properties of KAP glasses	90
4.3	Optical properties of KAP glasses	91
4.4	Athermalisation parameters of KAP glasses	108
5.1	Compositions of NaP, CaP and BaP glasses	114
5.2	Thermal properties of NaP, CaP and BaP glasses	116
5.3	Optical properties of NaP, CaP and BaP glasses	117
5.4	Athermalisation parameters of CaP and BaP glasses	131
5.5	Combination of core and clad glasses using potassium aluminophosphate and binary phosphate glasses	132
6.1	Compositions of BaBP and NaBP glasses	155
6.2	Thermal properties of BaBP and NaBP glasses	157
6.3	Optical properties of BaBP and NaBP glasses	158

6.4	Athermalisation parameters of BaBP and NaBP glasses	170
6.5	Combination of core and clad glasses using KAP and BaBP glasses	171
7.1	*dn/dT* semi-empirical equations	192

ACKNOWLEDGEMENTS

I would like to convey my utmost gratitude to my supervisor, Dr. E.R.M. Taylor, for the opportunity to work together with her, which has proved to be an invaluable experience. In addition, I would like to thank her for her advice, guidance and encouragement throughout the course of this project, which has helped tremendously in the development of this research work.

I would also like to thank Dr. H. Ebendorff-Heidipriem for her guidance and fruitful discussion on the general subject of glasses, including glass chemistry and the glass melting process.

Special mention of appreciation also goes to Neil Sessions, for his time spent in the workshop, building the heat chamber and sample holder for the interferometer set-up. Also, I appreciate his help with the SEM and EDAX equipment.

Appreciation is also due to Dr. C.B.E. Gawith for his help in writing UV channels and E. Bricchi and W. Yang for their assistance in writing femtosecond channels in the phosphate glasses. I would also like to thank Dr. A. Favre for her help with the spin-coating process, R. Moore for his effort in the fibre drawing process and K. Frampton for his help in machining the extrusion die and his input towards the extrusion process. Thanks also to Dr. P.G.R. Smith, for the use of his laboratory for the NA measurements.

I would also like to take this opportunity to thank Dr. E. Tarbox, for her constructive suggestions and comments with regards to this PhD thesis.

Last but not least, I want to thank my family and friends for their support and also to all that have helped me in one way or another throughout the course of my research.

Financial support has been provided by the EPSRC under the PHOTON project 'Physical-Layer High-Speed Optoelectronics for Tomorrow's Optical Networks' and the Committee of Vice-Chancellors and Principals under the Overseas Research Students Awards Scheme.

NOMENCLATURE

Subscript	***Definition***
cl	Clad
co	Core
eff	Effective

Symbol	***Definition***	***SI Unit***
a	Radius	m
a	Ion-oxygen bond distance	m
b	Fractional power	
dn/dT	Thermo-optic coefficient	K^{-1}
dS/dT	Change of optical path length with temperature	$m\ K^{-1}$
$d\phi/dT$	Change of phase with temperature	$rad\ K^{-1}$
$d\lambda_B/dT$	Change of Bragg wavelength with temperature	$m\ K^{-1}$
E	Young's modulus	Pa
h	Height	m
L	Length	m
l	Thickness	m
M_{TO}	Number of terminal oxygen per modifying cation	
N_A	Avogadro's number (6.022×10^{23})	
n	Refractive index	
n_D	Refractive index at λ = 589.3 nm	
n_e	Refractive index at λ = 546.1 nm	
P	Power	W
P	Pressure	Pa
P_e	Electronic polarisability	m^3
r	Absorption coefficient	m^{-1}

r_k	Ionic radius	m
r_{OH}	Relative OH content	m^{-1}
S	Optical path length	m
T	Temperature	K
T	Transmission	
T_f	Fibre drawing temperature	K
T_g	Glass transition temperature	K
T_p	Peak crystallisation temperature	K
T_s	Softening temperature	K
T_x	Onset of crystallisation temperature	K
ΔT	Temperature difference	K
V	Normalised frequency	
V_m	Molar volume	m^3
v	Poisson's ratio	
z	Ion valence	
α	Thermal expansion coefficient	K^{-1}
$\Delta\alpha$	Thermal expansion coefficient difference	K^{-1}
α_{loss}	Loss	dB/m
α_{sub}	Substrate thermal expansion coefficient	K^{-1}
γ	Change of (ln) polarisability with (ln) inter-ionic distance, $[\partial(lnP_e)/\partial(lnr)]_T$	
β	Change of (ln) polarisability with temperature, $d(lnP_e)/dT$	K^{-1}
ϕ	Diameter	m
φ	Phase	rad
$\Delta\varphi$	Phase difference	rad
Λ	Grating period	m
λ	Wavelength	m
λ_B	Bragg wavelength	m
$\lambda_{cut\text{-}off}$	Cut-off wavelength	m
θ	Angle	rad
θ_c	Critical angle	rad
σ	Stress	Pa

GLOSSARY OF TERMS

Term	***Definition***
ADC	Analogue-to-digital converter
ArF	Argon fluoride
Al^{3+}	Aluminium ion
Al(4)	Tetrahedral aluminium unit
Al(6)	Octahedral aluminium unit
$Al(OH)_3$	Aluminium hydroxide
$Al(PO_3)_3$	Aluminium phosphate
Al_2O_3	Aluminium oxide (Alumina)
B^{3+}	Boron ion
B(3)	Trigonal boron unit
B(4)	Tetrahedral boron unit
B/(B+P)	Ratio of boron to the sum of boron and phosphorus
$Ba(PO_3)_2$	Barium phosphate
B_2O_3	Boron oxide
Ba^{2+}	Barium ion
$BaCO_3$	Barium carbonate
BaO	Barium oxide
BaBP	Barium borophosphate
BaP	Barium phosphate
BO	Bridging oxygen
Ca^{2+}	Calcium ion
$CaCO_3$	Calcium carbonate
CaO	Calcium oxide
CaP	Calcium phosphate
CCD	Charge coupled device
CN	Coordination number
CW	Continuous wave

De/Mux	Demultiplexer/Multiplexer
DTA	Differential thermal analyser
DWDM	Dense wavelength division multiplexing
EDAX	Energy dispersive analysis of X-Ray
FBG	Fibre Bragg grating
Fe^{2+}	Iron (II) ion
Fe^{3+}	Iron (III) ion
FTIR	Fourier transform infrared
fs	Femtosecond
GeO_2	Germanium oxide (Germania)
He-Ne	Helium-neon
IBM	Ion beam milling
ID	Inner diameter
IR	Infrared
K^+	Potassium ion
K_2CO_3	Potassium carbonate
K_2O	Potassium oxide
KAP	Potassium aluminophosphate
KrF	Krypton fluoride
LPFG	Long period fibre grating
MeO	Modifying oxide
Na^+	Sodium ion
Na_2CO_3	Sodium carbonate
Na_2O	Sodium oxide
NaBP	Sodium borophosphate
NaP	Sodium phosphate
$NaPO_3$	Sodium phosphate
NA	Numerical aperture
NBO	Non-bridging oxygen
NIR	Near infrared
NMR	Nuclear magnetic resonance
O/P	Oxygen-to-phosphorus ratio

O_2	Oxygen
OD	Outer diameter
OH	Hydroxyl (water)
P^{5+}	Phosphorus ion
P_2O_5	Phosphorus oxide
Q^i	Phosphate tetrahedral units, i = number of bridging oxygens
RF	Radio frequency
rpm	Revolution per minute
SiO_2	Silicon oxide (Silica)
TIR	Total internal reflection
TMA	Thermomechanical analyser
TO	Terminal oxygen
UV	Ultraviolet
Vis	Visible
WDM	Wavelength division multiplexing

CHAPTER 1

INTRODUCTION

1.1 Objectives and Scope of the Research

This research served to develop and characterise various glass compositions which have application potential in athermal waveguide development. The glass systems of interest in this work were the phosphates and borophosphates, which exhibit negative refractive index change with temperature, also known as the thermo-optic coefficient, *dn/dT*. Fabrication of Bragg gratings and wavelength division multiplexing (WDM) components could then be implemented once the athermal waveguides were developed. The goal was to achieve a Bragg wavelength temperature sensitivity, $d\lambda_B/dT$, of less than 5 pm/°C at wavelength, λ = 1.55 μm, within the temperature range of 20 - 100°C. In summary, there were four main objectives within this research work to be carried out, in the following order, towards the final utilisation of these athermal glasses :

- *Construction of an interferometer set-up to measure the thermo-optic coefficient (dn/dT) of glasses.*
- *Preparation, characterisation and comparison of different phosphate glass systems.*
- *Design and development of glass compositions with negative thermo-optic coefficient (dn/dT) for athermalisation.*
- *Fabrication of athermal waveguides.*
- *Fabrication of temperature-independent De/Mux devices (future work).*

1.2 Motivation

The requirements of future low cost data communication systems are likely to be very demanding both in terms of cost and the required system performance. The trend towards WDM usage to increase system bandwidth in point-to-point telecommunication is likely to be mirrored in a shift to WDM in data communication networks. Dense wavelength division multiplexing (DWDM) technology has been an interesting growth area in the fibre optic communication industry in the past several years because it can efficiently increase the transmission capacity of the fibre optical networks and allows all optical routing functions to be implemented. However, the cost drivers in data communication networks are likely to prevent the use of actively temperature-stabilised components. This means that wavelength discriminating components such as add/drop multiplexers will need to have stable spectral responses over a large temperature range. A very attractive component for such a system would be a temperature insensitive fibre Bragg grating to define channel frequencies, filter noise, enable add/drop multiplexers, etc.

Lightwave devices such as resonators, filters and gratings have a serious problem in that the central resonance wavelength (or frequency) fluctuates with temperature. The sensitivity can be as large as 0.01 nm/K for silica-based waveguide filters and 0.08 nm/K for semiconductor-based waveguide filters (at λ = 1.55 μm) [1-5]. This dependence is generally caused by the temperature dependence of the optical path length, S, of the waveguide. Thus, a DWDM system with very close channel spacing, such as 5 GHz (40 pm at 1.55 μm) [6], would require a precise temperature control unit to avoid any crosstalk due to the temperature dependence of the central wavelength. Another solution is to mount the lightwave devices onto substrates with differing thermal expansion coefficients to offset the effect of temperature [7,8]. However, such methods will be an obstacle to the broad use of WDM systems from the viewpoint of cost, device size and reliability. Therefore a solution is to develop an athermal waveguide in which the optical path length change with temperature is zero.

Glasses are ideal candidates for athermal waveguide development due to their versatility. The chemical and physical properties of glass can be exploited to develop more efficient, low-cost and compact planar and fibre devices for the information industry. Chemically, glass compositions can be tailored to meet optical and thermal requirements such as selecting the spectroscopic

features of dopant ions, the photosensitivity, the refractive index (n), the glass transition temperature (T_g), the thermal expansion coefficient (α) and the thermo-optic coefficient (dn/dT), among others. Also, glasses are a suitable optical material for processing as they can be physically moulded, pressed, extruded and drawn into fibres.

In general, athermal glasses show a small or negative dn/dT value and a positive thermal expansion coefficient, α. They are currently used within laser systems to eliminate thermally induced distortion in lenses [9,10]. Today, these glasses can be exploited to support development of essential lightwave devices such as Bragg gratings in DWDM systems. Hence, the assessment of dn/dT of the glasses developed within this work as well as the understanding of how different ions and other glass properties affect dn/dT are essential. This will provide a basic foundation for tailoring the glass composition to meet the dn/dT requirement for specific applications, such as eliminating the thermal lensing effect in laser glasses and eliminating the temperature dependence of the resonance wavelength of devices such as gratings and filters.

Previous development on athermal waveguides had centred mainly on silica [1-5,11-13]. However, due to the positive α and dn/dT of silica glasses [14], athermal devices can only be achieved, either by producing multi-layer structures with the introduction of materials with negative dn/dT in some of the layers [1-5] or by mounting the devices on suitable substrates [7,8,12] to compensate for the effect of thermal expansion. The use of substrates can be an obstacle to the broad use of WDM systems from the viewpoint of cost, device size and reliability. Also, the small silica α restricts the α of the other layers in a multi-layer waveguide system or the substrates to a limited range within that of silica, hence restricting the choice of suitable materials and substrates that can be used.

Alternatively, athermal waveguides can be developed using glasses which intrinsically exhibit negative dn/dT to counter the effect of α. Such glasses fall under the categories of phosphate, borate and borophosphate glasses, and this is where this research comes in, which is to produce athermal phosphate glass-based devices. Manipulation of the glass compositions allows simultaneous modification of both α and dn/dT, without any restriction. This means that glasses with high α can be potentially used for athermalisation purposes, provided that there is a corresponding negative dn/dT. Table 1.1 lists the properties of the pure network formers [14].

The principles of athermalisation will be discussed in Section 1.3.

Glasses	n_e (at λ = 546.1 nm)	α (´ 10^{-6}/°C)	dn/dT (´ 10^{-6}/°C)
GeO_2	1.6056	7.1	+19.4
SiO_2	1.4601	0.6	+10.4
B_2O_3	1.4650	14.4	-35.0
P_2O_5	1.4930	13.7	-92.2

Table 1.1 : Properties of pure network formers

The main objective of this research was to develop and study different phosphate glasses and assess the viability of fabricating athermal devices in bulk phosphate glasses. Device fabrication in athermal bulk phosphate glasses is advantageous because the properties of the glasses can intrinsically compensate for changes in temperature to achieve athermalisation. This eliminates the need for an extrinsic substrate or extra processing steps.

1.3 Concept of Athermalisation

1.3.1 Bulk Glass

The optical path length, *S*, of an optical material is sensitive to changes in temperature due to the combined effect of thermal expansion and thermal refractive index change. Athermalisation is a process which eliminates the temperature dependence of the optical path length. The optical path length of a homogeneous bulk material can be defined as [1]

$$S = nL \tag{1.1}$$

where n is the refractive index of the medium and L is the length of the medium. The temperature dependence of S can then be defined as

$$\frac{1}{L}\left(\frac{dS}{dT}\right) = n\alpha + \frac{dn}{dT} \tag{1.2}$$

where α is the thermal expansion coefficient ($\alpha = (1/L)(dL/dT)$), dn/dT is the thermo-optic coefficient and T is temperature. Athermalisation is achieved by equating equation (1.2) to zero ($dS/dT = 0$), giving the athermal condition as

$$\frac{dn}{dT} = -n\alpha \tag{1.3}$$

As glasses generally exhibit positive α values, dn/dT must be negative to satisfy equation (1.3).

1.3.2 Bragg Grating

Using the same principle as discussed in Section 1.3.1, we can develop a similar argument for the athermalisation of a Bragg grating. The central Bragg wavelength, λ_B, is defined as [15]

$$\lambda_B = 2n\Lambda \tag{1.4}$$

where n is the refractive index and Λ is the grating period. Differentiating equation (1.4) with respect to temperature results in the temperature dependence of the Bragg wavelength, $d\lambda_B/dT$, being defined as

$$\frac{d\lambda_B}{dT} = 2\Lambda\left(n\alpha + \frac{dn}{dT}\right) \tag{1.5}$$

For an athermal grating, $d\lambda_B/dT$ must be zero. Hence we need to satisfy the following athermal condition

$$\frac{dn}{dT} = -n\alpha \tag{1.6}$$

This is similar to equation (1.3) for an athermal bulk material. This is due to the fact that equation (1.5) can be expressed as

$$\frac{d\lambda_B}{dT} = 2\Lambda\left(\frac{1}{L}\frac{dS}{dT}\right) \tag{1.7}$$

where from equation (1.2), $(1/L)(dS/dT) = n\alpha + dn/dT$. Equation (1.7) shows that we can develop an athermal material ($dS/dT = 0$) into which a grating can be fabricated in order to produce an athermal grating.

1.3.3 Optical Waveguides and Fibres

In this work, the fabrication of fibres and planar waveguides are explored using the glasses studied within this research to produce athermal waveguides. For optical waveguides, it is necessary to modify equations (1.2) and (1.5) to equations (1.8) and (1.9) respectively, incorporating effective refractive index, n_{eff}, and effective thermo-optic coefficient, dn_{eff}/dT, to take into account the evanescent wave leaking into the substrate as the light propagates through the core. The thermal expansion of the substrate, α_{sub}, dominates in the device due to the substrate's considerable thickness compared to the core layer and is therefore used in the equations. Similar athermal conditions apply as before, by making $dS/dT = d\lambda_B/dT = 0$.

$$\frac{1}{L}\frac{dS}{dT} = \left(n_{eff}\alpha_{sub} + \frac{dn_{eff}}{dT} \right) \tag{1.8}$$

$$\frac{d\lambda_B}{dT} = 2\Lambda\left(n_{eff}\alpha_{sub} + \frac{dn_{eff}}{dT} \right) \tag{1.9}$$

n_{eff} can be defined in equation (1.10). The analysis leading to this expression can be found in references [16-18].

$$n_{eff}^2 = b_{co}n_{co}^2 + b_{cl}n_{cl}^2 \tag{1.10}$$

where the subscripts *co* and *cl* refer to core and clad respectively and b_{co} and b_{cl} ($b_{cl} = 1 - b_{co}$) represent the fraction of the power confined in the core and clad respectively.

For a fibre, b_{co} can be represented by an empirical equation valid for $1.5 \leq V \leq 2.5$ [18]:

$$b_{co} = \left(A - \frac{B}{V} \right)^2 \tag{1.11}$$

where $A = 1.1428$ and $B = 0.996$ and V is the normalised frequency, defined as $V = \frac{2\pi}{\lambda} a(NA)$.

NA is known as the numerical aperture, defined as $NA = \sqrt{n_{co}^2 - n_{cl}^2}$ and a is the radius of the fibre core.

For a simple planar slab waveguide, b_{co} can be represented by an approximate expression valid for all V [19]:

$$b_{co} = 1 - \frac{ln\left(1 + 2V^2\right)}{2V^2} \tag{1.12}$$

dn_{eff}/dT can be obtained by differentiating equation (1.10) with respect to temperature and is defined below.

$$\frac{dn_{eff}}{dT} = b_{co}\frac{n_{co}}{n_{eff}}\frac{dn_{co}}{dT} + b_{cl}\frac{n_{cl}}{n_{eff}}\frac{dn_{cl}}{dT} + \frac{dn_{eff}}{db_{co}}\frac{db_{co}}{dT} \tag{1.13}$$

where $\frac{dn_{eff}}{db_{co}}\frac{db_{co}}{dT} = \frac{dn_{eff}}{db_{co}}\frac{db_{co}}{dV}\frac{dV}{dT}$ with $\frac{dn_{eff}}{db_{co}} = \frac{NA^2}{2n_{eff}}$, $\frac{db_{co}}{dV} = 2\left(A - \frac{B}{V}\right)\frac{B}{V^2}$ (fibre),

$\frac{db_{co}}{dV} = \frac{ln\left(1 + 2V^2\right)}{V^3} - \frac{2}{V\left(1 + 2V^2\right)}$ (planar) and $\frac{dV}{dT} = V\left[\alpha_{co} + \left(\frac{n_{co}\frac{dn_{co}}{dT}}{NA^2}\right) - \left(\frac{n_{cl}\frac{dn_{cl}}{dT}}{NA^2}\right)\right]$.

1.4 *dn/dT* of Glasses

The thermo-optic coefficient of glasses can be understood via the use of the Lorentz-Lorenz equation (equation (1.14) [20]) for refractive index.

$$\frac{n^2-1}{n^2+2}=\frac{4}{3}\frac{\pi N_A P_e}{V_m} \tag{1.14}$$

where n is the refractive index, N_A is the Avogadro's number (6.022×10^{23}), P_e is the electronic polarisability and V_m is the molar volume. The equation for dn/dT can be derived from equation (1.14) and is defined in equation (1.15), with the approximation of ($d(\ln V_m)/dT \sim 3\alpha$) [21]. The derivation leading to equation (1.15) is described in Appendix A.

$$\frac{dn}{dT}=A[\beta-3\alpha] \tag{1.15}$$

where $A = [(n^2-1)(n^2+2)/6n]$, $\beta = d(\ln P_e)/dT$ and T is temperature. Equation (1.15) shows that dn/dT is affected by n, P_e and α of the glass.

Equation (1.15) can be modified to equation (1.16) below, as polarisability is increased by an increase in the inter-ionic distance due to a change in temperature. This uses the expression of $\beta = [\partial(\ln P_e)/\partial(\ln r)]_T \cdot [d(\ln r)/dT]$ and $\alpha = [d(\ln r)/dT]$ [22].

$$\frac{dn}{dT}=A(\gamma-3)\alpha \tag{1.16}$$

where γ is the change in polarisability due to a change in inter-ionic distance ($\gamma = [\partial(\ln P_e)/\partial(\ln r)]_T$), *and* r is the inter-ionic distance.

The sign of *dn/dT* depends on γ as *A* and α are positive for glasses. The effects of γ on *dn/dT* are summarised in Table 1.2.

γ	*dn/dT*
> 3	+
3	0
< 3	-

Table 1.2 : Relationship between γ and *dn/dT*

For some multi-component glasses, $\gamma = \sum_i \gamma_i X_i = \sum_i g_i \alpha_i X_i$ holds [22,23]. Here, γ_i is the additive contribution from the glass' *i*-th component, which is equivalent to $g_i \alpha_i$, and X_i is the *i*–th component mole fraction. Hence a glass can be designed to give $\gamma < 3$ by varying its components simultaneously. It is found that γ increases with cationic field strength, as shown in Figure 1.1 [22], where cationic field strength is defined as the ratio of the ion valence to the square of the bond distance between the ion and oxygen (z/a^2) [24]. Therefore, in order to obtain a glass with negative *dn/dT*, we require modifiers with low cationic field strength.

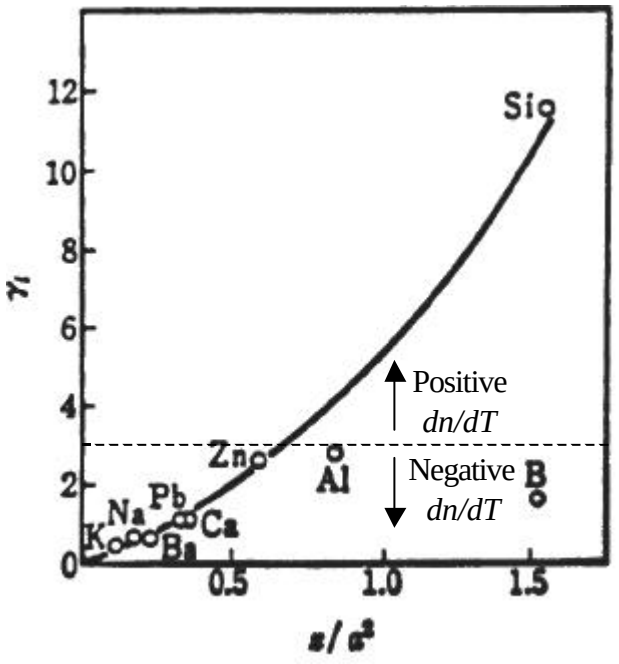

Figure 1.1 : Relationship between γ and z/a^2 [22]

1.5 Contribution of the Research

This research project integrated the knowledge from the fields of material science and device fabrication, starting with the development of glasses and property characterisation through to the athermal waveguide development phase, based on these glasses. The main contributions of this research towards the advancement of the fields of material development and athermalisation were listed below.

- *An extensive experimental study and the first reported dn/dT of some phosphate glass systems.*

- *Definition of semi-empirical equations relating dn/dT and α of some phosphate glass systems. These enable the dn/dT of glasses within these systems to be directly estimated from their α and n.*

- *The synthesis, characterisation and study of potassium aluminophosphate glasses of the K_2O-Al_2O_3-P_2O_5 system in the 2.8 < Oxygen-to-phosphorus ratio (O/P) < 3.1 range, encompassing the ultraphosphate, metaphosphate and polyphosphate compositions.*

- *The synthesis, characterisation and study of binary phosphate glasses of the following systems*
  - *$xBaO$-$(100-x)P_2O_5$ and $xCaO$-$(100-x)P_2O_5$ in the range of $20 \leq x \leq 50$.*
  - *xNa_2O-$(100-x)P_2O_5$ in the range of $40 \leq x \leq 50$.*

- *The synthesis, characterisation and study of borophosphate glasses of the following systems*
  - *$50BaO$-xB_2O_3-$(50-x)P_2O_5$ in the range of $5 \leq x \leq 12$.*
  - *$(100-x)Ba(PO_3)_2$-xB_2O_3 in the range of $10 \leq x \leq 60$.*
  - *$(100-x)NaPO_3$-xB_2O_3 in the range of $10 \leq x \leq 50$.*

- *Fabrication and characterisation of phosphate glass-based planar waveguides and fibres.*

1.6 Layout of Thesis

This thesis is a culmination of the work achieved during my PhD research project, reporting the various material development and characterisation work as well as waveguide fabrication. It is organised into seven chapters.

Chapter 1 states the aims of this project and the motivation behind the direction of this research. A thorough analysis of the concept of athermalisation is also carried out. A literature review on the various subjects relevant to my research is reported in Chapter 2.

Chapter 3 describes the principles behind the different processes, fabrication techniques and characterisation work performed. A section is dedicated to an experimental interferometer set-up, constructed specifically for the study of *dn/dT*.

The main experimental results of this thesis are contained in Chapters 4 – 6, describing the synthesis and property measurements of three different glass systems, along with the results obtained, discussions and fabrication of athermal waveguides using these glasses. The glasses studied are potassium aluminophosphate glasses (Chapter 4), binary calcium phosphate, barium phosphate and sodium phosphate glasses (Chapter 5) and barium borophosphate and sodium borophosphate glasses (Chapter 6).

The conclusions and future work for the phosphate glass development and athermal work are summarised in Chapter 7.

Various derivations of equations and calculations are included in the Appendices to supplement the main text within this thesis. In addition, Appendix E details an additional separate study on photolithography and ion beam milling (IBM) as a technique for fabricating channel waveguides in bismuthate glasses, which I carried out during the course of my PhD. The materials in Appendix E are extracts from the final report presented to ASAHI Glass Company Ltd, which funded the work.

REFERENCES

1. Y. Kokubun, N. Funato and M. Takizawa, *"Athermal waveguides for temperature-independent lightwave devices"*, IEEE Photonics Technology Letters 5 (11), pp 1297-1300 (1993).

2. Y. Kokubun, M. Takizawa and S. Taga, *"Three-dimensional athermal waveguides for temperature independent lightwave devices"*, Electronics Letters 30 (15), pp 1223-1224 (1994).

3. Y. Kokubun, S. Yoneda and H. Tanaka, *"Temperature-independent narrow-band filter by athermal waveguide"*, European Conference on Optical Communications, paper WeD.1.5, ECOC 1996, Oslo.

4. Y. Kokubun, S. Yoneda and H. Tanaka, *"Temperature-independent narrowband optical filter at 1.3mm wavelength by an athermal waveguide"*, Electronics Letters 32 (21), pp 1998-2000 (1996).

5. Y. Kokubun, S. Yoneda and S. Matsuura, *"Temperature-independent optical filter at 1.55mm wavelength using a silica-based athermal waveguide"*, Electronics Letters 34 (4), pp 367-369 (1998).

6. K. Inoue, N. Takato, H. Toba and M. Kawachi, *"A four-channel optical waveguide multi/demultiplexer for 5-GHz spaced optical FDM transmission"*, Journal of Lightwave Technology 6 (2), pp 339-345 (1988).

7. G.W. Yoffe, P.A. Krug, F. Ouellete and D. Thorncraft, *"Temperature-compensated optical fiber Bragg gratings"*, in: Conference on Optical Fiber Communication, OFC 1995, Technical Digest, pp 134-135 (1995).

8. M. Tamura, A. Urano, A. Inoue, D. Saitou, M. Inai, T. Itou, M. Shiozaki, H. Suganuma and I. Tsuchiya**, "***Development of a temperature-compensating fiber grating*", SEI Technical Review 51, pp 61-66 (2001).

9. M.J. Weber, *"Science and technology of laser glass"*, Journal of Non-Crystalline Solids 123, pp 208-222 (1990).

10. J.H. Campbell and T.I. Suratwala, *"Nd-doped phosphate glasses for high-energy/high-peak-power lasers"*, Journal of Non-Crystalline Solids 263&264, pp 318-341 (2000).

11. K. Shima, K. Himeno, T. Sakai, S. Okude and A. Wada, *"A novel temperature-insensitive long-period fiber grating using a boron-codoped-germanosilicate-core fiber*", in: Conference on Optical Fiber Communication, paper FB2, OFC 1997.

12. A. Sakamoto, T. Matano and H. Takeuchi**, "***Ceramic substrate with negative thermal expansion for athermalization of fiber Bragg grating*", IEICE Transactions on Electronics E83-C (9), pp 1441-1446 (2000).

13. K. Kintaka, J. Nishii, H. Nishiyama, Y. Kawamoto and A. Sakamoto, *"Athermalization of a silica-based waveguide with a UV-induced Bragg grating on a crystallized glass substrate"*, Journal of Lightwave Technology 21 (3), pp 831-836 (2003).

14. W. Vogel, *"Optical properties of oxide glasses"*, Optical Properties of Glass, D.R. Uhlmann and N.J. Kreidl (Eds), The American Ceramic Society Inc., OH, (1991).

15. T. Erdogan, *"Fiber grating spectra"*, Journal of Lightwave Technology 15 (8), pp 1277-1294 (1997).

16. D. Gloge, *"Weakly guiding fibers"*, Applied Optics 10 (10), pp 2252-2258 (1971).

17. D. Gloge, **"***Dispersion in weakly guiding fibers"*, Applied Optics 10 (11), pp 2442-2445 (1971).

18. A. Ghatak and K. Thyagarajan, Introduction to fibre optics, Chapter 8, Cambridge University Press, UK, (1998).

19. K.L. Chen and S. Wang, *"An approximate expression for the effective refractive index in symmetric DH lasers"*, IEEE Journal of Quantum Electronics QE-19, pp 1354-1356 (1983).

20. M. Born and E. Wolf, Principles of Optics, Chapter 2, Pergamon Press, Oxford, UK, (1984).

21. L. Prod'homme, *"A new approach to the thermal change in the refractive index of glasses"*, Physics and Chemistry of Glasses 1 (4), pp 119-122 (1960).

22. T. Izumitani and H. Toratani, *"Temperature coefficient of electronic polarizability in optical glasses"*, Journal of Non-Crystalline Solids 40, pp 611-619 (1980).

23. H. Toratani, *"Properties of laser glasses"*, PhD thesis, Kyoto University, Kyoto, Japan, 1989.

24. A. Dietzel, *"Die kationenfeldstarken und ihre beziehungen zu entglasungsvorgangen, zur verbindungsbildung und zu den schmelzpunkten von silicaten"*, Z. Elektrochem. 48 (1), pp 9-23 (1942).

CHAPTER 2

LITERATURE REVIEW

The main part of this research work involved the development and investigation of phosphate glasses as potential base glasses for athermalisation applications. Section 2.1, within this chapter, presents a topical review of phosphate glasses with emphasis on binary phosphate, aluminophosphate and borophosphate glasses, which were the three phosphate systems investigated within this work. The basic phosphate tetrahedral sites are presented and used to explain the different phosphate networks, as set by the oxygen-to-phosphorus (O/P) ratio. The structures of binary phosphate, aluminophosphate and borophosphate glasses are also examined as these affect the properties of the glasses.

In Section 2.2, a review of the different experimental techniques for measuring *dn/dT* is given. Measurement of *dn/dT* is essential within this work as it is one of the parameters critical in determining the potential of the glasses for athermalisation. Section 2.3 reviews the current development in athermal waveguides which serves as the starting point for this research.

2.1 Phosphate Glasses

2.1.1 Properties

The glass former component in phosphate glasses is P_2O_5. Pure P_2O_5 has a melting point of 560°C and a boiling point of 605°C. Some of the properties of pure P_2O_5 glass include n_e = 1.4930 (at λ = 546.1 nm), α = 13.7×10^{-6}/°C and *dn/dT* = -92.2×10^{-6}/°C [1]. Hypothetically, P_2O_5 has a UV edge of less than 150 nm (~ 8.27 eV), as shown in Figure 2.1. However, P_2O_5 generally contains water and this shifts the edge towards longer wavelengths. A more realistic structure is the HPO_3 glass, with a UV edge at ~ 270 nm (~ 4.60 eV).

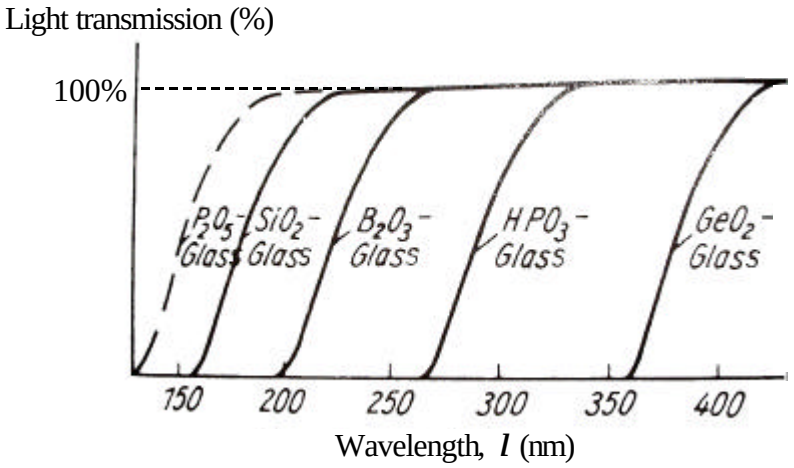

Figure 2.1 : UV edges for different glass formers [1]

Phosphate glasses are technologically and biologically important materials as they generally have a higher thermal expansion coefficient, α, and a lower transition temperature, T_g, than silicate and borate glasses [2] and many alkali, alkaline earth, transition metal and rare earth oxides can be added to modify these properties. There are also great interests in alkaline earth phosphate glasses due to their high transparency for ultraviolet (UV) light (Figure 2.1). However, phosphate glasses have poor chemical durability which often limits their practical applications, that is generally overcome by adding certain oxides to the phosphate glasses, such as PbO [3], Al_2O_3 and Fe_2O_3 [4,5].

Phosphate glasses have practical application potential in athermalisation as they generally exhibit negative thermo-optic coefficient, *dn/dT*, which is a pre-requisite for achieving athermalisation, as discussed in Section 1.3. Different modifying cations can be added to modify the properties of the phosphate glasses to meet the required optical and thermal requirements. Table 2.1 shows the properties of some metaphosphate glasses.

Glasses	n_e [6]	T_g (°C) [6]	α (´ 10^{-6}/°C) [6]	dn/dT (´ 10^{-6}/°C) [1]
$Zn(PO_3)_2$	1.5260	310	5.8	+5.1
$Al(PO_3)_3$	1.5310	-	5.7	+5.0
$Y(PO_3)_3$	-	-	-	+4.9
$Mg(PO_3)_2$	1.4974	510	8.3	+2.9
$La(PO_3)_3$	1.6000	570	7.8	+0.9
$Ca(PO_3)_2$	1.5469	500	11.0	-2.5
$Sr(PO_3)_2$	1.5614	495	12.4	-5.9
$LiPO_3$	-	-	-	-6.1
$Pb(PO_3)_2$	1.7720	350	14.6	-10.4
$Ba(PO_3)_2$	1.5899	455	14.2	-10.6
$NaPO_3$	1.4840	275	25.0	-15.0
KPO_3	1.4740 [7]	228 [7]	-	-23.3

Table 2.1 : Properties of metaphosphate glasses

Figure 2.2 shows the *dn/dT* of some metaphosphate glasses as a function of the difference of the Dietzel's field strength and the cation radius, r_k. Dietzel's field strength is defined as the ratio of the ion valence to the square of the bond distance between the cation and oxygen, z/a^2. In order to obtain negative thermo-optical behaviour, cations with small z/a^2 and large r_k are required. The cations circled in Figure 2.2 represent the modifying cations added to phosphate glasses studied within this work.

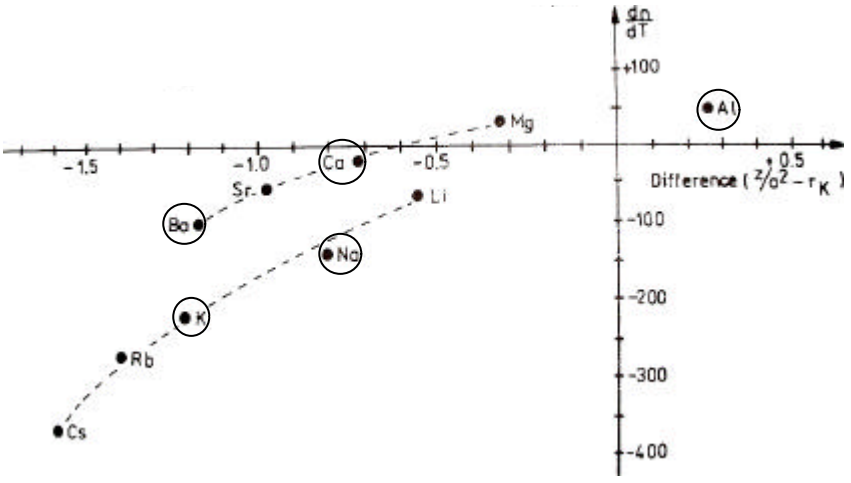

Figure 2.2 : Relationship between *dn/dT* and ((z/a^2)-r_k) in metaphosphate glasses [1]

2.1.2 Structures

The structure of a glass determines its optical, thermal and chemical properties. In this section, the structures of binary phosphate, aluminophosphate and borophosphate glasses are reviewed. These will later be used in Chapters 4 – 6 to explain the observed properties of the glasses prepared in this work.

The basic building blocks of crystalline and amorphous phosphates are the P-tetrahedra, which link via covalent bridging oxygens to form various phosphate anions. These tetrahedral units can be classified using the Q-site model proposed by Lippma *et al*. [8]. Although the model was initially used to describe the structures of binary silicate glasses, it can also be applied to phosphate glasses [9]. Based on this model, the phosphate anions can be described using the Q^i terminology, where '*i*' represents the number of bridging oxygens (BO) per tetrahedron, as shown schematically in Figure 2.3.

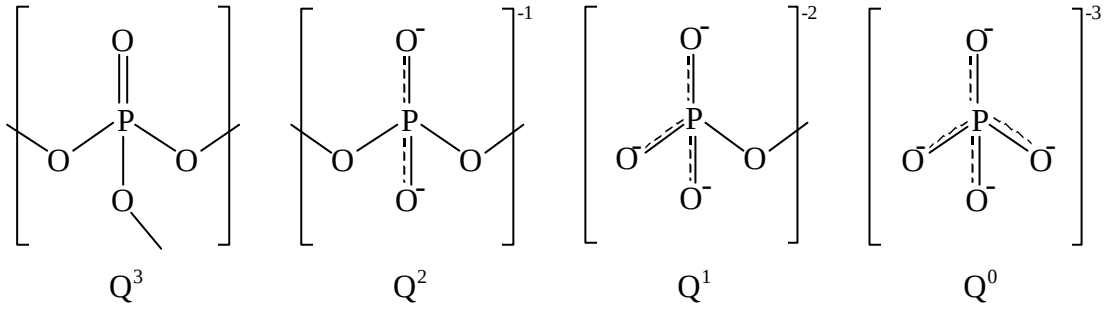

Figure 2.3 : Phosphate tetrahedral sites

P_2O_5 is different from the other single component glass-formers due to the existence of a terminal oxygen (TO) on each network forming cation. This terminal oxygen is a short double-bonded (P=O) bond, with a significant π-bond character that accounts for the additional valence electron [10]. The presence of such terminating oxygens results in less cross-linked phosphate glass structure compared to silicate glasses.

The phosphate glass networks can be classified by the O/P ratio, which describes the tetrahedral linkages via bridging oxygens between neighbouring P-tetrahedra [9], as summarised in Table 2.2. Vitreous P_2O_5 with O/P = 2.5 possesses a structure based on a cross-linked three-dimensional network of Q^3 tetrahedra which have three covalent bridging oxygens (BO) linked to neighbouring tetrahedra and one TO of the form of a (P=O) link. The addition of a modifying oxide (MeO) depolymerises the network structure by converting BOs (P-O-P links) to non-bridging oxygens (NBOs), resulting in (P-O-Me) links, and in the process forming an ultraphosphate network ($2.5 \leq O/P < 3.0$) dominated by Q^3 tetrahedra. As the modifying oxide content increases, the three-dimensional network is converted into metaphosphate chains and rings based on Q^2 tetrahedra (O/P = 3.0) [3,11], which are interconnected through ionic cross-links with modifying cations between NBOs of two different chains. Further increases in the modifier content results in polyphosphate compositions (O/P > 3.0) based on Q^2 chains terminated by Q^1 tetrahedra where the average chain lengths are shorter than that of the metaphosphate compositions. At the pyrophosphate stoichiometry (O/P = 3.5), the network is dominated by phosphate dimers (Q^1 - Q^1), while at the orthophosphate stoichiometry (O/P = 4.0), the glasses contain isolated Q^0 tetrahedra. Figure 2.4 shows a three-dimensional network based on Q^3 tetrahedra (left side) and a metaphosphate chain of Q^2 tetrahedra (right side).

Phosphate network	*Ultraphosphate*	*Metaphosphate*	*Polyphosphate*	
			Pyrophosphate	*Orthophosphate*
O/P	< 3.0	3.0	3.5	4.0

Table 2.2 : Relationship between the phosphate glass networks and the O/P ratio

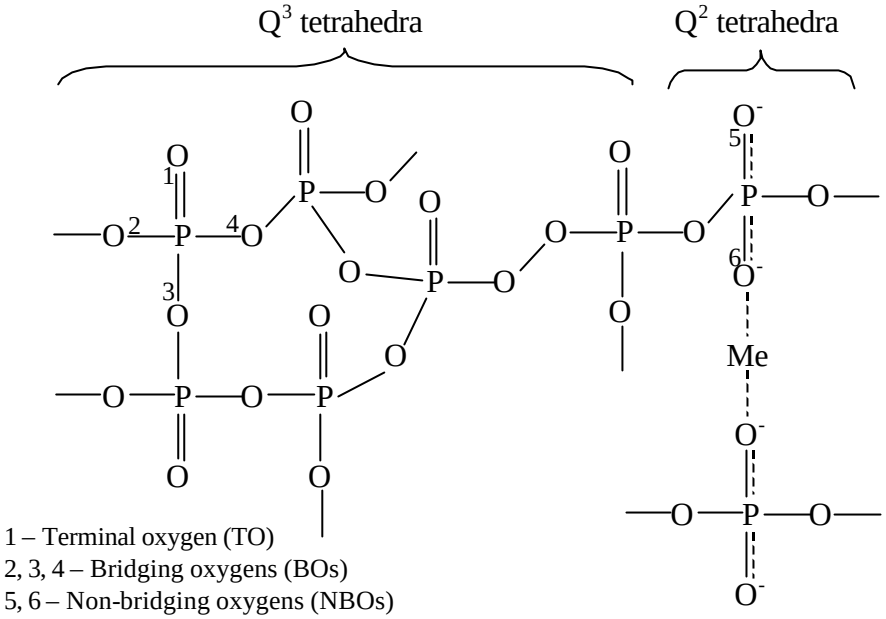

Figure 2.4 : Phosphate structural network

2.1.2.1 Binary Phosphate

The addition of a modifying oxide, such as an alkali oxide, Me_2O, depolymerises the phosphate network and can be described by the pseudo-reaction [9]

$$2Q^n + Me_2O \rightarrow 2Q^{n-1} \qquad (2.1)$$

For binary xMeO-(1-x)P_2O_5 glasses, the relative concentrations of Q^i tetrahedra can be estimated based on the glass compositions, and are summarised in Table 2.3 and Figure 2.5 [9].

	Compositional range		
	Ultraphosphate ($0 \le x \le 0.5$)	*Between metaphosphate and pyrophosphate* ($0.50 \le x \le 0.67$)	*Between pyrophosphate and orthophosphate* ($0.67 \le x \le 0.75$)
Q^i fractions	$f(Q^3) = \frac{1-2x}{1-x}$ $f(Q^2) = \frac{x}{1-x}$	$f(Q^2) = \frac{2-3x}{1-x}$ $f(Q^1) = \frac{2x-1}{1-x}$	$f(Q^1) = \frac{3-4x}{1-x}$ $f(Q^0) = \frac{3x-2}{1-x}$

Table 2.3 : Q^i fractions in binary phosphate glasses

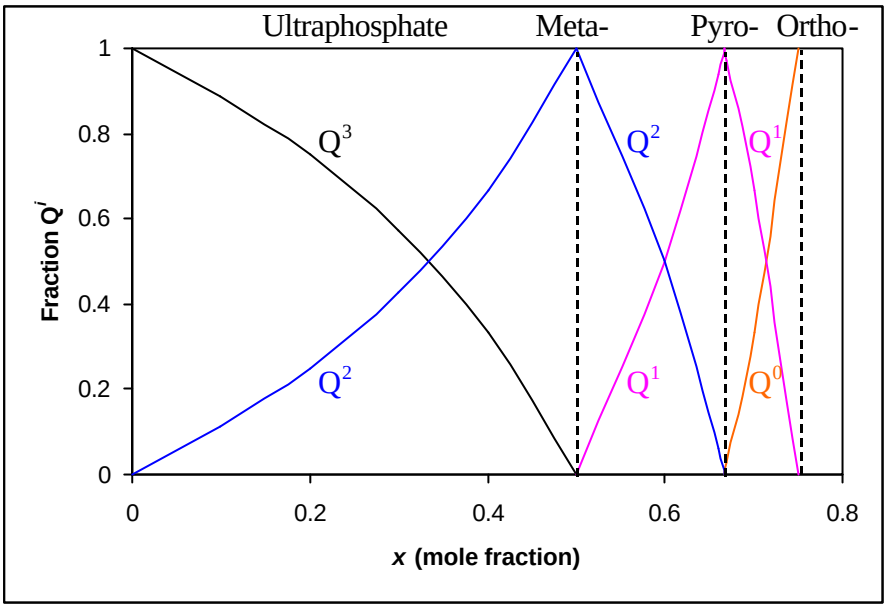

Figure 2.5 : Q^i fractions in binary phosphate glasses

Due to the hygroscopicity and volatility of P_2O_5 [12], ultraphosphate glasses must be prepared in sealed ampoules to minimise the water content. Water has a depolymerising effect on the phosphate network by forming (P-OH) bonds, which reduces the Q^3 fraction to much less than that expected from the nominal alkali-to-phosphorus ratio [13]. Hence the presence of (P-OH) bonds must be considered when describing the structures and properties of such glasses. However, with increasing MeO content, glass durability is improved due to the elimination of bridging (P-O-P) bonds associated with Q^2 tetrahedra [14].

Hoppe [15,16] presented a structural model describing the effect of modifier coordination environments (having coordination number CN_{Me}) on the properties and structures of ultraphosphate glasses. These would depend on the number of terminal oxygens available to coordinate the modifier ions (Me^{z+}, where z is the ion valence). The number of terminal oxygens, M_{TO}, per modifying ion for glasses with the stoichiometry $x(Me_{2/z}O)$-$(1-x)P_2O_5$ is given by equation (2.2).

$$M_{TO} = z(1/x) \tag{2.2}$$

Hoppe suggested two structurally different compositional ranges : when $M_{TO} > CN_{Me}$ (region I) and when $M_{TO} < CN_{Me}$ (region II). In region I, there are adequate individual TOs to coordinate

with each Me^{z+} ion so that these ions can exist at isolated sites within the phosphate network with no (Me-O-Me) bonds (Figure 2.6(a)). However, in region II, there are insufficient TOs to coordinate with each Me^{z+} ion and hence these ions must share the available TOs by forming (Me-O-Me) bonds and cross-linking neighbouring Q^2 polyhedra (Figure 2.6(b)).

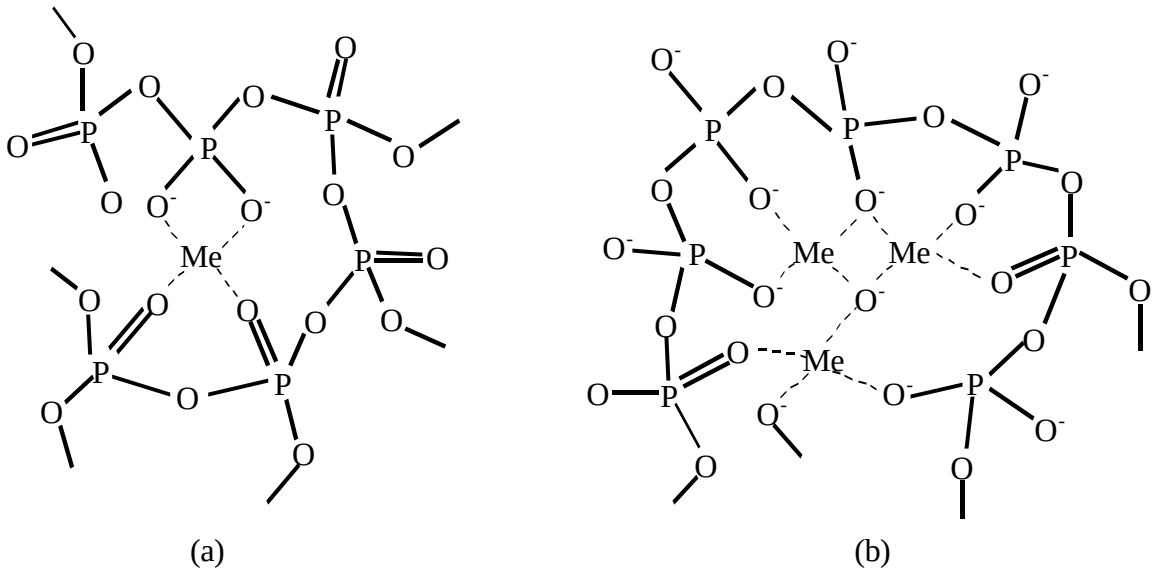

Figure 2.6 : Binary phosphate structure when (a) $M_{TO} > CN_{Me}$ and (b) $M_{TO} < CN_{Me}$

Based on equation (2.2), the transition from region I to region II occurs at ~ 20-25 mol% for Li (CN ~ 4-5) [17] and Na (CN ~ 5) [18,19], ~ 17 mol% for K and Cs (CN ~ 6) [20-22], ~ 50 mol% for Mg (CN ~ 4), ~ 33 mol% for Ca (CN ~ 6), ~ 25 mol% for Ba (CN ~ 8) [15,16] and ~ 43 mol% for La (CN ~ 7) [23]. However, such behaviour is not observed for aluminophosphate where the Al coordination number changes from 6 to 4 to avoid the formation of (Al-O-Al) substructure in response to the reduction in the number of TOs [22]. When divalent or trivalent ions are incorporated into an ultraphosphate network, their charge valence requires that at least two Q^2 tetrahedra must be present in their immediate coordination sphere.

The transition from isolated polyhedra to a modifier sub-structure with shared polyhedral corners generally causes changes in the glass properties, such as density [24,25] and T_g [22]. Figure 2.7 shows the density data for binary lithium and sodium phosphate [24,25]. In region I, the Q^3 network must expand to accommodate the alkali polyhedra, consequently causing a decrease in density. In region II, the alkali polyhedra must share the TOs, and hence causing an increase in density. At the same time, these polyhedra link neighbouring Q^2 and Q^3 tetrahedra, thus

increasing the strength of the network.

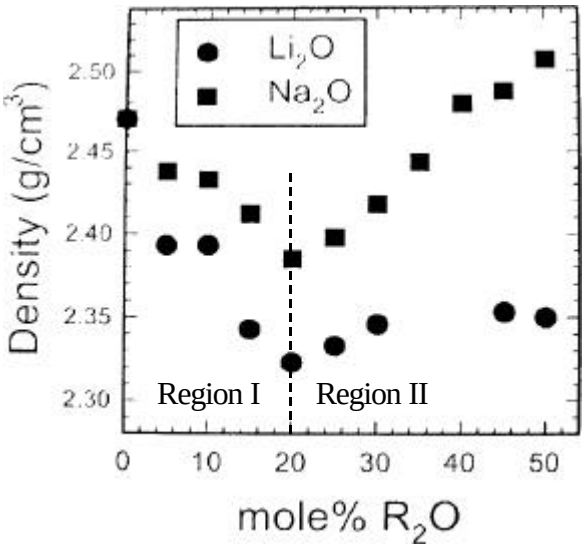

Figure 2.7 : Binary lithium and sodium phosphate density [24,25]

2.1.2.2 Aluminophosphate

Introducing Al_2O_3 to phosphate glasses decreases the structural density but increases the cross-link density by forming cross-linking aluminophosphate bonds between PO_4 tetrahedra. This results in an increase in the aqueous durability and T_g, and a decrease in α [26,27]. However, the properties of aluminophosphate glasses undergo a significant change when its composition crosses across either the pyrophosphate or the orthophosphate compositional boundaries. Figure 2.8 shows the T_g of sodium aluminophosphate glasses as a function of the glass O/P ratio [28].

^{27}Al nuclear magnetic resonance (NMR) studies show that octahedral aluminium, Al(6), is the preferred moiety in the structures of aluminophosphate glasses with metaphosphate stoichiometries while tetrahedral aluminium, Al(4), is preferred when O/P > 3.5 [26,29]. Al(4) sites form at high O/P ratios in order to maintain charge balance [30]. This change in the Al coordination number, Al(6) $\rightarrow$ Al(4), converts the glass structure from a phosphate to an aluminophosphate network and is responsible for the changes observed at O/P = 3.5 and O/P = 4 in Figure 2.8.

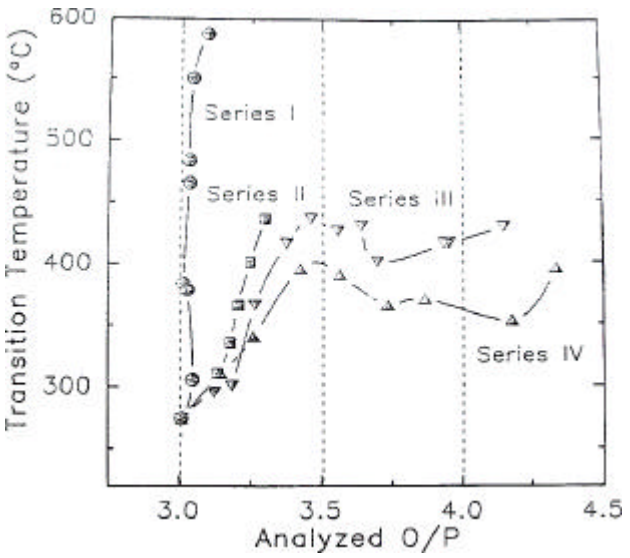

Figure 2.8 : Glass transition temperature of sodium aluminophosphate glasses as a function of the O/P ratio [28]

Figure 2.9 shows the possible sodium aluminophosphate structural network at the metaphosphate, pyrophosphate and orthophosphate compositions.

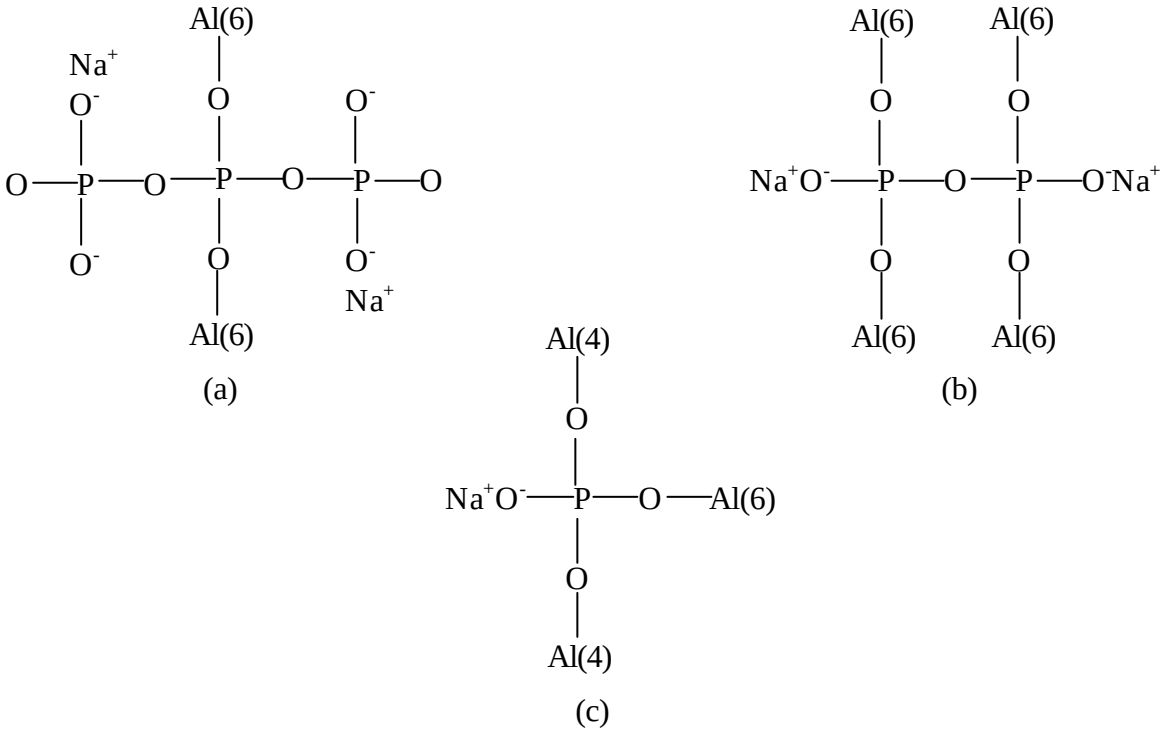

Figure 2.9 : Sodium aluminophosphate structure : (a) Metaphosphate, (b) Pyrophosphate and (c) Orthophosphate [26]

2.1.2.3 Borophosphate

Borophosphate glasses have interesting structural network due to the presence of two glass formers, B_2O_3 and P_2O_5, thus incorporating mixtures of borate, phosphate and borophosphate units. A range of cations had previously been studied in borophosphates to assess the structures and some glass properties. These include Li^+ [31], Na^+ [32], K^+ [32,33], Ca^{2+} [34], Ba^{2+} [35] and Zn^{2+} [36]. The addition of B_2O_3 modifies the properties of phosphate glasses by cross-linking phosphate chains to improve chemical durability [37].

Previous structural studies of borophosphate glasses [32,33,38,39] indicate that boron atoms form either trigonal, B(3), or tetrahedral, B(4), sites within the borophosphate glass network, depending on composition. The possible borophosphate [40] (analogous to $AlPO_4$ structure [26]) and borate units [41] present in borophosphate structural networks are shown in Figure 2.10. In the phosphate-rich composition range, boron atoms are mostly B(4), while in the borate-rich range, B(3) dominates. This change in the coordination number will affect the properties of the glasses, similar to that observed in aluminophosphate glasses as described in Section 2.1.2.2. Figure 2.11 [34] shows the glass T_g as a function of the B/(B+P) ratio for calcium borophosphate glasses, where the maximum observed at B/(B+P) = 0.3 denotes the transition from a B(4)-network to a B(3)-network.

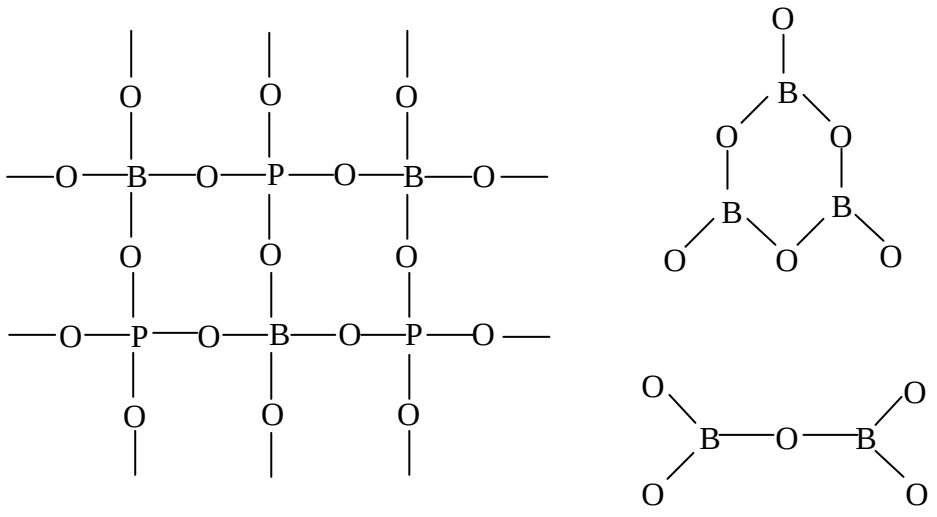

Figure 2.10 : Borophosphate and borate groups in borophosphate glass network

The incorporation of B(4) sites results in the formation of (B-O-P) bridges cross-linking neighbouring phosphate chains, leading to increased structural cross-link density. This causes an increase in the glass properties, namely density and glass transition temperature, as per Figure 2.11. Further increases in B_2O_3 results in a structural change from a disordered borophosphate network to a borate network, as the boron coordination number changes, B(4) → B(3). This decreases the covalent cross-link density and weakens the glass network.

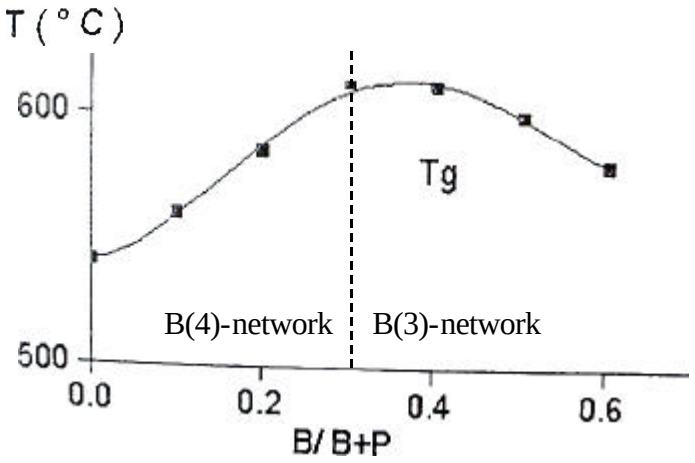

Figure 2.11 : Glass transition temperature of calcium borophosphate glasses [34]

2.1.3 Applications

Phosphate glasses have been developed for numerous applications and different cations have also been added to tailor the glasses for specialty applications. Phosphate glasses have been used as the primary host materials for high power laser applications [42,43]. Such glasses contain rare-earth oxides and are desirable as they possess high-stimulated emission cross-sections and low thermo-optic coefficients. Low *dn/dT* values are required to prevent any thermal lensing effect.

In addition, B_2O_3 [44,45] and P_2O_5 [46], with their intrinsic negative thermo-optic coefficients, have been used for co-doping in germanosilicate core fibres for athermalisation purposes. These applications will be described further in Section 2.3.

In this work, phosphate glass exhibiting negative *dn/dT* had been developed as possible athermal glasses. The main thrust of this research was to develop phosphate bulk glasses which are

athermal so that optical devices can be fabricated directly on these glasses without the need for further processing steps.

2.2 *dn/dT* Measurement

The *dn/dT* of a glass, besides *n* and α, is important in determining the athermal characteristics of a glass, as described in Section 1.3.1. Therefore, it is necessary to have a method which can determine this parameter.

dn/dT is measured experimentally via an interferometric technique. This method had been extensively used on various samples such as ZnSe, ZnS, CdTe, CaF_2, BaF_2, KCl and TI-20 at 0.6328 μm, 1.15 μm, 3.39 μm and 10.6 μm for 25 - 65°C [47], ZBLA at 0.6328 μm, 1.15 μm and 1.319 μm for 25 - 160°C [48], ZBL, ZBLA and ZBLAN at 0.6328 μm for 50 - 250°C [49], $CdSe_xS_{1-x}$ doped glasses (Corning Sharp Cut Filter CS 3-69) at 0.6328 μm for 25 - 45°C [50], crystalline silicon at 1.523 μm from room temperature to 300°C [51] and hydrogenated amorphous silicon (a-Si:H) at 1.55 μm for 30 - 200°C [52].

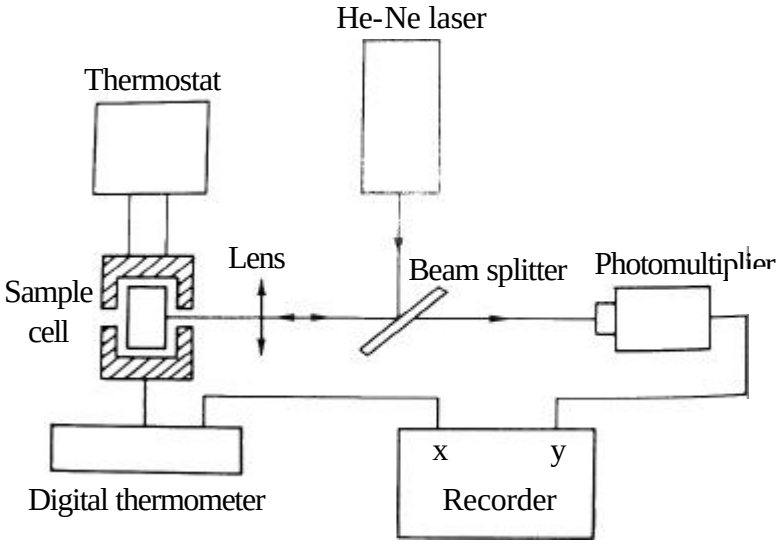

Figure 2.12 : Example of an interferometer set-up for *dn/dT* measurement [50]

Figure 2.12 shows the interferometer set-up used by Abbate *et al.* [50] to measure *dn/dT*. The interferometer set-ups used in the literature were slightly different in terms of the choice of apparatus and the set-up layout. However, all the interferometer set-ups generally employed the same basic principle. *dn/dT* measurements are made by monitoring the change in the optical path in a sample as the temperature of the sample is changed. Generally, a light path is incident upon the sample, which is located within a furnace. The light is then reflected by the front and back surfaces of the sample, causing an interference. Hence, the reflected beam intensity is modulated by constructive and destructive interference, leading to a periodic fringe pattern. As the temperature is varied, the optical path length of the two reflective beams from the opposite surfaces of the sample changes due to the combined effects of α and *dn/dT*. This leads to a change of the interference fringes. By measuring the temperature separation between successive maxima or minima, ΔT, the corresponding *dn/dT* can be extracted, based on equation (2.3) [47,53].

$$\frac{dn}{dT} = \left(\frac{\lambda}{2l\Delta T} \right) - n\alpha \tag{2.3}$$

where λ is the laser wavelength, l is the glass thickness, n is the refractive index, α is the thermal expansion coefficient and T is the temperature.

A Fabry-Perot type interferometer had also been designed to permit the concurrent measurement of α and *dn/dT* [53]. This had the advantage over other interferometer set-ups, which required a separate measurement or an assumed value of α [48-50,54]. In this set-up, the additional features consisted of the laser beam being expanded to illuminate the entire sample cross-section to minimise alignment difficulty and the presence of a hole through the sample thickness. The interference fringes observed due to the air gap can be used to monitor the thermal expansion of the glass as the temperature changed.

In addition, De Nicola *et al.* demonstrated an interferometric technique based on two-dimensional Fourier fringe analysis to measure the *dn/dT* of $CdSe_xS_{1-x}$ doped glasses (Schott GG-495 and OG-515) at 0.6328 μm for 25 - 85°C [54]. This technique made use of an automated fast-Fourier-transform-based fringe analysis method for phase retrieval, which made

accurate measurements of the interference fringe shift as a function of the sample temperature, possible. Figure 2.13 shows their experimental set-up. The He-Ne laser beam was expanded and reflected towards the measurement system. An object beam was directed towards the sample, enclosed in a heater cell, at normal incidence and then diffracted along the +1 diffraction order by the grating, while a reference beam was directed towards a tiltable mirror towards the grating and diffracted along the –1 diffraction order. The superposition of these two diffraction orders produced an interference fringe pattern. As the sample temperature changed, the temperature-dependent optical phase changed as well. This happened due to the shift in the fringe pattern and the intensity distributions [55] of the fringe patterns corresponding to the temperatures, $T + \Delta T$ and T, and can be fast-Fourier transformed to extract the optical phase change, Δf. Knowing the optical phase change as a function of temperature, df/dT, dn/dT of the sample can be determined from equation (2.4).

$$\frac{df}{dT} = \frac{2\pi l}{\lambda}\left(\frac{dn}{dT} + (n-1)\alpha\right) \tag{2.4}$$

In principle, this set-up worked in the same way as the other interferometer set-ups described. The difference with this method was that it was able to determine the phase change of the fringe pattern for any amount of change in the sample temperature while the other methods measured a specific optical phase change of 2π as a function of temperature.

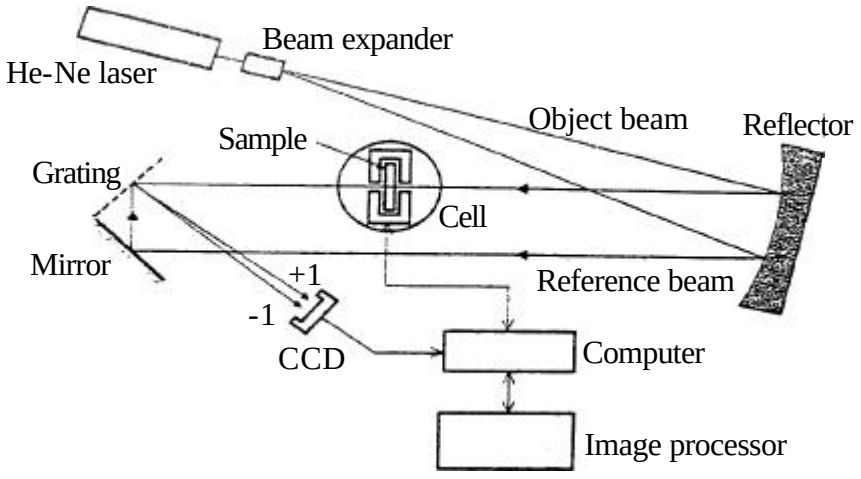

Figure 2.13 : Interferometer for fast-Fourier-transform-based fringe analysis [54]

As all interferometer set-ups described in this section work on the same principle, there is no difference as to how the interferometer set-up is constructed for the measurement of *dn/dT*. However, the set-up used within this work, as described in Section 3.4, had been constructed based on the set-up by Jewell *et al.* [53], with the initial idea to measure simultaneously α and *dn/dT* of the sample. Eventually, α of the sample was separately measured using a thermo-mechanical analyser (TMA) as it did not vary significantly over the temperature range of interest, 20 - 100°C. Furthermore, drilling a hole into the sample for real-time measurement of α would be a destructive process for the sample. The set-up constructed did not include a beam expander but had a lens that focused the interference fringe pattern towards the detector. In addition, the laser beam was allowed to reflect directly from the front and back faces of the sample, rather than being sandwiched by mirrors or reflecting surfaces as in ref [53]. This was advantageous as the sample was in direct thermal contact with the sample holder and also eliminated the problem of unwanted reflections from the other faces of the reflecting surfaces not in contact with the sample, which could otherwise interfere with the fringe pattern.

Apart from experimental measurement using interferometry, Toratani *et al.* [56,57] presented a method for calculating *dn/dT* of phosphate and silicate laser glasses, respectively, by estimating the temperature coefficient of the electronic polarisability, β. This method was based on the assumption that β can be expressed as the sum of the contributions of each glass component via equation (2.5). This relationship had been mentioned earlier in Section 1.4.

$$\beta = \sum_i \beta_i X_i = \sum_i \gamma_i \alpha_i X_i \tag{2.5}$$

where the subscript *i* represents the *i*-th component of the glass, γ is the change in polarisability due to a change in inter-ionic distance, α is the thermal expansion coefficient and *X* is the mole fraction. Once the overall glass β had been estimated, it can be used together with *n* and α of the glass in equation (1.15) to determine the glass *dn/dT*.

In order to determine β_i for each oxide component, Toratani *et al.* [56,57] experimentally measured the *dn/dT* and α values of different optical glasses. These results were then used to calculate β of the glasses using equation (1.15) to estimate β_i. Table 2.4 lists the estimated β_i

values for different oxides in silicate and phosphate laser glasses [56,57], valid for 20 - 40°C at λ = 632.8 nm. These values were determined so as to give the minimum deviation between the calculated β values based on equation (2.5) and the measured β values in Toratani's studies. The glass components used within the present study of athermal phosphate glasses are highlighted.

Component	β_i (´ 10^{-6}/°C)	
	Silicates	Phosphates
SiO_2	17.4	-
$PO_{2.5}$	-	20
$BO_{1.5}$	13.8	16
$AlO_{1.5}$	22.2	26
$LiO_{0.5}$	-	-
$NaO_{0.5}$	50.0	44
$KO_{0.5}$	43.9	45
MgO	-	-
CaO	42.0	-
BaO	36.1	35
PbO	50.2	47
TiO_2	19.3	15
ZnO	39.4	-

Table 2.4 : β_i of various oxides in silicate and phosphate laser glasses

2.3 Athermalisation

The central wavelength of lightwave devices such as narrow-band optical filters and gratings is sensitive to temperature, due to the temperature dependence of the optical path length of the devices. It can degrade the performance of such devices since the central wavelength for which they are designed, will shift as the operating temperature changes. Assuming a WDM system with channels spaced apart by 50 GHz (400 pm at 1550 nm), a grating operating in the temperature range of 0 - 100°C would require a temperature sensitivity of the central wavelength of less than 4 pm/°C in order to prevent any cross-talk between the different channels. Hence, the concept of

athermalisation is essential in addressing this matter.

The temperature sensitivity of the resonance wavelength for both Bragg gratings and long period gratings can be reduced by carefully selecting the choice of materials for the core and clad/substrate. The analysis for these two gratings are presented here, where the difference between Bragg gratings (also known as reflection gratings) and long period gratings (also known as transmission gratings) is how the modes are coupled. For a Bragg grating, coupling occurs between modes travelling in opposite directions. The resonant wavelength for a Bragg grating, involving the reflection of a mode of index n_{eff1} into a mode of index n_{eff2} is given by [58]

$$\boldsymbol{l} = \left(n_{eff\,1} + n_{eff\,2}\right)\boldsymbol{L} \tag{2.6}$$

where $\boldsymbol{l}$ is the resonance wavelength and $\boldsymbol{L}$ is the grating period. For Bragg reflection, the two modes are identical, leading to equation (2.7) for the Bragg wavelength, $\boldsymbol{l}_B$.

$$\boldsymbol{l}_B = 2n_{eff}\boldsymbol{L} \tag{2.7}$$

For a long period grating, coupling occurs between modes travelling in the same direction. The resonant wavelength for a long period grating, involving a co-propagating core mode of index n_{eff1} and a cladding mode of index n_{eff2} is given by [58]

$$\boldsymbol{l} = \left(n_{eff\,1} - n_{eff\,2}\right)\boldsymbol{L} \tag{2.8}$$

Using equations (2.7) and (2.8) for Bragg and long period gratings, respectively, the temperature dependence of the resonance wavelength can be expressed as equation (2.9) for a Bragg grating and equation (2.10) for a long period grating.

$$\frac{d\,\boldsymbol{l}_B}{dT} = 2\,\boldsymbol{L}\left(n_{eff}\,\boldsymbol{a} + \frac{dn_{eff}}{dT}\right) \tag{2.9}$$

$$\frac{d\lambda}{dT} = \lambda\left[\left(n_{eff1} - n_{eff2}\right)\alpha + \left(\frac{dn_{eff1}}{dT} - \frac{dn_{eff2}}{dT}\right)\right] \tag{2.10}$$

where α is the thermal expansion coefficient and dn_{eff}/dT is the effective thermo-optic coefficient.

In their research into athermal waveguides, Kokubun *et al*. managed to design three-dimensional ridge-loaded silica-based waveguides with reduced temperature sensitivity [59-62]. These waveguides worked by cancelling out the positive dependence of ordinary optical materials with the negative temperature coefficient of the refractive index of polymers such as methyl methacrylate (MMA), polymethyl methacrylate (PMMA) and tri-fluoroethyl methacrylate (TFMA). As discussed in Section 1.3.3, the athermal condition for a waveguide is

$$\frac{1}{L}\frac{dS}{dT} = \left(n_{eff}\alpha_{sub} + \frac{dn_{eff}}{dT}\right) \tag{2.11}$$

Since optical materials generally have positive α, it is necessary for the athermal waveguides to have materials, such as polymers, with negative dn/dT in order to realise $dn_{eff}/dT < 0$. In comparison to the values of the wavelength fluctuation with temperature, which can be as large as 10 pm/°C for silica-based waveguide filters and 80 pm/°C for semiconductor-based waveguide filters, Kokubun *et al*. managed to demonstrate a ring resonator based on these waveguides, with reported reduction of the temperature coefficient of the wavelength at 1.3 μm and 1.55 μm to 0.7 pm/°C [61] and < 0.4 pm/°C [62] respectively. Figure 2.14 shows the design of their athermal waveguide for operation at 1.3 μm, with the properties of the materials summarised in Table 2.5.

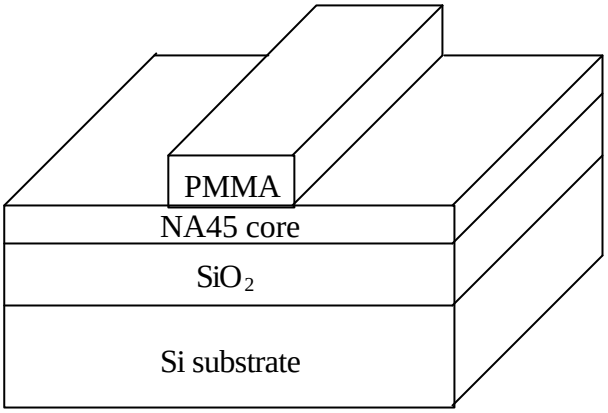

Figure 2.14 : Ridge-loaded silica-based athermal waveguide

Material	***n*** **(*l* = 1.3 mm)**	***dn/dT* (´ 10^{-6}/°C)**	
		Bulk (*l* = 0.633 mm)	**Film formed on Si (*l* = 1.3 mm)**
PMMA	1.481	-105	-183.6 (TE), -151.6 (TM)
NA45 [59-61]	1.547	4.8	5.76 (TE), 5.45 (TM)
SiO_2	1.455	10.1	7.65 (TE)

Table 2.5 : Properties of optical materials for ridge-loaded silica-based athermal waveguide

The temperature sensitivity of a waveguide can also be eliminated by modifying the refractive-index profile of the host fibre, such as using a boron co-doped germano-silicate core fibre as proposed by Shima *et al.*[44]. This is because pure B_2O_3 has negative *dn/dT*, which compensates for the positive *dn/dT* of the germanosilicate glass [1] (Table 1.1). Their result showed a temperature sensitivity of ~ 5 pm/°C over –40 to 80 °C for long period fibre gratings (LPFG). Figure 2.15 shows the result obtained by Shima *et al.*. Following the same principle, Enomoto *et al.* [46] used P_2O_5 as the negative *dn/dT* material. Their fabricated LPFG in P_2O_5 co-doped GeO_2-SiO_2 fibres showed a temperature sensitivity of ~ 3.8 pm/°C over 0 – 75 °C. They also showed that by extrapolating their results, zero temperature sensitivity can be achieved by doping P_2O_5 at the ratio of P_2O_5:GeO_2 = 0.75, as shown in Figure 2.16.

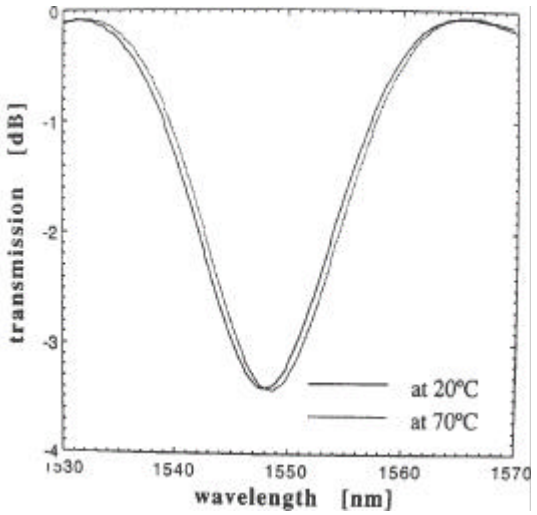

Figure 2.15 : Transmission spectrum of an athermal LPFG in a boron co-doped germanosilicate core fibre [44]

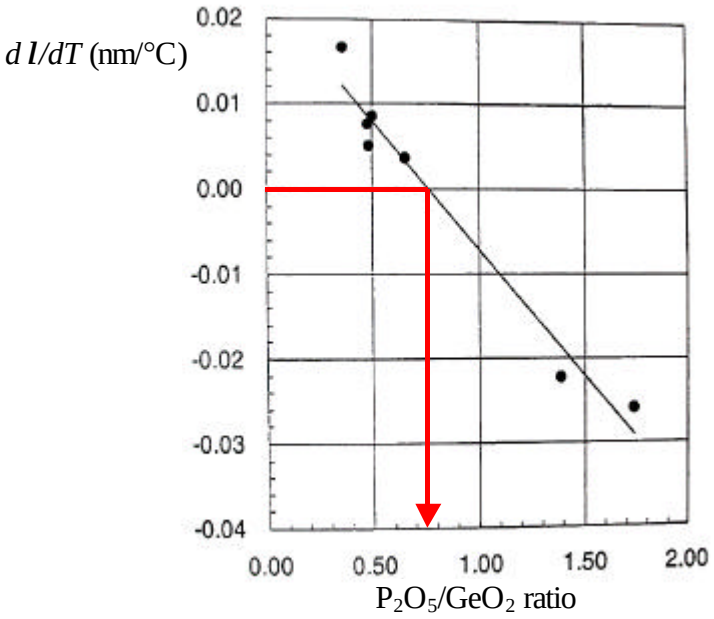

Figure 2.16 : Relationship between P_2O_5:GeO_2 ratio and *d l/dT* [46]

Ng *et al.* [63] proposed mounting a bent LPFG on a suitable substrate to eliminate the temperature dependence of the central wavelength, as in Figure 2.17. In separate experiments, they observed that the central wavelength of a straight, unmounted LPFG shifted to lower wavelengths as temperature increased and that the resonance wavelength of a LPFG fixed at two points shifted to lower wavelengths as the lateral displacement, *h*, increased. Both these effects can be utilised to compensate for the temperature effect on the LPFG. Their device consisted of a bent LPFG attached onto a mount, which in this case was a plastic slab with $\alpha = 1.5\times10^{-4}$/°C. As

the temperature increased, the thermal effect on the LPFG shifted the resonance wavelength to a lower wavelength while the thermal expansion of the mount caused a reduction in h, consequently shifting the resonance wavelength to a higher wavelength. These two effects provided the temperature compensation for the LPFG and a temperature sensitivity of 8 pm/°C over 15 – 55 °C was reported for their device.

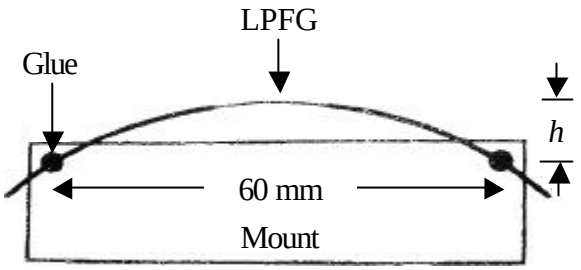

Figure 2.17 : Bent LPFG for temperature compensation [63]

Sakamoto *et al.* [64] also used a single substrate, which in their case was a Negative Expansion Ceramic Substrate (NECS), to compensate for the temperature dependence of the Bragg wavelength of a fibre Bragg grating (FBG) mounted onto it. A pre-tensioned FBG was fixed with an epoxy adhesive at both ends of the grating onto an NECS of $\alpha = -8.2\times10^{-6}$/°C. Experimentally, $d\lambda_B/dT$ = -2.3 pm/°C was reported for their device in the temperature range of – 40 to 85 °C.

Yoffe *et al.* [65] managed to improve the wavelength temperature sensitivity of a FBG by using a hybrid substrate to counter the change induced in the fibre. Figure 2.18 shows their temperature compensating set-up, involving a combination of two materials of different α as an athermalisation method for a pre-tensioned FBG. When the temperature changed, the substrate would either expand or contract and this led to a change in the FBG tension. This in turn changed the period of the grating, which would offset the effect of the refractive index change on the Bragg wavelength. The use of a hybrid substrate is advantageous as there is flexibility in the choice of materials to obtain the required thermal expansion coefficients, compared to a single material with large negative thermal expansion coefficient, which also have problems with long-term reliability and hysteresis in the physical properties. This same principle was also used by Tamura *et al.* [66] to produce a temperature-compensating grating. In their work, they used a combination of an

aluminium block with a high α of 23.8×10^{-6}/°C and silica glass with a low α of 0.55×10^{-6}/°C to create a localised negative thermal expansion coefficient between the two grating ends. The tension of the fibre grating was first adjusted to obtain the required resonance wavelength and resin was then applied to attach the fibre onto the hybrid substrate. A temperature sensitivity of < 5 pm/°C over –40 to 50 °C was obtained for their FBG.

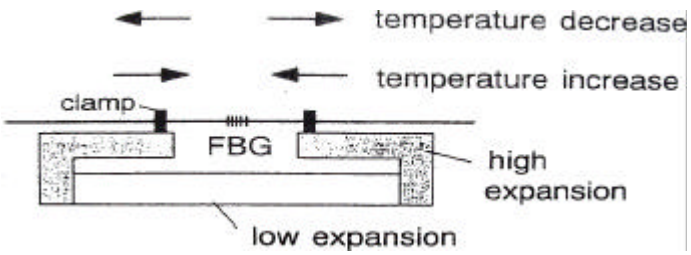

Figure 2.18 : Athermalisation with a hybrid substrate [65]

In their research work towards suppressing $d\lambda_B/dT$ in a silica-based waveguide, Bosc *et al.* [67] used a polymer material with negative dn/dT (~ -10^{-4}/°C). Figure 2.19 shows the design of their athermal waveguide. Plasma enhanced chemical vapour deposition (PECVD) was used to deposit the SiO_2 buffer layer, the SiO_2-GeO_2 core layer as well as the SiO_2 cladding layer on the edges of the waveguide. The Bragg grating was then written into the central part of the sample with a 244 nm UV CW laser through a phase mask before a polymer layer was deposited by spin coating. The device was then subjected to heating and $d\lambda_B/dT$ was found to be 2 pm/°C over 20 – 100 °C.

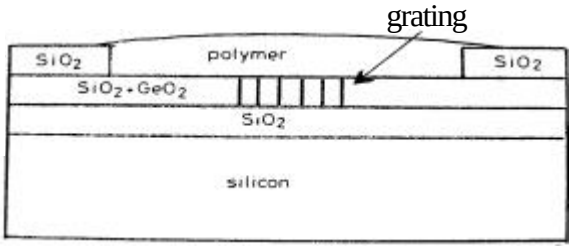

Figure 2.19 : Cross-section of silica waveguide with polymer layer [67]

Kintaka *et al*. [45,68,69] studied different core and clad compositions on Si, SiO_2 and ZrO_2-LiO_2-Al_2O_3-SiO_2 glass ceramic substrates and managed to produce athermal silica-based waveguides with UV-induced Bragg gratings, formed with a KrF excimer laser at 248 nm through a phase mask. Figure 2.20 shows the designs of the fabricated waveguides. In the first design, the grating was formed on a B_2O_3 co-doped Ge-SiO_2 core layer with cladding layers of B_2O_3-SiO_2. The co-doping of B_2O_3 is essential as it has a negative *dn/dT* [1] to minimise $d\lambda_B/dT$ and to enhance photosensitivity [70]. The best reported temperature sensitivity for such structure was 4.1 (TE) and 5.8 (TM) pm/°C over 10 – 70 °C. The differences for TE-like and TM-like modes were due to the asymmetric stress caused by the substrate. In the second design, the grating was formed on a B_2O_3 co-doped Ge-SiO_2 grating layer with a core layer of B_2O_3-SiO_2 and cladding layers of F_2-B_2O_3-SiO_2. A reduced $d\lambda_B/dT$ value of 4 pm/°C (TE and TM) was reported for this design. This was because the core did not contain any GeO_2, which has a positive *dn/dT* [1] that increases the temperature sensitivity of the Bragg wavelength, as well as the co-doping of F_2 in the cladding layers, which reduces α and *dn/dT* [1,71].

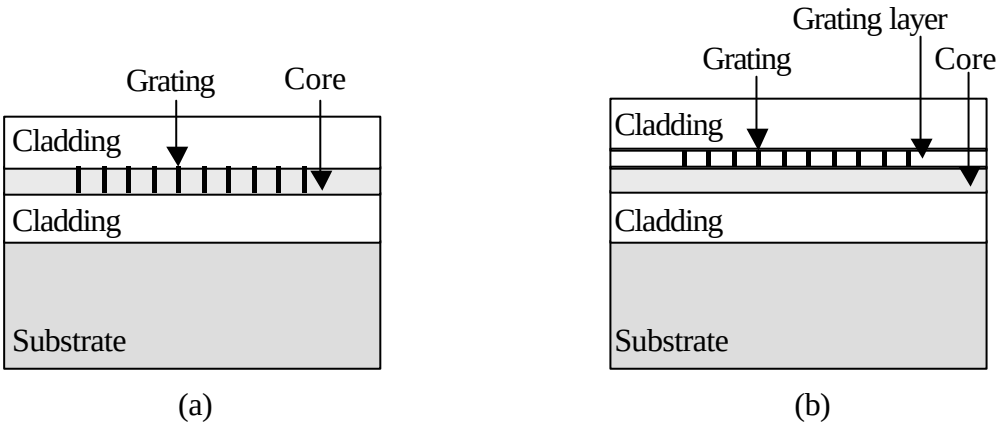

Figure 2.20 : Athermal silica-based waveguides (a) without and (b) with a grating layer

Table 2.6 summarises the athermal work described in this section, with their reported $d\lambda_B/dT$.

Author	$d\lambda/dT$	Base material	Temperature range	Reference
Kokubun et al.	0.7 pm/°C at 1.3 μm	Silica	Not stated	[61]
Kokubun et al.	< 0.4 pm/°C at 1.55 μm	Silica	25 to 90 °C	[62]
Shima et al.	5 pm/°C at 1.55 μm	B_2O_3-GeO_2-SiO_2 fibre	–40 to 80 °C	[44]
Enomoto et al.	3.8 pm/°C at 1.55 μm	P_2O_5-GeO_2-SiO_2 fibre	0 to 75 °C	[46]
Ng et al	8 pm/°C at 1.5 μm	Plastic slab	15 to 55 °C	[63]
Sakamoto et al	-2.3 pm/°C at ~ 1.5 μm	LiO_2-Al_2O_3-SiO_2	–40 to 85 °C	[64]
Tamura et al	< 5 pm/°C at 1.55 μm	Hybrid aluminium block-silica glass	–40 to 50 °C	[66]
Bosc et al	2 pm/°C at ~ 1.55 μm	Silica	20 to 100 °C	[67]
Kintaka et al	4 pm/°C at 1.55 μm	Silica glass ceramic	10 to 70 °C	[45,69]

Table 2.6 : Summary of the research work on lower temperature sensitivity

In this research, different phosphate glasses had been studied and assessed, as set out in Chapters 4 to 6, with the aim of developing glasses with negative dn/dT for the purpose of athermalisation. Looking at equation (2.11), it is essential to have glasses exhibiting negative dn/dT in order to obtain negative dn_{eff}/dT to compensate for the positive α. As phosphate glasses generally exhibit negative dn/dT, they can be potentially developed for athermalisation applications. Ideally, bulk phosphate glasses with their intrinsic negative dn/dT can be used for the fabrication of athermal devices, without the need for extrinsic components such as substrates or passive temperature control units, to compensate for the change in temperature.

REFERENCES

1. W. Vogel, *"Optical properties of oxide glasses"*, Optical Properties of Glass, D.R. Uhlmann and N.J. Kreidl (Eds), The American Ceramic Society Inc., OH, (1991).

2. H.A.A. Sidek, I.T. Collier, R.N. Hampton, G.A. Saunders and B. Bridge, *"Electrical conductivity and dielectric constant of samarium phosphate glasses"*, Philosophical Magazine B 59 (2), pp 221-232 (1989).

3. B.C. Sales and L.A. Boatner, *"Lead-iron phosphate glass : A stable storage medium for high-level nuclear waste"*, Science 226 (4670), pp 45-48 (1984).

4. Y.B. Peng and D.E. Day, *"High thermal expansion phosphate glasses. Part 1"*, Glass Technology 32 (5), pp 166-173 (1991).

5. X. Yu, D.E. Day, G.J. Long and R.K. Brow, *"Properties and structure of sodium-iron phosphate glasses"*, Journal of Non-Crystalline Solids 215, pp 21-31 (1997).

6. D. Ehrt, P. Ebeling and U. Natura, *"UV transmission and radiation-induced defects in phosphate and fluoride-phosphate glasses"*, Journal of Non-Crystalline Solids 263&264, pp 240-250 (2002).

7. E. Metwalli and R.K. Brow, *"Modifier effects on the properties and structures of aluminophosphate glasses"*, Journal of Non-Crystalline Solids 289, pp 113-122 (2001).

8. E. Lippma, M. Magi, A. Samoson, G. Englehardt and A.R. Grimmer, *"Structural studies of silicates by solid-state high-resolution ^{29}Si NMR"*, Journal of The American Ceramic Society 102, pp 4889-4893 (1980).

9. J.R. Van Wazer, The Phosphorus and its Compounds 1 and 2, Interscience, New York, (1958).

10. T. Uchino and Y. Ogata, *"Ab initio molecular orbital calculations on the electronic structure of phosphate glasses : sodium phosphate glasses"*, Journal of Non-Crystalline Solids 181, pp 175-188 (1995).

11. B.C. Bunker, G.W. Arnold and J.A. Wilder, *"Phosphate glass dissolution in aqueous solutions"*, Journal of Non-Crystalline Solids 64, pp 291-316 (1984).

12. H.D. Park and E.R. Kreidler, *"Phase equilibria in the system La_2O_3- P_2O_5"*, Journal of The American Ceramic Society 67 (1), pp 23-26 (1984).

13. K. Suzuya, D.L. Price, C. Loong and S.W. Martin, *"Structure of vitreous P_2O_5 and alkali phosphate glasses"*, Journal of Non-Crystalline Solids 232-234, pp 650-657 (1998).

14. R.K. Brow, C.M. Arens, X. Yu and D.E. Day, *"An XPS study of Fe-phosphate glasses"*, Physics and Chemistry of Glasses 35 (3), pp 132-136 (1994).

15. U. Hoppe, G. Walter, R. Kranold, D. Stachel and A. Barz, *"The dependence of structural pecularities in binary phosphate glasses on their network modifier content"*, Journal of Non-Crystalline Solids 192&193, pp 28-31 (1995).

16. U. Hoppe, *"A structural model for phosphate glasses"*, Journal of Non-Crystalline Solids 195, pp 138-147 (1996).

17. T.M. Alam, S. Conzone, R.K. Brow and T.J. Boyle, *"^6Li, ^7Li nuclear magnetic resonance investigation of lithium coordination in binary phosphate glasses"*, Journal of Non-Crystalline Solids 258, pp 140-154 (1999).

18. U. Hoppe, *"Short-range order of phosphate glasses studied by a difference approach using X-ray diffraction results"*, Journal of Non-Crystalline Solids 183, pp 85-91 (1995).

19. U. Hoppe, G. Herms, W. Gerike and J. Sakowski, *"The increased intensity of the first sharp diffraction peak of a $NaPO_3$ melt"*, Journal of Physics: Condensed Matter 8 (43), pp 8077-8087 (1996).

20. K. Handa, Y. Kita, S. Kohara, K. Suzuya, T. Fukunaga, M. Misawa, T. Iida, H. Iwasaki and N. Umesaki, *"Structure of M_2O-B_2O_3 (M: Na and K) glasses and melts by neutron diffraction"*, Journal of Physics and Chemistry of Solids 60 (8-9), pp 1465-1471 (1990).

21. W.C. Huang, H. Jain and G. Meitzner, *"The structure of potassium germanate glasses by EXAFS"*, Journal of Non-Crystalline Solids 196, pp 155-161 (1996).

22. R.K. Brow, C.A. Click and T.M. Alam, *"Modifier coordination and phosphate glass networks"*, Journal of Non-Crystalline Solids 274, pp 9-16 (2000).

23. U. Hoppe, R. Kranold, D. Stachel, A. Barz and A.C. Hannon, *"A neutron and X-ray diffraction study of the structure of the LaP_3O_9 glass"*, Journal of Non-Crystalline Solids 232-234, pp 44-50 (1998).

24. J.J. Hudgens and S.W. Martin, *"Glass transition and infrared spectra of low-alkali, anhydrous lithium phosphate glasses"*, Journal of The American Ceramic Society 76 (7), pp 1691-1696 (1993).

25. J.J. Hudgens, *"The structure and properties of anhydrous, alkali ultra-phosphate glasses"*, PhD thesis, Iowa State University, US, 1994.

26. R.K. Brow, R.J. Kirkpatrick and G.L. Turner, *"Nature of alumina in phosphate glass: II, Structure of sodium aluminophosphate glass"*, Journal of The American Ceramic Society 76 (4), pp 919-928 (1993).

27. T. Minami and J.D. Mackenzie, *"Thermal expansion and chemical durability of phosphate glasses"*, Journal of The American Ceramic Society 60 (5-6), pp 232-235 (1979).

28. R.K. Brow, *"Nature of alumina in phosphate glass: I, Properties of sodium aluminophosphate glass"*, Journal of The American Ceramic Society 76 (4), pp 913-918 (1993).

29. E. Metwalli, R.K. Brow and F.S. Stover, *"Cation effects on anion distributions in aluminophosphate glasses"*, Journal of The American Ceramic Society 84 (5), pp 1025-1032 (2001).

30. R.K. Brow, R.J. Kirkpatrick and G.L. Turner, *"Local structure of $xAl_2O_3.(1-x)NaPO_3$ glasses: An NMR and XPS study"*, Journal of The American Ceramic Society 73 (8), pp 2293-2300 (1990).

31. M. Villa, M. Scagliotti and G. Chiodelli, *"Short range order in the network of the borophosphate glasses: a ^{31}P NMR-MAS (Magic Angle Spinning) study"*, Journal of Non-Crystalline Solids 94, pp 101-121 (1987).

32. H. Yun and P.J. Bray, *"Nuclear magnetic resonance studies of the glasses in the system K_2O-B_2O_3- P_2O_5"*, Journal of Non-Crystalline Solids 30, pp 45-60 (1978).

33. N.H. Ray, *"A study of the coordination of boron in potassium borophosphate glasses by Raman spectroscopy"*, Physics and Chemistry of Glasses 16, pp 75-80 (1975).

34. N. Hadj Youssef, M.S. Belkhiria, J.J. Videau and M.B. Amara, *"Investigation of the physico-chemical properties of calcium borophopshate glasses. Effect of the substitution of sodium for calcium"*, Materials Letters 44, pp 269-274 (2000).

35. G. Sedmale, J. Vaivads, U. Sedmalis, V.O. Kabanov and O.V. Yanush, *"Formation of borophosphate glass structure within the system BaO-B_2O_3- P_2O_5"*, Journal of Non-Crystalline Solids 129, pp 284-291 (1991).

36. L. Koudelka and P. Mošner, *"Borophosphate glasses of the ZnO-B_2O_3-P_2O_5 system"*, Materials Letters 42, pp 194-199 (2000).

37. N.H. Ray, Inorganic polymers, pp 79, Academic Press, London, (1978).

38. M. Scagliotti, M. Villa and G. Chiodelli, *"Short range order in the network of the borophosphate glasses : Raman results"*, Journal of Non-Crystalline Solids 93, pp 350-360 (1987).

39. R.K. Brow and D.R. Tallant, *"Structural design of sealing glasses"*, Journal of Non-Crystalline Solids 222, pp 396-406 (1997).

40. S. Kumar, P. Vinatier, A. Levasseur and K.J. Rao, *"Investigations of structure and transport in lithium and silver borophosphate glasses"*, Journal of Solid State Chemistry 177 (4-5), pp 1723-1737 (2004).

41. N. J. Kreidl, *"Inorganic glass-forming systems"*, Glass: Science and Technology 1, pp 162, Academic Press, Inc., (1983).

42. J.H. Campbell and T.I. Suratwala, *"Nd-doped phosphate glasses for high-energy/high-peak-power lasers"*, Journal of Non-Crystalline Solids 263&264, pp 318-341 (2000).

43. M.J. Weber, *"Science and technology of laser glass"*, Journal of Non-Crystalline Solids 123, pp 208-222 (1990).

44. K. Shima, K. Himeno, T. Sakai, S. Okude and A. Wada, *"A novel temperature-insensitive long-period fiber grating using a boron-codoped-germanosilicate-core fiber*", in: Conference on Optical Fiber Communication, paper FB2, OFC 1997.

45. K. Kintaka, J. Nishii, H. Nishiyama, Y. Kawamoto and A. Sakamoto, *"Athermalization of a silica-based waveguide with a UV-induced Bragg grating on a crystallized glass substrate"*, Journal of Lightwave Technology 21 (3), pp 831-836 (2003).

46. T. Enomoto, M. Harumoto, M. Shigehara, S. Ishikawa and H. Kanamori, "*Temperature-insensitive long-period fiber gratings written in P_2O_5 co-doped GeO_2-SiO_2 core optical fibers*", in : Topical Meeting on Bragg Gratings, Photosensitivity and Poling, paper ThE9, BGPP 1999, Florida, US, September 1999.

47. R.J. Harris, G.T. Johnston, G.A. Kepple, P.C. Krok and H. Mukai, "*Infrared thermooptic coefficient measurement of polycrystalline ZnSe, ZnS, CdTe, CaF_2 and BaF_2, single crystal KCl and TI-20 glass*", Applied Optics 16 (2), pp 436-438 (1977).

48. P. Greason, J. Detrio, B. Bendow and D.J. Martin, "*Temperature dependence of the refractive index of fluorozirconate glass*", Materials Science Forum 6, pp 607-610 (1985).

49. W.J. Cho, T.S. Kahn, S.S. Choi and K.H. Chung, "*Thermo-optic coefficients of ZrF_4-based glasses*", Materials Science Forum 32-33, pp 361-366 (1988).

50. G. Abbate, U. Bernini, P. Maddalena, S. De Nicola, P. Mormile and G. Pierattini, "*Interferometric technique for the determination of thermal nonlinearitities in semiconductor glasses*", Optics Communications 70 (6), pp 502-508 (1989).

51. G. Cocorullo, F.G. Della Corte and I. Rendina, "*Temperature dependence of the thermo-optic coefficient in crystalline silicon between room temperature and 550 K at the wavelength of 1523nm*", Applied Physics Letters 74 (22), pp 3338-3340 (1999).

52. G. Cocorullo, F.G. Della Corte, L. Moretti, I. Rendina and A. Rubino, "*Measurement of the thermo-optic coefficient of a-Si:H at the wavelength of 1500nm from room temperature to 200°C*", Journal of Non-Crystalline Solids 299-302, pp 310-313 (2002).

53. J.M. Jewell, C. Askins and I.D. Aggarwal, "*Interferometric method for concurrent measurement of thermo-optic and thermal expansion coefficients*", Applied Optics 30 (25), pp 3656-3660 (1991).

54. S. De Nicola, P. Ferraro, A. Finizio, G. Pierattini and S. Pelli, **"***Interferometric measurement of the refractive index and the thermo-optic coefficient of semiconductor-doped glasses*", J. Opt. A : Pure Appl. Opt. 1, pp 702-705 (1999).

55. S. De Nicola and P. Ferraro, "*Fourier-transform calibration method for phase retrieval of carrier-coded fringe pattern*", Optics Communications 151, pp 217-221 (1998).

56. H. Toratani, "*Properties of laser glasses*", PhD thesis, Kyoto University, Kyoto, Japan, 1989.

57. T. Izumitani and H. Toratani, "*Temperature coefficient of electronic polarizability in optical glasses*", Journal of Non-Crystalline Solids 40, pp 611-619 (1980).

58. T. Erdogan, "*Fiber grating spectra*", Journal of Lightwave Technology 15 (8), pp 1277-1294 (1997).

59. Y. Kokubun, N. Funato and M. Takizawa, "*Athermal waveguides for temperature-independent lightwave devices*", IEEE Photonics Technology Letters 5 (11), pp 1297-1300 (1993).

60. Y. Kokubun, M. Takizawa and S. Taga, "*Three-dimensional athermal waveguides for temperature independent lightwave devices*", Electronics Letters 30 (15), pp 1223-1224 (1994).

61. Y. Kokubun, S. Yoneda and H. Tanaka, "*Temperature-independent narrowband optical filter at 1.3mm wavelength by an athermal waveguide*", Electronics Letters 32 (21), pp 1998-2000 (1996).

62. Y. Kokubun, S. Yoneda and S. Matsuura, "*Temperature-independent optical filter at 1.55mm wavelength using a silica-based athermal waveguide*", Electronics Letters 34 (4), pp 367-369 (1998).

63. M.N. Ng, Z. Chen and K.S. Chiang, *"Temperature compensation of long-period fiber grating for refractive-index sensing with bending effect"*, IEEE Photonics Technology Letters 14 (3), pp 361-362 (2002).

64. A. Sakamoto, T. Matano and H. Takeuchi, *"Ceramic substrate with negative thermal expansion for athermalization of fiber Bragg grating*", IEICE Transactions on Electronics E83-C (9), pp 1441-1446 (2000).

65. G.W. Yoffe, P.A. Krug, F. Ouellette and D. Thorncraft, *"Temperature-compensated optical fiber Bragg gratings"*, in: Conference on Optical Fiber Communication, OFC 1995, Technical Digest, pp 134-135 (1995).

66. M. Tamura, A. Urano, A. Inoue, D. Saitou, M. Inai, T. Itou, M. Shiozaki, H. Suganuma and I. Tsuchiya, *"Development of a temperature-compensating fiber grating*", SEI Technical Review 51, pp 61-66 (2001).

67. D. Bosc, B. Loisel, M. Moisan, N. Devoldère, F. Legall and A. Rolland, *"Temperature and polarisation insensitive Bragg gratings realised on silica waveguide on silicon"*, Electronics Letters 33 (2), pp 134-136 (1997).

68. K. Kintaka, J. Nishii, Y. Kawamoto, A. Sakamoto and P.G. Kazansky, *"Temperature sensitivity of Ge-B-SiO_2 waveguide Bragg gratings on a crystallized glass substrate"*, Optics Letters 27 (16), pp 1394-1396 (2002).

69. J. Nishii, K. Kintaka, H. Nishiyama, and M. Takahashi, *"Photosensitive and athermal glasses for optical channel waveguides"*, Journal of Non-Crystalline Solids 326&327, pp 464-471 (2003).

70. D.L. Williams, B.J. Ainslie, J.R. Armitage, R. Kashyap and R. Campbell, *"Enhanced UV photosensitivity in boron codoped germanosilicate fibres*", Electronics Letters 29 (1), pp 45-47 (1993).

71. A.J. Bruce, *"Silica glass-based fibers"*, Infrared Fiber Optics, J.S. Sanghera and I.D. Aggarwal (Eds), pp 31, CRC Press, Boca Raton (FL), (1998).

CHAPTER 3

EXPERIMENTAL WORK

Throughout the course of this work, various processes and measurements were carried out to melt and prepare the glasses and to characterise their properties. Different fabrication techniques were also used to fabricate waveguides and fibres using these glasses. The general principles of these processes and techniques are described in the following sections. Specific details of these processes involving the glasses studied will be described in the relevant chapters.

3.1 Glass Preparation

3.1.1 Glass Melting

Glass synthesis involves the preparation of the appropriate mixtures of raw materials, a melting process and an annealing process. Table 3.1 shows the different raw materials used, with their respective supplier and purity level, to melt glass samples of different phosphate glass systems for this work. The appropriate amounts of raw materials required for each glass sample were calculated according to the mol% of each component of the glass and weighed to produce the reaction mixture. Appendix B shows examples of raw material calculations for some glasses.

A silica crucible or a platinum crucible was used to batch the mixture of raw materials for melting. Batching was carried out in a dry nitrogen-purged glovebox. The raw materials were weighed and mixed in a glass beaker, homogenised with a porcelain spoon and then transferred to the crucible. Generally, the reaction mixture was melted in an oxygen atmosphere for 60 - 90 minutes in a crucible in a melting furnace, which was preheated to temperatures between 1000°C and 1500°C (melting temperature, T_m), depending on glass compositions. The crucible was covered with a platinum lid to avoid excessive loss of materials during the melting process. The melt was then cast into a casting mould, within an annealing furnace, which had been pre-heated approximately to the glass T_g, to form a rectangular sample. Table 3.2 shows the materials that can be used for

the casting mould, as the glass does not wet them due to their lower expansion coefficients. The glass was then annealed near its T_g for 60 minutes and finally cooled to room temperature at a rate of 0.5°C/min.

Raw materials	Supplier	Purity
Potassium carbonate, K_2CO_3	BDH Laboratory Sigma-Aldrich	99.9% 99.99%
Sodium carbonate, Na_2CO_3	Alfa Aesar	99.5%
Calcium carbonate, $CaCO_3$	Alfa Aesar	99.95%
Barium carbonate, $BaCO_3$	Alfa Aesar	99.95%
Aluminium hydroxide, $Al(OH)_3$	Testbourne Ltd.	99.9%
Boron oxide, B_2O_3	Alfa Aesar	99.98%
Phosphorus (V) oxide, P_2O_5	Alfa Aesar	99.99%

Table 3.1 : Raw materials for glass melting

Material	Thermal expansion, α (´ 10^{-6}/°C)
Graphite	~ 3.0
Brass	~ 11.0
Stainless steel	~ 6.5
Phosphate glasses	~ 6.0 – 22.0

Table 3.2 : Casting material

The annealing schedule followed for all the glasses was as follows : from casting, the glasses were held at a temperature near their T_g for 60 minutes and then slowly cooled to the room temperature at a rate of 0.5°C/min. This was carried out to eliminate the stresses that might be present in the glass. In a homogeneous glass, these stresses can be caused by rapid cooling of the glass through the glass transition region (approximated by the glass T_g), leaving inadequate time for the constituent atoms to occupy the lowest energy sites. Within the transition region, microstructure changes can occur. These changes require an increasing amount of time to occur as the temperature is reduced. Hence, most glass properties, such as T_g and the thermal

expansion coefficient (α), depend on time and temperature (thermal history). This means that a change in the heating and cooling rate can induce variations in glass properties. For a glass cooled at a low rate, the glass is able to shrink to a metastable equilibrium volume and becomes dense. However, if the glass undergoes rapid cooling, there is insufficient time for contraction and the glass structure that freezes has a greater volume. Upon heating to the glass transition region, the structure elements of the glass are rearranged into denser and lower energy sites, leading to a reduction of the glass volume. Such structural changes can affect the glass property measurements. In this thesis, the effect of different annealing schedules on the glass properties of T_g, α and dn/dT were not investigated. It is possible that the absolute values of these glass parameters will change using different schedules. In this work, only one annealing schedule has been used for all the glasses, where the results for dn/dT showed good consistency of results.

The use of silica crucibles can cause contamination of the glass melts. This was because the crucibles can dissolve during melting at high temperatures and traces of silica were mixed in with the glass melts (typically 1 mol%). The crucibles were also not reusable as they normally cracked upon cooling. The use of platinum crucibles directly with P_2O_5 powder can cause damage to the crucible (damage can be minimised by melting in oxygen atmosphere) but they did not crack during heating and cooling, due to the platinum's low thermal expansion (8.8×10^{-6}/°C) and high thermal conductivity (72 W/mK), and hence were reusable. To prevent damage to the platinum crucibles, reduce striae and improve homogeneity as well as to store large volumes of melts, the initial glass was melted in a silica crucible and then cast in a graphite mould at room temperature. The glass was then transferred to a platinum crucible and remelted and finally cast into a graphite mould and annealed. Figure 3.1 shows the glass synthesis procedures while Figure 3.2 shows the timeline involved in the melting process.

In this work, melting of small batches (~ 30 g) of glasses for characterisations, as described in Chapter 4 to 6, was carried out in either a silica crucible or a platinum crucible. However, melting of glasses for fibre and planar waveguide fabrication was carried out in a silica crucible, followed by remelting in a platinum crucible. This was done mainly to improve the glass homogeneity and to reduce striae. Also, remelting in a platinum crucible allowed large volumes of melts to be stored for future use, such as the core and overclad melts for the spin-coating process. In contrast, silica crucible cracked upon cooling after the melting process, preventing further use.

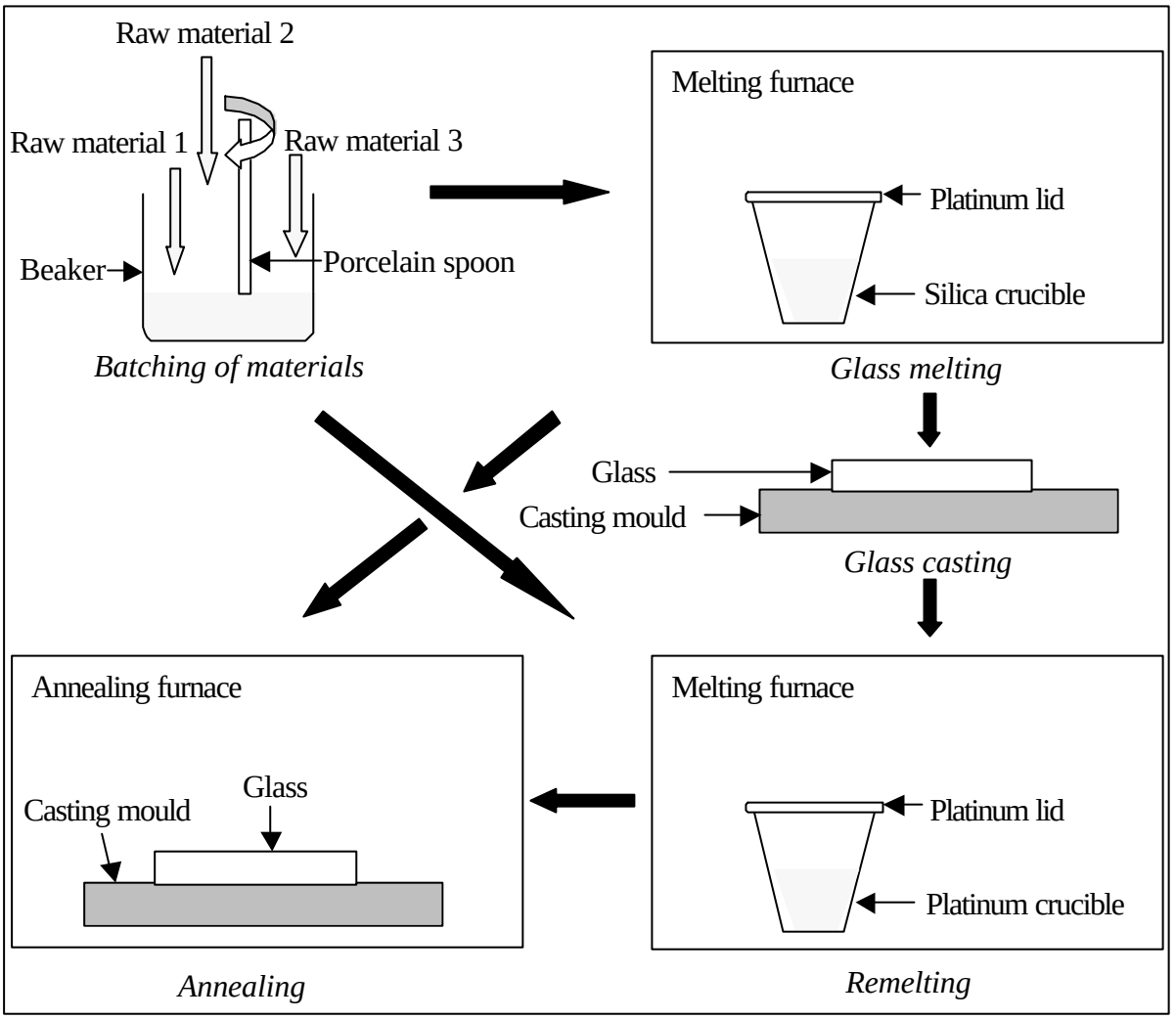

Figure 3.1 : Glass synthesis procedures

Energy dispersive analysis of X-ray (EDAX) was carried out on a random selection of glasses and the results of some of these glasses are shown in Appendix C. The analysed glass compositions were found to be ~ ±3 mol% from the nominal compositions that were prepared and melted, with an error of ±3% due to changes in the experimental conditions over time during the analysis. Analysis carried out on a few spots on each sample showed good sample homogeneity with a composition consistency of ±2% throughout the sample. The samples were also analysed for the presence of SiO_2 to assess the level of contamination from the melting process.

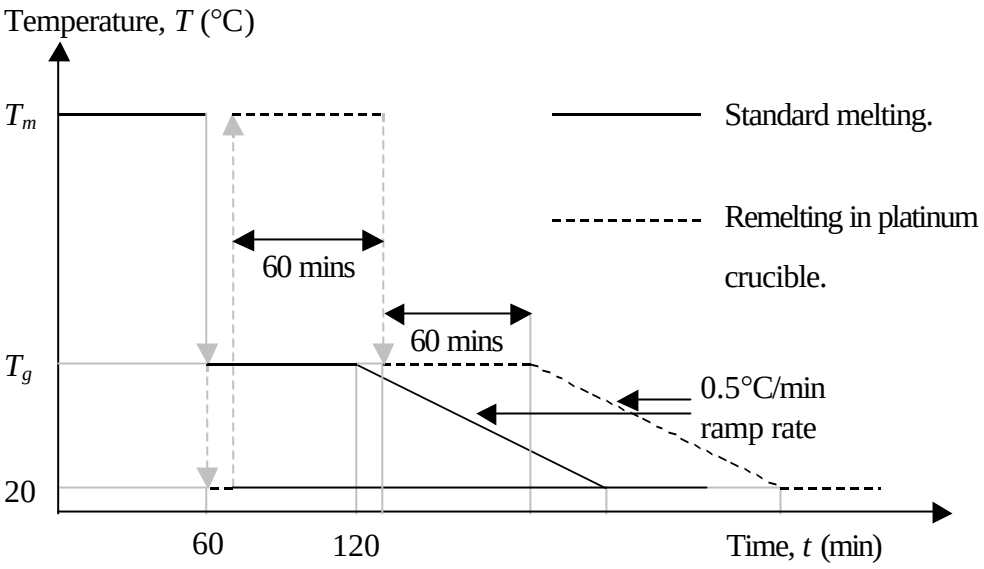

Figure 3.2 : Timeline for glass synthesis

Photograph 3.1 shows a silica crucible containing a reaction mixture in a melting furnace while Photograph 3.2 shows a rectangular glass sample cast into a graphite mould.

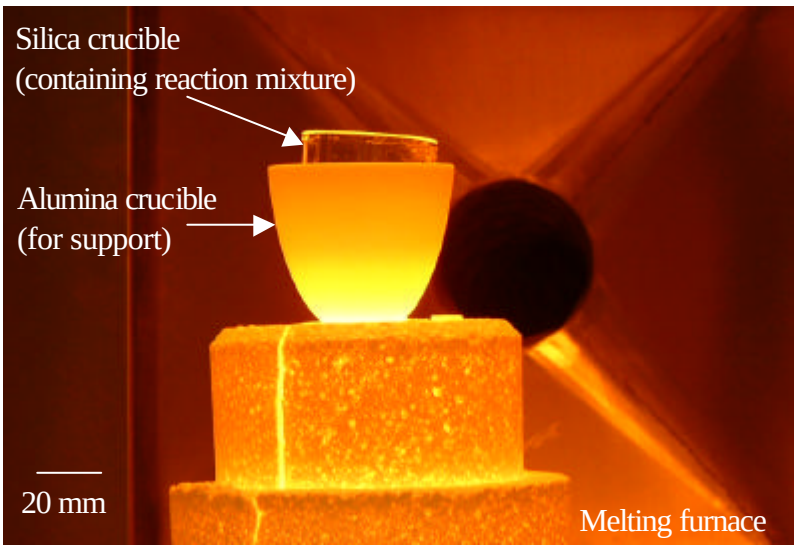

Photograph 3.1 : Glass melting

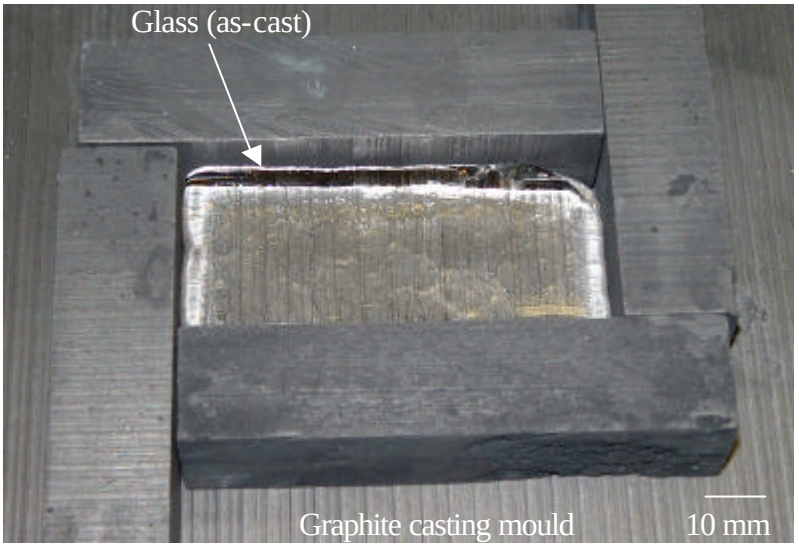

Photograph 3.2 : Glass casting

3.1.2 Glass Polishing

Before the glasses could be characterised for optical and thermal properties, it was necessary to polish the glasses. This was because the melted glasses can have rough and uneven surfaces. A 3-step procedure using three different solutions containing 9 μm calcined alumina powder, 3 μm calcined alumina powder and 0.125 μm silica particles (Syton) respectively, was used to produce glasses with smooth, flat and optically transparent surfaces.

The first two steps involving alumina solutions are known collectively as the 'lapping' process. The glasses were first lapped using the coarse grit size of 9 μm on a cast iron plate to shape, flatten as well as to thin the glasses to the required dimensions. This was then followed by the solution containing grit size of 3 μm to reduce scratches and edge damage caused by the previous step. The final step involving the Syton solution on a polyurethane plate is the 'polishing' process. This improved the quality of the surface by removing surface roughness, surface scratches and edge damage.

For the various thermal and optical measurements carried out within this work, sample flatness was not a critical aspect and the above lapping and polishing procedures described were sufficient in producing transparent and optically polished glass surfaces for characterisation. In

fact, for *dn/dT* measurement, a slight wedge on one of the glass surfaces was desired, so that the interference fringes could be observed, as described in Section 3.4.

For different property measurements, the samples were lapped and polished to the required dimensions as shown in Table 3.3.

Property	Required sample thickness (mm)
Thermal expansion coefficient *Refractive index* *Thermo-optic coefficient*	~ 10.0
UV spectrum *OH concentration*	~ 2.0

Table 3.3 : Sample thickness for property measurements

3.2 Thermal Properties

3.2.1 Glass Transition Temperature, T_g

A Differential Thermal Analyser (Perkin Elmer DTA7) was used to measure the glass transition temperature in nitrogen atmosphere. In addition, the extrapolated onset of crystallisation, T_x, peak crystallisation, T_p, and melting, T_m, temperatures can also be determined. The DTA (Figure 3.3) enables the characterisation and analysis of thermal properties of materials. It consists of a cell base and a high temperature furnace, capable of heating up to 1600°C. Within the furnace, there is a matched pair of thermocouples constructed of platinum and platinum/10% rhodium. Each thermocouple monitors the temperature of an alumina cup, one cup containing alumina powder as reference while the other cup contains a small piece of glass sample, about 20 - 30 mg, in alumina powder. As the furnace ramps up, the thermocouples measure the differential temperature, ΔT, between the two alumina cups, due to the endothermic and exothermic reactions in the glass. A background measurement is first carried out without the glass sample. A second measurement is then carried out with the sample in one of the alumina cups, corrected for the background measurement. In this way, the data obtained corresponds only to the thermal changes in the

sample itself.

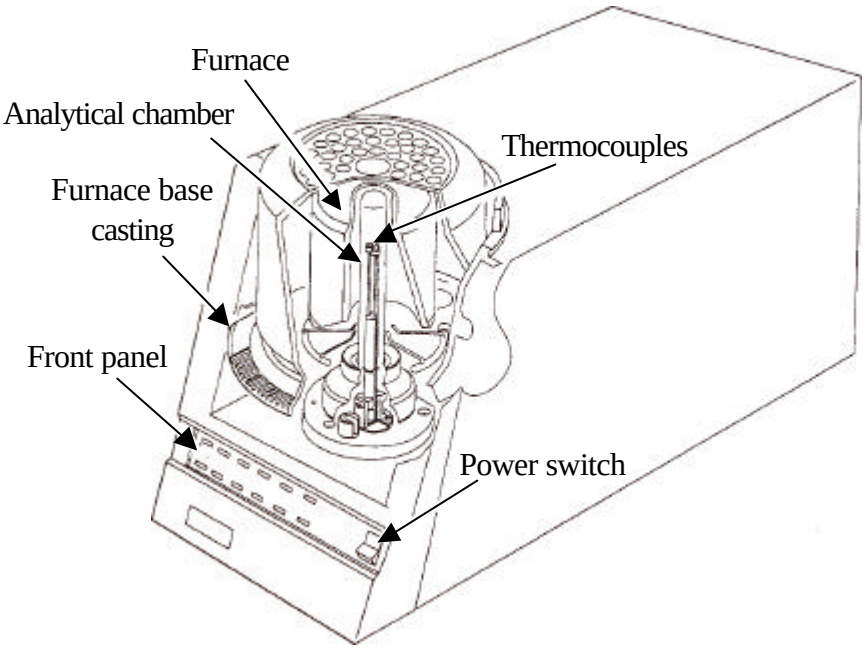

Figure 3.3 : Differential thermal analyser (DTA)

For T_g measurement, the glass samples were heated at a rate of 40°C/min from room temperature to about 150°C below their respective T_g and then heated at a rate of 10°C/min to about 900°C. Repeated measurements of samples with similar nominal composition showed an uncertainty of ±5°C. This uncertainty could be attributed to differences in the melted compositions between samples. This could be due to error while weighing raw materials during batching, material evaporation during melting as well as SiO_2 contamination and sample homogeneity. A typical DTA trace is shown in Figure 3.4, recorded as ΔT between the alumina cups against sample temperature. The transition temperatures on the figure were estimated as the intercepts of the tangents to the curves.

As the temperature increases, the disordered rigid glassy structure with little molecular mobility changes to a 'liquid' state with increased molecular mobility and flow. This is denoted by the first endothermic event (T_g). Further increase in temperature results in nucleation and crystal growth, characterised by the onset of crystallisation (T_x) and an exothermic peak (T_p). When the DTA curve returns to the baseline after the melting event, the liquidus has been reached. The thermal stability of the glass is generally determined from (T_x-T_g) and (T_p-T_x). (T_x-T_g) should be large

(ideally ≥ 150°C) to provide the maximum working temperature range for the glass before crystallisation sets in. (T_p-T_x) should also be large as this generally means that there are a number of crystal events happening and competing against each other such that crystallisation will not progress rapidly once started.

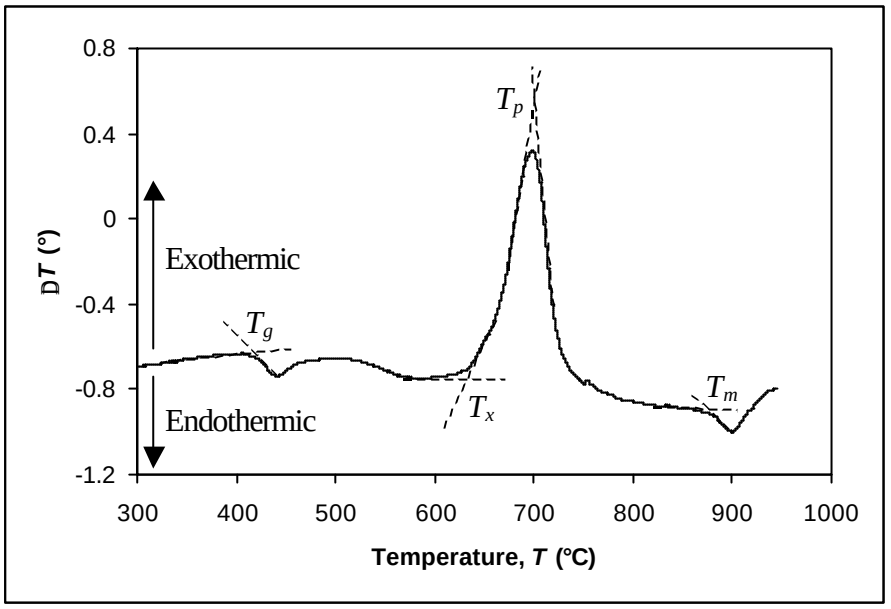

Figure 3.4 : Typical T_g measurement data (*KAP-1b* sample data from Chapter 4)

3.2.2 Thermal Expansion Coefficient, α

The thermal expansion coefficient was measured using a Thermo-Mechanical Analyser (Perkin Elmer TMA7). The TMA (Figure 3.5) permits the measurement of dimensional changes in materials as a function of temperature or time. It consists of a highly sensitive linear variable differential transformer (LVDT) with a displacement sensitivity of 50 nm and a furnace capable of heating up to 1000°C. The glass sample is sandwiched between two Inconel disks and held in place by a probe in the sample holder. As the furnace ramps up, the sample heats up and expands and causes a change in the probe position. The sensitive temperature-controlled LVDT and a precise linear probe control motor enables accurate monitoring of this change.

α was measured in the temperature range of 50 - 300°C with a force of 110 mN. The glass samples, in rectangular shape approximately 4×4×10 mm^3, were heated to 300°C at 5°C/min.

Repeated measurements of samples show an experimental error within $\pm 0.2\times10^{-6}$/°C. Figure 3.6 shows a typical TMA curve, presented as sample height, h, against temperature, T. The expansion coefficient, α, is defined as $(1/h)(dh/dT)$ where dh/dT can be determined from the slope. If the measurement was carried out to higher temperatures, the glass transition temperature, T_g, of the glass can also be measured, as indicated in Figure 3.6 by a change in the slope representing a change in the glass viscosity.

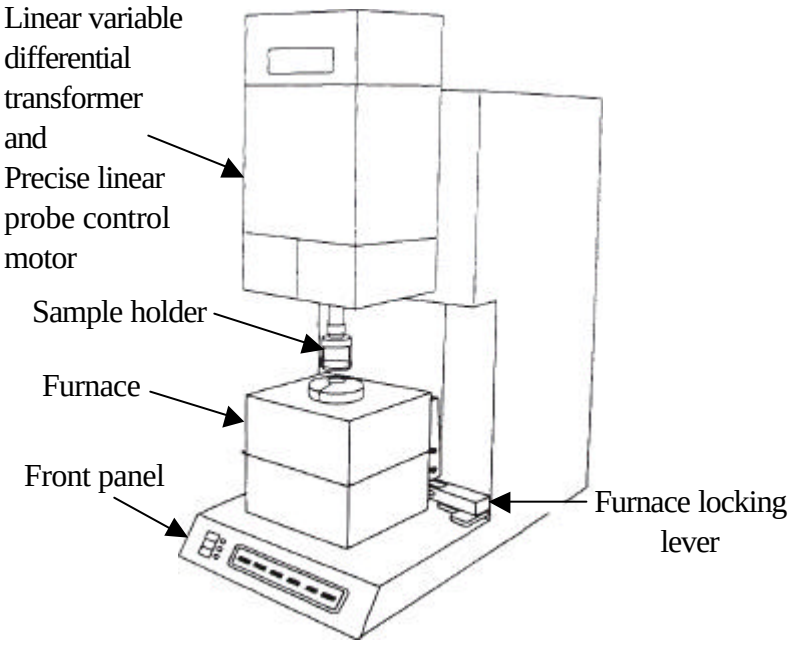

Figure 3.5 : Thermomechanical analyser (TMA)

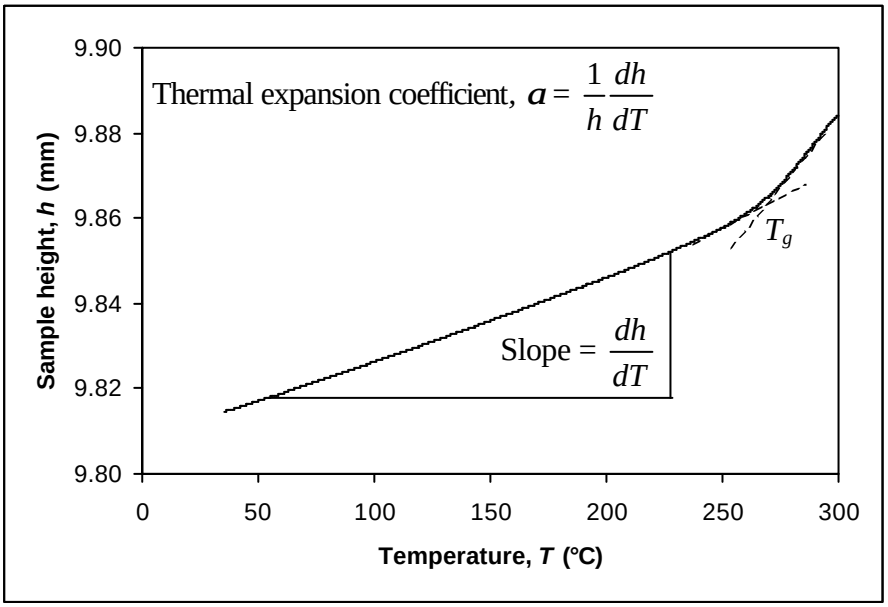

Figure 3.6 : Typical α measurement data (*KAP-2a* sample data from Chapter 4)

3.3 Optical Properties

3.3.1 Refractive Index, *n*

An Abbe '60' refractometer (Bellingham & Stanley Ltd.), as shown in Figure 3.7, was used to measure the refractive index of the glasses at room temperature, by means of the total internal reflection phenomenon, at the sodium D-line (λ = 589.3 nm). Measurement error was estimated to be within ±0.0005, due to instrument limitation. Measurement of different samples with the same nominal composition gave an estimated uncertainty of ±0.001. This could be due to changes in the compositions during batching, melting as well as SiO_2 contamination and sample homogeneity.

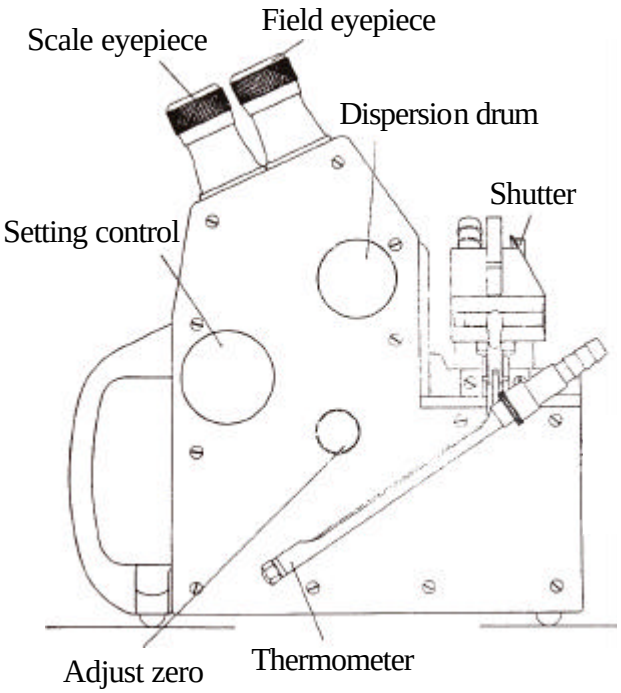

Figure 3.7 : Abbe '60' refractometer

Figure 3.8 shows the basic principle of the refractometer. There is a prism within the refractometer where the 'AB' and 'CA' faces are polished while 'BC' is grey to increase contrast. The prism generally has a high refractive index, $n_1 \sim 1.7$. To measure the refractive index of a sample, n_2 ($n_2 < n_1$), the sample is placed onto the prism, with its polished face

downwards. Generally, a few drops of index matching fluid with refractive index n_f, where $n_1 > n_f > n_2$, is used to avoid any trapped bubbles at the interface.

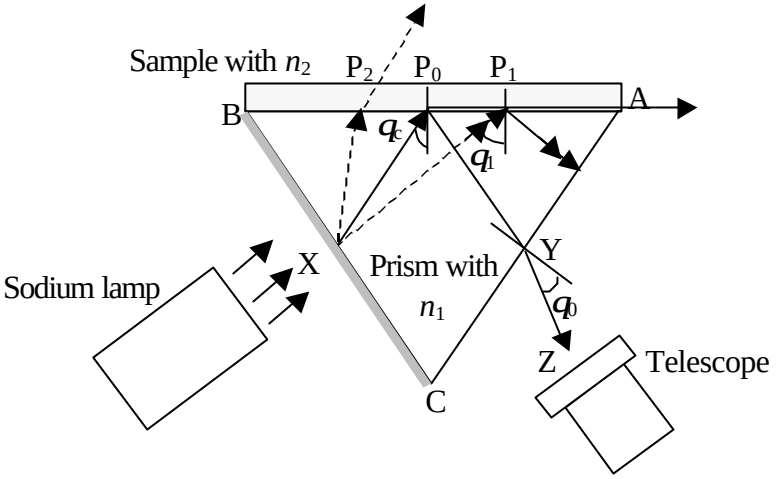

Figure 3.8 : Total internal reflection in a prism

Light from a sodium lamp is incident on the 'BC' face of the prism. From point X, the radiation is diffusely scattered into the prism. The light path 'XP_0' traces the boundary condition for total internal reflection where the angle of incidence is equal to the critical angle between the prism and sample, θ_c. Hence, any light paths having incident angles less than the critical angle, such as 'XP_2', will partly propagate into the sample. However, light paths such as the 'XP_1' path with $\theta_1 > \theta_c$ will be total internally reflected and emerge from the 'CA' face. If we view in the direction of 'YZ', the field across the telescope view will be divided into a dark region for $\theta > \theta_0$ and a bright region for $\theta < \theta_0$. Knowing the properties of the prism, the instrument is calibrated such that the observed value of θ_0 directly corresponds to the sample refractive index.

3.3.2 Thermo-optic Coefficient, *dn/dT*

The thermo-optic coefficient was measured using an interferometer set-up in the temperature range of 20 - 100°C at a rate of 40°C/hour. *dn/dT* values were reproducible to ±5%, due to the uncertainty of ±0.1°C for ΔT, extracted from the measurements to calculate *dn/dT*, as well as the errors in the measured values of n and α. The experimental set-up and principles of operation are described in detail in Section 3.4.

3.3.3 UV Spectrum

Ultraviolet (UV) resonance of glasses is generally associated with the band-to-band transition of electrons. High energy photons (short wavelength UV radiation) exceeding the electron band gap can optically excite the electrons from the valence to the conduction band. However, if a particular photon energy is insufficient, no electron excitation occurs and the glass will be transparent at that particular wavelength.

UV spectra of the glasses were collected using a Varian Cary 500 Scan UV/Vis/NIR Spectrophotometer. The spectrophotometer was able to generate discrete wavelengths of light, from 175 nm up to 3300 nm, which were passed through a sample in order to measure the amount of light absorbed. Hence this equipment can be used to measure the transmission/absorption of a glass sample from the UV to the near infrared (NIR). It also included a chopper, made up of a mirrored section to reflect the light beam, a section which allowed the light beam to pass and a section which was 'dark' to block the light beam. This arrangement allowed the light beam to be directed to two different directions, alternating between the sample and reference, and to allow the change of the grating to the next wavelength during its 'dark' section. This had the advantage that results reported were averaged over each discrete wavelength and not over several wavelengths.

The UV edge spectra of the glasses were collected using polished samples approximately 2 mm thick, in the wavelength range of 190 – 500 nm. A 'Zero/baseline correction' was first carried out. Measurements were taken without the glass sample to collect the '100 % transmission' background and then the sample beam was blocked off to collect the '0 % transmission' background. The UV spectrum for the sample was then taken, corrected for the background measurements. Figures 3.9 and 3.10 show the typical UV transmission spectrum and UV absorption spectrum, corrected for Fresnel reflection, respectively. The data for transmission can be converted to absorbance and vice versa using equation (3.1).

$$\text{Absorbance} = log\left(\frac{T_{max}}{T_m}\right) \tag{3.1}$$

where T_{max} is the maximum transmission and T_m is the measured transmission at a particular wavelength. The absorbance data for a sample can also be represented by the absorption coefficient, as determined by equation (3.2)

$$rl = ln\left(\frac{T_{max}}{T_m}\right) \tag{3.2}$$

where r is the absorption coefficient and l is the sample thickness.

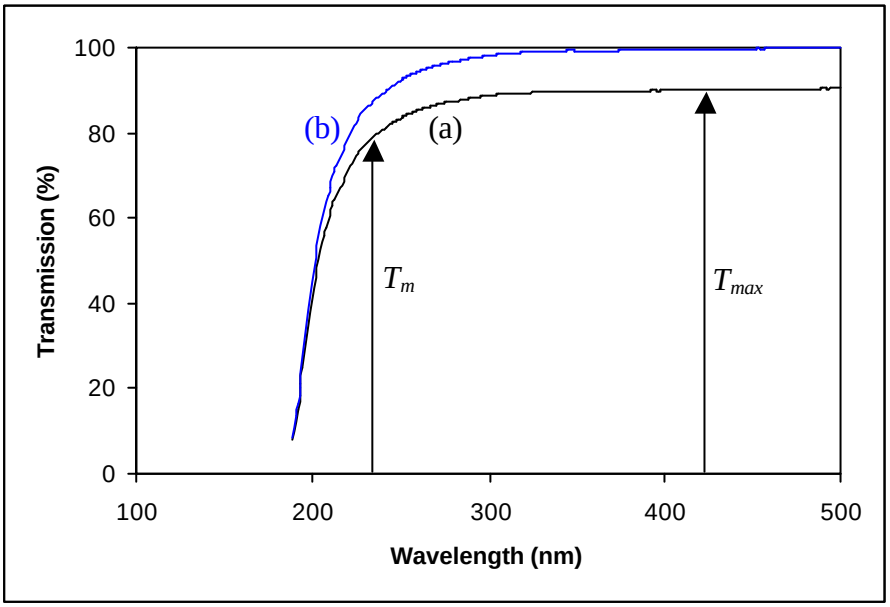

Figure 3.9 : Typical UV transmission spectrum : (a) Measured data and (b) Corrected for Fresnel reflection (*CaP-1b* sample data from Chapter 5)

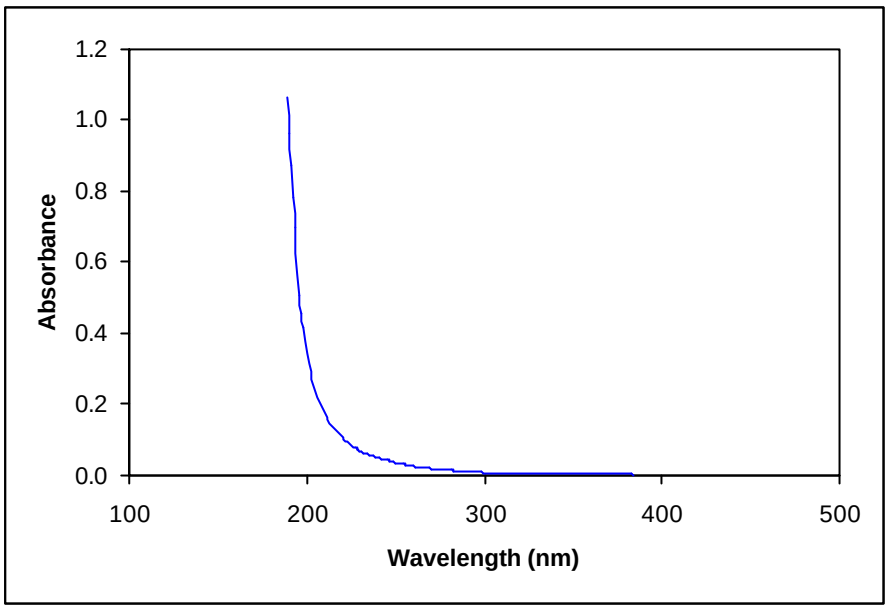

Figure 3.10 : Typical UV absorption spectrum, corrected for Fresnel reflection (*CaP-1b* sample data from Chapter 5)

3.3.4 OH Content, r_{OH}

Infrared measurements of relative OH concentrations were collected using a Fourier transform infrared (FTIR) spectrophotometer (Perkin Elmer System 2000). An FTIR spectrophotometer records the interaction of IR radiation with experimental samples, measuring the frequencies at which the sample absorbs the radiation and the intensities of the absorptions. Hence different absorption bands can be detected to identify the components and impurities within the samples.

The Perkin Elmer System 2000 uses a tungsten halogen lamp source and a tri-glycine sulphate detector in the NIR range. The source radiation is directed through an interferometer and onto the sample. The light passes through a beamsplitter and splits into two perpendicular directions towards a stationary mirror and a moving mirror, respectively, creating a difference in the path lengths when the light paths are reflected back to the beamsplitter and recombine. This creates an interferogram, due to constructive and destructive interference. The recombined beam is then passed through the sample, which absorbs the wavelengths specific to the sample, and corrected for the interferogram to produce the absorption data.

Measurements were taken with polished samples approximately 2 mm thick, in the transmission mode in the range of 2000 - 5000 cm^{-1} (5000 – 2000 nm) with a resolution of 4 cm^{-1}, averaged over 30 scans. Background subtraction was performed for each sample analysis to eliminate the effects of IR-active atmospheric components such as carbon dioxide (CO_2) and water (H_2O). Figure 3.11 shows a typical FTIR scan in transmission mode. For phosphate glasses, there is a broad OH absorption band at around 3000 cm^{-1} (~ 3.3 μm) [1]. From the FTIR scan, the relative OH concentration can be expressed in terms of the OH absorption coefficient, r_{OH} [2]:

$$r_{OH} = \frac{\left(-ln\left(\frac{T_{3000}}{T_{5000}} \right) \right)}{l} \tag{3.3}$$

Equation (3.3) determines the relative concentration of OH from the transmission % at 3000 cm^{-1} (T_{3000}), normalised to the transmission % at 5000 cm^{-1} (T_{5000}) and the sample thickness, l. T_{5000} serves as a background transmission and includes the Fresnel reflection losses. This equation is essentially similar to equation (3.2) except for the longer wavelength range that the FTIR is capable of measuring. The resolution of FTIR is better due to the longer path length traversed by the light beam before it is incident upon the sample.

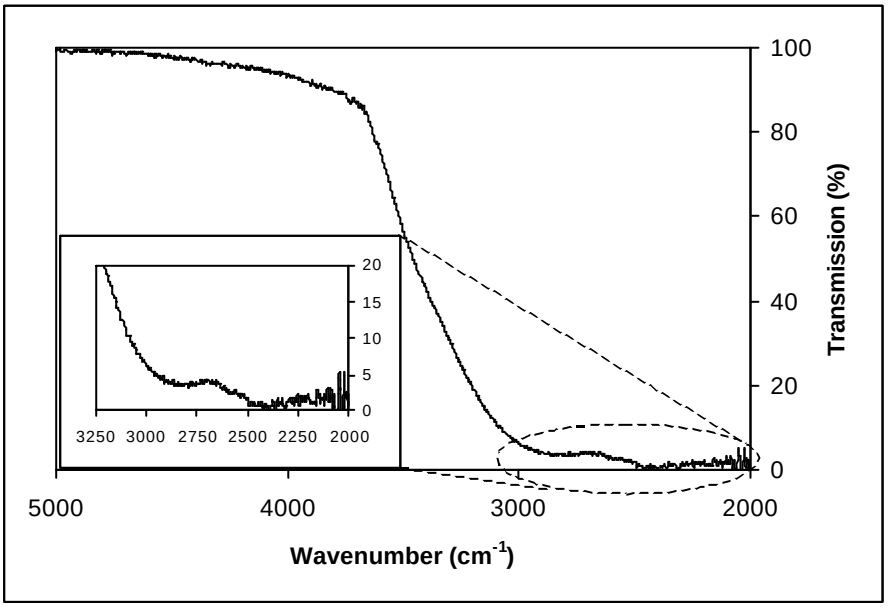

Figure 3.11 : Typical FTIR spectrum, corrected for Fresnel reflection.
(Inset) OH absorption at ~ 3000 cm^{-1} (*KAP-1b* sample data from Chapter 4)

3.4 Study of *dn/dT*

This part of the work involved the study of the *dn/dT* of glasses, which was one of the main objectives of my research work. As no such measurement had been done previously in the Optoelectronics Research Centre, the Author had to build an interferometer set-up to perform this measurement. Several substantial improvements were made to the set-up iteratively in terms of the design of the sample holder and heater position, in order to be able to measure *dn/dT* accurately.

3.4.1 Theory of Interference

Wave interference is a phenomenon which occurs when two waves meet while travelling along the same medium. Constructive interference occurs when two interfering waves are in phase. In this situation, both the interfering waves have a displacement in the same direction and hence add up to make a resulting wave with a greater displacement than the individual interfering waves in the same direction. Destructive interference happens when two interfering waves are out of phase. In this situation, each wave has a displacement in the opposite direction to the other wave and hence cancels each other, either completely or partially depending on the initial displacements, to produce a resulting wave with a smaller displacement than the individual interfering waves.

In either case, the meeting of two waves along a medium does not alter the individual waves or even deviate them from their path. A composite wave, made up of two harmonic sinusoidal waves with identical frequency, will also be harmonic and of the same frequency although its amplitude and phase will be different.

3.4.2 Interferometer Set-up

An interferometric technique was set up to measure the thermo-optic coefficient, *dn/dT*. The experimental set-up is shown in Photograph 3.3 and schematically in Figure 3.12. This set-up was constructed based on the work described by Jewell *et al*. [3], but with slightly different apparatus set-up and sample design.

The sample was held in place by a sample holder within a heat chamber, which was heated by two small heaters (20 W cartridge heaters by RS). The construction of the sample holder and heaters is shown in Photograph 3.4. The sample holder consisted of two aluminium plates, with the front plate graphite-coated. This prevented any reflection from the plate and provided good thermal contact with the front face of the sample. The front plate was spring loaded to provide good sample stability and prevent strain-induced distortion from thermal cycling during the measurement, while the back plate was fixed in place.

In this set-up, light from a He-Ne laser with a power of 5 mW and a spot size of 1 mm was used to illuminate the sample. The light was then reflected from the front and back faces of the sample. These two reflected light paths formed an interference pattern, which could be detected and collected by a silicon photodetector, via the beamsplitter. The photodetector was connected to an analogue-to-digital converter (ADC16 by Pico Technology Ltd.) together with the thermocouple of the temperature controller in order to feed the required data into a computer for analysis. This thermocouple was attached to the base of the sample holder where this position offers the most stable temperature ramping. Heating was carried out at a slow rate of 40°C/hour to allow enough time for the sample to reach the desired temperature. A rate of 20°C/hour was previously tested and there was no difference in the results obtained at these two heating rates. Three other thermocouples were attached separately to the base, front plate and back plate of the sample holder, respectively, to monitor the temperatures at these locations. A temperature difference of about 5°C was observed among the three locations.

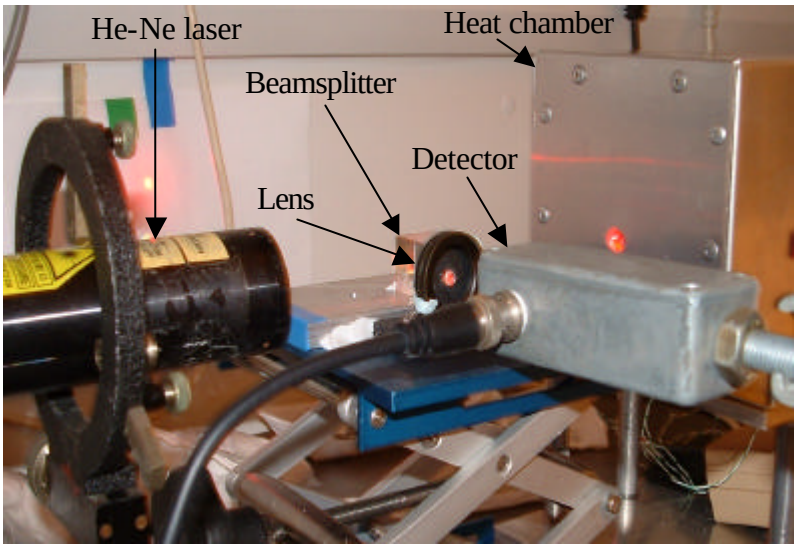

Photograph 3.3 : Interferometer set-up

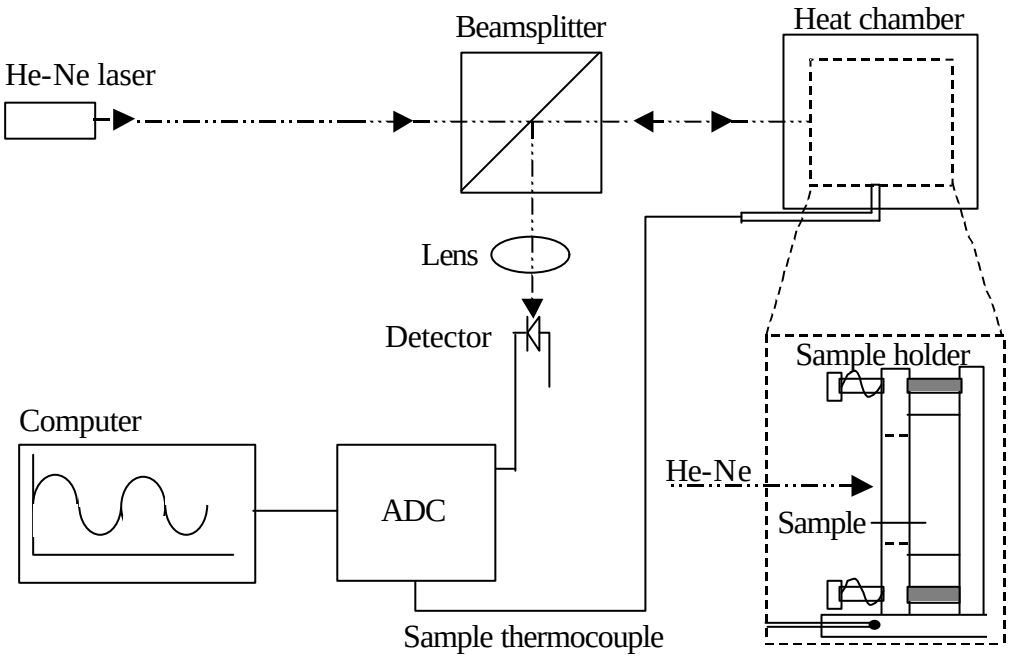

Figure 3.12 : Interferometer set-up

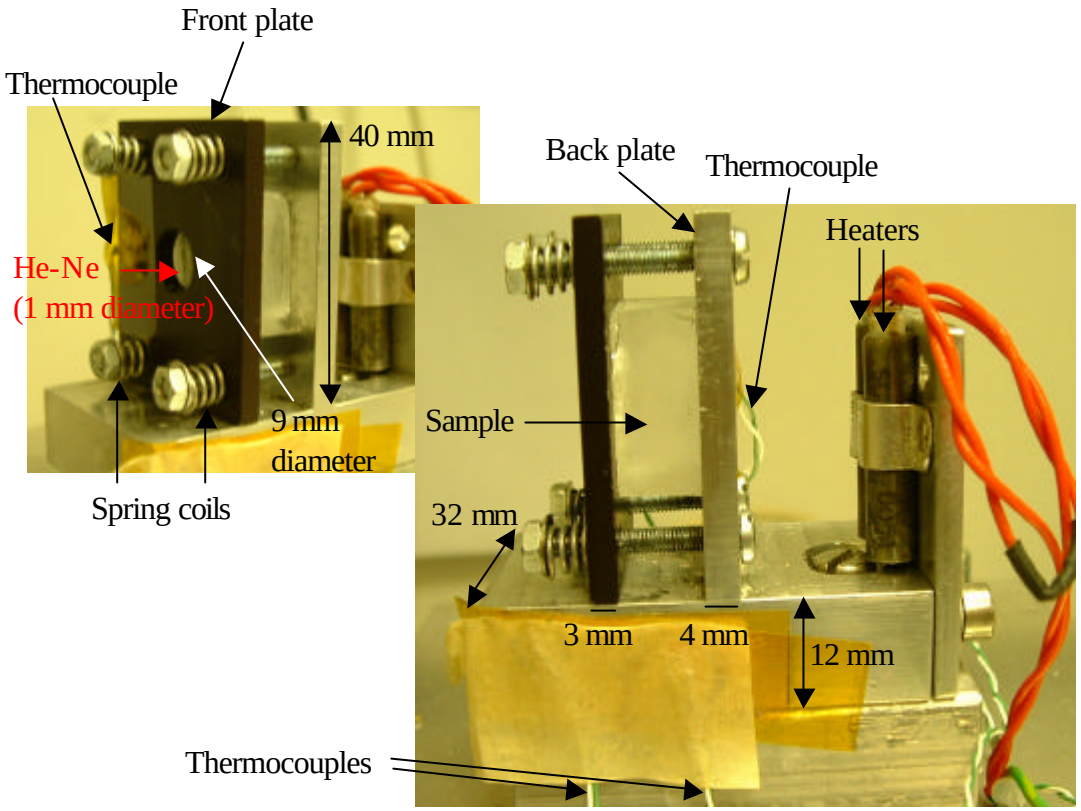

Photograph 3.4 : Sample holder

3.4.3 Analysis of Fringe Pattern

The interference pattern formed from the reflected beams from the front and back faces of the glass sample can then be analysed to calculate *dn/dT*. Photograph 3.5 below shows a typical interference fringe pattern (far field) obtained, and a schematic representation of where the detector was positioned with respect to the fringes.

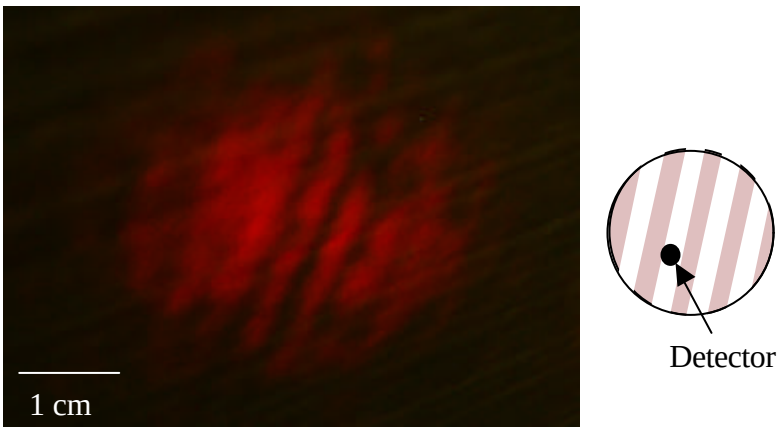

Photograph 3.5 : Fringe pattern

A silicon photodetector, which was connected to the ADC, was used to detect the intensity of the light reflected from the sample. The detector was first positioned on either a bright fringe or a dark fringe. As the sample was heated, the optical path length between the front and back faces of the sample changed due to the combined effects of α and *dn/dT* of the sample. When the net path length increased, the fringes moved and was recorded as oscillations in the intensity of the light upon the detector. Hence the output of the ADC as observed on a computer showed an approximate sinusoidal wave. Figure 3.13 shows the typical sinusoidal interference pattern obtained. The measurement was recorded as a function of time but can be directly converted to temperature as every elapsed 90 seconds corresponded to 1°C change in temperature (heating rate of 40°C/hour).

The general relative phase of two interfering beams, $\Delta\phi$, as a function of temperature, *T*, is given as [4]

$$\Delta\phi = \left(\frac{4\pi}{\lambda}\right) l \left[n\alpha + \left(\frac{\partial n}{\partial T}\right)\right] T \tag{3.4}$$

where λ is the laser wavelength, *l* is the glass thickness, *n* is the refractive index, α is the thermal expansion coefficient, ¶*n*/¶*T* is the thermo-optic coefficient and *T* is the temperature.

By measuring ΔT, corresponding to the temperature difference between successive maxima or minima of the fringes, or equivalently, to a phase difference of 2π ($\Delta\phi = 2\pi$), equation (3.4) can be rearranged to equation (3.5) below to calculate *dn/dT* [3,5],

$$\frac{dn}{dT} = \left(\frac{\lambda}{2 l \Delta T}\right) - n\alpha \tag{3.5}$$

Throughout this work, λ = 632.8 nm (He-Ne laser), *l* was typically 10 mm and *n* measured at λ = 589.3 nm. *n* was measured at the sodium D-line (λ = 589.3 nm) because of the available lamp source, compared to the measurement of *dn/dT* at λ = 632.8 nm. The use of *n* at λ = 589.3 nm, instead of λ = 632.8 nm did not significantly affect the results for *dn/dT* because the values of *n* at these wavelengths did not vary greatly. At the most, the values of *n* would differ by 0.002.

The error in *dn/dT* can be analysed in terms of the errors in the measured values of ΔT, n and α. If the errors associated with ΔT, n and α are $\Delta(\Delta T)$, Δn and $\Delta\alpha$, then the error in *dn/dT*, $\Delta(dn/dT)$, can be evaluated using the following equation:

$$\Delta\left(\frac{dn}{dT}\right) = \frac{dn}{dT}\sqrt{\left(\frac{\Delta(\Delta T)}{\Delta T}\right)^2 + \left(\frac{\Delta n}{n}\right)^2 + \left(\frac{\Delta\alpha}{\alpha}\right)^2} \qquad (3.6)$$

where $\Delta(\Delta T) = \pm 0.1°C$, $\Delta n = \pm 0.0005$ and $\Delta\alpha = \pm 0.2\times10^{-6}/°C$, as stated in the previous sections.

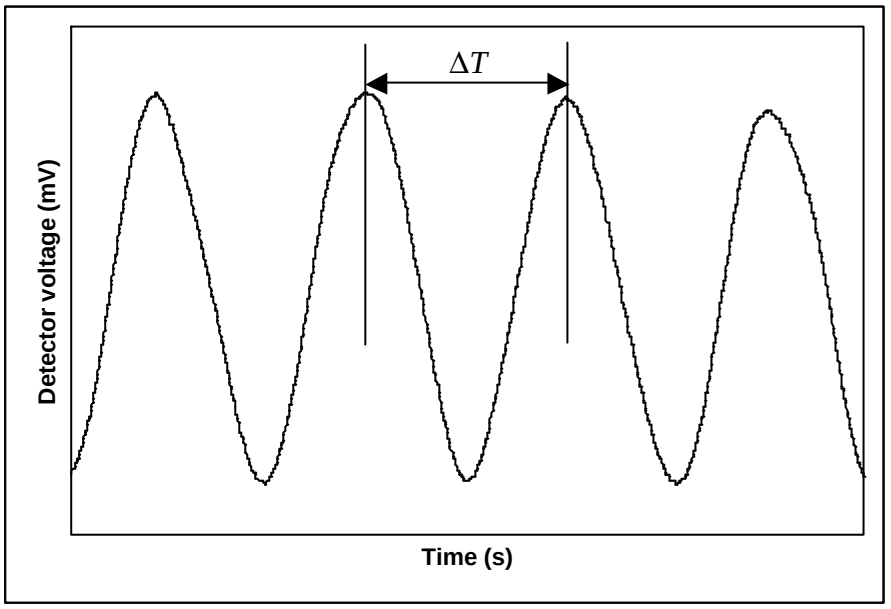

Figure 3.13 : Sinusoidal interference pattern

3.4.4 *dn/dT* Measurements

In order to verify the reproducibility and accuracy of the measurements taken with the interferometer, some glasses were put through the experimental set-up to determine their *dn/dT* values. These were carried out at a wavelength of 632.8 nm (He-Ne), measured over 20 – 100 °C using 10 mm thick samples. The results obtained are shown in Table 3.4. Ref [6] did not give the wavelength and temperature range for the measurements. The *dn/dT* values from ref [7] were estimated for λ = 632.8 nm and T = 20 - 40°C while that for ref [8] was quoted for

λ = 508 nm and T = 20 - 120°C. The measured and literature *dn/dT* values were comparable, indicating that the interferometer was functioning properly within experimental errors and able to determine *dn/dT* accurately.

Glass	*dn/dT* (´ 10^{-6}/°C) (Experimental)	*dn/dT* (´ 10^{-6}/°C) (Literature)	Reference
Silica	10.90 ± 0.18	10.40	[6]
N-PK51 (Schott)	-7.09 ± 0.35	-7.32	[7]
N-FK51 (Schott)	-6.34 ± 0.28	-6.37	[7]
Barium metaphosphate (BaP-1c sample from Chapter 5)	-10.24 ± 0.36	-10.60 -10.30	[6] [8]

Table 3.4 : *dn/dT* of trial glasses

3.4.4.1 Effect of Sample Thickness on *dn/dT*

In equation (3.5), l and ΔT are variables, being inversely proportional to one another, while at a particular wavelength and temperature, n, α and *dn/dT* are constants, for a particular glass sample. Hence, decreasing the thickness of a sample under test increases ΔT for constant *dn/dT*. This suggests that *dn/dT* is independent of sample thickness. A series of *dn/dT* measurements, under similar conditions, were taken to verify the above observation, using a barium metaphosphate glass sample at various thickness. A 13.6 mm thick sample was initially used and after every measurement, the sample was thinned down through lapping and polishing, as described in Section 3.1.2. Table 3.5 shows the measured *dn/dT* values at different thickness with the errors calculated according to equation (3.6). Measurements were repeated four times for sample A5 to verify the reproducibility of the results. The *dn/dT* values were approximately the same but nevertheless varied slightly. This was due to offsets in ΔT, as shown in Figure 3.14, comparing the measured and literature ΔT values. The literature ΔT values were determined from equation (3.5) based on the n, α and *dn/dT* results of Shchavelev *et al.* [8] and substituting for λ (632.8 nm) and l (10 mm). Despite the offset in ΔT, the results showed that the measured ΔT varied with the glass thickness, l. Throughout this research work, glass samples with thickness of

approximately 10 mm were used.

Sample	*l* (mm)	*dn/dT* (´ 10^{-6}/°C)
A1	13.62	-10.05 ± 0.52
A2	13.01	-10.09 ± 0.50
A3	11.97	-10.17 ± 0.47
A4	10.92	-10.08 ± 0.43
A5a	10.07	-10.03 ± 0.40
A5b	10.07	-10.03 ± 0.40
A5c	10.07	-10.45 ± 0.40
A5d	10.07	-10.45 ± 0.40
A6	8.98	-10.30 ± 0.36
A7	7.78	-10.05 ± 0.32
A8	7.05	-10.45 ± 0.30

Table 3.5 : *dn/dT* values for barium metaphosphate sample at different thickness. (*dn/dT* measured at *l* = 632.8 nm over 20 – 100 °C)

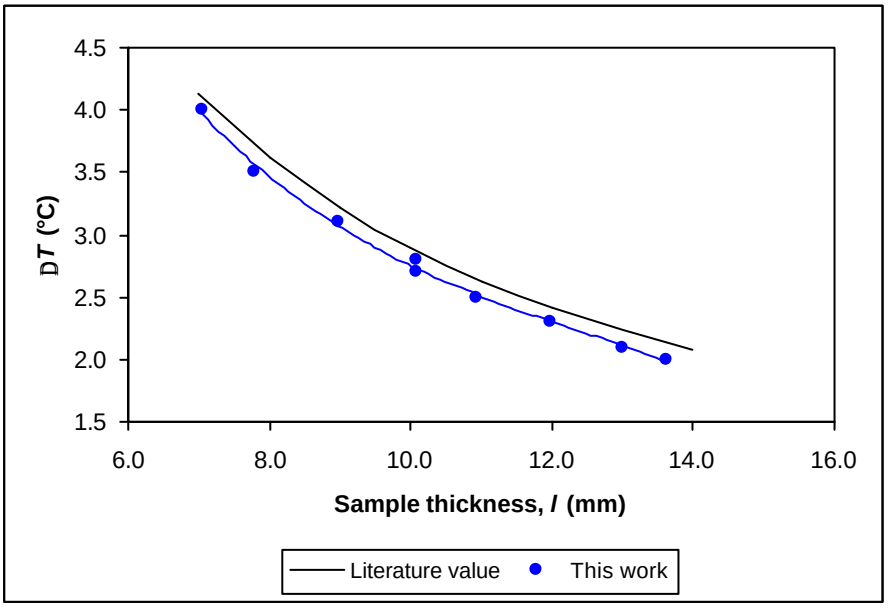

Figure 3.14 : D*T* values for barium metaphosphate sample at different thickness

3.5 Fibre Fabrication

When the glasses had been fully characterised, samples were prepared for fibre fabrication and waveguide fabrication (Section 3.6). This section gives a general overview of the procedures involved in the fibre fabrication process investigated as part of this work. Section 3.5.1 describes the extrusion process used to obtain a preform for fibre drawing while Section 3.5.2 describes the fibre drawing process. Details of the specific glasses and fabrication conditions used in this work will be described in the relevant chapters.

3.5.1 Extrusion

The extrusion process was used to prepare the preform for fibre pulling. This process has the advantages of low processing temperature and flexibility in the shape and size of the extruded product. The process was initially investigated for the extrusion of an alkali lime silicate glass and a calcium aluminate glass [9], and since then, glass ceramic materials [10] and glass matrix composites [11] had also been extruded.

In general, core and cladding glass disks of 5 – 10 mm thick and 29 mm diameter were first cast and prepared. Before the extrusion process, an extrusion body was prepared, containing the following, in the order in which they were first placed into the body. All parts were made from stainless steel and of 29 mm diameter.

1. Clad die (5 mm thick) with a central hole (2 mm diameter).
2. Clad glass.
3. Core die (5 mm thick) with a central hole (2 - 4 mm diameter), to which a core glass had been directly cast to fill the hole in order to minimise trapped air.
4. A flat plate (1 mm thick).
5. Three carbon papers (1 mm thick each).
6. A spacer (2 mm thick).

Parts 2 – 6 were contained in a stainless steel sleeve. Both the core and clad die had sloping wedges to aid slippage of the glass along the die wall and improve glass flow, resulting in increased extrusion rate. Photograph 3.6 shows the body parts for extrusion.

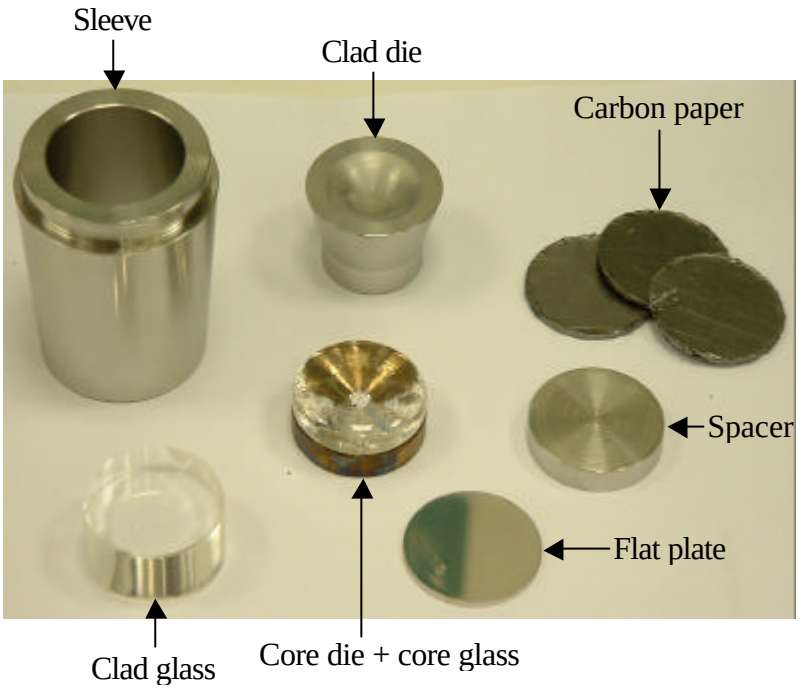

Photograph 3.6 : Body parts for extrusion

The body construction was then placed into the extrusion rig (Photograph 3.7) and heated to the softening temperature of either the core or cladding glass, whichever was higher. Pressure, up to 75 bar (7.5 MPa), was then applied uniformly via a plunger, to the body to force the molten glasses through the small holes of their respective die to extrude a cane. The diameters of the die holes can be designed to produce the required core to clad ratio. In order to further decrease the ratio for fibre fabrication, a cladding glass tube of large outer diameter (depending on the required ratio) was extruded, into which the cane can be inserted to form the final preform for fibre pulling. The extrusion rate and shape of the extruded products are affected by temperature, pressure and the die friction [12]. Figure 3.15 shows the extrusion process.

The specific details for the extrusion work on different glasses will be discussed later in the relevant chapters.

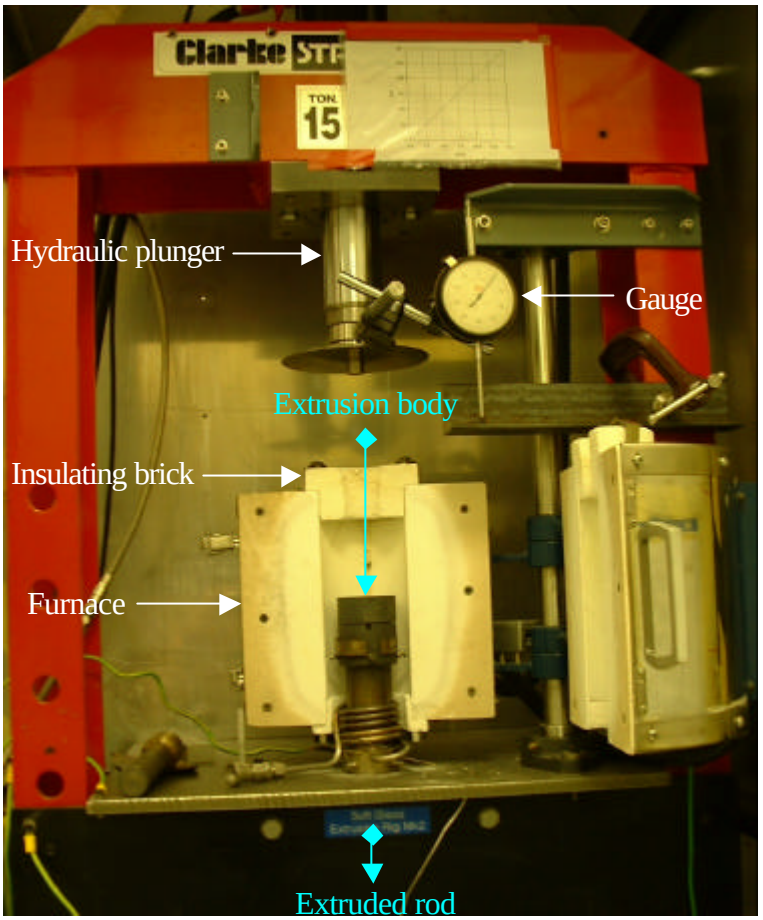

Photograph 3.7 : Extrusion rig

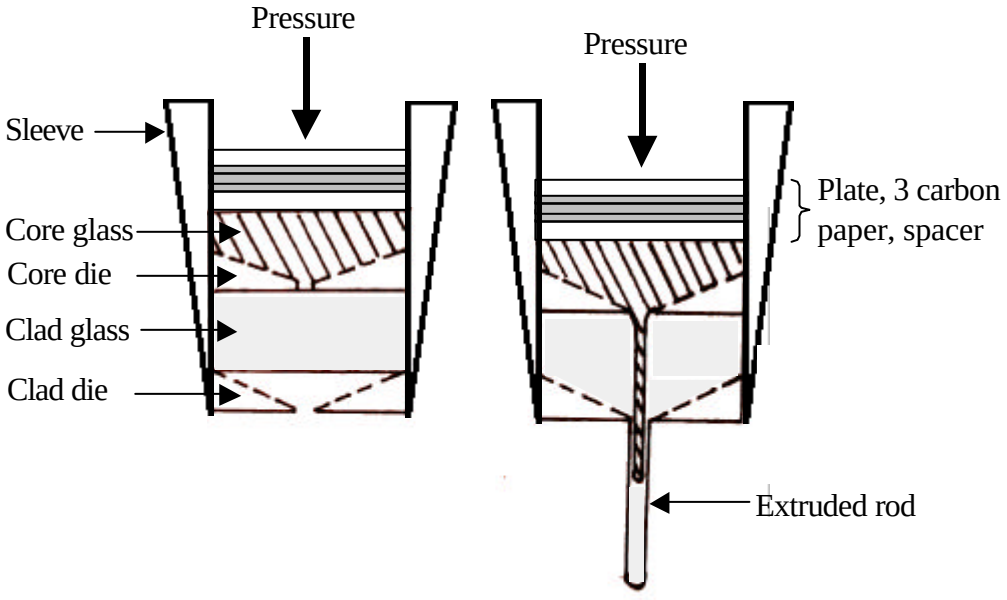

Figure 3.15 : Extrusion process

3.5.2 Fibre Drawing

When the cane and cladding tube had been extruded, the cane was inserted into the tube to form a preform, which was then placed in the fibre drawing tower, shown schematically in Figure 3.16, for fibre pulling. The tower consists of a 'feeding system' which feeds the preform, a radio frequency (RF) furnace (Stanelco STA 3B RF generator) which heats and softens the preform, a 'diameter monitoring system' (Anritsu M501A SLB) which measures the fibre diameter with a He-Ne laser, by way of scattering, and a drum to spool the drawn fibre.

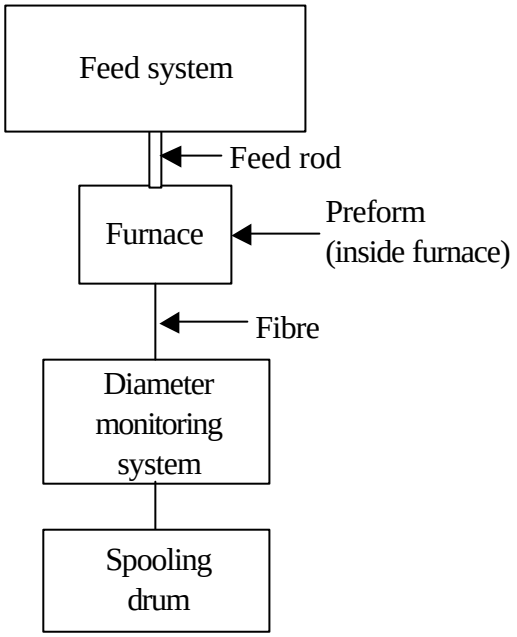

Figure 3.16 : Fibre drawing tower

The construction of the furnace is shown in Figure 3.17. The preform was held either by a stainless steel chuck or suspended by wires in the furnace, which was kept under an oxygen atmosphere where the rates of oxygen flow were 7 *l*/min and 2 *l*/min at the top and bottom of the furnace, respectively. This difference in oxygen flow created a positive pressure within the furnace to prevent particles or contaminants entering from the bottom of the furnace. The RF generator generated an output power of 3 kW at a frequency of 400 kHz, which coupled into the stainless steel susceptor via some RF coils, creating a localised heating zone for the preform. The furnace was heated at a rate of 100°C/min to the fibre pulling temperature of the preform where the preform would soften and begin to neck down (Photograph 3.8) within the susceptor. The required diameters of the fibres can be achieved by controlling the feeding rate, typically 300 rpm

(~ 2.5 mm/min), and the spooling rate, typically 240 – 280 rpm (~ 9.1 – 10.6 m/min) for 125 – 150 μm diameter fibres. The specific details of the fibres pulled will be set out in the relevant chapters.

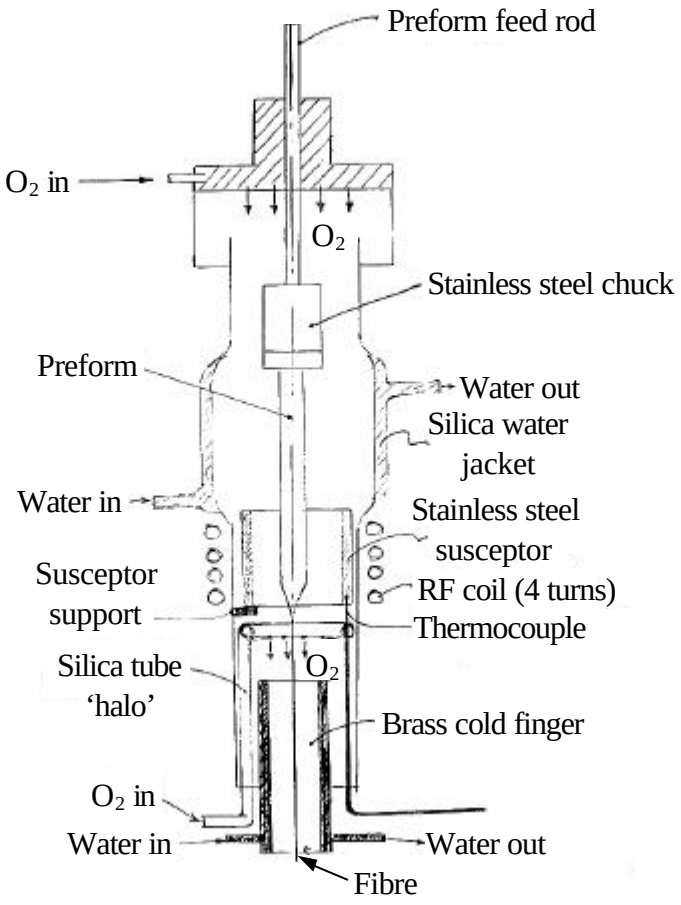

Figure 3.17 : Fibre drawing furnace [courtesy of Roger Moore, ORC]

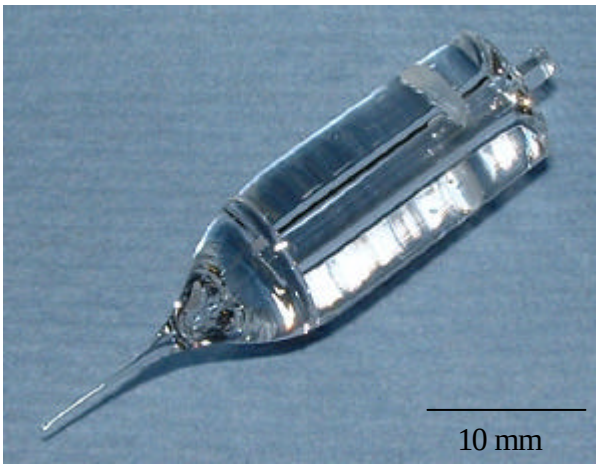

Photograph 3.8 : Fibre neck down

3.6 Waveguide Fabrication

This section describes the procedures involved in waveguide fabrication. Section 3.6.1 describes a technique for depositing glass layers onto a substrate, creating a multi-layer glass structure. Sections 3.62 and 3.63 describe the techniques for directly writing channel waveguides in bulk glasses. Specific details of the processes performed in this work will be described in the relevant chapters.

3.6.1 Hot-dip Spin-coating

Multi-layer planar waveguides can be prepared using the hot-dip spin-coating process. This process had previously been developed at the Optoelectronics Research Centre, University of Southampton (UK) to fabricate low-loss planar fluoride glass optical waveguides (0.1 dB/cm at λ = 1.05 μm) [13]. Using this process, different layers can be obtained by spinning glass films onto the substrate whereby the centripetal forces act to thin out the layer. To date, the process had also been demonstrated successfully in chalcogenide [14] and bismuthate [15] glasses.

The glass substrate is generally heated to its transition temperature, T_g, to minimise thermal stresses. As the substrate comes into contact with the high temperature molten glasses for the core layer, the substrate may be at a high enough temperature to reflow. This effect of reflowing can be exploited to reflow and thin down the core layer by spin-coating an overclad layer [16].

Figure 3.18 shows the spin-coating rig [17], which is fully automated via a computer. A flat optically polished sample approximately 2 mm thick and 32 mm diameter was held by a vacuum chuck in the upper furnace and heated to its T_g. Glass melt for the core layer (in a platinum crucible) was melted in a separate furnace and then transferred to the lower furnace, which was preheated to 750°C. An Aerotech ATS200 positioning system was used to bring the crucible to the upper furnace close to the substrate. Accurate measurement of the melt level resulted in the surface of the substrate just being dipped into the molten glass. The spinning of the substrate began once the crucible had been withdrawn into the lower furnace. This spinning process

created a uniform thin film on the substrate approximately 25 μm. The sample was then annealed in the upper furnace for one hour before being cooled to room temperature at a rate of 1°C/min. If an overclad layer was required, similar procedures were repeated as per the core layer after the core layer had been deposited. The core layer normally thinned down to approximately 5 μm as a consequence of this second spinning.

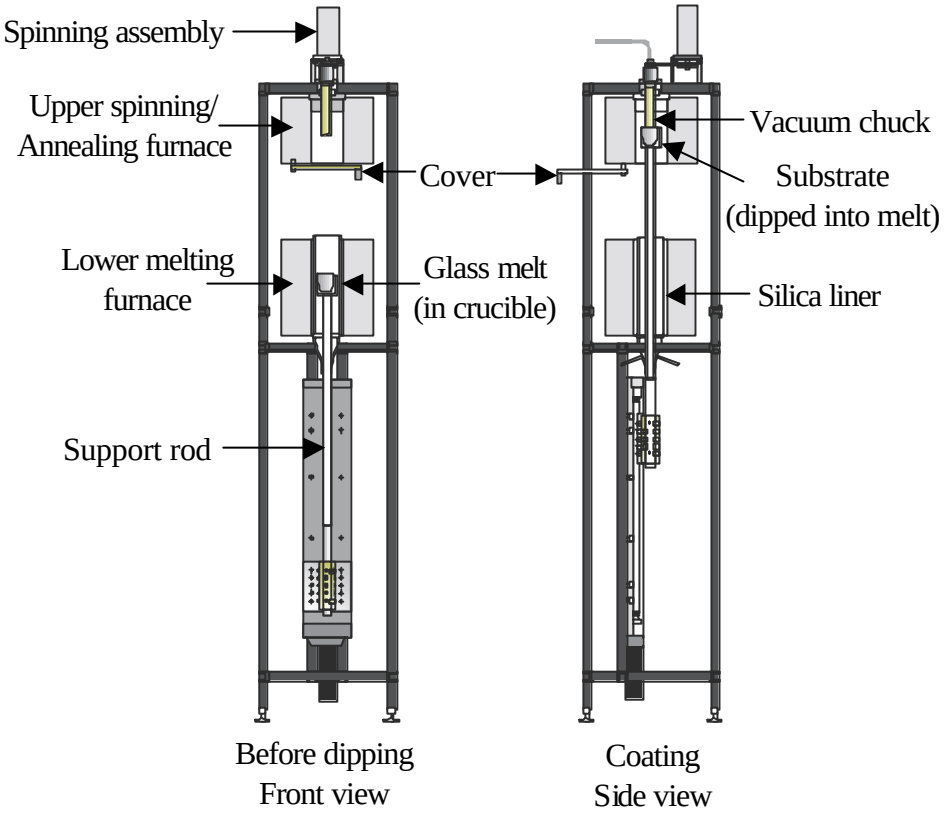

Figure 3.18 : Spin-coating rig (courtesy of D. Harwood [17])

For channel definition, direct laser writing has been investigated using UV and femtosecond writing, as described in the following sections.

3.6.2 UV Writing

The direct UV-writing is based on a localised change in refractive index induced by short-wave radiation and enables the fabrication of various optical devices such as waveguides [18], Bragg gratings [19,20] and directional couplers [21] in photosensitive materials. It is a mature technology in device fabrication in germania-doped silica fibres and waveguides [19,22,23].

Photosensitivity is related to the bleaching of the 240nm absorption band, which is associated with the germanium related oxygen vacancy defects [19]. Absorption of energy into this band appears to lead to a permanent increase in the refractive index of the material. In addition to the above, refractive index change can also be caused by densification of the glass structure [23,24].

The direct UV-writing apparatus used to write waveguides consisted of a frequency doubled Ar ion laser (Coherent FRED Sabre 500) with a continuous wave output at 244 nm. The samples were held in place by vacuum on a computer controlled air-bearing translation stage, which travelled perpendicularly to the incident UV laser beam. Figure 3.19 shows the UV-writing process. Powers up to 100 mW can be used to write channel waveguides at different speeds, ranging from 5 to 3000 mm/min, and different channel separation distances.

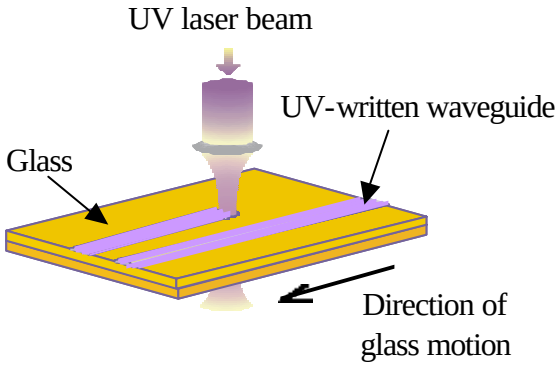

Figure 3.19 : Direct UV writing (courtesy of D. Harwood [16])

3.6.3 Femtosecond Writing

Femtosecond (fs) laser pulses have presented a technique for direct writing of waveguides and gratings [25-27]. The laser beam can be focused to deposit energy in transparent materials in the immediate volume around the focus. The mechanism of energy deposition for fs laser pulses includes multiphoton ionisation, avalanche ionisation and energy transfer to lattice [28-30]. The pulses generate a hot, high-density electron plasma which transfers its excess energy to the lattice, causing increased temperature and pressure around the focus spot and creates a local densification, leading to increased refractive index. Energy can be deposited not only on the surface but also inside the bulk material due to non-linear absorption and hence, fs laser writing

offers three-dimensional capabilities.

The femtosecond writing apparatus comprised a regeneratively amplified Ti:sapphire laser generating 798 nm, 150 fs laser pulses at 100 kHz repetition rate. This whole system consisted of a pump (COHERENT 'Verdi'), pumping at 532 nm, a femtosecond cavity (COHERENT 'Mira') and an amplifier (COHERENT 'RegA').

Channel waveguides were written by using a microscope objective (10X - 50X) to focus the laser beam inside the glass samples. The samples were translated perpendicularly to the incident laser beam to write waveguides along the length of the samples, as shown in Figure 3.20. A range of powers up to 280 mW (up to 2.8 μJ/pulse) were used to write the waveguides at speeds between 20 to 100 μm/s.

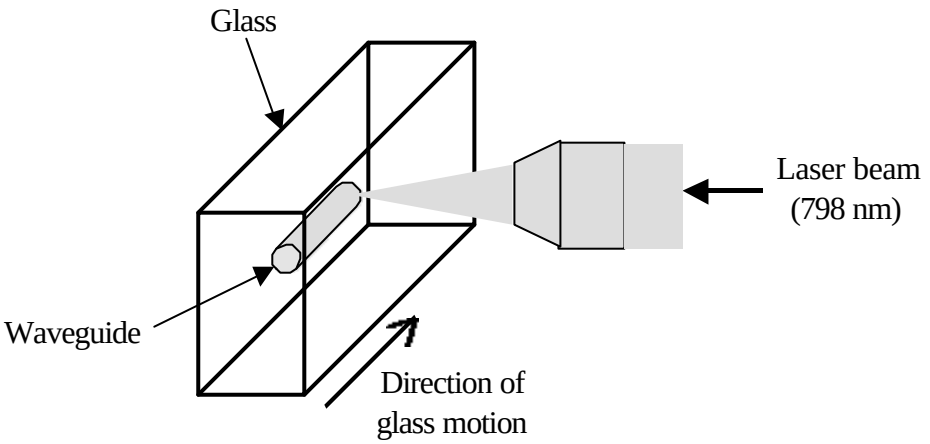

Figure 3.20 : Femtosecond writing

REFERENCES

1. R.V. Adams, *"Infra-red absorption due to water in glasses"*, Physics and Chemistry of Glasses 2 (2), pp 39-49 (1961).

2. J.S. Hayden, A.J. Marker III, T.I. Suratwala and J.H. Campbell, *"Surface tensile layer generation during thermal annealing of phosphate glass"*, Journal of Non-Crystalline Solids 263&264, pp 228-239 (2000).

3. J.M. Jewell, C. Askins and I.D. Aggarwal, *"Interferometric method for concurrent measurement of thermo-optic and thermal expansion coefficients"*, Applied Optics 30 (25), pp 3656-3660 (1991).

4. G. Abbate, U. Bernini, P. Maddalena, S. De Nicola, P. Mormile and G. Pierattini, *"Interferometric technique for the determination of thermal nonlinearities in semiconductor glasses"*, Optics Communications 70 (6), pp 502-508 (1989).

5. R.J. Harris, G.T. Johnston, G.A. Kepple, P.C. Krok and H. Mukai, *"Infrared thermooptic coefficient measurement of polycrystalline ZnSe, CdTe, CaF_2 and BaF_2, single crystal KCl and T1-20 glass"*, Applied Optics 16 (2), pp 436-438 (1997).

6. W. Vogel, *"Optical properties of oxide glasses"*, Optical Properties of Glass, D.R. Uhlmann and N.J. Kreidl (Eds), The American Ceramic Society Inc., OH, (1991).

7. Schott glass catalogue – Product range 2000 (1998).

8. O.S. Shchavelev and V.A. Babkina, *"Properties of glasses of the systems P_2O_5-SrO and P_2O_5-BaO"*, Neorg. Mater. 6 (12), pp 2183-2186 (1970).

9. E. Roeder, *"Extrusion of glass"*, Journal of Non-Crystalline Solids 5, pp 377-388 (1971).

10. K.G.H. Ashbee, *"Anisotropic glass-ceramic produced by extrusion through opposed die"*, Journal of Material Science 10, pp 911-917 (1975).

11. E.J. Minay, V. Desbois and A.R. Boccaccini, *"Innovative manufacturing technique for glass matrix composites : extrusion of recycled TV set screen glass reinforced with Al_2O_3 platelets"*, Journal of Materials Processing Technology 142, pp 471-478 (2003).

12. E. Roeder, *"Flow behaviour of glass during extrusion"*, Journal of Non-Crystalline Solids 7, pp 203-220 (1972).

13. D.W.J. Harwood, A. Fu, E.R. Taylor, R.C. Moore, Y.D. West and D.N. Payne, *"A 1317 nm neodymium doped fluoride glass waveguide laser"*, in : European Conference on Optical Communications, paper 6.4.8, ECOC 2000, Munich, Germany, September 2000.

14. A.K. Mairaj, R.J. Curry and D.W. Hewak, *"Direct laser written channel and spin-coated thin film waveguides in amorphous chalcogenide (Ga:La:S)"*, in : Photonics Conference 2002, paper T2E6, Korea, 2002.

15. A. Favre, E. Lee, V. Apostolopoulos, C.B.E. Gawith, C.Y. Tai, E. Taylor, Y. Kondo and F. Koizumi, *"Fabrication and characterisation of planar and channel waveguides in bismuth-based oxide glasses"*, in: SPIE Photonics West 2003 Conference, paper 4990-21, San Jose, California (US), January 2003.

16. D.W.J. Harwood, *"Towards a 1.3mm planar neodymium doped fluoride glass waveguide amplifier"*, PhD thesis, Department of Electronic Engineering and Computer Science, University of Southampton, UK, 2000.

17. D.W. Harwood, E.R. Taylor, R. Moore and D. Payne, *"Fabrication of fluoride glass planar waveguides by hot dip spin coating"*, Journal of Non-Crystalline Solids 332, pp 190-198 (2003).

18. M. Svalgaard, C.V. Poulsen, A. Bjarklev and O. Poulsen, *"Direct UV writing of buried singlemode channel waveguides in Ge-doped Si films"*, Electronics Letters 30, pp 1401-1403 (1994).

19. G. Meltz, W.W. Morey and W.H. Glenn, *"Formation of Bragg gratings in optical fibers by a transverse holographic method"*, Optics Letters 14 (15), pp 823-825 (1989).

20. M. Svalgaard, *"Optical waveguides and grating made by photogeneration"*, European Conference on Integrated Optics, ECIO 99, Turin, Italy, April 1999.

21. M. Svalgaard, *"Direct writing of planar waveguide power splitters and directional couplers using a focused ultraviolet laser beam"*, Electronics Letters 33, pp 1694-1695 (1997).

22. P.J. Lemaire, R.M. Atkins, V. Mizrahi and W.A. Reed, *"High pressure H_2 loading as a technique for achieving ultrahigh UV sensitivity and thermal sensitivity in GeO_2 doped optical fibres"*, Electronics Letters 29 (13), pp 1191-1193 (1993).

23. E. Salik, D.S. Starodubov and J. Feinberg**, "***Increase of photosensitivity in Ge-doped fibers under strain"*, Optics Letters 25 (16), pp 1147-1149 (2000).

24. D.L. Williams, B.J. Ainslie, J.R. Armitage, R. Kashyap and R. Campbell**, "***Enhanced UV photosensitivity in boron codoped germanosilicate fibres"*, Electronics Letters 29 (1), pp 45-47 (1993).

25. K.M. Davis, K. Miura, N. Sugimoto and K. Hirao, *"Writing waveguides in glass with a femtosecond laser"*, Optics Letters 21 (21), pp 1729-1731 (1996).

26. K. Miura, J. Qiu, H. Inouye, T. Mitsuyu and K. Hirao, *"Photowritten optical waveguides in various glasses with ultrashort pulse laser"*, Applied Physics Letters 71 (23), pp 3329-3331 (1997).

CHAPTER 4

POTASSIUM ALUMINOPHOSPHATE GLASSES

4.1 Introduction

Phosphate glasses were the subject for our research study as they exhibit negative *dn/dT*; -92.2×10^{-6}/K [1], and their properties could be modified by suitable addition of glass modifiers. Negative *dn/dT* is a requirement to achieve athermalisation, as described in Section 1.3.

The main aim of this part of the work was to assess the optical and thermal properties of potassium aluminophosphate glasses (designated as KAP), with the view for potential athermalisation applications, and examine the compositional effects (ultraphosphate, metaphosphate, and polyphosphate compositions) on these properties. Potassium was chosen due to the fact that potassium phosphate exhibits the most negative *dn/dT* (-23.3×10^{-6}/°C [1]) among the metaphosphate glasses (the *dn/dT* of some metaphosphate glasses can be compared in Table 2.1). Aluminium, despite aluminophosphate exhibiting positive *dn/dT* ($+5.0\times10^{-6}$/°C [1]), was added to improve the chemical durability of the glasses [2,3].

4.2 Glass Preparation

Various compositions of ternary KAP glasses of the K_2O-Al_2O_3-P_2O_5 system were prepared with oxygen-to-phosphorus (O/P) ratio ranging approximately between 2.8 and 3.1. This range encompassed ultraphosphate (O/P < 3), metaphosphate (O/P = 3) and polyphosphate (O/P > 3) compositions. Four series of glasses were prepared, corresponding to (mol%) :

- Series 1 : $x$$K_2O$-$y$$Al_2O_3$-($x$+3$y$)$P_2O_5$ metaphosphate composition with $10 \le x \le 40$, $5 \le y \le 20$.
- Series 2 : $x$$K_2O$-(35-$x$)$Al_2O_3-65P_2O_5$ with $15 \le x \le 30$ (P_2O_5 was fixed at 65 mol%).
- Series 3 : 20K_2O-$y$$Al_2O_3$-(80-$y$)$P_2O_5$ with $10 \le y \le 17.5$ (K_2O was fixed at 20 mol%).

- Series 4 : xK_2O-$15Al_2O_3$-$(85-x)P_2O_5$ with $10 \leq x \leq 25$ (Al_2O_3 was fixed at 15 mol%).

The glass melting process followed the procedures outlined in Section 3.1.1. Batches were prepared from the appropriate mixtures of high purity powder K_2CO_3 (99.9%), $Al(OH)_3$ (99.9%) and P_2O_5 (99.99%). The batches were melted in silica crucibles under an oxygen atmosphere (oxidising effect) for 60 - 90 minutes at temperatures between 1050°C and 1500°C, depending on the glass compositions. The crucibles were covered with a platinum lid to avoid excessive loss of materials during the melting process. The melts were then cast into a graphite mould and annealed in air for 60 minutes at the respective glass T_g, before being slowly cooled at a rate of 0.5°C/min to room temperature.

Table 4.1 shows the batch compositions of the KAP glasses that were melted while Figure 4.1 shows the KAP glass melting region for this work.

Sample	**Batch composition (mol%)**			**O/P**	**Phosphate**
	K_2O	**Al_2O_3**	**P_2O_5**		
KAP-1a	40	5	55	3.00	Meta-
KAP-1b	30	10	60	3.00	Meta-
KAP-1c	20	15	65	3.00	Meta-
KAP-1d	16.5	16.75	66.75	3.00	Meta-
KAP-1e	10	20	70	3.00	Meta-
KAP-2a	30	5	65	2.85	Ultra-
KAP-2b	27.5	7.5	65	2.88	Ultra-
KAP-2c	25	10	65	2.92	Ultra-
KAP-2d	15	20	65	3.08	Poly-
KAP-3a	20	10	70	2.86	Ultra-
KAP-3b	20	12.5	67.5	2.93	Ultra-
KAP-3c	20	17.5	62.5	3.08	Poly-
KAP-4a	10	15	75	2.87	Ultra-
KAP-4b	15	15	70	2.98	Ultra-
KAP-4c	25	15	60	3.08	Poly-

Table 4.1 : Batch compositions of KAP glasses

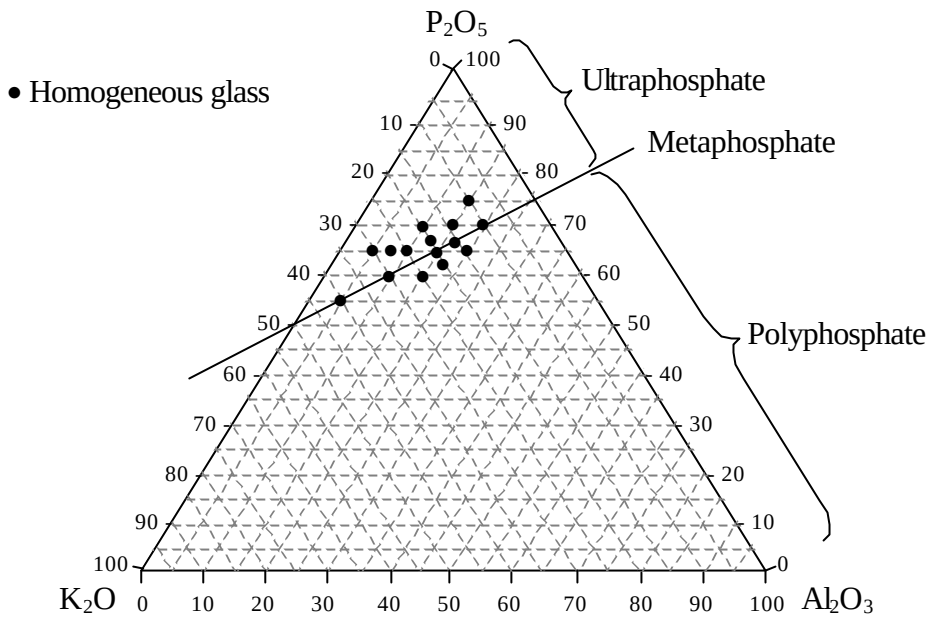

Figure 4.1 : KAP glass melting

4.3 Property Measurements

The glass samples were first polished, following the methods detailed in Section 3.1.2, before any property measurements were performed. The principles of the measurements carried out had been described in details in Chapter 3.

The refractive index, n, of the glasses was measured at room temperature using an Abbe '60' refractometer at the sodium D-line (λ = 589.3nm). T_g, T_x and T_p were determined using a DTA at a heating rate of 10°C/min. α was measured with a TMA at a heating rate of 5°C/min in the temperature range of 50 - 120°C.

dn/dT of the glasses was determined in the temperature range of 20 - 100°C with 10 mm thick polished samples, using the interferometer set-up described in Section 3.4. UV spectrum analysis in the range of 190 – 500 nm using a UV/Vis/NIR spectrophotometer and infrared measurement of relative OH concentrations using an FTIR spectrophotometer in the transmission mode over the range of 2000 - 5000 cm^{-1} were performed on 2 mm thick polished samples.

4.4 Results and Discussion

The batch compositions of the KAP glasses prepared, along with their associated thermal and optical properties, are shown in Tables 4.2 and 4.3, respectively. Sample *KAP-1c* and its properties are repeated alongside the results for KAP series 2 – 4 in order to show the changes in the glass properties as the phosphate glass network systematically progresses from an ultraphosphate network to a metaphosphate and finally to a polyphosphate network.

Sample	Batch composition (mol%)			T_g (°C)	T_x (°C)	T_p (°C)	α (´ 10^{-6}/°C) (50 - 120°C)
	K_2O	Al_2O_3	P_2O_5				
KAP-1a	40	5	55	326	452	552	21.25
KAP-1b	30	10	60	418	633	697	15.20
KAP-1c	20	15	65	507	759	849	11.02
KAP-1d	16.5	16.75	66.75	543	771	880	8.71
KAP-1e	10	20	70	621	773	823	7.67
KAP-2a	30	5	65	272	558	670	19.70
KAP-2b	27.5	7.5	65	329	636	696	17.40
KAP-2c	25	10	65	400	618	782	13.34
KAP-1c	20	15	65	507	759	849	11.02
KAP-2d	15	20	65	567	814	882	7.23
KAP-3a	20	10	70	415	755	800	12.91
KAP-3b	20	12.5	67.5	475	736	793	12.15
KAP-1c	20	15	65	507	759	849	11.02
KAP-3c	20	17.5	62.5	526	702	798	10.15
KAP-4a	10	15	75	580	>900	>900	6.84
KAP-4b	15	15	70	539	749	>850	9.80
KAP-1c	20	15	65	507	759	849	11.02
KAP-4c	25	15	60	479	704	748	13.13

Table 4.2 : Thermal properties of KAP glasses

Sample	Batch composition (mol%)			*n* (λ = 589.3 nm)	*dn/dT* (´ 10^{-6}/°C) (λ = 632.8 nm, 20 - 100°C)	r_{OH} (cm^{-1})
	K_2O	Al_2O_3	P_2O_5			
KAP-1a	40	5	55	1.484	-16.61	35.88
KAP-1b	30	10	60	1.493	-8.54	30.61
KAP-1c	20	15	65	1.505	-2.76	27.87
KAP-1d	16.5	16.75	66.75	1.511	+1.65	34.32
KAP-1e	10	20	70	1.519	+3.41	30.20
KAP-2a	30	5	65	1.469	-14.99	33.17
KAP-2b	27.5	7.5	65	1.488	-11.39	31.26
KAP-2c	25	10	65	1.495	-5.48	28.51
KAP-1c	20	15	65	1.505	-2.76	27.87
KAP-2d	15	20	65	1.515	+3.30	12.68
KAP-3a	20	10	70	1.497	-4.83	28.96
KAP-3b	20	12.5	67.5	1.502	-4.45	26.46
KAP-1c	20	15	65	1.505	-2.76	27.87
KAP-3c	20	17.5	62.5	1.508	-0.99	18.52
KAP-4a	10	15	75	1.515	+6.63	28.12
KAP-4b	15	15	70	1.509	-0.47	24.37
KAP-1c	20	15	65	1.505	-2.76	27.87
KAP-4c	25	15	60	1.502	-4.66	16.84

Table 4.3 : Optical properties of KAP glasses

The results for n, T_g and α in this work agreed with those in the literature having similar compositions [4]. For example, from ref [4], their glass sample with nominal composition similar to sample *KAP-1c* exhibited n = 1.502, T_g = 535°C and $\alpha = 11.10\times10^{-6}$/°C. It should be noted that the starting raw materials that were used to melt the glasses were considerably different. However, they did not seem to cause any disparity in our results compared to literature.

4.4.1 OH Content and UV Spectrum

The presence of high field strength (defined as (z/a^2) [5]) Al^{3+} cations generally reduces the OH content in the glasses as the cations form hydration-resistant bonds with the phosphate NBOs [6]. Therefore any increase in alumina decreases the OH content, as reported in literature [4]. This is shown in Figure 4.2, where the absorption near 3000 cm^{-1} is assigned to OH absorption. In general, however, as evident from Table 4.3, the present work showed that there was little change in the relative OH content of the KAP glasses as the alumina content changed. However, there were some exceptions with several glasses having just half the amount of OH relatively, such as samples *KAP-2d* ($15K_2O$-$20Al_2O_3$-$65P_2O_5$) and *KAP-3c* ($20K_2O$-$17.5Al_2O_3$-$62.5P_2O_5$), which had high amount of alumina. Although sample *KAP-1e* ($10K_2O$-$20Al_2O_3$-$70P_2O_5$) also had 20 mol% Al_2O_3, it had high OH content due to its high P_2O_5 content, which made it hygroscopic [7]. Sample *KAP-4c* ($25K_2O$-$15Al_2O_3$-$60P_2O_5$) also had low OH content, possibly due to its high K_2O content and low P_2O_5 content . The lack of sensitivity of the relative OH content with the alumina content, compared to ref [4], was possibly due to the different raw material used and the melting procedures, most notably the longer glass melting time and the sealed crucible used within this work. An increased melting time reduces the OH content due to evaporation until equilibrium is achieved [8]. Thus our results showed that the trend in the measured values of n, T_g, α and dn/dT was not related to the OH content of the glass. In Figure 4.2, the IR edge shown is an overtone of the asymmetric (PO_2) vibration mode [9].

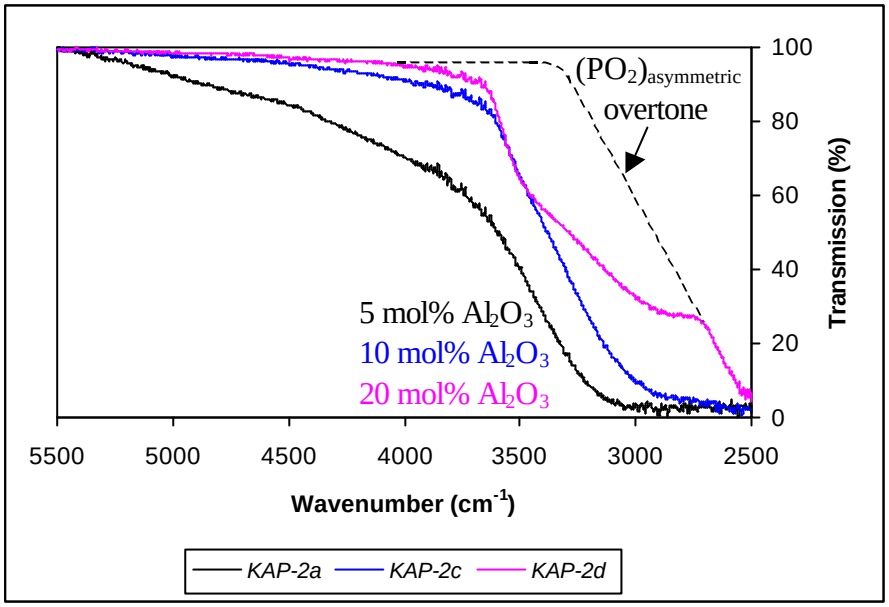

Figure 4.2 : Infrared transmission spectra through xK_2O-$(35-x)Al_2O_3$-$65P_2O_5$ glasses. The spectra are normalised for a 1 mm thick sample and corrected for Fresnel loss.

The intrinsic UV absorption is generally due to the electronic band gap transitions, which depend on the glass structure and chemical bonding within the network [10,11]. This is evident in Figure 2.1, which shows the different UV edges for different glass formers possessing different bonding networks with oxygen. Glasses with strong structural networks tend to have UV edges at lower wavelengths. However, the UV absorption of phosphate glasses can also be affected extrinsically by the presence of impurities, such as Fe^{2+} and Fe^{3+} [10,11], which can be introduced via the raw materials and melting process [12-14]. In his study of UV transmission of silver phosphate glasses, Bartholomew [15] concluded that a decrease in the NBO atoms shifted the UV edge to a lower wavelength. Based on this conclusion, KAP glasses with ultraphosphate composition, low K^+ content or high Al^{3+} content should exhibit UV absorption edges at a lower wavelength compared to other compositions. This was because of the higher degree of cross-linking and bridging oxygen bonds present in the glass network. The UV spectra obtained in this work, as shown in Figures 4.3 and 4.4, however did not show any conclusive evidence to that effect as the spectra was distorted by the Fe^{3+} absorption at ~ 230 – 250 nm. Iron, in the form of Fe^{2+} and Fe^{3+}, were present as impurities in the raw materials used. As the glasses were melted under oxidising conditions, Fe^{3+} species would dominate and the presence of this ion reduced the UV transmission of the glasses near 230 nm. The difference in the intensity of the Fe^{3+} absorption could be attributed to changes in the glass composition, the melting time, the melting temperature

as well as the supply of oxygen during the melting procedures.

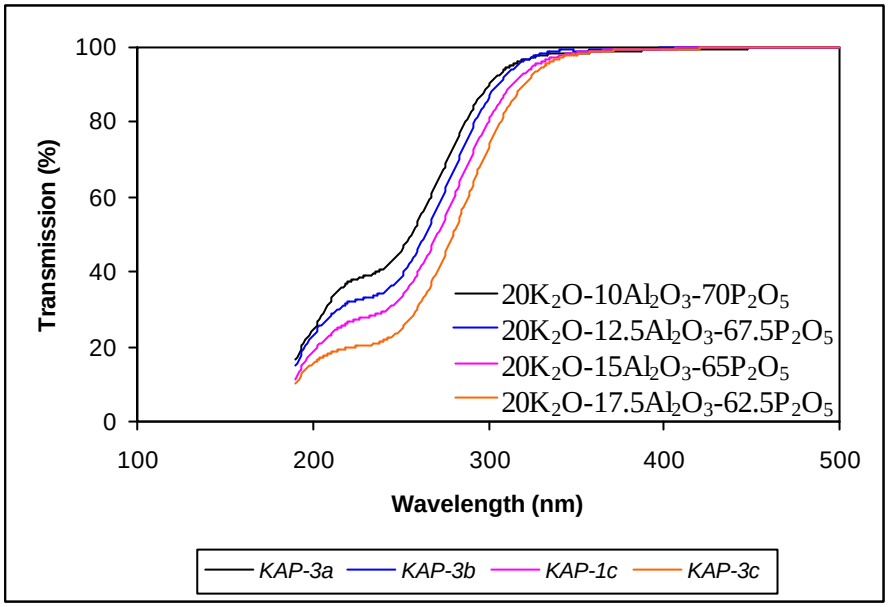

Figure 4.3 : Ultraviolet transmission spectra through $20K_2O$-yAl_2O_3-$(80-y)P_2O_5$ glasses. The spectra are normalised for a 1 mm thick sample and corrected for Fresnel loss.

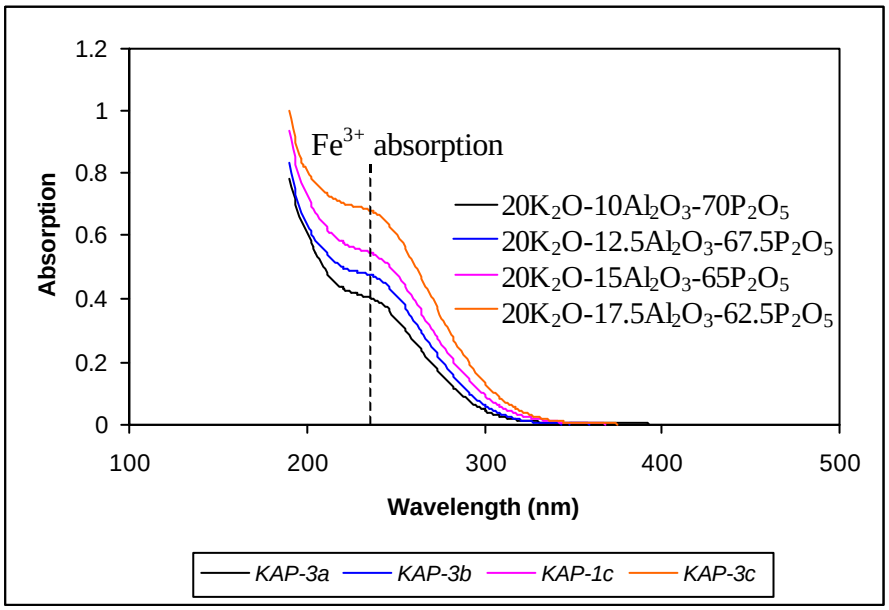

Figure 4.4 : Ultraviolet absorption spectra through $20K_2O$-yAl_2O_3-$(80-y)P_2O_5$ glasses. The spectra are normalised for a 1 mm thick sample and corrected for Fresnel loss.

4.4.2 Refractive Index

The measured refractive index, *n*, of the KAP glasses is shown in Figure 4.5a for the series 1 - 3 glasses as a function of Al_2O_3 and in Figure 4.5b for the series 4 glasses as a function of K_2O. As shown in Figure 4.5a, the refractive index of the series 1 - 3 KAP glasses increased monotonically as the alumina content increased, consistent with the results reported in the literature [2,4]. For the series 4 KAP glasses where the Al_2O_3 component was fixed at 15 mol%, an increase in the K_2O mol% decreased the refractive index, as shown in Figure 4.5b.

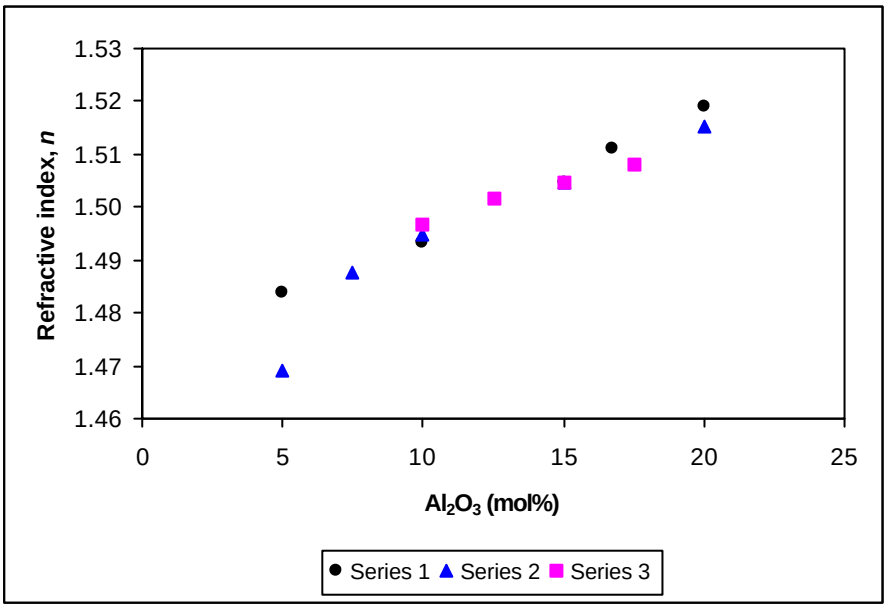

Figure 4.5a : Refractive index (*n*) of series 1 (metaphosphate), 2 (65 mol% P_2O_5) and 3 (20 mol% K_2O) KAP glasses, measured at λ = 589.3 nm.

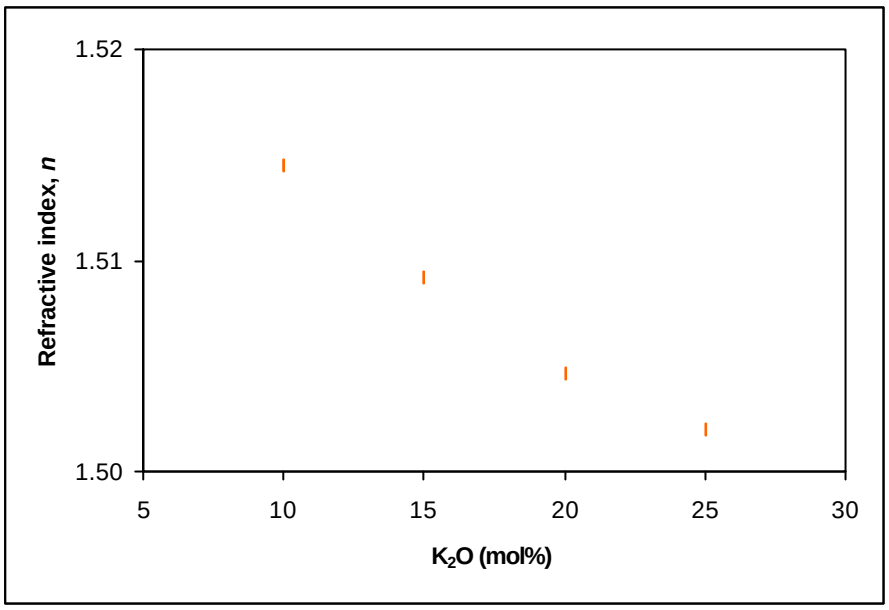

Figure 4.5b : Refractive index (*n*) of series 4 (15 mol% Al_2O_3) KAP glasses, measured at λ = 589.3 nm.

The refractive index of a particular glass is dependent on the polarisability and molar volume of the glass, as given by the Lorentz-Lorenz equation [16]:

$$\frac{n^2-1}{n^2+2}=\frac{4}{3}\frac{\pi N_A P_e}{V_m} \qquad (1.14)$$

where n is the refractive index, N_A is the Avogadro's number (6.022×10^{23}), P_e is the electronic polarisability and V_m is the molar volume. Hence, when the amounts of K^+, Al^{3+} and P^{5+} changed, n changed due to the ionic refractivity difference between the cations as well as the molar volume change.

When cations are added to phosphate glasses, the modifiers depolymerise the phosphate network, thus diminishing the cross-linking of the phosphate glass network to create a more open structure. Also, the addition of modifying cations causes the glass structure to expand to accommodate the cations at interstitial sites. Therefore an increase in molar volume leads to the decrease of the refractive index of the glasses. This is evident from Figure 4.5b, when K_2O was substituted for P_2O_5, which also coincided with the glass network changing from a cross-linked (ultraphosphate) to a depolymerised network (polyphosphate).

However, when a high field strength cation, such as Al^{3+}, is added, the cation forms strong bridging bonds [17] between the phosphate chains. This strengthening effect was considered by Kreidl *et al.* [18], whose model suggested that Al^{3+} cross-links the phosphate chains, resulting in an increase in structural polymerisation of the glass network and the packing density of atoms. This creates a more rigid network and causes a decrease in the molar volume, leading to higher refractive index, as in Figure 4.5a. Such observations had been previously noted for sodium aluminophosphate glasses [2].

The potassium aluminophosphate glass structural network is shown in Figure 4.6, based on the description in Section 2.1.2.2. The network comprises Q^3 and Q^2 phosphate tetrahedral units. At the ultraphosphate composition, the network is highly cross-linked and dominated by Q^3 units. However, as the amount of modifiers increases, Q^3 units are converted to Q^2 units as bridging oxygens are converted to non-bridging oxygens. The K^+ cations form ionic bonds with the non-bridging oxygens, depolymerising the network, while Al^{3+}, in octahedral coordination, form strong covalent bridging bonds between phosphate chains.

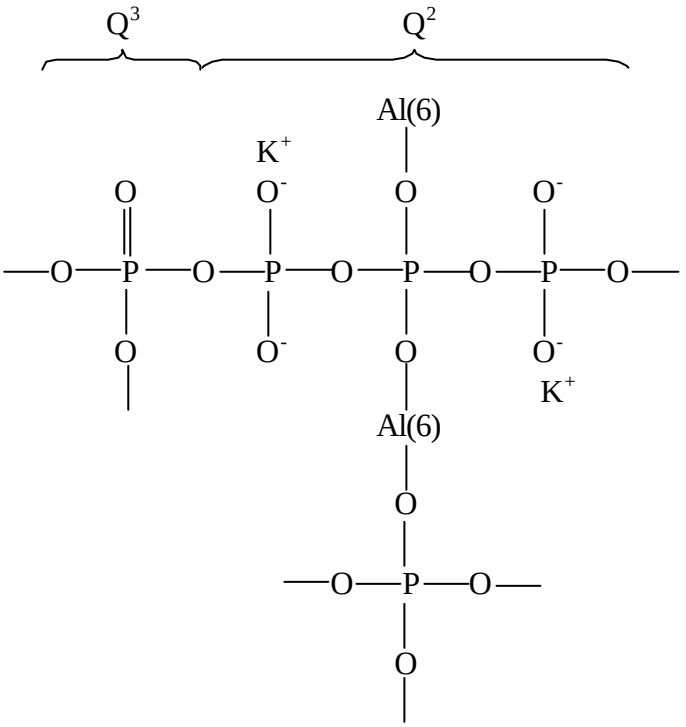

Figure 4.6 : Potassium aluminophosphate structure

Therefore, the substitution of Al_2O_3 for K_2O and P_2O_5 (series 1 KAP glasses), Al_2O_3 for K_2O (series 2 KAP glasses) and Al_2O_3 for P_2O_5 (series 3 KAP glasses) increased the refractive index while the substitution of K_2O for P_2O_5 decreased the refractive index (series 4 KAP glasses).

4.4.3 Glass Transition Temperature and Thermal Expansion Coefficient

Figures 4.7a and 4.8a show the variation of T_g and α, respectively, of the series 1 - 3 KAP glasses as a function of Al_2O_3 mol% while Figures 4.7b and 4.8b show how T_g and α, respectively, of the series 4 KAP glasses vary as a function of K_2O mol%. For the series 1 - 3 KAP glasses, the addition of alumina into the phosphate network increased the glass T_g (Figure 4.7a) and decreased the glass α (Figure 4.8a). These effects on the thermal properties were consistent with the strengthening effect of Al^{3+} on the glass structure. As discussed earlier, the incorporation of Al^{3+} increased the degree of polymerisation and strength of the glass structural network. This was due to the formation of (P-O-Al) bridging bonds between the phosphate chains, resulting in increased T_g and decreased α. Such observations had also been reported in the literature when Al_2O_3 was added to phosphate glasses containing sodium [2,19], potassium [4,20], barium [4], magnesium [4] and cesium [21].

The T_g (Figure 4.7b) and α (Figure 4.8b) of the series 4 KAP glasses, however, showed a reversed trend compared to the series 1 - 3 glasses, when the amount of K_2O in the glass increased, with the Al_2O_3 content fixed. This was due to the low field strength of K^+, where the addition of such cation broke up and depolymerised the phosphate cross-linked network. This effect weakened the bond strength of the glass structure, leading to decreased T_g and increased α.

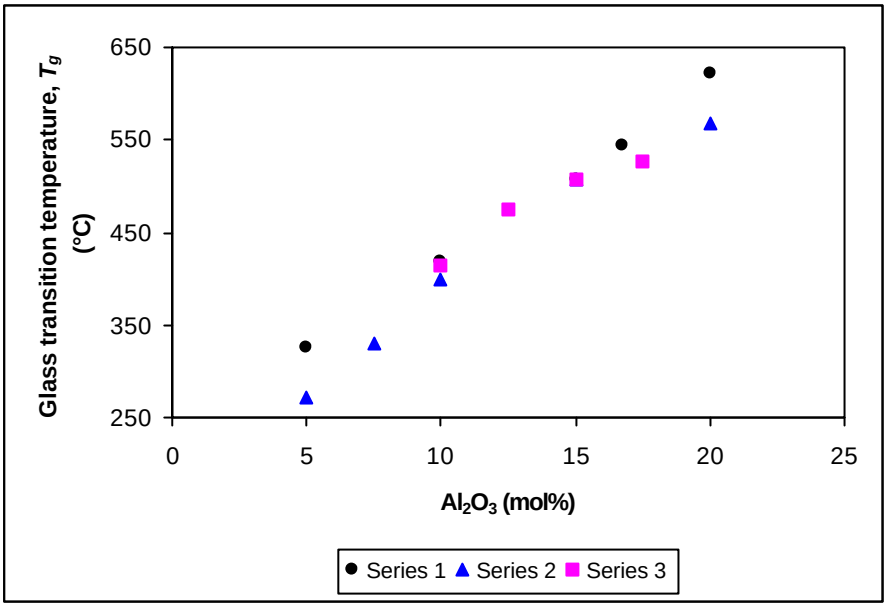

Figure 4.7a : Glass transition temperature (T_g) of series 1 (metaphosphate), 2 (65 mol% P_2O_5) and 3 (20 mol% K_2O) KAP glasses

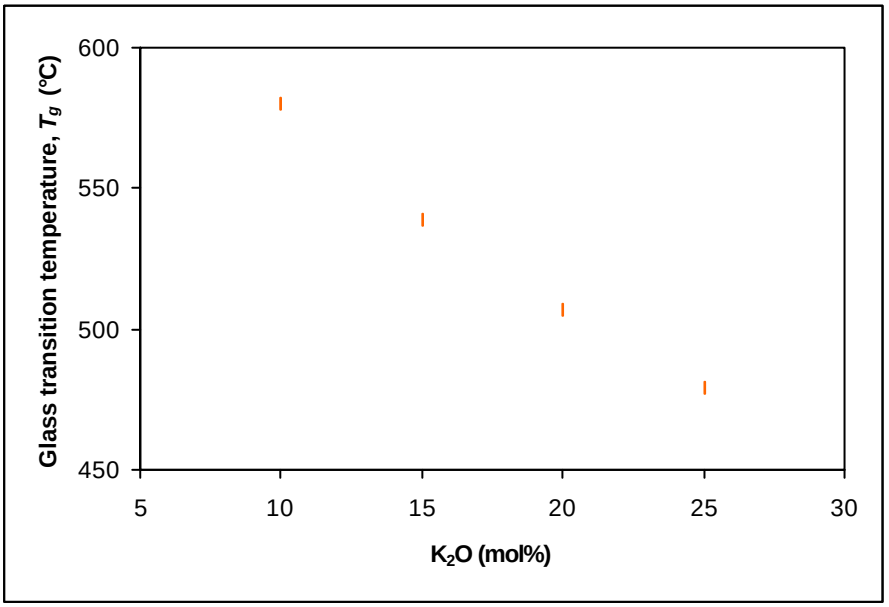

Figure 4.7b : Glass transition temperature (T_g) of series 4 (15 mol% Al_2O_3) KAP glasses

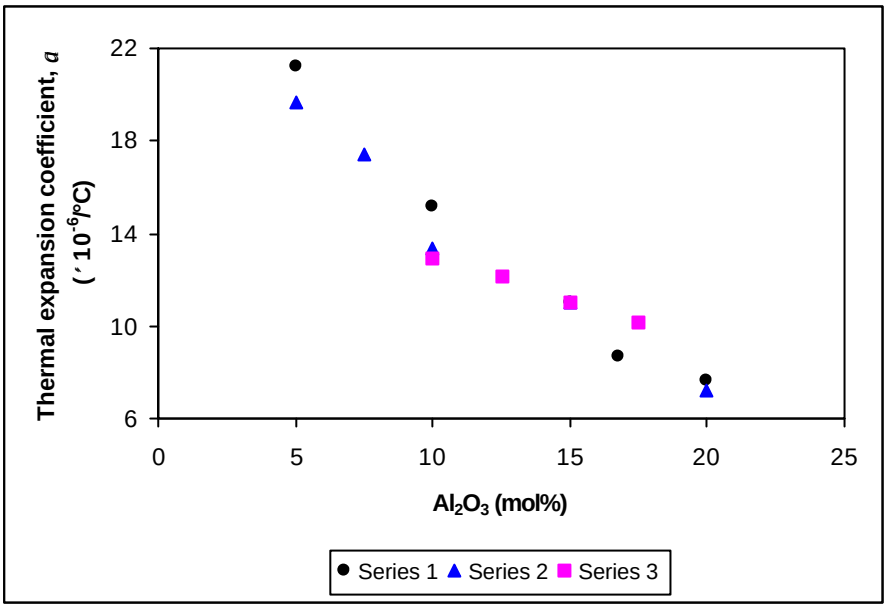

Figure 4.8a : Thermal expansion coefficient (α) of series 1 (metaphosphate), 2 (65 mol% P_2O_5) and 3 (20 mol% K_2O) KAP glasses, measured over 50 - 120°C.

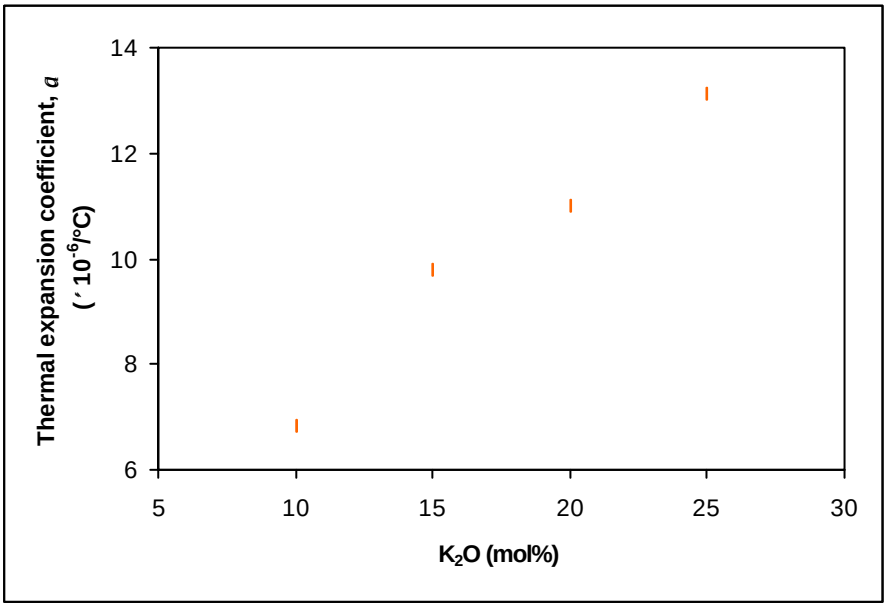

Figure 4.8b : Thermal expansion coefficient (α) of series 4 (15 mol% Al_2O_3) KAP glasses, measured over 50 - 120°C.

4.4.4 Thermo-optic Coefficient

Figure 4.9a shows the compositional effects on the *dn/dT* of the series 1 - 3 KAP glasses as a function of Al_2O_3 mol%, where the addition of alumina (at the expense of K_2O and/or P_2O_5) changed the negative values of *dn/dT* towards positive values. Figure 4.9b shows how the *dn/dT* of the series 4 KAP glasses changed with K_2O mol% in which the *dn/dT* exhibited negative values as the K_2O content increased (at the expense of P_2O_5).

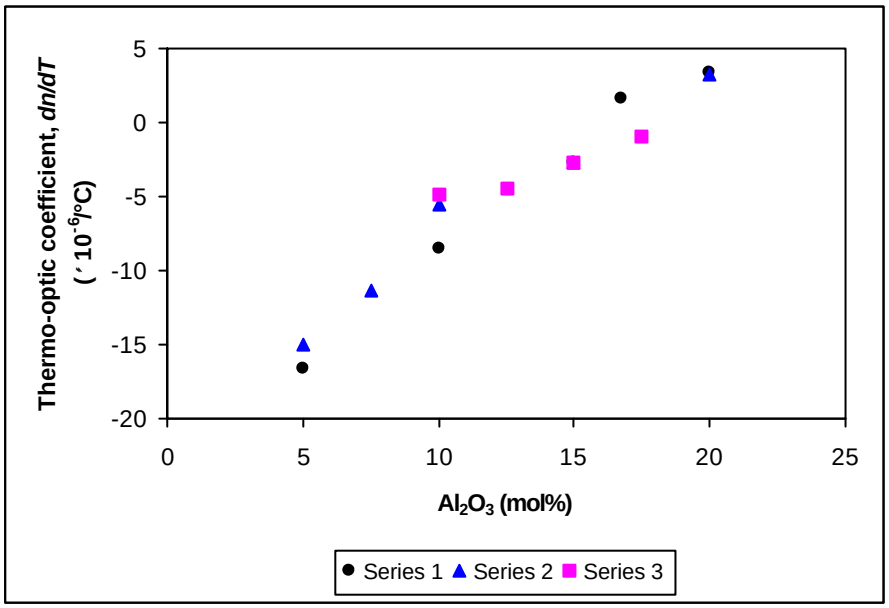

Figure 4.9a : Thermo-optic coefficient (*dn/dT*) of series 1 (metaphosphate), 2 (65 mol% P_2O_5) and 3 (20 mol% K_2O) KAP glasses, measured at λ = 632.8 nm over 20 – 100 °C.

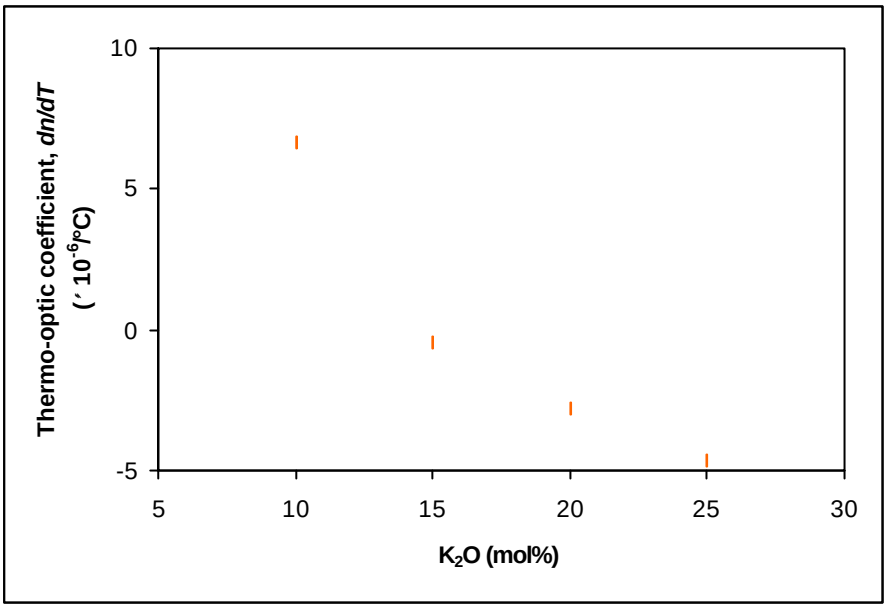

Figure 4.9b : Thermo-optic coefficient (*dn/dT*) of series 4 (15 mol% Al_2O_3) KAP glasses, measured at λ = 632.8 nm over 20 – 100 °C.

The behaviour of *dn/dT* can be explained in terms of the glass thermal expansion. The link between α and *dn/dT* can be established by the equation for *dn/dT* as derived from the Lorentz-Lorenz equation, using the approximation of ($d(\ln V_m)/dT \sim 3\alpha$), as shown below.

$$\frac{dn}{dT} = A\left[\frac{d(\ln P_e)}{dT} - 3\alpha\right] \qquad (1.15)$$

where $A = [(n^2-1)(n^2+2)/6n]$. The discussion, together with equations (including equation (1.15)) describing the *dn/dT* of glasses, had been discussed earlier in Section 1.4. Equation (1.15) shows that apart from α, polarisability also has an effect on *dn/dT*. However there is little available $d(\ln P_e)/dT$ data in the literature. Nevertheless, the equation shows that in order to obtain negative *dn/dT*, α must be high enough so that $3\alpha > d(\ln P_e)/dT$.

The variation of α and *dn/dT* of the KAP glasses as a function of the $Al(PO_3)_3$ mole fraction is shown in Figure 4.10. One can see that as the $Al(PO_3)_3$ mole fraction increased, its corresponding α decreased while *dn/dT* increased. The results showed that the KAP glasses which exhibited high α also exhibited negative *dn/dT*, consistent with the prediction based on equation (1.15). The minimum α value required for the KAP glasses to exhibit negative *dn/dT* was ~ 9.5×10^{-6}/°C.

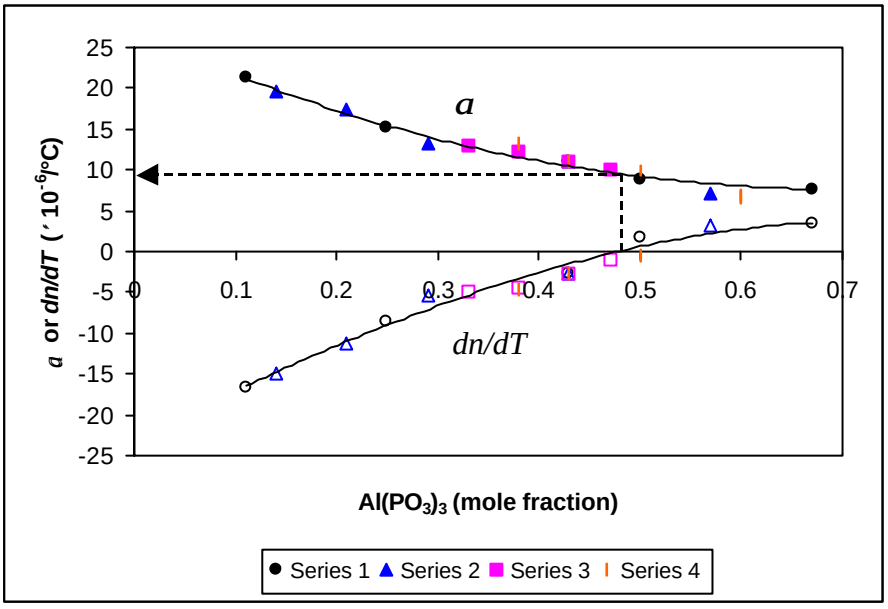

Figure 4.10 : α and *dn/dT* of KAP glasses as a function of $Al(PO_3)_3$ mole fraction

Figure 4.10 shows that the α and *dn/dT* of the four KAP glass series lie on the same curves, suggesting that the phosphate glass networks gradually and systematically changed from a network of cross-linked phosphate tetrahedra to a network of metaphosphate and polyphosphate chains of phosphate tetrahedra with the addition of either Al_2O_3 or K_2O. It also suggested that any deficiency in P_2O_5 (polyphosphates) or excess P_2O_5 (ultraphosphates) did not affect α and *dn/dT* abnormally.

A comparison between the experimentally measured *dn/dT* values and the estimated *dn/dT* for the KAP glasses is shown in Figure 4.11. The estimated *dn/dT* values were determined based on the additivity relationship of equation (2.5) discussed in Section 2.2, using the estimated β_i of each glass component (Table 2.4) in the KAP glasses. Using *KAP-1c* as an example, β was estimated to be 25.9×10^{-6}/°C, giving *dn/dT* = -4.28×10^{-6}/°C, in comparison to the measured

values of dn/dT = -2.77×10^{-6}/°C and β = 28.4×10^{-6}/°C. Figure 4.11 shows that the trend for both sets of data was similar, where dn/dT of the glasses changed to positive values as the $Al(PO_3)_3$ mole fraction within the glasses increased. However, there was an offset between the two sets of data, due to the limitations of the β_i data and the additivity relationship, as discussed in Section 2.2. The estimated values were consistently lower than the measured values. On the average, the difference between the measured and estimated value was 2×10^{-6}/°C. Some of the glasses had similar $Al(PO_3)_3$ mole fraction, despite having different glass compositions and exhibiting different dn/dT values, such as the data points observed at $Al(PO_3)_3$ = 0.38 and 0.50.

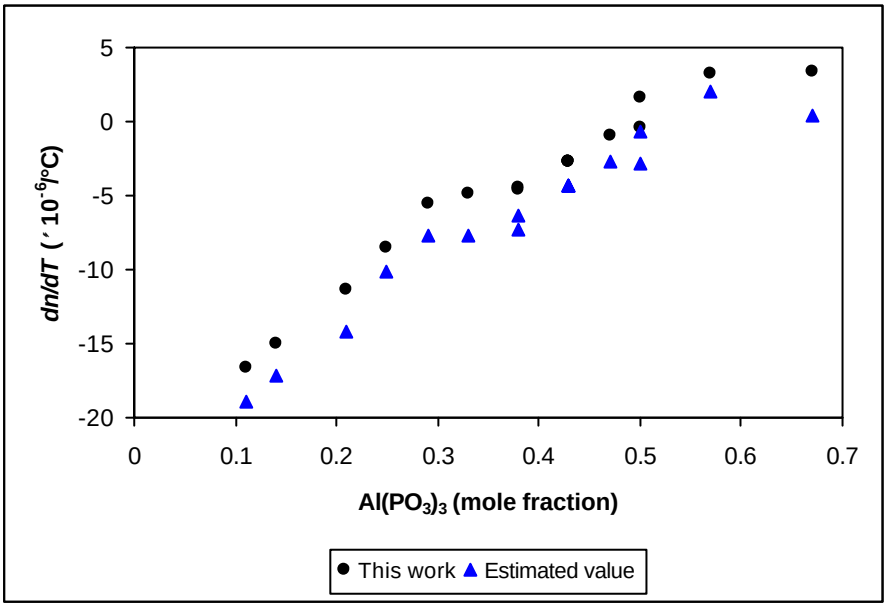

Figure 4.11 : Comparison of measured and estimated *dn/dT* of KAP glasses

Figure 4.12 shows the linear dependence of dn/dT on α. This linear dependence was valid as α was a linear function of the Al_2O_3 content (Figure 4.8a) and K_2O content (Figure 4.8b) as well as A being a linear function of n (Figure 4.13). The result represented a semi-empirical fit of dn/dT = -1.514α + 14.82, which can be used to deduce the dn/dT of any KAP glasses within this system in the range of 1.469 ≤ n ≤ 1.519 and 6.84×10^{-6}/°C ≤ α ≤ 21.25×10^{-6}/°C. The values for n were quoted for λ = 589.3 nm, the values for α were quoted over 50 - 120°C and dn/dT values were measured at λ = 632.8 nm over 20 - 100°C.

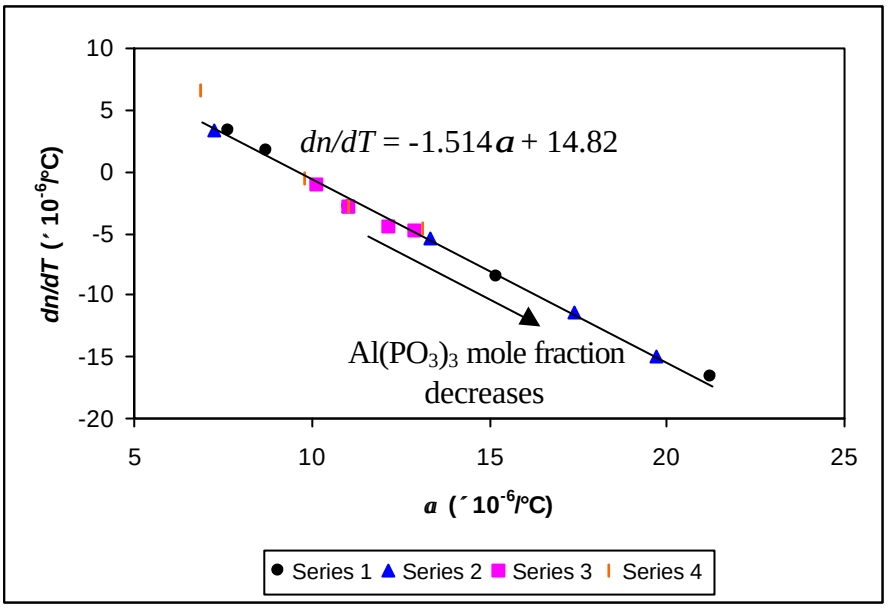

Figure 4.12 : *dn/dT* of KAP glasses as a function of *α*

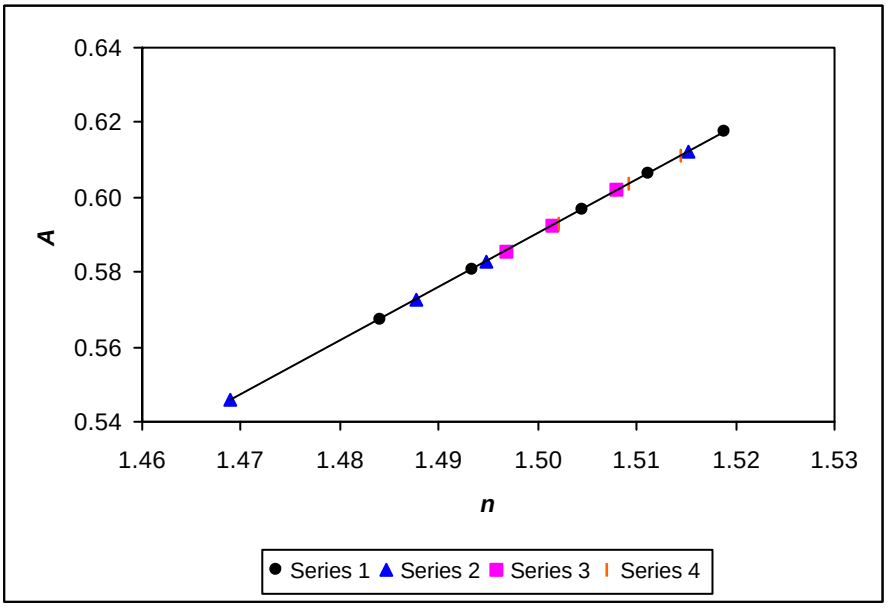

Figure 4.13 : *A* of KAP glasses as a function of *n*

Equation (1.15) can also be represented in another form, as in equation (1.16), by assuming that polarisability is increased by an increase in the inter-ionic distance due to an increase in temperature, as discussed in Section 1.4.

$$\frac{dn}{dT} = A(\gamma - 3)\alpha \qquad (1.16)$$

where γ is the change in polarisability due to a change in inter-ionic distance ($\gamma = \partial(\ln P_e)/\partial(\ln r)_T$), and r is the inter-ionic distance.

Figure 4.14 shows the γ values of the KAP glasses as a function of $Al(PO_3)_3$ mole fraction. The γ values were determined using equation (1.16) and the measured properties of n, α, and dn/dT and found to range from approximately 4.59 to 1.61 as the $Al(PO_3)_3$ mole fraction in the glass decreased. The decrease in γ accounted for the negative slope observed in Figure 4.12. From Figure 4.14, we can see that in order to have $\gamma < 3$ to obtain negative dn/dT, the glass composition must have $Al(PO_3)_3$ mole fraction < 0.5.

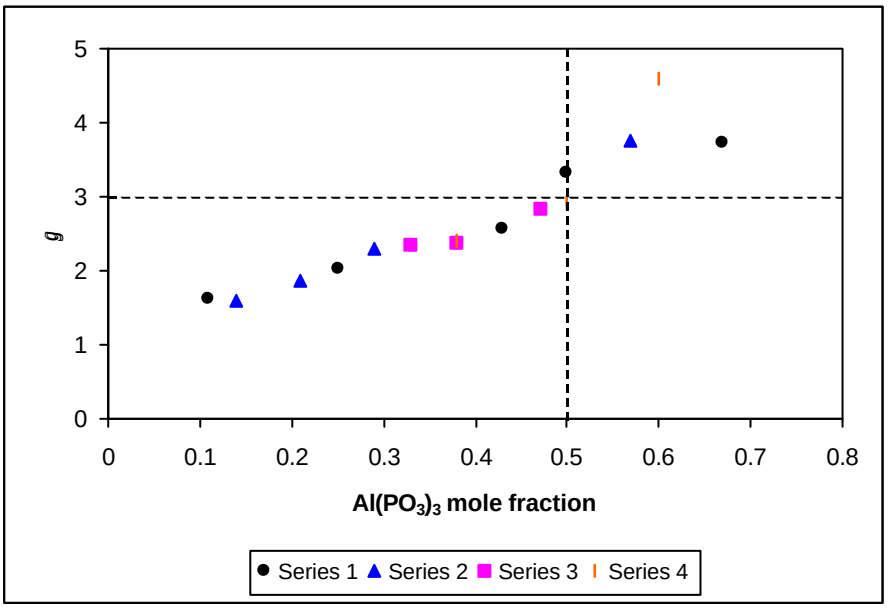

Figure 4.14 : γ of KAP glasses as a function of $Al(PO_3)_3$ mole fraction

4.4.5 Athermalisation

As discussed in Section 1.3, the positive values of α for most glasses dictate that the glasses must exhibit negative *dn/dT* to counter the effect of thermal expansion in order to fulfil the athermal condition. From Table 4.4, we can see that a number of samples exhibited negative *dn/dT*. Therefore, KAP glasses have the potential for athermalisation application. However, the glasses characterised in this work were not athermal on their own as their temperature dependence of optical path length, *1/L(dS/dT)*, were not zero. *1/L(dS/dT)* can be calculated from equation (1.2), which had been derived in Section 1.3.

$$\frac{1}{L}\left(\frac{dS}{dT}\right) = n\alpha + \frac{dn}{dT} \tag{1.2}$$

where *dS/dT* is the optical path length change with temperature and *L* is the medium length. From Table 4.4, we can see that the *1/L(dS/dT)* values are not zero, with silica being slightly better compared to the potassium aluminophosphate glasses. Therefore, the bulk KAP glasses cannot be used directly for the fabrication of athermal devices. A multi-layer approach with suitable substrates [22-25] must be employed in order to obtain athermal waveguides or gratings (discussed earlier in Section 1.3.3), where the KAP glasses will be suitable as the core glass due to their negative *dn/dT*.

By using the multi-layer approach, the thermal expansion of the substrate, α_{sub}, will dominate in the overall device, because of its considerable thickness. Hence, using a substrate with low α_{sub} can reduce the *1/L(dS/dT)* value, leading to an improved temperature-insensitive device. Equation (1.2) for bulk glass must be modified to the following equation for waveguide.

$$\frac{1}{L}\frac{dS}{dT} = \left(n_{eff}\alpha_{sub} + \frac{dn_{eff}}{dT}\right) \tag{1.8}$$

As an example, by assuming $n_{co} \sim n_{eff}$ and $dn_{co}/dT \sim dn_{eff}/dT$ (*co* represents core glass), a channel waveguide fabricated from samples *KAP-1b* and *KAP-1d* as the core glass and substrate respectively, produces an overall *1/L(dS/dT)* approximately 4.47×10^{-6}/°C. This is calculated

using n (1.493) and dn/dT (-8.54×10^{-6}/°C) of sample *KAP-1b* and α (8.71×10^{-6}/°C) of sample *KAP-1d* (highlighted in Table 4.4). This is an improvement over the individual KAP glasses and silica values of 11×10^{-6}/°C - 15×10^{-6}/°C and comparable to the best silica athermal waveguide of 3.77×10^{-6}/°C, based on the results obtained by Kintaka *et al.* [25]. The principles and realisation of such athermal waveguides will be discussed in Section 4.5.

Sample	**Composition (mol%)**			***dn/dT***	***nα***	***(1/L)(dS/dT)***
	K_2O	**Al_2O_3**	**P_2O_5**	**(´ 10^{-6}/°C)**	**(´ 10^{-6}/°C)**	**(´ 10^{-6}/°C)**
KAP-1a	40	5	55	-16.61	31.54	14.93
KAP-1b	30	10	60	-8.54	22.69	14.15
KAP-1c	20	15	65	-2.76	16.59	13.83
KAP-1d	16.5	16.75	66.75	+1.65	13.16	14.81
KAP-1e	10	20	70	+3.41	11.62	15.03
KAP-2a	30	5	65	-14.99	28.94	13.95
KAP-2b	27.5	7.5	65	-11.39	25.89	14.50
KAP-2c	25	10	65	-5.48	19.94	13.80
KAP-1c	20	15	65	-2.76	16.59	13.83
KAP-2d	15	20	65	+3.30	10.95	14.25
KAP-3a	20	10	70	-4.83	19.33	14.50
KAP-3b	20	12.5	67.5	-4.45	18.25	13.80
KAP-1c	20	15	65	-2.76	16.59	13.83
KAP-3c	20	17.5	62.5	-0.99	15.31	14.32
KAP-4a	10	15	75	+6.63	10.35	16.98
KAP-4b	15	15	70	-0.47	14.79	14.32
KAP-1c	20	15	65	-2.76	16.59	13.83
KAP-4c	25	15	60	-4.66	19.72	15.06
Silica [1]				+10.40	0.80	11.20

Table 4.4 : Athermalisation parameters of KAP glasses

4.5 Device Fabrication

It is essential to understand the compositional effects on the glass properties so that the properties can be tailored for specific applications by changing the glass compositions. The next step after the characterisation work on the developed KAP glasses was to fabricate fibres and planar waveguides in order to show the possibility and viability of producing these devices. The procedures and details of the fabrications using the KAP glasses would be presented in Section 5.5 because the fabricated fibres and planar waveguides included one of the binary phosphate glasses discussed in Chapter 5 as part of the device.

4.6 Summary

The properties of potassium aluminophosphate glasses of different compositions, encompassing ultraphosphates, metaphosphates and polyphosphates had been assessed. The addition of Al^{3+}, with its high field strength, resulted in the formation of bridging bonds between phosphate chains. This polymerisation effect strengthened the glass structural network and created a compact network. This led to increased densities and refractive indices, increased glass transition temperatures, lower thermal expansion coefficients and consequently positive thermo-optic coefficients. For low field strength modifiers such as K^{+}, the progression from ultraphosphate to polyphosphate weakened and depolymerised the glass network, resulting in lower refractive indices, lower glass transition temperatures, higher thermal expansion coefficients and consequently negative thermo-optic coefficients. Ultraphosphate and polyphosphate compositions did not affect α and *dn/dT* abnormally, suggesting a gradual change in structural network.

dn/dT and α were linked and a value of $\alpha > 9.5\times10^{-6}$/°C was required to obtain negative *dn/dT* for the potassium aluminophosphate glasses. A semi-empirical fit of $dn/dT = -1.514\alpha + 14.82$ was obtained, allowing the *dn/dT* of any potassium aluminophosphate glasses within the compositional range of $1.469 \leq n \leq 1.519$ and 6.84×10^{-6}/°C $\leq \alpha \leq 21.25\times10^{-6}$/°C to be deduced. Glasses with negative *dn/dT*, up to -16.61×10^{-6}/°C, had been achieved and this showed that phosphate glasses are promising candidates for athermal waveguide development, via a multi-layer system with the use of suitable low expansion substrates.

REFERENCES

1. W. Vogel, *"Optical properties of oxide glasses"*, Optical Properties of Glass, D.R. Uhlmann and N.J. Kreidl (Eds), The American Ceramic Society Inc., OH, (1991).

2. R.K. Brow, *"Nature of alumina in phosphate glass: I, Properties of sodium aluminophosphate glass"*, Journal of The American Ceramic Society 76 (4), pp 913-918 (1993).

3. Y. Lin, Y. Zhang, W. Huang, K. Lu, Y. Zhao, *"Structural study of iron in phosphate glasses"*, Journal of Non-Crystalline Solids 112, pp 136-141 (1993).

4. E. Metwalli and R.K. Brow, *"Modifier effects on the properties and structures of aluminophosphate glasses"*, Journal of Non-Crystalline Solids 289, pp 113-122 (2001).

5. A. Dietzel, *"Die kationenfeldstarken und ihre beziehungen zu entglasungsvorgangen, zur verbindungsbildung und zu den schmelzpunkten von silicaten"*, Z. Elektrochem. 48 (1), pp 9-23 (1942).

6. B.C. Bunker, G.W. Arnold, J.A. Wilder, *"Phosphate glass dissolution in aqueous solutions"*, Journal of Non-Crystalline Solids 64, pp 291-316 (1984).

7. H.D. Park and E.R. Kreidler, *"Phase equilibria in the system La_2O_3- P_2O_5"*, Journal of The American Ceramic Society 67 (1), pp 23-26 (1984).

8. H. Ebendorff-Heidepriem, W. Seeber and D. Ehrt, *"Dehydration of phosphate glasses"*, Journal of Non-Crystalline Solids 163, pp 74-80 (1993).

9. R.K. Brow, D.R. Tallant, J.J. Hudgens and S.W. Martin, *"Raman spectroscopy study of the structure of lithium and sodium ultraphosphate glasses"*, Journal of Non-Crystalline Solids 223, pp 21-31 (1998).

10. D. Ehrt and W. Seeber, *"Glass for high performance optics and laser technology"*, Journal of Non-Crystalline Solids 129, pp 19-30 (1991).

11. J.A. Duffy, *"Charge transfer spectra of metal ions in glass"*, Physics and Chemistry of Glasses 38 (6), pp 289 (1997).

12. D. Ehrt, M. Carl, T. Kittel, M. Miller and W. Seeber, *"High-performance glass for the deep ultraviolet range"*, Journal of Non-Crystalline Solids 177, pp 405-419 (1994).

13. H. Ebendorff-Heidepriem and D. Ehrt, *"UV radiation effects in fluoride phosphate glasses"*, Journal of Non-Crystalline Solids 196, pp 113-117 (1996).

14. D. Ehrt, *"Redox behaviour of polyvalent ions in the ppm range"*, Journal of Non-Crystalline Solids 196, pp 304-308 (1996).

15. R.F. Bartholomew, *"Structure and properties of silver phosphate glasses – Infrared and visible spectra"*, Journal of Non-Crystalline Solids 7, pp 221-235 (1972).

16. M. Born and E. Wolf, Principles of Optics, Chapter 2, Pergamon Press, Oxford, (1984).

17. A. Eisenberg, H. Farb and L.G. Cool, *"Glass transitions in ionic polymers"*, Journal of Polymer Science: PartA-2 4 (6), pp 855-868 (1966).

18. N.J. Kreidl and W.A. Weyl, *"Phosphates in ceramic ware : IV, Phosphate glasses"*, Journal of The American Ceramic Society 24 (11), pp 372-378 (1941).

19. L.C. Klein and P.E. Gray, *"Sodium ultraphosphate glasses with Al_2O_3 and B_2O_3 substitutions"*, Glastech. Ber. 56K (2), pp 868-873 (1983).

20. Y.B. Peng and D.E. Day, *"High thermal expansion phosphate glasses. Part 1"*, Glass Technology 32 (5), 166-173 (1991).

21. T. Minami and J.D. Mackenzie, "*Thermal expansion and chemical durability of phosphate glasses*", Journal of The American Ceramic Society 60 (5-6), pp 232-235 (1977).

22. Y. Kokubun, N. Funato and M. Takizawa, "*Athermal waveguides for temperature-independent lightwave devices*", IEEE Photonics Technology Letters 5 (11), pp 1297-1300 (1993).

23. Y. Kokubun, S. Yoneda and H. Tanaka, "*Temperature-independent narrowband optical filter at 1.3mm wavelength by an athermal waveguide*", Electronics Letters 32 (21), pp 1998-2000 (1996).

24. Y. Kokubun, S. Yoneda and S. Matsuura, "*Temperature-independent optical filter at 1.55mm wavelength using a silica-based athermal waveguide*", Electronics Letters 34 (4), pp 367-369 (1998).

25. K. Kintaka, J. Nishii, H. Nishiyama, Y. Kawamoto and A. Sakamoto, "*Athermalization of a silica-based waveguide with a UV-induced Bragg grating on a crystallized glass substrate*", Journal of Lightwave Technology 21 (3), pp 831-836 (2003).

27. Y. Kondo, K. Nauchi, T. Mitsuyu, M. Watanabe, P.G. Kazansky and K. Hirao, *"Fabrication of long-period fiber gratings by focused irradiation of infrared femtosecond laser pulses"*, Optics Letters 24 (10), pp 646-648 (1999).

28. D. Du, X.Liu, G. Korn, J. Squier and G. Mourou, *"Laser-induced breakdown by impact ionisation in SiO_2 with pulse widths from 7 ns to 150 fs"*, Applied Physics Letters 64 (23), pp 3071-3073 (1994).

29. B.C. Stuart, M.D. Feit, A.M. Rubenchik, B.W. Shore and M.D. Perry, *"Laser-induced damage in dielectrics with nanosecond to subpicoseond pulses"*, Physical Review Letters 74 (12), pp 2248-2251 (1995).

30. E.N. Glezer and E. Mazur, *"Ultrafast-laser driven micro-explosions in transparent materials"*, Applied Physics Letters 71 (7), pp 882-884 (1997).

CHAPTER 5

BINARY PHOSPHATE GLASSES

5.1 Introduction

Phosphate glasses formed the basis of this research work due to their inherent negative *dn/dT* [1]. In this chapter, the optical and thermal properties of some binary phosphate glasses were investigated to assess their suitability for athermalisation applications. The compositional effects on the properties of the glasses were investigated by varying the glass compositions from metaphosphate to ultraphosphate. Calcium phosphate and barium phosphate glasses were the subject of the investigation as they exhibit negative *dn/dT* [1]. Binary alkali phosphate glasses were not considered because of their poor chemical durability for practical uses, although they also exhibit negative *dn/dT*. However, some samples of sodium phosphate glasses were prepared for comparison purposes. *dn/dT* of some metaphosphate glasses is shown in Table 2.1.

5.2 Glass Preparation

Three sets of binary phosphate glasses were prepared, corresponding to (mol%) :

- $x\mathrm{Na_2O}$-$(100-x)\mathrm{P_2O_5}$ (designated as NaP) in the range $40 \le x \le 50$
- $x\mathrm{CaO}$-$(100-x)\mathrm{P_2O_5}$ (designated as CaP) in the range $20 \le x \le 50$
- $x\mathrm{BaO}$-$(100-x)\mathrm{P_2O_5}$ (designated as BaP) in the range $20 \le x \le 50$

Glasses were prepared using the melting process described in Section 3.1.1, with Na_2CO_3 (99.5%), $CaCO_3$ (99.95%), $BaCO_3$ (99.95%) and P_2O_5 (99.99%) powder in the appropriate proportions. The batches were melted in silica crucibles, covered with a platinum lid, in an oxygen atmosphere at temperatures between 1000°C and 1400°C, depending on the glass compositions. After 60 minutes of melting, the glass melts were then cast into a graphite mould and annealed in air for 60 minutes at their respective T_g, before being cooled to room temperature at a rate of

0.5°C/min.

Table 5.1 shows the batch compositions of the NaP, CaP and BaP glasses that were prepared.

Sample	**Batch composition (mol%)**	
	Na_2O	**P_2O_5**
NaP-1a	50	50
NaP-1b	45	55
NaP-1c	40	60
Sample	**CaO**	**P_2O_5**
CaP-1a	50	50
CaP-1b	40	60
CaP-1c	30	70
CaP-1d	20	80
Sample	**BaO**	**P_2O_5**
BaP-1a	60	40
BaP-1b	55	45
BaP-1c	50	50
BaP-1d	45	55
BaP-1e	40	60
BaP-1f	30	70
BaP-1g	20	80

Table 5.1 : Batch compositions of NaP, CaP and BaP glasses

5.3 Property Measurements

The glass samples were polished (procedures described in Section 3.1.2) to obtain flat, smooth and transparent surfaces for property characterisation. The measurement technique for each equipment is described in Chapter 3.

An Abbe '60' refractometer was used to measure n at the sodium D-line (λ = 589.3 nm) at room temperature. A TMA was used to measure α in the temperature range of 50 - 120°C while a DTA was used to measure T_g, T_x, and T_p. The heating rates used were 5°C/min and 10°C/min for α and T_g, respectively.

Polished glass samples approximately 10 mm thick were used for *dn/dT* measurements using the interferometer set-up shown schematically in Figure 3.12. Measurements were performed in the temperature range of 20 - 100°C at a heating rate of 40°C/hour. An FTIR spectrophotometer was used to determine the relative OH concentrations within the glasses. This was performed in the 2000 - 5000 cm^{-1} range with 2 mm thick samples. A UV/Vis/NIR spectrophotometer was used to obtain the UV spectra of the glasses.

5.4 Results and Discussion

Table 5.2 shows the thermal properties while Table 5.3 shows the optical properties of the NaP, CaP and BaP glasses prepared. Figures 5.1 to 5.11 show the results for the binary phosphate glasses. In Figures 5.4 to 5.8, 5.10 and 5.11, lines are drawn as guides to the eye. The optical properties of the NaP glasses were not measured as the glasses were susceptible to hydrolysis, which makes it difficult to obtain smooth and transparent surfaces for the measurements.

Available data from ref [2] for barium phosphate glasses have been included for comparison with the results of this work. It should be noted that the measurements in ref [2] were performed under different conditions compared to this work and there was also no mention of the OH content in ref [2].

Sample	**Batch composition (mol%)**		T_g **(°C)**	T_x **(°C)**	T_p **(°C)**	α **(´ 10^{-6}/°C) (50 - 120°C)**
	Na_2O	**P_2O_5**				
NaP-1a	50	50	325	373	422	22.03
NaP-1b	45	55	276	388	428	21.48
NaP-1c	40	60	258	491	>500	20.40
Sample	**CaO**	**P_2O_5**	T_g **(°C)**	T_x **(°C)**	T_p **(°C)**	α **(´ 10^{-6}/°C) (50 - 120°C)**
CaP-1a	50	50	547	719	799	10.22
CaP-1b	40	60	510	734	788	9.39
CaP-1c	30	70	504	781	841	9.10
CaP-1d	20	80	533	811	875	8.60
Sample	**BaO**	**P_2O_5**	T_g **(°C)**	T_x **(°C)**	T_p **(°C)**	α **(´ 10^{-6}/°C) (50 - 120°C)**
BaP-1a	60	40	Phase-separated sample			
BaP-1b	55	45	Phase-separated sample			
BaP-1c	50	50	478	651	699	13.67
BaP-1d	45	55	458	637	673	13.35
BaP-1e	40	60	452	645	694	13.07
BaP-1f	30	70	421	674	766	12.38
BaP-1g	20	80	419	704	>780	11.62

Table 5.2 : Thermal properties of NaP, CaP and BaP glasses

Sample	**Batch composition (mol%)**		***n*** **(λ = 589.3 nm)**	***dn/dT*** **(´ 10^{-6}/°C) (λ = 632.8 nm, 20 - 100°C)**	r_{OH} **(*cm*$^{-1}$)**
	Na_2O	**P_2O_5**			
NaP-1a	50	50	Not measured		
NaP-1b	45	55	Not measured		
NaP-1c	40	60	Not measured		
Sample	**CaO**	**P_2O_5**	***n*** **(λ = 589.3 nm)**	***dn/dT*** **(´ 10^{-6}/°C) (λ = 632.8 nm, 20 - 100°C)**	r_{OH} **(*cm*$^{-1}$)**
CaP-1a	50	50	1.551	-2.98	8.08
CaP-1b	40	60	1.535	-0.92	12.86
CaP-1c	30	70	1.526	-0.39	15.27
CaP-1d	20	80	1.527	+0.36	14.28
Sample	**BaO**	**P_2O_5**	***n*** **(λ = 589.3 nm)**	***dn/dT*** **(´ 10^{-6}/°C) (λ = 632.8 nm, 20 - 100°C)**	r_{OH} **(*cm*$^{-1}$)**
BaP-1a	60	40	Phase-separated sample		
BaP-1b	55	45	Phase-separated sample		
BaP-1c	50	50	1.585	-10.24	14.04
BaP-1d	45	55	1.575	-9.14	13.24
BaP-1e	40	60	1.569	-8.19	14.73
BaP-1f	30	70	1.556	-7.06	21.92
BaP-1g	20	80	1.547	-5.76	22.26

Table 5.3 : Optical properties of NaP, CaP and BaP glasses

5.4.1 OH Content and UV Spectrum

As discussed in Section 2.1.2.1, the hygroscopic and volatile nature of P_2O_5 [3] require ultraphosphate glasses to be prepared in sealed crucibles. This is to minimise the water content in the glasses, which can depolymerise the phosphate structural network by converting BOs to NBOs through the formation of (P-OH) bonds. This effect can change the structures and

properties, such as density and T_g, of the glasses and hence, (P-OH) bonds must be considered when describing ultraphosphate glasses.

The CaP and BaP glasses prepared in this work generally possessed similar relative OH content, as shown in Table 5.3, despite the difference in the amount and the cation type of the modifying oxides. This was possibly due to the long melting time and the covered crucible used within this work, where an equilibrium was eventually reached between the water content in the glass melt and the atmosphere within the crucible, preventing further evaporation [4]. However, samples *CaP-1a*, *BaP-1f* and *BaP-1g* exhibited slightly different relative OH content. *CaP-1a* (50CaO-50P_2O_5) had slightly lower OH content due to its high modifier content and low P_2O_5 content. Ca^{2+} formed ionic bonds with the available phosphate NBOs, thus minimising the formation of (P-OH) bonds. However, samples *BaP-1f* (30BaO-70P_2O_5) and *BaP-1g* (20BaO-80P_2O_5) contained slightly higher OH content, which would affect the properties of these two glasses. This was due to the higher P_2O_5 content in these glasses compared to the other samples. CaP glasses were more resistant to hydrolysis than BaP glasses because of the higher field strength (z/a^2 [5]) of Ca^{2+}. This is evident from Figure 5.1, which shows that the transmission of the *BaP-1c* sample with 50 mol% BaO at around 3000 cm^{-1} (coinciding with the OH absorption band) is lower compared to the transmission of the *CaP-1a*, having 50 mol% CaO.

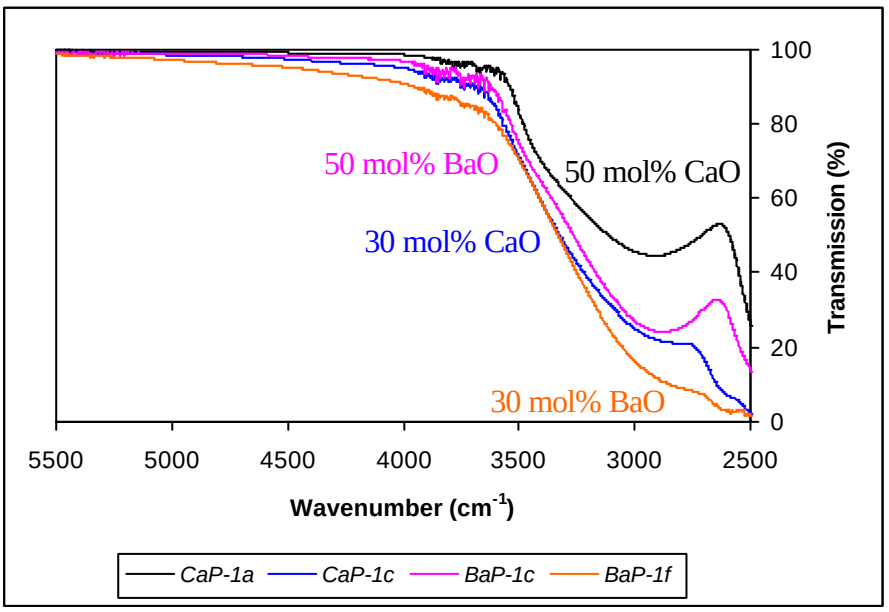

Figure 5.1 : Infrared transmission spectra through *x*MO-(100-*x*)P_2O_5 glasses. The spectra are normalised for a 1 mm thick sample and corrected for Fresnel loss.

The ultraviolet (UV) transmission of optical materials is affected by both intrinsic and extrinsic effects. Intrinsically, the incorporation of different cations produces different bonding and structure within the phosphate network, affecting the electronic band gap transitions, thus influencing the UV transmission [6,7]. Generally, glasses with higher field strength cations have UV edges at a lower wavelength. Extrinsically, absorption of trace impurities such as Fe^{2+} and Fe^{3+} in the glasses can also affect the UV transmission [6,7]. Ehrt *et al.* [8] found that ultraphosphate and metaphosphate glasses corresponding to $35MeO\text{-}65P_2O_5$ and $50MeO\text{-}60P_2O_5$ (Me = Mg, Zn, Ca, Ba, $Al_{2/3}$), respectively, did not show much difference in their UV absorption spectra. The UV spectra obtained for some CaP and BaP glasses, as shown in Figures 5.2 and 5.3, also show that there was no significant difference in the spectra despite the difference in compositions, although the spectra were affected by the Fe^{3+} absorption at ~ 230 nm. The slight difference in the intensity of the Fe^{3+} absorption could be attributed to variable conditions such as the melting time, melting temperature and the supply of oxygen during the melting procedures [9].

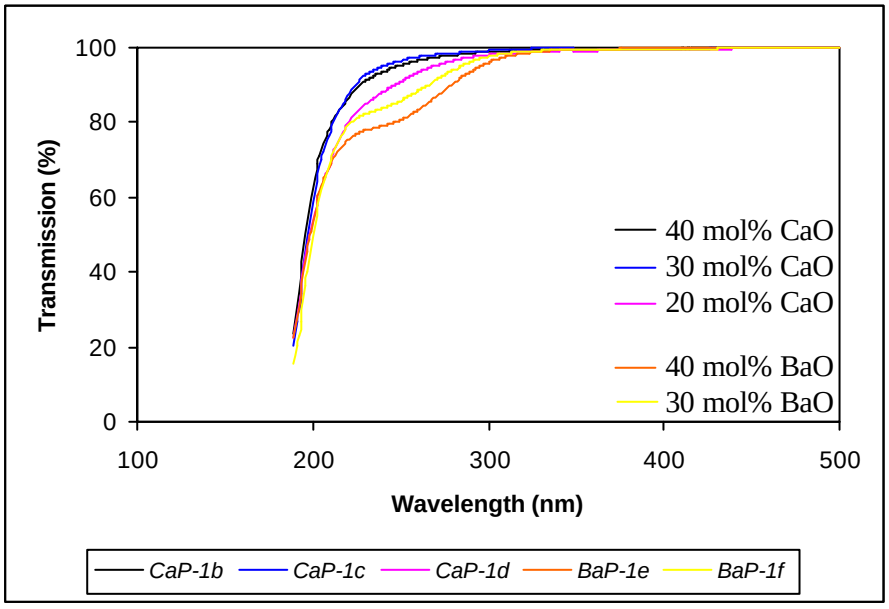

Figure 5.2 : Ultraviolet transmission spectra through xMO-(100-x)P_2O_5 glasses. The spectra are normalised for a 1 mm thick sample and corrected for Fresnel loss.

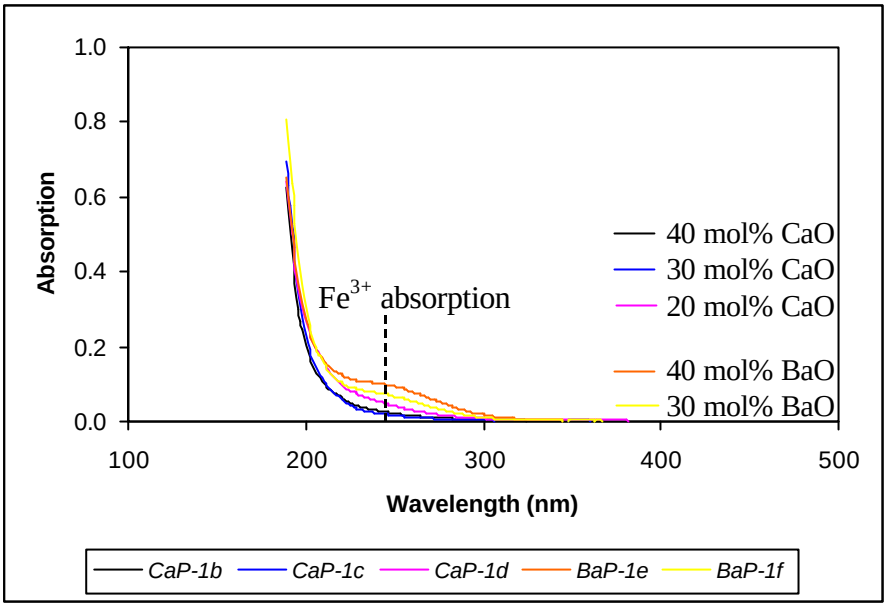

Figure 5.3 : Ultraviolet absorption spectra through xMO-(100-x)P_2O_5 glasses. The spectra are normalised for a 1 mm thick sample and corrected for Fresnel loss.

5.4.2 Refractive Index and Glass Transition Temperature

Figure 5.4 shows the refractive index of the CaP and BaP glasses as a function of the MeO mol%. As the CaO content in the CaP glasses increased, n decreased at low CaO content to a minimum at around 25 mol% before increasing at higher CaO content. For the BaP glasses, n increased monotonically with BaO mol%. From Figure 5.4, it can be seen that n increases in the order $Ca^{2+} < Ba^{2+}$. This is consistent with the fact that Ba^{2+} is a larger ion compared to Ca^{2+} and hence more polarisable, leading to an increase in n, according to the Lorentz-Lorenz equation [10]. The $M_{TO} > CN_{Me}$ and $M_{TO} < CN_{Me}$ regions in the figure will be explained later, based on the structural model proposed by Hoppe for binary phosphates [11].

Available n data for BaP glasses from ref [2] are plotted in Figure 5.4 for comparison. Both sets of BaP data show good agreement in the range of 45 - 50 mol% BaO. However, there are significant deviations in the results at low BaO mol%. It is difficult to explain this deviation because of a lack of information from ref [2], such as the melting and annealing conditions, the OH content and the temperature at which the measurements were taken.

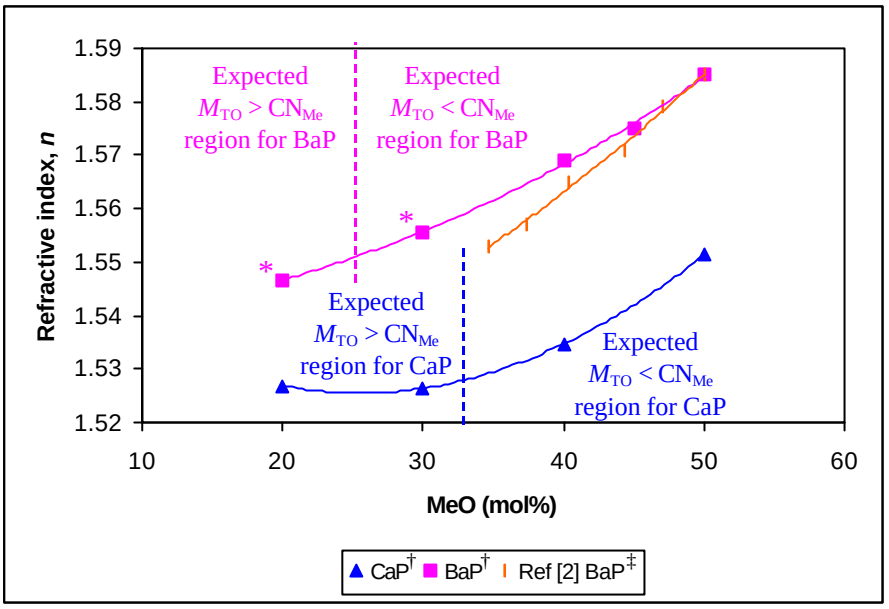

* contains relatively higher OH content, †, ‡ measured at λ = 589.3 nm

Figure 5.4 : Refractive index (n) of CaP and BaP glasses, measured at λ = 589.3 nm.

The glass transition temperatures of the CaP and BaP glasses also followed similar trend as that observed for n, as shown in Figure 5.5a. However, the minimum point observed for the CaP glasses was more pronounced and at a slightly higher CaO mol% (33 mol%) while a minimum point can be observed at around 25 mol% BaO for the BaP glasses. There were no T_g data available from ref [2].

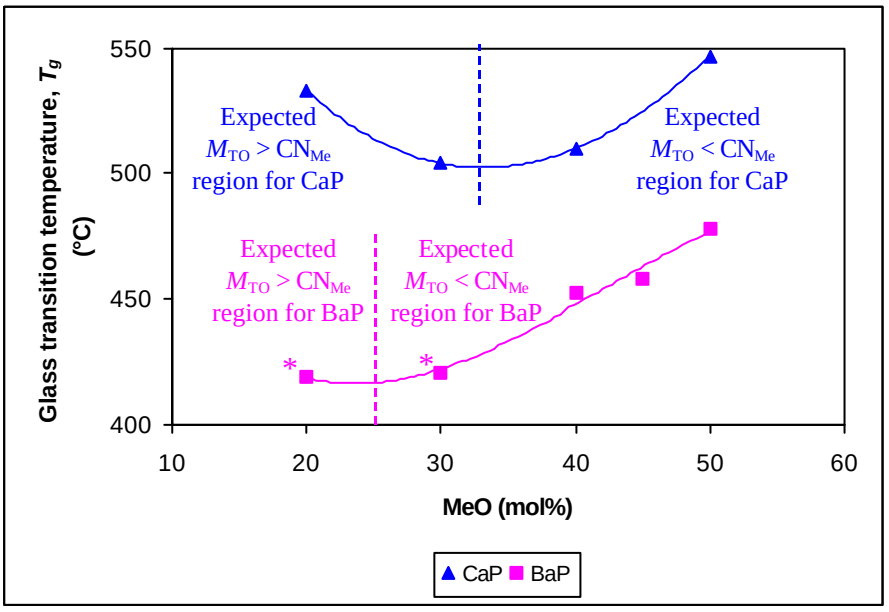

* contains relatively higher OH content

Figure 5.5a : Glass transition temperature (T_g) of CaP and BaP glasses

The observation of minimum points in the n and T_g results for the CaP glasses have also been reported in the literature for some binary glasses properties, such as the Ca and Ba ultraphosphate packing density [11], the Li and Na ultraphosphate density [12,13], and the Na and Cs ultraphosphate T_g [14].

Hoppe [11] presented a structural model to explain such a behaviour, based on the roles of the modifier coordination (with coordination number, CN_{Me}) and the number of terminal oxygens (M_{TO}) available to coordinate the modifier cations. By assuming that all TOs participate in coordinating the modifier cations, the number of available TOs per modifying cation for binary phosphates having the stoichiometry $x Me_{2/z}O\text{-}(100\text{-}x)P_2O_5$ is [11]

$$M_{TO} = z(100/x) \tag{5.1}$$

This structural model has been previously discussed in Section 2.1.2.1. Briefly, when $M_{TO} > CN_{Me}$, the cations can exist at isolated sites within the ultraphosphate network (Figure 2.6(a)). However, when $M_{TO} < CN_{Me}$, the cations must share the available TOs, and in the process create sub-structures of modifying cations which act as bridging bonds between neighbouring phosphate polyhedra (Figure 2.6(b)).

Based on the above model, in the region of $M_{TO} > CN_{Me}$, density decreases as the phosphate network expands to accommodate the additional cations, subsequently leading to a decrease in n (as per Figure 5.4 for CaO < 25 mol%). The addition of cations also depolymerises the phosphate network and reduces the structural cross-link density, causing a decrease in T_g (as per Figure 5.5a for CaO < 33 mol%). In the region of $M_{TO} < CN_{Me}$, the formation of a modifier sub-structure creates a more compact network and therefore increases the density and n of the glass (as per Figure 5.4 for CaO > 25 mol%). By sharing the TOs, the modifying cations also cross-link neighbouring phosphate polyhedra, thereby strengthening the glass network and increasing the glass T_g (as per Figure 5.5a for CaO > 33 mol%).

The structural transition from a network with isolated modifier sites to a network with a modifier sub-structure can be predicted based on the coordination number of the cation. Setting $M_{TO} = CN_{Me}$ and based on equation (5.1), the transition for Ca ($CN_{Ca} \sim 6$ [11]) occurs at x = 33 mol%

and the transition for Ba (CN_{Ba} ~ 8 [11]) occurs at x = 25 mol%. The points at which these transitions are expected to occur are denoted by the dotted lines in Figures 5.4 and 5.5a. These numbers coincided with the position of the minima points observed for the T_g of the CaP and BaP glasses within this work. However, there was no apparent minimum point observed for the BaP glasses in the n results. This can be attributed to the relatively higher water content in the glasses with low modifier content. The presence of water reduced the number of available TOs through the formation of (P-OH) bonds and this effectively extended the $M_{TO} < CN_{Me}$ region to lower modifying cation mol% than expected theoretically or even eliminated the existence of the $M_{TO} > CN_{Me}$ region. Hence the cations began to share the available TOs the moment they were added, increasing the density and refractive index of the glasses. It has been reported that anhydrous sodium ultraphosphates exhibited a minimum in density at around 20 mol% Na_2O [13], which was absent in the sodium ultraphosphate glasses prepared in open crucibles [15,16]. This confirmed the water effect on the refractive index of the BaP glasses in this work. The absence of a minimum in the n data for BaP glasses and the shift of the minimum point observed at 33 mol% CaO (T_g) to 25 mol% CaO (n) suggested that the glass T_g was less sensitive to changes in the glass OH content.

Three NaP glasses were also prepared and Figure 5.5b shows the T_g of these glasses. Using the same principles for determining the structural transition point for the CaP and BaP glasses, the minimum point for the NaP glasses should be observed at x = 20 mol% (CN_{Na} ~ 5 [17]). The hygroscopic nature of the NaP glasses, especially at low Na_2O content, made it difficult to prepare the glasses and measure their properties. Nevertheless, the results obtained for the NaP were consistent with the results expected in the $M_{TO} < CN_{Me}$ region. Comparing Figures 5.5a and 5.5b, T_g increased in the order $Na^+ < Ba^{2+} < Ca^{2+}$, which was expected from the increasing field strength in the same order, Na^+ (~ 0.19) < Ba^{2+} (~ 0.26) < Ca^{2+} (~ 0.35) [1]. Higher field strength cations form stronger bonds between the phosphate chains, increasing the structural strength of the glass network and hence, resulting in higher T_g.

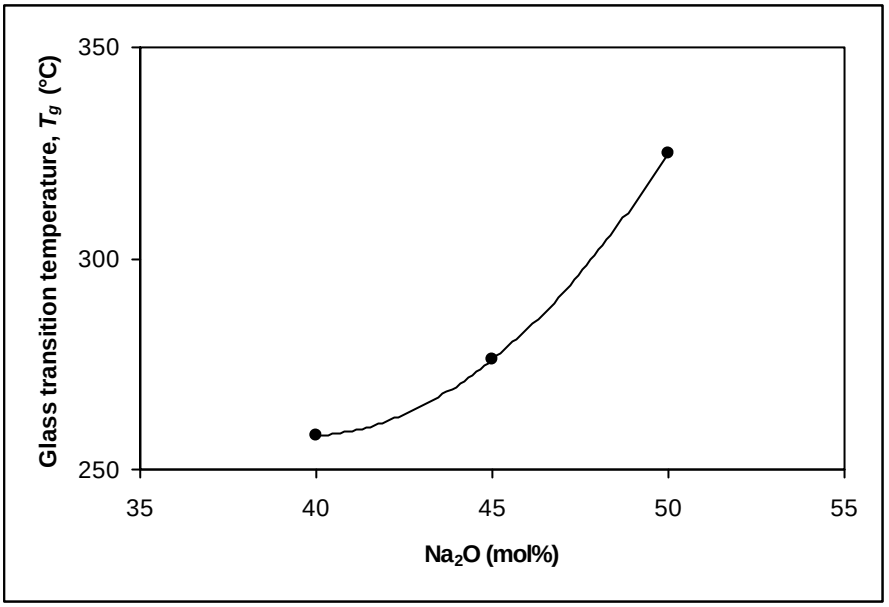

Figure 5.5b : Glass transition temperature (T_g) of NaP glasses

5.4.3 Thermal Expansion Coefficient and Thermo-optic Coefficient

Figure 5.6a shows the change in α for the CaP and BaP glasses as a function of MeO content while Figure 5.6b shows the results of α for the NaP glasses. As the amount of modifiers in the glass increased, the glass network became increasingly depolymerised as the BOs were converted to NBOs. This reduced the structural cross-linking of the glass, leading to an increase in α. α decreased with increasing cationic field strength [18] and this was evident from Figures 5.6a and 5.6b, where α decreased in the order $Na^+ > Ba^{2+} > Ca^{2+}$. Comparison between the α of this work and that of ref [2] showed a difference of ~ 0.3×10^{-6}/°C. The only available information from ref [2] to explain this difference was that α was measured over 20 - 120°C. Other possible explanations for this discrepancy could be the different thermal history of the glasses and conditions at which the measurements were made.

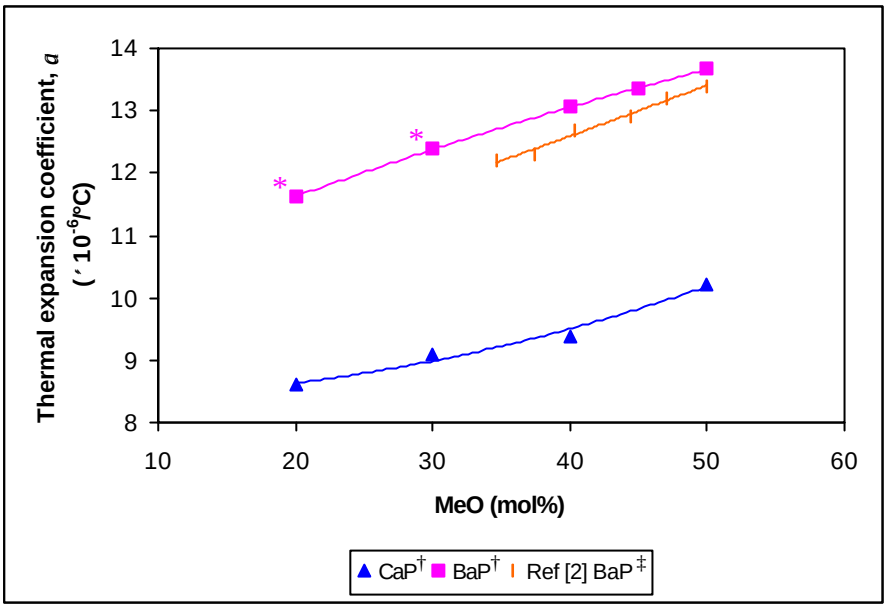

* contains relatively higher OH content

† measured over 50-120°C, ‡ measured over 20-120°C

Figure 5.6a : Thermal expansion coefficient (α) of CaP and BaP glasses, measured over 50 - 120°C.

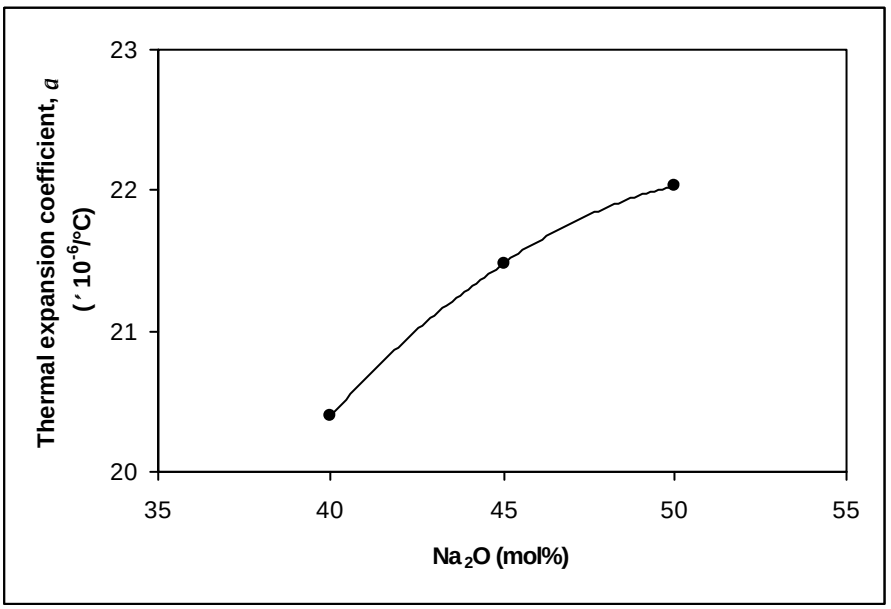

Figure 5.6b : Thermal expansion coefficient (α) of NaP glasses, measured over 50 - 120°C.

Figure 5.7 shows that the glass *dn/dT* progresses towards negative values as the modifier content increases. There was no evidence of a maximum or minimum point for α and *dn/dT* throughout the whole range of glasses examined, in contrast to the minimum point observed for T_g when the glass underwent a structural network change. The *dn/dT* data from ref [2] agreed with the results of this work, despite the different temperature ranges and wavelengths at which the measurements were taken.

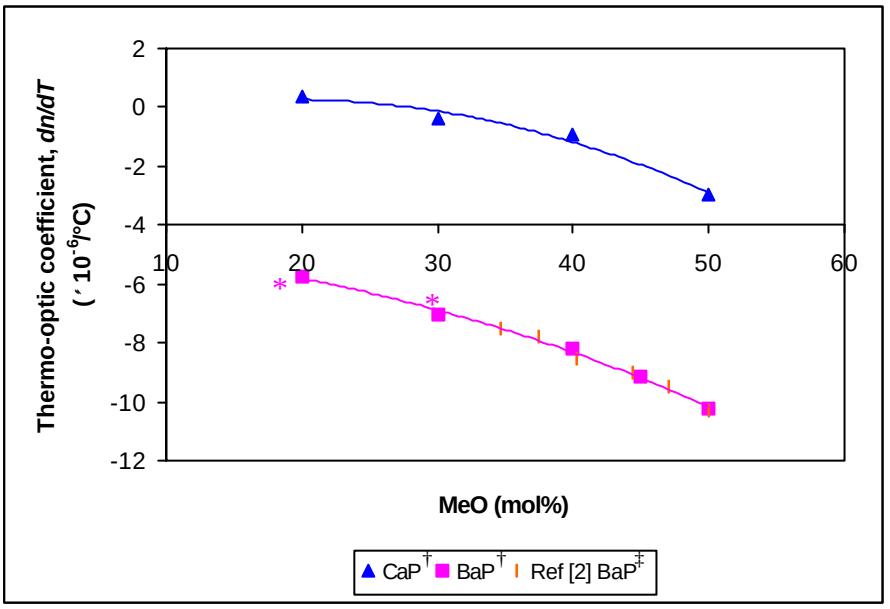

* contains relatively higher OH content

† measured over 20-100°C at λ = 632.8 nm, ‡ measured over 20-120°C at λ = 508 nm

Figure 5.7 : Thermo-optic coefficient (*dn/dT*) of CaP and BaP glasses

The change in *dn/dT* can be explained via the change in α. As discussed in Section 1.4, the relationship can be given as

$$\frac{dn}{dT} = A\left[\frac{d(\ln P_e)}{dT} - 3\alpha\right] \qquad (1.15)$$

where $A = [(n^2-1)(n^2+2)/6n]$. For a glass to exhibit negative *dn/dT*, it must have α that is large enough so that 3α can overcome the effect of $d(\ln P_e)/dT$. Figure 5.8 shows the compositional effects on the α and *dn/dT* of the CaP and BaP glasses. As the MeO mol% increased, α increased and correspondingly, *dn/dT* decreased.

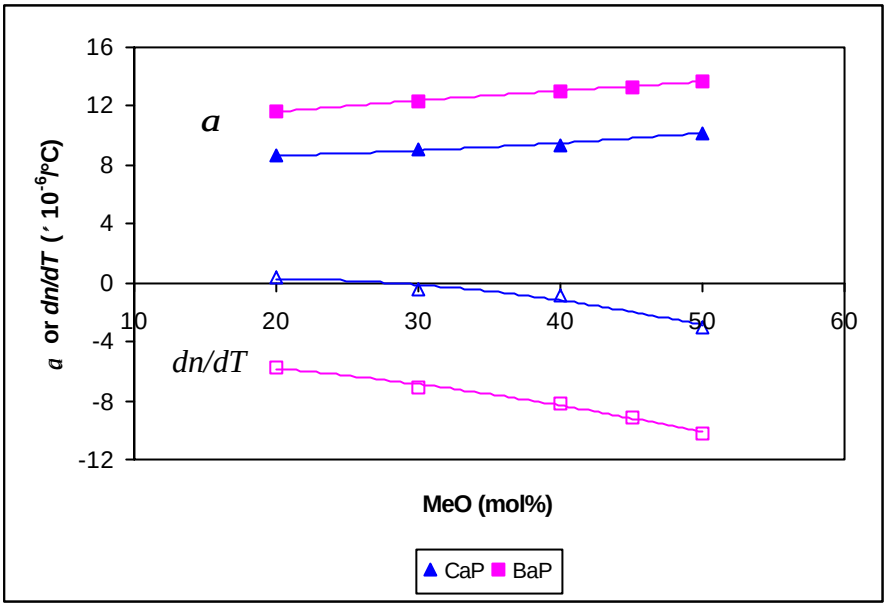

Figure 5.8 : α and *dn/dT* of CaP and BaP glasses as a function of MeO mol%

Figure 5.9 shows the comparison between the experimentally measured *dn/dT* values and the estimated *dn/dT* for the BaP glasses, where the estimated *dn/dT* values were determined from the additivity relationship of equation (2.5) and the estimated β_i data from Table 2.4, described in Section 2.2. The differences in the *dn/dT* results are mainly due to the limitations of the β_i data and the additivity relationship, as discussed in Section 2.2. There was no available β_i value for the CaO component in phosphate glasses. In Figure 5.9, the 50 mol% BaO point represents the metaphosphate composition ($BaO + P_2O_5 = Ba(PO_3)_2$), where the agreement between the measured and estimated value was good. However, as the composition deviated from the stoichiometric metaphosphate composition, the difference increased and the additivity relationship failed.

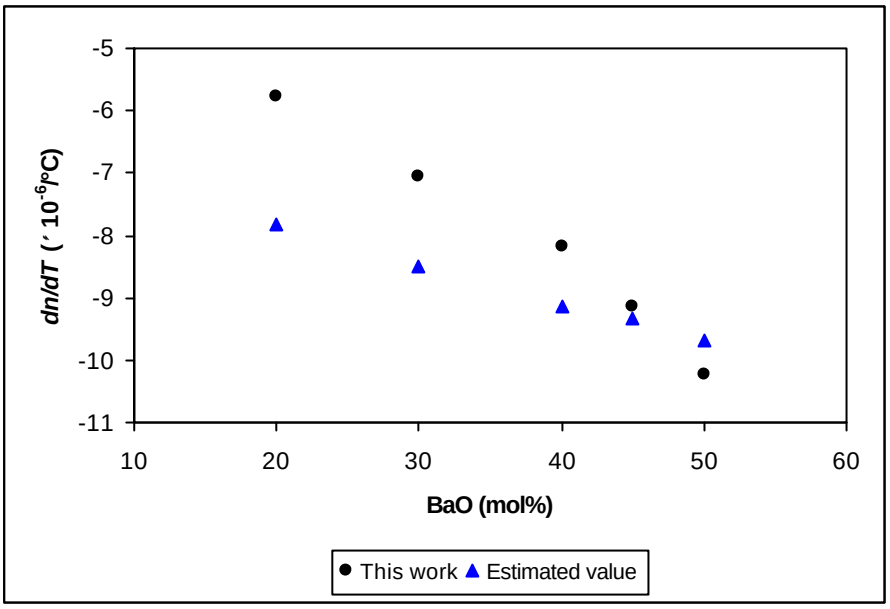

Figure 5.9 : Comparison of measured and estimated *dn/dT* of BaP glasses

Figure 5.10 shows the linear dependence of *dn/dT* on α for the CaP and BaP glasses. These relationships enabled semi-empirical equations to be defined, allowing the estimation of the *dn/dT* of any CaP glasses within the composition range of $1.526 \leq n \leq 1.551$ and $8.60\times10^{-6}/°C \leq \alpha \leq 10.22\times10^{-6}/°C$ and any BaP glasses within the composition range of $1.547 \leq n \leq 1.585$ and $11.62\times10^{-6}/°C \leq \alpha \leq 13.67\times10^{-6}/°C$. The values for *n* were quoted for λ = 589.3 nm, the values for α were quoted over 50 - 120°C and *dn/dT* values were measured at λ = 632.8 nm over 20 - 100°C. The results also showed that in order to obtain negative *dn/dT*, $\alpha > 9\times10^{-6}/°C$ was required for the CaP and BaP (from extrapolation) glasses. Also, the CaP and BaP data in Figure 5.10 practically fall on the same line, implying that the behaviour was predominantly due to the phosphate matrix.

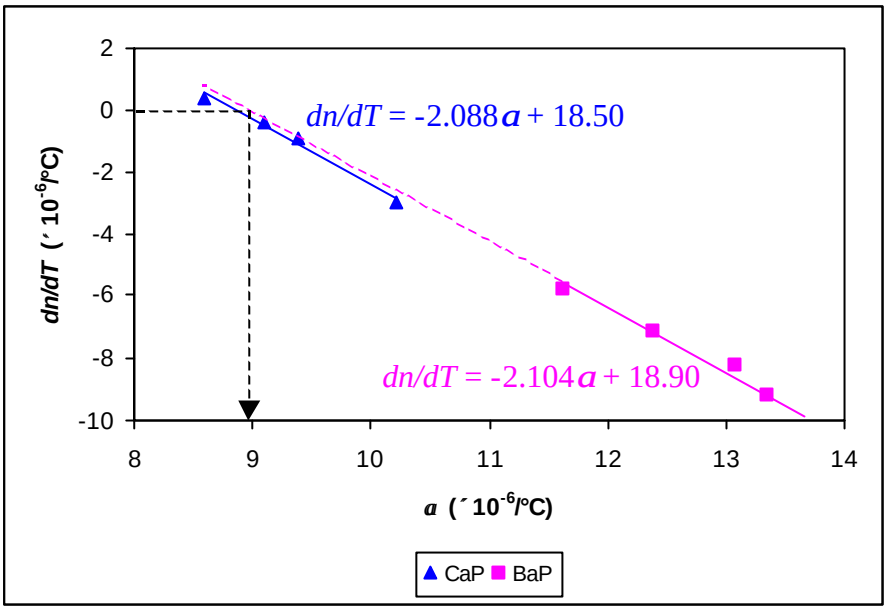

Figure 5.10 : *dn/dT* of CaP and BaP glasses as a function of α

As described in Section 1.4, equation (1.15) can also be represented as equation (1.16).

$$\frac{dn}{dT} = A(g-3)\alpha \tag{1.16}$$

Based on equation (1.16), g must be less than 3 in order to obtain negative *dn/dT*. The g values for the CaP and BaP glasses have been determined using the respective *n*, α, and *dn/dT* and are plotted as a function of the modifier content in Figure 5.11. The results showed that for the CaP glasses, the glass composition must have at least ~ 28 mol% CaO to exhibit negative *dn/dT*, while the BaP glasses always exhibit negative *dn/dT*, irrespectively of the modifier content.

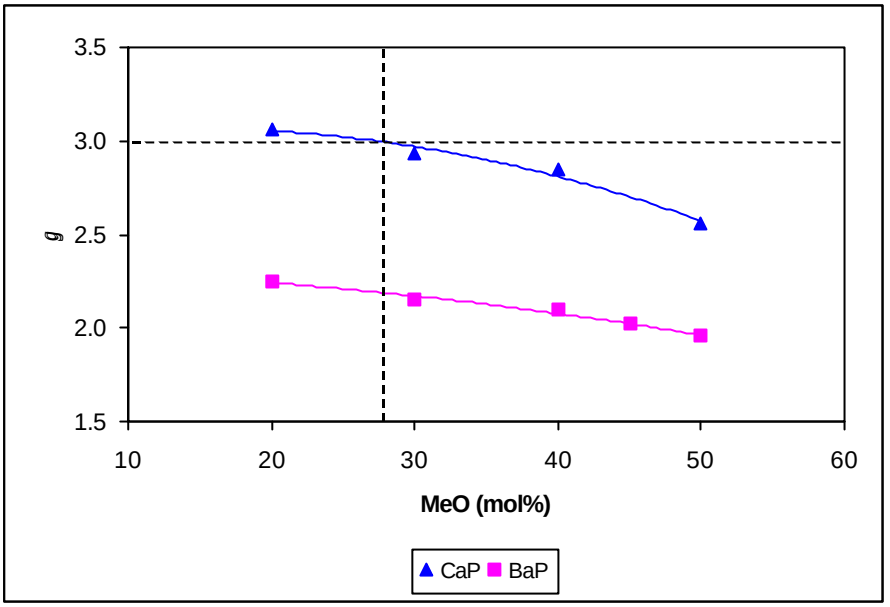

Figure 5.11 : *g* of CaP and BaP glasses as a function of MeO mol%

5.4.4 Athermalisation

Table 5.4 shows the athermalisation parameters of the binary phosphate glasses described in this work. The principles of athermalisation have been set out in Section 1.3 and it has been shown that glasses must exhibit negative *dn/dT* to satisfy the athermal condition due to the fact that glasses generally exhibit positive α. From Table 5.4, a number of samples show negative *dn/dT*, and therefore these glasses can be potentially used for athermalisation work. However, the CaP and BaP bulk glasses were not athermal, as the temperature dependence of their optical path lengths were not zero, as shown by their *1/L(dS/dT)* values. Therefore, in order to fabricate athermal devices, a multi-layer system approach has to be used so that the properties of the different glass layers can be utilised to compensate each other. The way this multi-layer system works has been previously described in Section 4.4.5.

Sample	**Composition (mol%)**		***dn/dT*** **(´ 10^{-6}/°C)**	***nα*** **(´ 10^{-6}/°C)**	***(1/L)(dS/dT)*** **(´ 10^{-6}/°C)**
	CaO	**P_2O_5**			
CaP-1a	50	50	-2.98	15.85	12.87
CaP-1b	40	60	-0.92	14.41	13.49
CaP-1c	30	70	-0.39	13.89	13.50
CaP-1d	20	80	+0.36	13.13	13.49
Sample	**BaO**	**P_2O_5**	***dn/dT*** **(´ 10^{-6}/°C)**	***nα*** **(´ 10^{-6}/°C)**	***(1/L)(dS/dT)*** **(´ 10^{-6}/°C)**
BaP-1a	60	40	Phase-separated sample		
BaP-1b	55	45	Phase-separated sample		
BaP-1c	50	50	-10.24	21.67	11.43
BaP-1d	45	55	-9.14	21.03	11.89
BaP-1e	40	60	-8.19	20.51	12.32
BaP-1f	30	70	-7.06	19.26	12.20
BaP-1g	20	80	-5.76	17.98	12.22
Silica [1]			+10.40	0.80	11.20

Table 5.4 : Athermalisation parameters of CaP and BaP glasses

5.5 Device Fabrication

Once the glasses have been developed and characterised, fabrication of planar waveguides and fibres based on these phosphate glasses can be carried out. The first step was to determine the core and clad glasses. As discussed in Section 1.3.3, the temperature dependence of both optical path length, *dS/dT*, and Bragg wavelength, $d\lambda_B/dT$, for optical waveguides can be described by equations (1.8) and (1.9), respectively.

$$\frac{1}{L}\frac{dS}{dT} = \left(n_{eff}\alpha_{sub} + \frac{dn_{eff}}{dT} \right) \tag{1.8}$$

$$\frac{d\lambda_B}{dT} = 2\Lambda\left(n_{eff}\alpha_{sub} + \frac{dn_{eff}}{dT}\right) \tag{1.9}$$

Looking at equations (1.8) and (1.9), in order to reduce the temperature sensitivity of dS/dT and $d\lambda_B/dT$, we need to choose a glass with low thermal expansion coefficient as the clad or substrate. Also, as glasses generally exhibit positive α, we need to choose the core and clad glasses with the appropriate dn/dT, so that we can achieve an effective refractive index change with temperature, dn_{eff}/dT, < 0.

The appropriate glasses for core and clad can be determined using the analysis for fibre Bragg gratings set out in Section 1.3.3. Table 5.5 shows the possible combinations of glasses for fibre fabrication using the KAP glasses (Chapter 4) and the binary phosphate glasses (this chapter), assuming the normalised frequency, V = 2.405 (single-mode operation), cut-off wavelength, $\lambda_{cut\text{-}off}$ = 1000 nm and Bragg wavelength, λ_B = 1040 nm. λ_B was chosen to be 1040 nm because of a combination of the refractive index of the glasses, the availability of the appropriate grating phase mask and the available source. Calculations had been performed based on the results of n at λ = 589.3 nm, α in the 50 – 120 °C temperature range and dn/dT at λ = 632.8 nm over 20 – 100 °C.

Core	Clad	NA	n_{eff}	dn_{eff}/dT (´ 10^{-6}/°C)	$(T_g)_{co} - (T_g)_{cl}$ (°C)	$\alpha_{co} - \alpha_{cl}$ (´ 10^{-6}/°C)	$d\lambda_B/dT$ (pm/°C)
BaP-1c	*KAP-1d*	0.478	1.549	-7.61	-65	4.96	3.95
	KAP-3c	0.488	1.548	-8.07	-48	3.52	5.13
	KAP-4b	0.484	1.548	-7.98	-61	3.86	4.84
	CaP-1a	0.325	1.568	-8.69	-69	3.45	4.87
BaP-1d	*KAP-4b*	0.450	1.543	-7.14	-81	3.54	5.39
	CaP-1a	0.272	1.563	-7.85	-89	3.13	5.41
	CaP-1b	0.354	1.555	-7.37	-52	3.96	4.84
	CaP-1c	0.388	1.551	-7.23	-46	4.25	4.62

Table 5.5 : Combination of core and clad glasses using potassium aluminophosphate and binary phosphate glasses

The parameter, numerical aperture (NA), will be explained in Section 5.5.1.1.

The combination of *BaP-1c* and *KAP-1d* was chosen for fibre and planar waveguide fabrications because it offered considerably lower $d\lambda_B/dT$ compared to the other combinations. The details of the fabrication processes are detailed in the following sections.

5.5.1 Fibre Fabrication

This section describes the fibre fabrication process. The requirements for fibre fabrication are first set out, followed by a section on the extrusion work.

5.5.1.1 Fabrication Requirements

An optical fibre is a waveguide that consists of a thin central glass core surrounded by a glass cladding. In order to produce a light guiding fibre, the combination of core and cladding glasses must satisfy certain optical and thermal requirements such as the following conditions:

- The refractive index of the core must be higher than that of the clad, $n_{co} > n_{cl}$.
- The thermal expansion coefficient of the core should be higher than that of the clad, $\alpha_{co} > \alpha_{cl}$.

n_{co} must be higher than n_{cl} so that light can be total internally reflected within the core. The difference in n means that the interface between the core and the cladding acts as a perfect 'mirror' and light travelling along the core is confined by this 'mirror' to stay within the core. Figure 5.12 shows the propagation of light in a fibre core via total internal reflection (TIR). For TIR to occur, the light must reach the interface at an angle greater than the critical angle ($\theta_2 > \theta_c$) between the core and cladding glasses.

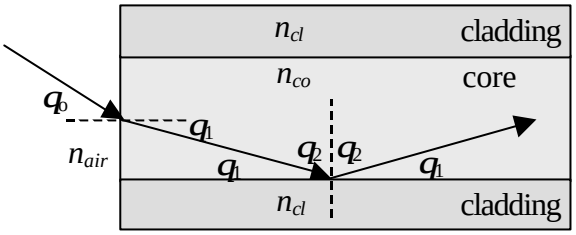

Figure 5.12 : Total internal reflection in a fibre

When light enters through the end-face of a fibre, it will be refracted and will encounter the core-cladding interface. However, only light reaching the fibre at certain angles will reach the interface at $\theta_2 > \theta_c$ such that it will experience TIR and propagate as a bound mode along the fibre. Hence there is a 'cone' of acceptance and the sine of the largest angle contained within this cone is defined as the numerical aperture, NA. From Figure 5.12, NA is sin θ_o [19]. In addition, NA can also be given by equation (5.2). A high NA means that rays can bounce at greater angles and hence, more modes can propagate within the core.

$$NA = \sqrt{n_{co}^2 - n_{cl}^2} \tag{5.2}$$

In terms of the thermal requirement, the pair of core and clad glasses used for fibre fabrication must have matched thermal expansion coefficients. This is essential in order to minimise the stresses within the fibre, which will otherwise reduce the fibre strength and eventually cause the fibre to fracture. In the presence of a difference in the α of the core and cladding glasses, the stress, σ, that develops in the fibre can be determined from equation (5.3) [20].

$$\sigma_{cl} = \frac{(\alpha_{co} - \alpha_{cl})(T_g - T_o)}{\left(\frac{a_{cl}^2}{a_{co}^2}\right)\left(\frac{1-\nu}{E}\right)} \tag{5.3}$$

where the subscripts *co* and *cl* represent core and clad respectively, α is the thermal expansion coefficient, T_g is the glass transition temperature, T_o is the room temperature, a is the radius, ν is Poisson's ratio and E is Young's modulus.

For the case of $\alpha_{co} > \alpha_{cl}$, compression stresses build up in the cladding and results in an increase in the fibre strength [20]. For the case of $\alpha_{co} < \alpha_{cl}$, tension stresses develop in the cladding, resulting in a decrease in the fibre strength and can eventually lead to the breakage of the fibre if surface flaws are present. Figure 5.13 shows the stresses that develop in the core and cladding for the two cases. The requirement for $\alpha_{co} > \alpha_{cl}$ also satisfies the athermalisation requirement where a lower α_{cl} compared to α_{co} is necessary to reduce the temperature sensitivity, as described in Section 4.4.5.

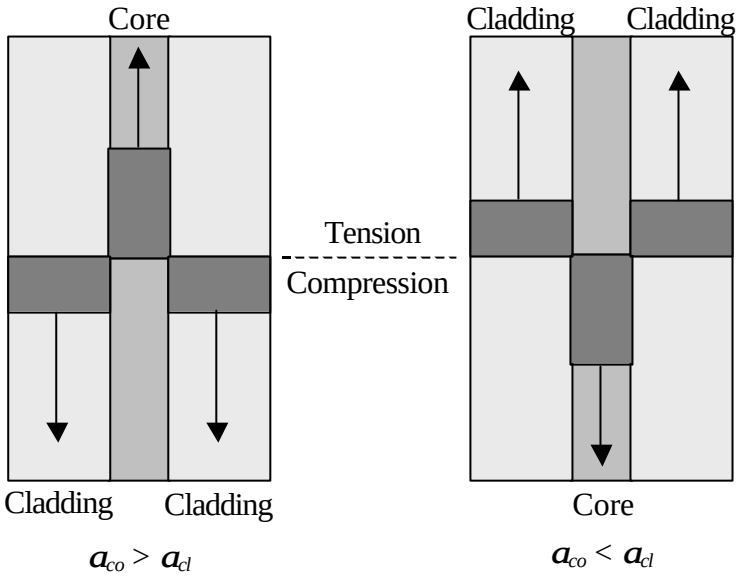

Figure 5.13 : Axial stress in a fibre

5.5.1.2 Extrusion

The combination of *BaP-1c* (core), with the composition $50BaO\text{-}50P_2O_5$, and *KAP-1d* (cladding), with the composition $16.5K_2O\text{-}16.75Al_2O_3\text{-}66.75P_2O_5$, was used for fibre fabrication. *BaP-1c* had the properties of n_{co} = 1.585, α_{co} = 13.67×10^{-6}/°C and dn/dT_{co} = -10.24×10^{-6}/°C, while *KAP-1d* had the properties of n_{cl} = 1.511, α_{cl} = 8.71×10^{-6}/°C and dn/dT_{cl} = $+1.65\times10^{-6}$/°C. Comparison between these properties showed that $n_{co} > n_{cl}$ so that TIR could occur in the fibre, and that $\alpha_{co} > \alpha_{cl}$ so that the fibre strength was increased. However, the difference between the thermal expansion coefficients, (α_{co} - α_{cl}), was 4.96×10^{-6}/°C, which was large. Therefore, the decision was to fabricate fibres with a (core/clad) ratio of 0.02 to compensate for the large $\Delta\alpha$. This can be achieved by first extruding a cane of

(core/clad) ratio of 0.1 with an outer diameter, OD, of 2 mm. The cane could then be inserted into a cladding tube with an OD of 10 mm to achieve the final (core/clad) ratio of 0.02. Figure 5.14 shows the cladding stresses for different (core/clad) ratios for different (α_{co} - α_{cl}) values. It can be seen that the stress in the cane was ~ 2 MPa (for (core/clad) = 0.1 and (α_{co} - α_{cl}) = 5×10^{-6}/°C). However this stress can be substantially reduced to ~ 0.09 MPa for a fibre with (core/clad) = 0.02, so that the fibre can possibly survive without any cracks, even with a high (α_{co} - α_{cl}).

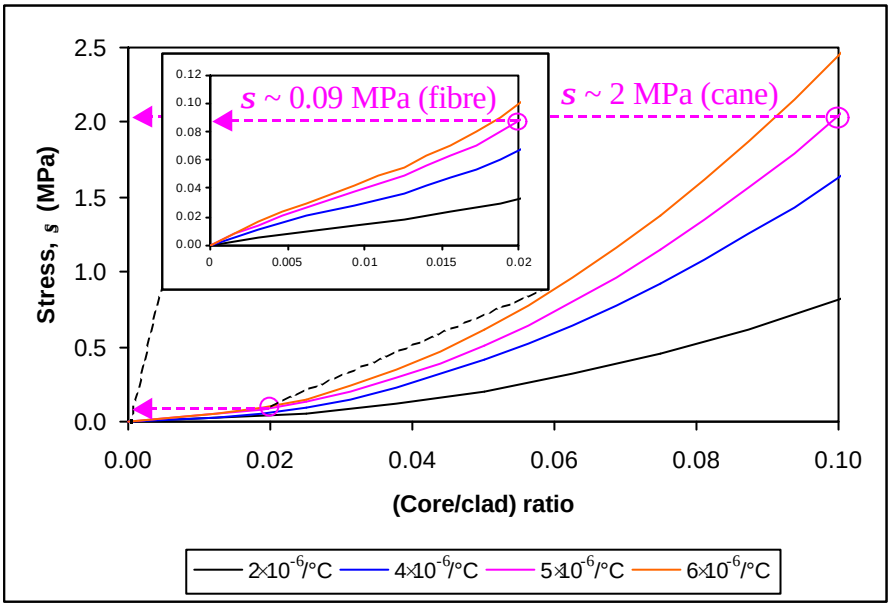

Figure 5.14 : Cladding stress as a function of (core/clad) ratio for different (α_{co}-α_{cl}) values. Inset : Cladding stress for (core/clad) ratio less than 0.02

We need to determine the softening temperature, T_s, of each glass, in order to determine the temperature at which extrusion should be carried out. T_s is defined as the temperature at which the glass deforms under its own weight. Figure 5.15 shows the working range possible for extrusion, with the aid of the viscosity-temperature curve of a soda lime silicate glass [21]. By equating the annealing point and the working point to T_g and T_x, respectively, T_s (°C) can be approximated by equation (5.4).

$$T_s \sim \frac{(T_x - T_g)}{3} + T_g \qquad (5.4)$$

This approximation is generally valid for most glasses [21,22]. The estimation of T_s provides a starting temperature for extrusion and is not critical. A lower extrusion temperature can be compensated by a higher applied pressure for glass extrusion [21]. Figure 5.16 shows the DTA plots for both *BaP-1c* and *KAP-1d* glasses, where T_s for the core and clad glasses were estimated to be 536°C and 619°C, respectively, via the use of equation (5.4).

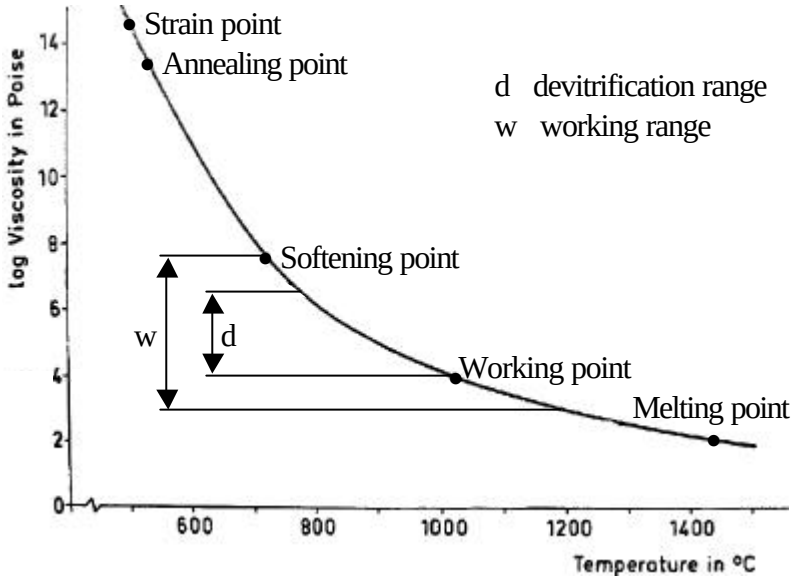

Figure 5.15 : Viscosity ranges for extrusion (based on soda lime silicate) [21]

(1 Poise = 0.1 Pa s)

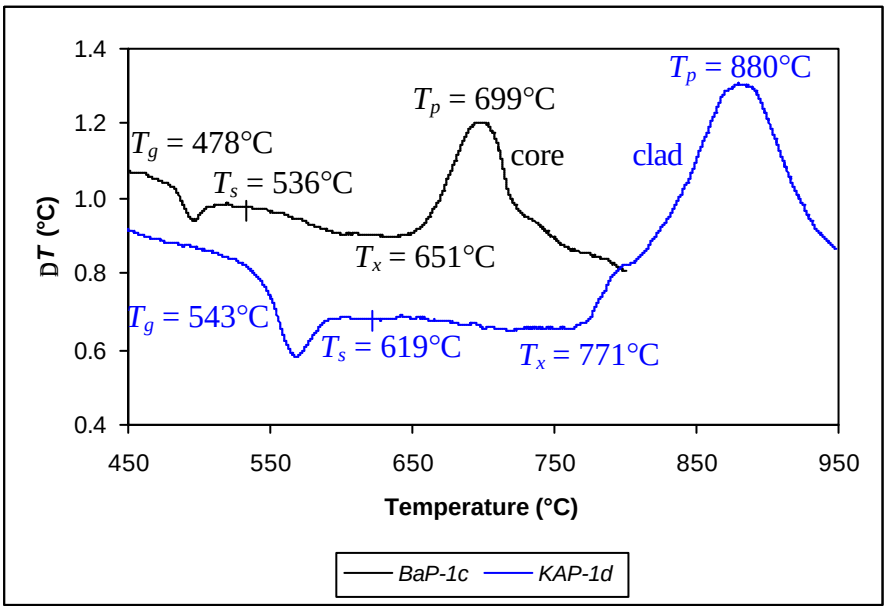

Figure 5.16 : DTA plots for *BaP-1c* (core) and *KAP-1d* (clad) glasses

(The curves have been displaced to fit the same D*T* range)

The core (*BaP-1c*) and clad (*KAP-1d*) glasses were first melted and cast, using the 2-step melting procedures in a silica crucible and then in a platinum crucible as discussed in Section 3.1.1. The detailed procedures for the extrusion process have been set out in Section 3.5.1. Core and clad glasses with dimensions of height, h = 14 mm and diameter, f = 29 mm were prepared. Due to the marked difference in the T_s of the glasses, a two-die assembly was used, comprising a core die and a clad die. The extrusion assembly as described in Section 3.5.1 was as follows : first, the clad die with a hole f of 2 mm was inserted, then the clad glass, whose top surface had been polished to prevent any air entrapment, next to be inserted was the core die with a hole f of 2 mm and finally the core glass.

The extrusion rig furnace was first pre-heated to ~ 620°C, which was the clad glass T_s but well above the core glass T_s. At this point, the core glass was molten and 'soft'. Pressure, P, up to 75 bar (7.5 MPa) was then applied to force the glasses out, with an increment of 10 bar (1 MPa) every 2 minutes. The extrusion rate was found to be 0.01 mm/min. The furnace temperature was then increased to ~ 640°C. At this point, the extrusion rate was still low at 0.025 mm/min. The furnace temperature was further increased to ~ 660°C and this condition increased the extrusion rate to 0.076 – 0.1 mm/min. The conditions of T = 660°C and P = 75 bar (7.5 MPa) were maintained for the remainder of the extrusion process, which in the end produced a yield of > 2 m. The diameter of the final cane was about 2.08 mm.

Unfortunately, upon checking under an optical microscope, there was no core within the extruded cane. The extrusion body was then disassembled and upon checking, it was found that the core glass had crystallised. This was not a surprise as the final furnace temperature of 660°C was about 10°C above the core glass T_x. Furthermore, the temperature stability of the core glass in terms of $T_p - T_x$ was only 48°C, which caused crystallisation to progress rapidly once started.

In addition to the purpose of extruding a cane, the extrusion was also carried out to see whether the core might flow through the clad layer, due to the fact that the core was softer than the clad. This effect will be shown later with a different pair of core and clad glass in Section 6.5.1.1.

The extruded clad cane (*KAP-1d*) was then analysed in terms of attenuation, which would give a rough estimate of the cladding loss. This was carried out using the cut-back method in the

experimental set-up shown in Figure 5.17, where the detector was a power meter. Measurement was first taken for an initial cane length and another measurement after a certain length was cut from the cane. Comparison between these two measurements gave an estimate of the loss, α_{loss}, which can be determined using equation (5.5). Measurements were taken for a few cut-back lengths and the average cladding loss was estimated to be ~ 5 dB/m at 632.8 nm.

$$\alpha_{loss} = \frac{10\,log\left(\frac{P_s}{P_l}\right)}{\left(L_l - L_s\right)} \tag{5.5}$$

where the subscripts *s* and *l* for a measurement denote a measurement after a cut-back and a measurement before a cut-back, respectively, *P* is power and *L* is the length of the sample.

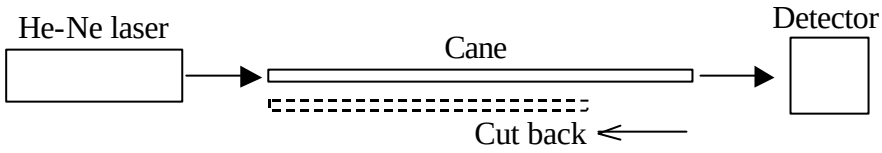

Figure 5.17 : Cane cut-back attenuation measurement set-up

Despite crystallisation of the core glass, the successful extrusion of a rod of clad glass showed that the process was a viable method. The next step in this extrusion trial was to use a combination of core and clad glass that was matched in terms of the thermal properties. This has been carried out with the successful extrusion of a cane with core and clad glasses as well as fibre pulling of borophosphate glasses, which is described in Section 6.5.1.

5.5.2 Planar Waveguide Fabrication

For the fabrication of planar devices, the spin-coating process was used to deposit glass layers on glass substrates. The principles and procedures of this process have been discussed in Section 3.6.1. A substrate with dimensions of h = 3 mm and ϕ = 32 mm was first cast and then optically polished on one surface and flat polished on the other surface. The glass substrate was prepared using the 2-step melting procedures described in Section 3.1.1 and optically polished using the

procedures described in Section 3.1.2. For this work, a 3-layer planar device was fabricated. The *BaP-1c* glass of $50BaO\text{-}50P_2O_5$ was used for the core glass while the *KAP-1d* glass of $16.5K_2O\text{-}16.75Al_2O_3\text{-}66.75P_2O_5$ was used for the overcladding glass and substrate.

The polished substrate, approximately 3 mm thick, was fixed with the flat polished surface to the vacuum chuck in the upper furnace of the spin-coating rig (Figure 3.18) and heated to ~ 550°C (substrate T_g). The core glass was then melted in a platinum crucible in a separate furnace at 1350°C and then transferred to the lower furnace of the spin-coating rig. The crucible was subsequently raised to the upper furnace so that the substrate could be dipped into the molten core glass. Once the crucible was withdrawn, the substrate was spun at 2000 rpm to produce a thin and uniform core layer on the substrate. The sample was then annealed at the substrate T_g, while at the same time, the overcladding glass was melted in a second platinum crucible in a separate furnace at 1450°C. The crucible was then transferred to the spin-coating rig and an overcladding layer was deposited onto the sample using similar procedures as described for the deposition of the core glass layer. The 3-layer sample was annealed at the substrate T_g for 60 minutes before being cooled to room temperature at a rate of 1°C/min.

Photograph 5.1 shows the fabricated 3-layer *BaP-1c* : *KAP-1d* planar sample. The spin-coated sample had turned pink from the original colourless substrate, core and overclad glasses, which was unexpected. There were also cracks appearing close to the surface of the sample.

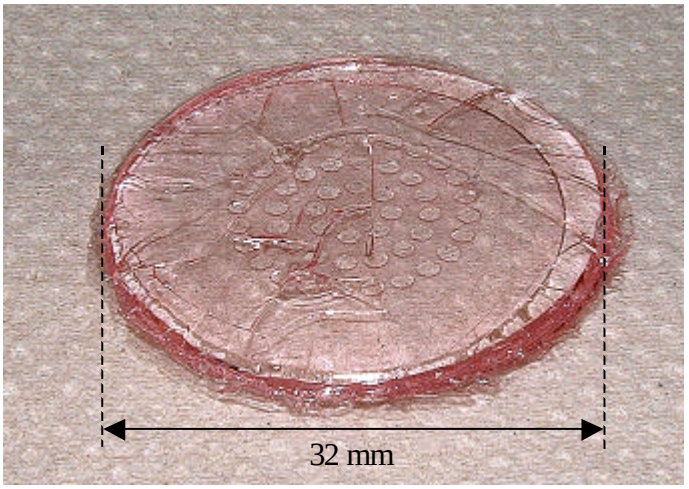

Photograph 5.1 : *BaP-1c* : *KaP-1d* planar sample

Hosono *et al.* [23] discovered that amorphous red phosphorus was formed in 'reduced' phosphate glasses. Therefore, it seemed that the spin-coated sample had undergone a reduction process. A sample of the *KAP-1d* glass (substrate and overclad glass) in 'reduced state' was prepared for comparison of glass properties compared to a sample in 'oxidised state'. The glass was melted in a reduced oxygen atmosphere to achieve the reducing condition. The refractive index of the 'reduced' phosphate glass was measured to be 1.508, compared to $n \sim 1.511$ for similar glass under oxidising condition. However, the thermal characteristics of both glasses did not show any significant difference, as shown by the DTA plots in Figure 5.18.

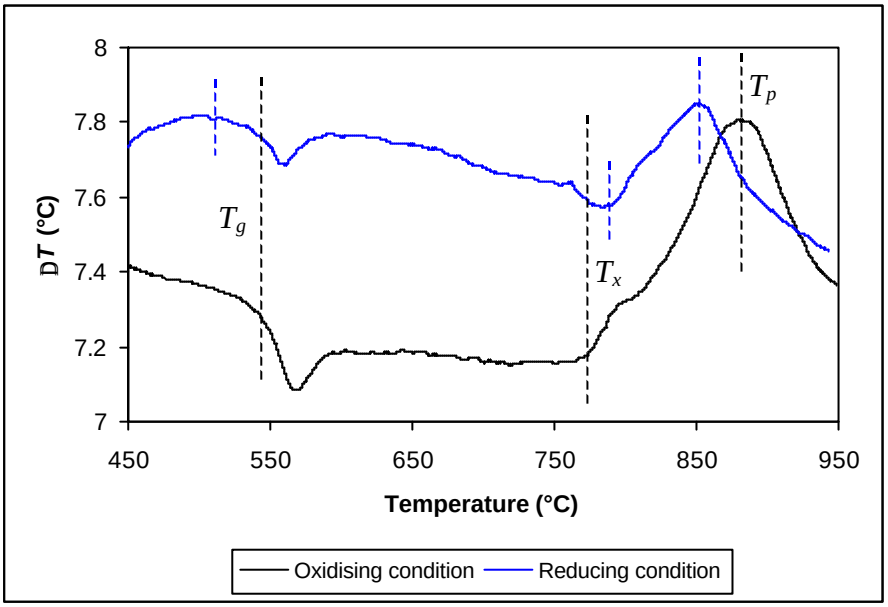

Figure 5.18 : DTA plots of *KaP-1d* sample under oxidising and reducing conditions. (The curves have been displaced to fit the same Δ*T* range)

Figure 5.19 shows the cross-section of the planar sample. There was no evidence of the presence of crystals in the core glass as shown by the SEM picture of Figure 5.19(b), in contrast to the crystallisation of the core glass observed for the extrusion process described in Section 5.5.1.

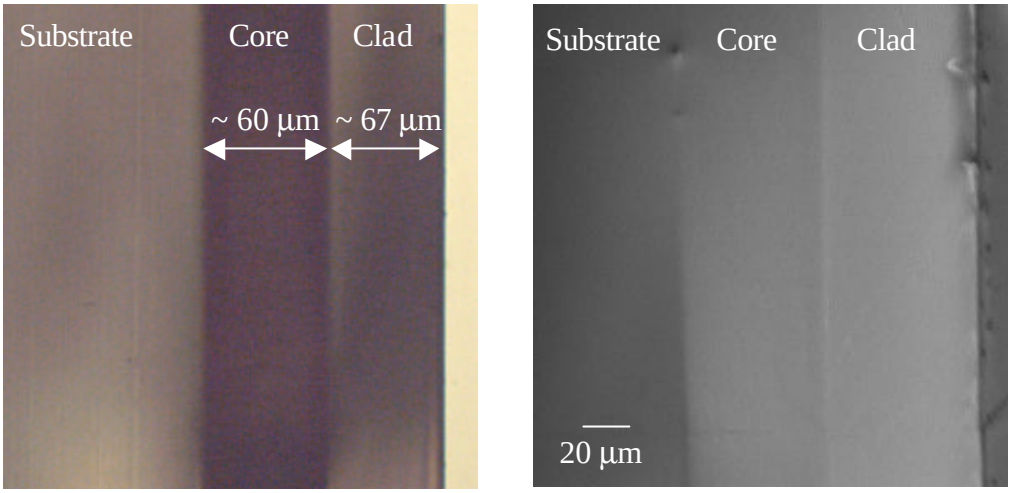

(a) (b)

Figure 5.19 : Cross-section of *BaP-1c* : *KaP-1d* planar sample : (a) optical microscope and (b) SEM

The cracks on the sample appeared due to stresses in both the core and overclad layers. These were caused by the $\Delta\alpha$ between the glasses as well as the thickness of the glass layers. The stress, σ, in each layer can be determined from equations (5.6) and (5.7) [24]. As the sample was a 3-layer planar sample, the total stress within the core layer was the sum of the stresses induced by both the overclad layer and the substrate [25].

$$\sigma_{co} = \frac{-E_{co}(\alpha_{cl} - \alpha_{co})DT}{(1-\nu_{co})K}\left[3\frac{l_{co}}{l_{cl}} + 2\left(\frac{l_{co}}{l_{cl}}\right)^2 - \frac{E_{cl}l_{cl}}{E_{co}l_{co}}\left(\frac{1-\nu_{co}}{1-\nu_{cl}}\right)\right] \tag{5.6}$$

$$\sigma_{cl} = \frac{E_{cl}(\alpha_{cl} - \alpha_{co})DT}{(1-\nu_{cl})K}\left[3\frac{l_{co}}{l_{cl}} + 2 - \frac{E_{co}}{E_{cl}}\left(\frac{l_{co}}{l_{cl}}\right)^3\left(\frac{1-\nu_{cl}}{1-\nu_{co}}\right)\right] \tag{5.7}$$

where $K = 4 + 6\frac{l_{co}}{l_{cl}} + 4\left(\frac{l_{co}}{l_{cl}}\right)^2 + \frac{E_{co}}{E_{cl}}\left(\frac{l_{co}}{l_{cl}}\right)^3\left(\frac{1-\nu_{cl}}{1-\nu_{co}}\right) + \frac{E_{cl}l_{cl}}{E_{co}l_{co}}\left(\frac{1-\nu_{co}}{1-\nu_{cl}}\right)$, the subscripts *co* and *cl* denote core and clad (and substrate), respectively, α is the thermal expansion coefficient, l is the thickness, ΔT is the difference between the deposition temperature and room temperature, E is Young's modulus and ν is Poisson's ratio.

From equations (5.6) and (5.7) and using the appropriate properties for the glasses, the stresses induced in the core and clad layers can be determined. Assuming $E_{co} = E_{cl} = 64$ GPa and $\nu_{co} = \nu_{cl} = 0.29$ [26], the stress in the core, σ_{co}, was –162.71 MPa while the stress in the overcladding layer, σ_{cl}, was –63.75 MPa. The large compressive stress in the core as well as the large difference in both compressive stresses in the core and overcladding layers caused cracks to appear on the sample.

As a reference, a successful deposition of a core and overcladding layers ($\Delta\alpha = 1\times10^{-6}$/°C) had been demonstrated in fluoroaluminate glasses [27]. The substrate was 2 mm thick while the core and overclad layers were 6 μm and 20 μm thick, respectively. The calculated stresses were σ_{co} = –44.71 MPa and σ_{cl} = –11.02 MPa. Thus, experimentally, we know that this level of stress value was tolerable using the spin-coating process.

Despite the 'reduced state' of the planar sample with its pink colour and cracks on the surface, the successful fabrication of the planar sample showed that spin-coating offers the possibility of fabricating phosphate-based planar devices. I have shown that even when the thermal properties of the core glass were poor, spin-coating can successfully deposit a layer free of crystals. Further improvement on the fabrication can be done by developing compatible core and clad glasses in terms of the thermal properties. In order to minimise stresses, the film thickness should be reduced. This can be done through optimisation of the spinning speed, spinning time and viscosity of the glass. Also, $\Delta\alpha$ between the core and clad glasses should be small but not to the extent of compromising the athermalisation of the device.

5.6 Channel Definition

The techniques of direct UV writing and direct femtosecond writing have been explored to write channel waveguides on the bulk glasses. General overviews of these techniques are presented in Sections 3.6.2 and 3.6.3.

5.6.1 UV Writing

The *BaP-1c* glass was used for this experiment. Direct UV writing into the bulk glasses was performed using a frequency doubled argon-ion laser (Coherent FRED Sabre 500) at 244 nm. Straight channel confinement was created by translating the sample under the focused UV beam. Writing was carried out using a UV beam focused to a spot size of approximately 6.5 μm at writing powers of 50 mW and 100 mW and scan speeds of 5 – 500 mm/min. The separation between the written channels was 200 μm. Figure 5.20 shows the written channels in the *BaP-1c* glass.

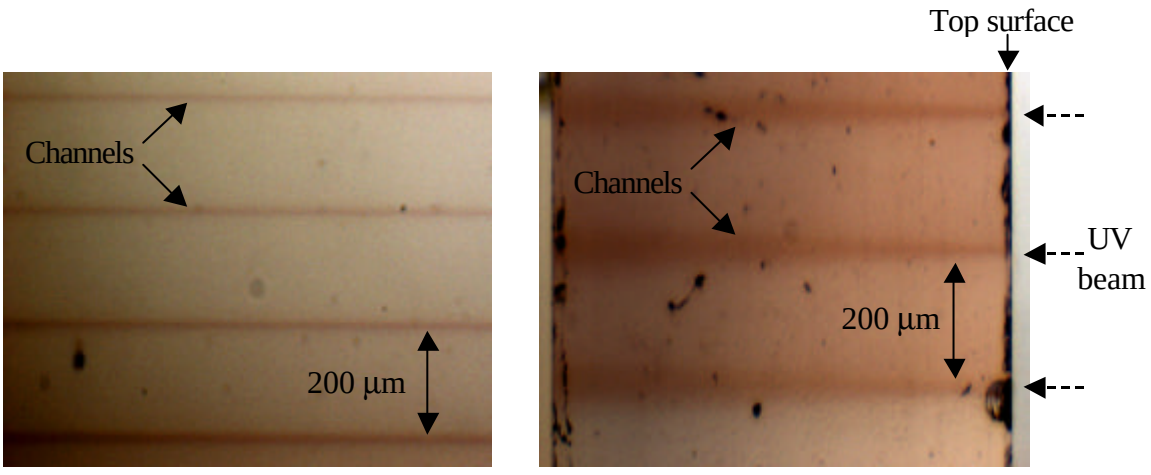

Figure 5.20 : UV written channels in *BaP-1c* bulk glass :
(a) top view and (b) cross-section

It is clear from Figure 5.20 that direct UV writing has produced slab channels, indicating the weak absorption of the phosphate glasses at 244 nm. A check on the waveguiding effect of these channels using He-Ne laser showed that none of the waveguides was guiding. Although there was

coloration of the glass from UV writing, this did not correspond to a change in the refractive index. UV writing on other samples (*CaP-1a*, *BaP-1e*, *KAP-2d*) produced similar slab channels, with no apparent waveguiding effect. This was consistent with the earlier result that showed that the 'reduced' pink glass had a lower *n* than the 'oxidised' glass, meaning that UV writing in these glasses would produce a negative index change and if guiding was to be observed, this will be between the written channels. However, this was not observed, and it may be because the change in *n* was too small.

5.6.2 Femtosecond Writing

Femtosecond writing was performed using a regeneratively amplified Ti:sapphire laser generating 798 nm, 150 fs laser pulses at 100 kHz repetition rate. For this work, a *KAP-1d* bulk glass sample was used. Microscope objectives of 10X and 50X were used to focus the beam to a depth of 100 µm inside the sample, which was translated perpendicularly to the focused beam for the writing of straight channel waveguides. Different powers between 50 - 270 mW (up to 2.7 µJ/pulse) at scan speeds of 40 - 160 µm/s were used and the separation between the written channels was 100 µm. Figure 5.21 shows the channels written at 50 mW at speeds of 120 and 160 µm/s.

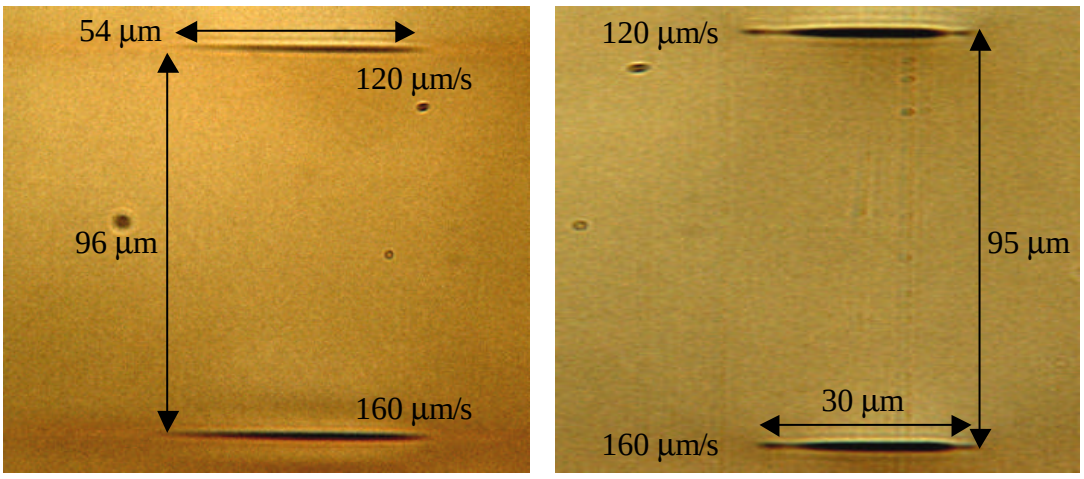

(a) (b)

Figure 5.21 : Cross-section of femtosecond written channels at 50 mW in *KAP-1d* bulk glass with a (a) 10X objective and (b) 50X objective

It can be seen from Figure 5.21 that the waveguides were asymmetric with an elongated profile in the longitudinal direction. This asymmetry was due to the different profiles of the laser beam along, and perpendicular to, the beam propagation direction. Perpendicularly to the beam direction, the waveguide size is approximately the beam focal diameter, $2w_o$, while along the propagation direction, the waveguide size is approximately given by the confocal parameter, $b = 2\pi(w_o)^2/\lambda$ [28]. The asymmetry of the waveguide profiles was more pronounced for waveguides written with large focal beam spot, such as with a 10X microscope objective with a smaller NA compared to a 50X objective.

NA measurement of the waveguides was carried out using the set-up shown in Figure 5.22. Light from the laser was first passed through an attenuator and focused by the microscope objective into the single-mode fibre. The function of the attenuator was to vary the power into the fibre to prevent saturation of the CCD (charge coupled device) camera. The sample and single-mode fibre were aligned so that light could be coupled into the waveguides. The output light was then passed through another microscope objective and captured by the CCD camera. The objective lens and CCD camera were mounted on a translation stage equipped with a micro-gauge to vary the distance from the sample end. When the focus was reached, the micro-gauge was set to zero. Profiles were then taken at distances of 0 - 400 μm at every 100 μm interval. The images were digitised by the computer and the 5% beam widths measured using a Gaussian beam profile fit.

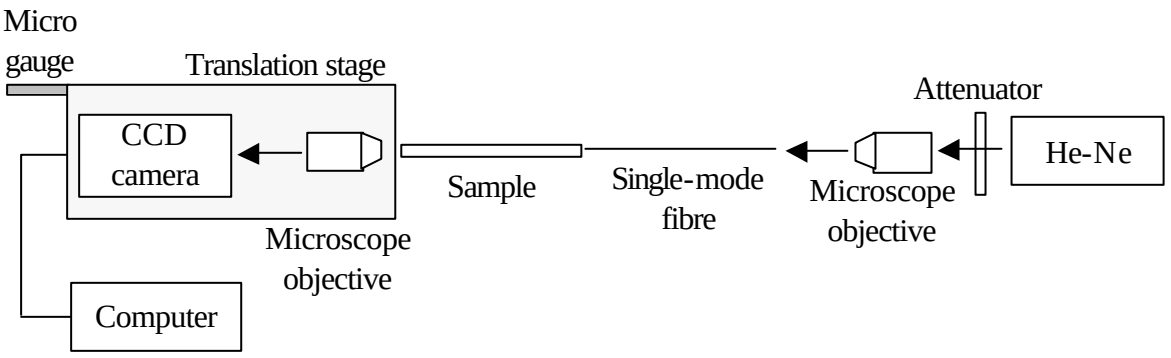

Figure 5.22 : NA measurement set up

NA can be obtained by measuring the spreading of the beam with distance, as shown in Figure 5.23. In the figure, NA is given by sin θ and for small θ, NA = sin $\theta \approx \tan \theta$.

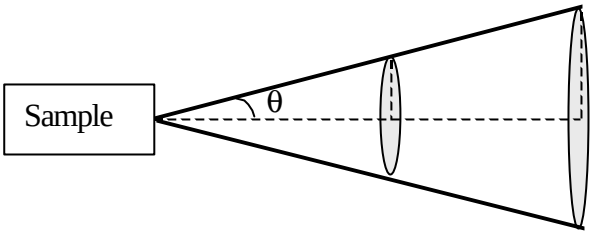

Figure 5.23 : Estimation of NA

Figure 5.24 shows the modal output from the waveguide written at a power of 150 mW and a scan speed of 80 μm/s using a 50X microscope objective. Characterisation of this waveguide showed an NA of 0.07 ($\Delta n \sim 1.6\times10^{-3}$) along the beam propagation direction and an NA of 0.02 ($\Delta n \sim 1.3\times10^{-4}$) in the direction perpendicular to the beam propagation.

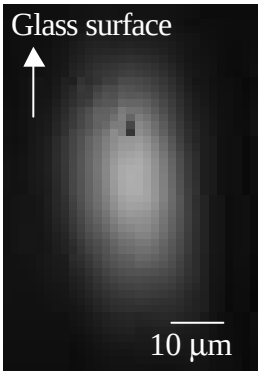

Figure 5.24 : Modal output of the waveguide written at 150 mW and 80 mm/s with a 50X objective

Figure 5.25 shows the cross-section and modal output of the waveguide written at a power of 270 mW and a scan speed of 80 μm/s using a 50X microscope objective. The high power used seemed to have damaged the waveguide. This caused densification around the rim of the immediate volume surrounding the laser focus spot, where light was guided.

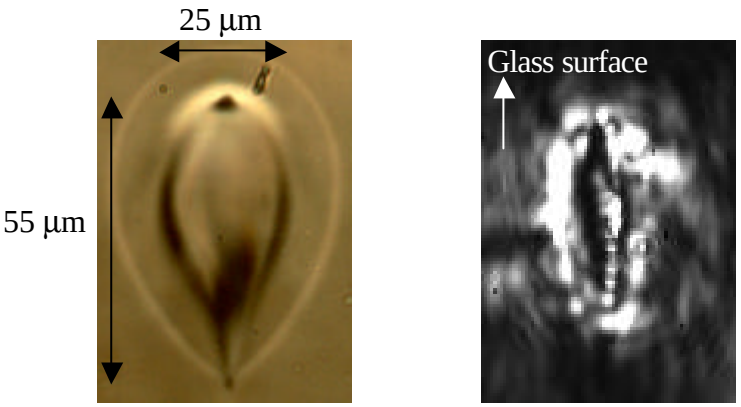

Figure 5.25 : (a) Cross-section and (b) modal output of the waveguide written at 270 mW and 80 mm/s with a 50X objective

5.7 Summary

A range of binary calcium phosphate, barium phosphate and sodium phosphate glasses at the ultraphosphate and metaphosphate compositions has been synthesised and their optical and thermal properties assessed. The glass transition temperatures of the calcium phosphate and barium phosphate glasses exhibited a minimum point and such behaviour can be explained by the transition of the ultraphosphate network from a network containing modifiers at isolated sites to a network with modifier sub-structures sharing terminal oxygens. When modifiers were initially added, the glass structure had to expand to accommodate these modifiers, leading to reduced density. In addition, the modifiers depolymerised the network, reducing the structural cross-linking density and weakening the glass structure. However, when the modifier content was high, the modifying cations must begin to share the available terminal oxygens, creating a more compact network and cross-linking the phosphate chains.

Generally, the refractive indices of the glasses should follow the same trend as the glass transition temperatures. However, the presence of water in the phosphate network has affected and changed the refractive indices of the glasses from that expected from the nominal compositions. This was due to the formation of (P-OH) bonds, converting bridging oxygens to non-bridging oxygens and thus depolymerising the phosphate structural network. The structural network

transition, apparently did not seem to affect the thermal expansion coefficients and thermo-optic coefficients of the glasses, where the systematic addition of modifiers led to the increase of the thermal expansion coefficient and the subsequent progress towards negative thermo-optic coefficient values.

dn/dT was strongly dependent on α and a value of $\alpha > 9\times10^{-6}$/°C was required for the calcium phosphate and barium phosphate glasses to exhibit negative *dn/dT*. Semi-empirical equations for the determination of *dn/dT* have been defined for the calcium phosphate and barium phosphate glasses. For the calcium phosphate glasses, the *dn/dT* for glasses within the composition range of $1.526 \leq n \leq 1.551$ and 8.60×10^{-6}/°C $\leq \alpha \leq 10.22\times10^{-6}$/°C can be deduced from $dn/dT = -2.088\alpha + 18.50$. For the barium phosphate glasses, the *dn/dT* for glasses within the composition range of $1.547 \leq n \leq 1.585$ and 11.62×10^{-6}/°C $\leq \alpha \leq 13.67\times10^{-6}$/°C can be deduced from $dn/dT = -2.104\alpha + 18.90$. The similarity of the two semi-empirical equations suggested that the electronic polarisability was dominated by the phosphate matrix. Based on this assumption, the semi-empirical equation can be generalised for any calcium phosphate and barium phosphate within 8.60×10^{-6}/°C $\leq \alpha \leq 13.67\times10^{-6}$/°C.

Device fabrication was carried out using the combination of *BaP-1c* and *KAP-1d* glasses as the core and clad, respectively. The extrusion process managed to produce a cane consisting only of the clad glass as the core glass crystallised at the extrusion temperature used. However, the fact that a cane was successfully extruded shows that this process can be used to produce the preform required for fibre drawing. The next step would be to use a combination of core and clad glasses that are closely matched in terms of their thermal properties.

The spin-coating process was used to deposit uniform glass layers on glass substrates and a 3-layer planar sample was successfully fabricated. However the sample had undergone a reduction process, the reason for this occurrence is still not fully understood, and there were cracks near the surface of the sample due to stresses. Nevertheless, the process can successfully deposit glass layers free of crystals. As with the extrusion process, improvement can be made by using compatible core and clad glasses and optimising the spin-coating parameters to minimise stresses in the glass layers.

Channels were written into the glasses using direct UV writing at 244 nm and direct femtosecond writing at 798 nm at different powers and writing speeds. Due to the weak absorption of the phosphate glasses at 244 nm, UV writing produced slab channels that had no waveguiding effect. This could be due to the small induced refractive index change. Femtosecond writing managed to produce some waveguides in the *KAP-1d* sample and an NA of 0.07 ($\Delta n \sim 1.6\times10^{-3}$) was obtained for the waveguide written at a power of 150 mW and a scan speed of 80 μm/s using a 50X microscope objective.

REFERENCES

1. W. Vogel, *"Optical properties of oxide glasses"*, Optical Properties of Glass, D.R. Uhlmann and N.J. Kreidl (Eds), The American Ceramic Society Inc., OH, (1991).

2. O.S. Shchavelev and V.A. Babkina, *"Properties of glasses of the systems P_2O_5-SrO and P_2O_5-BaO"*, Neorg. Mater. 6 (12), pp 2183-2186 (1970).

3. H.D. Park and E.R. Kreidler, *"Phase equilibria in the system La_2O_3- P_2O_5"*, Journal of The American Ceramic Society 67 (1), pp 23-26 (1984).

4. H. Ebendorff-Heidepriem, W. Seeber and D. Ehrt, *"Dehydration of phosphate glasses"*, Journal of Non-Crystalline Solids 163, pp 74-80 (1993).

5. A. Dietzel, *"Die kationenfeldstarken und ihre beziehungen zu entglasungsvorgangen, zur verbindungsbildung und zu den schmelzpunkten von silicaten"*, Z. Elektrochem. 48 (1), pp 9-23 (1942).

6. D. Ehrt and W. Seeber, *"Glass for high performance optics and laser technology"*, Journal of Non-Crystalline Solids 129, pp 19-30 (1991).

7. J.A. Duffy, *"Charge transfer spectra of metal ions in glass"*, Physics and Chemistry of Glasses 38 (6), pp 289 (1997).

8. D. Ehrt, P. Ebeling and U. Natura, *"UV transmission and radiation-induced defects in phosphate and fluoride-phosphate glasses"*, Journal of Non-Crystalline Solids 263&264, pp 240-250 (2002).

9. D. Ehrt, *"Redox behaviour of polyvalent ions in the ppm range"*, Journal of Non-Crystalline Solids 196, pp 304-308 (1996).

10. M. Born and E. Wolf, Principles of Optics, Chapter 2, Pergamon Press, Oxford, (1984).

11. U. Hoppe, *"A structural model for phosphate glasses"*, Journal of Non-Crystalline Solids 195, pp 138-147 (1996).

12. J.J. Hudgens and S.W. Martin, *"Glass transition and infrared spectra of low-alkali, anhydrous lithium phosphate glasses"*, Journal of The American Ceramic Society 76 (7), pp 1691-1696 (1993).

13. J.J. Hudgens, *"The structure and properties of anhydrous, alkali ultra-phosphate glasses"*, PhD Thesis, Iowa State University, 1994.

14. R.K. Brow, C.A. Click and T.M. Alam, *"Modifier coordination and phosphate glass networks"*, Journal of Non-Crystalline Solids 274, pp 9-16 (2000).

15. E. Kordes and H. Becker, *"Glaser der binaren Systeme von P_2O_5 mit CdO, Na_2O und Li_2O"*, Z. Anorg. Allgem. Chemie 260, pp 185-207 (1949).

16. P.E. Gray and L.C. Klein, *"The chemical durability of sodium ultraphosphate glasses"*, Glass Technology 24 (4), pp 202-206 (1983).

17. U. Hoppe, *"Short-range order of phosphate glasses studied by a difference approach using X-ray diffraction results"*, Journal of Non-Crystalline Solids 183, pp 85-91 (1995).

18. T. Minami and J.D. Mackenzie, *"Thermal expansion and chemical durability of phosphate glasses"*, Journal of The American Ceramic Society 60 (5-6), pp 232-235 (1977).

19. E. Hecht, Optics, Addison-Wesley, Massachusetts, (1998).

20. I.S. Gilev, Yu.N. Kondrat'ev and S.S. Safiullina, *"Effect of cladding thickness and the difference in the glass thermal expansion coefficients on the strength of lightguides"*, Soviet Journal of Optical Technology 52 (6), pp 349-352 (1985).

21. E. Roeder, *"Extrusion of glass"*, Journal of Non-Crystalline Solids 5, pp 377-388 (1971).

22. N.P. Bansal and R.H. Doremus, Handbook of glass properties, Chapter 9, Academic Press Inc, Orlando, (1986).

23. H. Hosono, T. Satake, M. Hosoe and Y. Abe, *"Reversible optical change of amorphous red phosphorus in reduced phosphate glasses"*, Journal of The American Ceramic Society 68 (1), pp 7-9 (1985).

24. W.C. Young, *"Roark's formulas for stress and strain"*, General Engineering Series, McGraw-Hill, NY, (1989).

25. J. Canning, *"Birefringence control in planar waveguides using doped top layers"*, Optics Communications 191, pp 225-228 (2001).

26. Schott glass catalogue – Product range 2000 (1998).

27. D.W.J. Harwood, *"Towards a 1.3mm planar neodymium doped fluoride glass waveguide amplifier"*, PhD thesis, Department of Electronic Engineering and Computer Science, University of Southampton, UK, 2000.

28. R. Osellame, S. Taccheo, M. Marangoni, R. Ramponi, P. Laporta, D. Polli, S. De Silvestri and G. Cerullo, *"Femtosecond writing of active optical waveguides with astigmatically shaped beams"*, Journal of the Optical Society of America B 20 (7), pp 1559-1567 (2003).

CHAPTER 6

BOROPHOSPHATE GLASSES

6.1 Introduction

This chapter reviews the properties of some borophosphate glasses prepared in this work. B_2O_3 [1,2] and P_2O_5 [3], due to their negative *dn/dT*, had previously been co-doped with germanosilicate core fibres to minimise $d\lambda_B/dT$. Pure phosphate, pure borate, barium metaphosphate and sodium metaphosphate glasses exhibit negative *dn/dT* [4]: -92.2×10^{-6}/°C, -35.0×10^{-6}/°C, -10.6×10^{-6}/°C and -15×10^{-6}/°C, respectively. Hence barium borophosphate and sodium borophosphate glasses can be potentially used for fabricating athermal devices, by tailoring the compositions to obtain the required *n*, α and *dn/dT*.

In this work, the compositional effects of barium borophosphate glasses (designated as BaBP) and sodium borophosphate glasses (designated as NaBP) on their optical and thermal properties were assessed. Two series of BaBP glasses and a series of NaBP glasses were examined to determine, first, the effect of adding B_2O_3 to phosphate glasses; second, the change in properties as the glass composition changed from a phosphate-rich composition to a borate-rich composition and, third, the minimum α required to obtain negative *dn/dT* in the BaBP and NaBP series.

6.2 Glass Preparation

Two series of BaBP glasses and a series of NaBP glasses were synthesised, corresponding to (mol%) :

- BaBP series 1 : $50BaO\text{-}xB_2O_3\text{-}(50\text{-}x)P_2O_5$ with $5 \le x \le 20$
- BaBP series 2 : $(100\text{-}x)Ba(PO_3)_2\text{-}xB_2O_3$ with $10 \le x \le 60$
- NaBP : $(100\text{-}x)NaPO_3\text{-}xB_2O_3$ with $10 \le x \le 50$

Glasses were melted in platinum crucibles, covered with a platinum lid, using high-purity powder of $BaCO_3$ (99.95%), Na_2CO_3 (99.5%), B_2O_3 (99.98%) and P_2O_5 (99.99%), according to the melting process described in Section 3.1.1. The mixtures were melted in an oxygen atmosphere for 60 minutes at temperatures between 1200°C and 1300°C, depending on the glass compositions. The melts were then cast into a graphite mould and annealed in air for 60 minutes near the respective glass T_g before being cooled at a rate of 0.5°C/min to room temperature.

Table 6.1 shows the batch compositions of the BaBP and NaBP glasses that were melted while Figure 6.1 shows the BaBP and NaBP glass melting region for this work.

Sample	**Batch composition (mol%)**		
	BaO	**B_2O_3**	**P_2O_5**
BaBP-1a	50	5	45
BaBP-1b	50	8	42
BaBP-1c	50	10	40
BaBP-1d	50	12	38
BaBP-1e	50	15	35
BaBP-1f	50	20	30
Sample	**$Ba(PO_3)_2$**	**B_2O_3**	
BaBP-2a	90	10	
BaBP-2b	80	20	
BaBP-2c	70	30	
BaBP-2d	60	40	
BaBP-2e	50	50	
BaBP-2f	40	60	
Sample	**$NaPO_3$**	**B_2O_3**	
NaBP-1a	90	10	
NaBP-1b	80	20	
NaBP-1c	70	30	
NaBP-1d	60	40	
NaBP-1e	50	50	

Table 6.1 : Batch compositions of BaBP and NaBP glasses

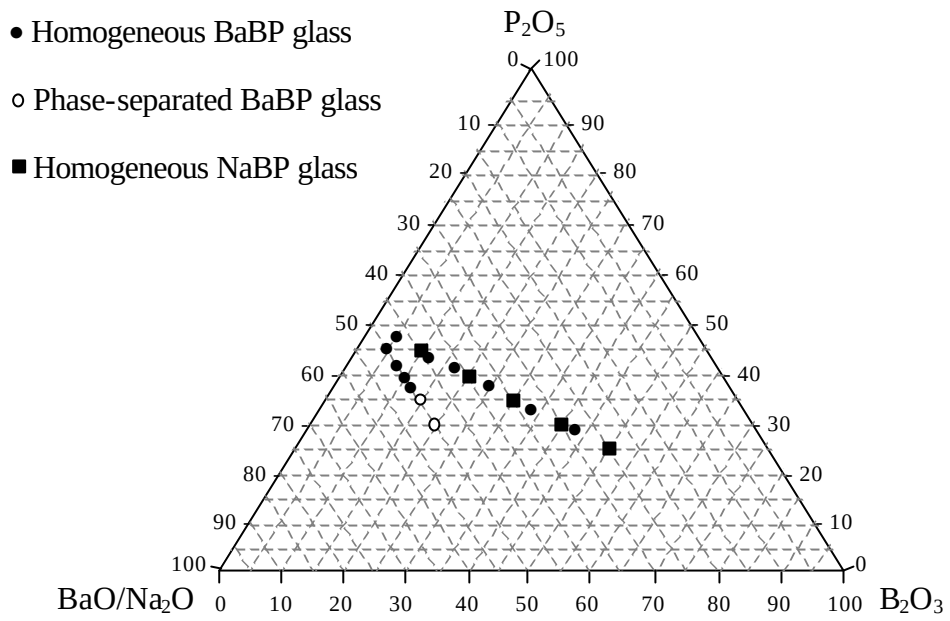

Figure 6.1 : BaBP and NaBP glass melting

6.3 Property Measurements

Before any characterisation work was done, the glass samples were first polished, using the procedures described in Section 3.1.2. The descriptions and the principles of the instruments used for characterisation are described in Chapter 3.

T_g, T_x and T_p were determined using a DTA at a heating rate of 10°C/min. α was measured in the temperature range of 50 - 120°C with a TMA at a heating rate of 5°C/min. n was measured using an Abbe '60' refractometer at the sodium D-line (λ = 589.3nm) at room temperature.

dn/dT measurements were performed on polished glass samples approximately 10 mm thick using the interferometer set-up detailed in Section 3.4. Spectroscopic analysis in the UV was carried out using a UV/Vis/NIR spectrophotometer in the 190 – 500 nm range while relative OH concentration was determined using an FTIR spectrophotometer in the 2000 - 5000 cm^{-1} range. Both UV and IR analysis were performed on 2 mm thick samples.

6.4 Results and Discussion

The properties of the BaBP and NaBP glasses are given in Tables 6.2 and 6.3. The *NaBP-1e* sample *dn/dT* was not measured as the glass was hygroscopic, where the coarse and non-transparent appearance of the glass surfaces prevented any measurement.

Sample	**Batch composition (mol%)**			T_g **(°C)**	T_x **(°C)**	T_p **(°C)**	α **(´ 10^{-6}/°C) (50 - 120°C)**
	BaO	**B_2O_3**	**P_2O_5**				
BaBP-1a	50	5	45	507	706	740	13.23
BaBP-1b	50	8	42	545	729	762	12.52
BaBP-1c	50	10	40	565	748	787	12.23
BaBP-1d	50	12	38	586	749	809	11.58
BaBP-1e	50	15	35	Phase-separated sample			
BaBP-1f	50	20	30	Phase-separated sample			
Sample	**$Ba(PO_3)_2$**	**B_2O_3**		T_g **(°C)**	T_x **(°C)**	T_p **(°C)**	α **(´ 10^{-6}/°C) (50 - 120°C)**
BaBP-2a	90	10		497	705	778	12.63
BaBP-2b	80	20		533	783	825	11.63
BaBP-2c	70	30		571	802	848	10.48
BaBP-2d	60	40		596	848	871	9.42
BaBP-2e	50	50		589	810	864	7.53
BaBP-2f	40	60		564	806	844	5.68
Sample	**$NaPO_3$**	**B_2O_3**		T_g **(°C)**	T_x **(°C)**	T_p **(°C)**	α **(´ 10^{-6}/°C) (50 - 120°C)**
NaBP-1a	90	10		358	540	622	19.91
NaBP-1b	80	20		415	600	660	16.70
NaBP-1c	70	30		445	613	675	13.43
NaBP-1d	60	40		450	645	689	11.57
NaBP-1e	50	50		439	650	707	11.20

Table 6.2 : Thermal properties of BaBP and NaBP glasses

Sample	**Batch composition (mol%)**			***n*** **(*l* = 589.3 nm)**	***dn/dT* (´ 10^{-6}/°C) (*l* = 632.8 nm, 20 - 100°C)**	r_{OH} **(*cm*$^{-1}$)**
	BaO	**B_2O_3**	**P_2O_5**			
BaBP-1a	50	5	45	1.600	-9.27	9.88
BaBP-1b	50	8	42	1.604	-8.97	7.46
BaBP-1c	50	10	40	1.606	-7.82	6.93
BaBP-1d	50	12	38	1.610	-7.52	6.38
BaBP-1e	50	15	35	Phase-separated sample		
BaBP-1f	50	20	30	Phase-separated sample		
Sample	**$Ba(PO_3)_2$**	**B_2O_3**		***n*** **(*l* = 589.3 nm)**	***dn/dT* (´ 10^{-6}/°C) (*l* = 632.8 nm, 20 - 100°C)**	r_{OH} **(*cm*$^{-1}$)**
BaBP-2a	90	10		1.591	-8.45	17.88
BaBP-2b	80	20		1.593	-7.26	14.38
BaBP-2c	70	30		1.594	-5.01	13.79
BaBP-2d	60	40		1.596	-3.68	15.43
BaBP-2e	50	50		1.592	-0.69	21.96
BaBP-2f	40	60		1.589	+2.72	37.79
Sample	**$NaPO_3$**	**B_2O_3**		***n*** **(*l* = 589.3 nm)**	***dn/dT* (´ 10^{-6}/°C) (*l* = 632.8 nm, 20 - 100°C)**	r_{OH} **(*cm*$^{-1}$)**
NaBP-1a	90	10		1.490	-12.75	18.05
NaBP-1b	80	20		1.501	-8.43	15.61
NaBP-1c	70	30		1.511	-3.61	14.28
NaBP-1d	60	40		1.512	-2.36	27.44
NaBP-1e	50	50		1.511	Not measured	38.14

Table 6.3 : Optical properties of BaBP and NaBP glasses

The results for the BaBP and NaBP glasses are also shown in Figures 6.2 to 6.10. In Figures 6.2 to 6.4, 6.6 and 6.7, lines are drawn as guides to the eye. Barium metaphosphate (*BaP-1c*) and sodium metaphosphate (*NaP-1a*) glasses from Chapter 5 are included in the figures for comparison purposes.

6.4.1 Refractive Index and Glass Transition Temperature

The refractive indices of the BaBP and NaBP glasses as a function of the B/(B+P) ratio are shown in Figures 6.2a and 6.2b, respectively. Figure 6.2a shows that the addition of B_2O_3 increased the glass *n* at low boron concentrations (BaBP series 1 and 2 glasses). However, as the amount of B_2O_3 increased further, the results of BaBP series 2 showed that *n* reached a maximum at around B/(B+P) = 0.4 and then decreased for higher boron concentrations. Figure 6.2b shows a similar trend for the NaBP glasses as that observed for the BaBP series 2 glasses, with a maximum point observed at around B/(B+P) = 0.6. By comparing Figures 6.2a and 6.2b, it can be seen that BaBP glasses had higher *n* than NaBP glasses. This was due to the larger size of the Ba^{2+} ion compared to Na^{+}, making Ba^{2+} more polarisable and consequently higher *n*, as expected from the Lorentz-Lorenz equation [5].

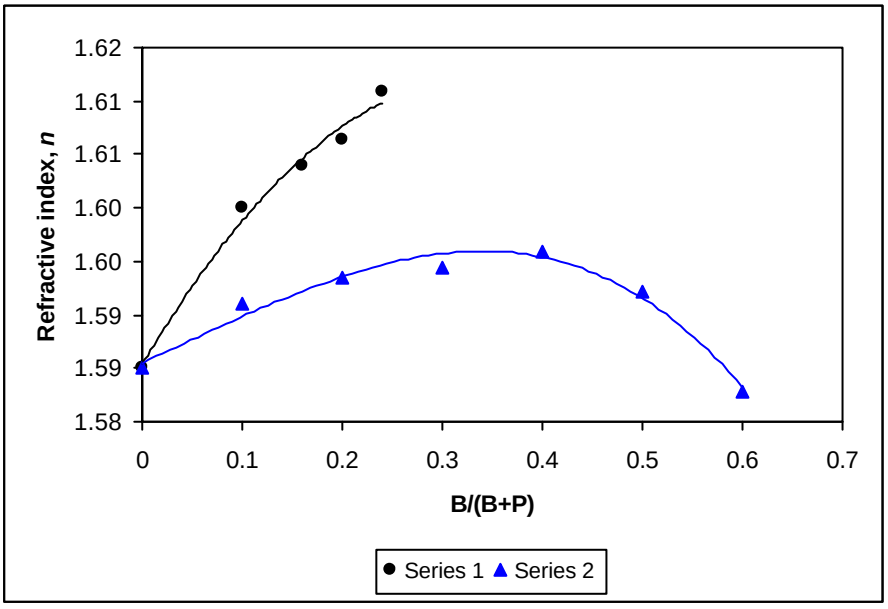

Figure 6.2a : Refractive index (*n*) of BaBP glasses, measured at *l* = 589.3 nm.

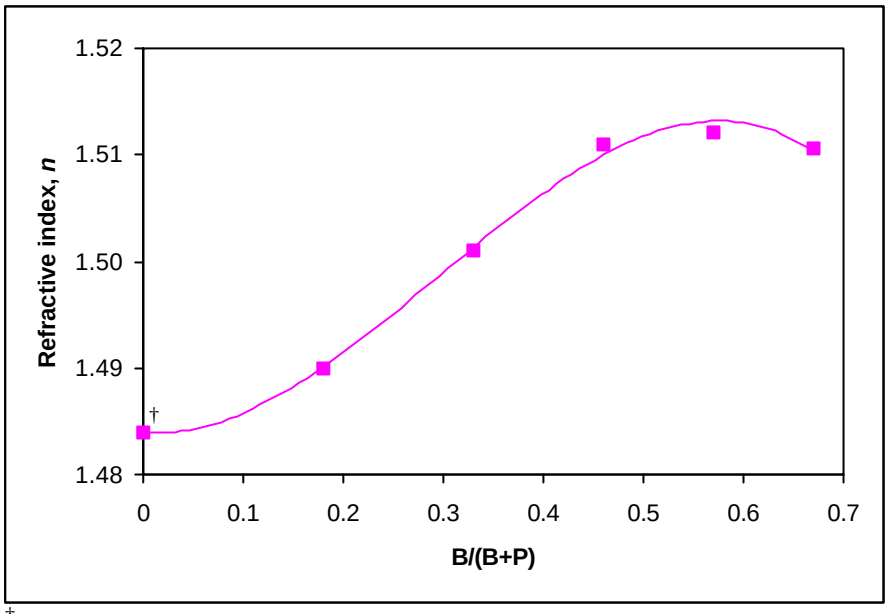

† n_e (measured at λ = 546.1 nm) [6]

Figure 6.2b : Refractive index (n) of NaBP glasses, measured at λ = 589.3 nm.

Figures 6.3a and 6.3b show the changes in the T_g of the BaBP and NaBP glasses, respectively, as the B/(B+P) ratio increases. The T_g of the BaBP series 1 glasses increased with increasing boron content throughout the range of composition studied. As with the case for n, the T_g of the BaBP series 2 and NaBP glasses increased to a peak value at B/(B+P) = 0.4 and B/(B+P) = 0.6, respectively, before T_g started to decrease as more boron was added. The presence of a maximum point has also been observed for the T_g of calcium borophosphate glasses [7].

Previous structural studies of borophosphate glasses [8-11] show that boron atoms exist as either tetrahedral units, B(4), or trigonal units, B(3), within the glass network, depending on glass compositions. It was found that B(4) units dominate at compositions with high phosphate content (phosphate-rich) while B(3) units dominate at compositions with high boron content (borate-rich).

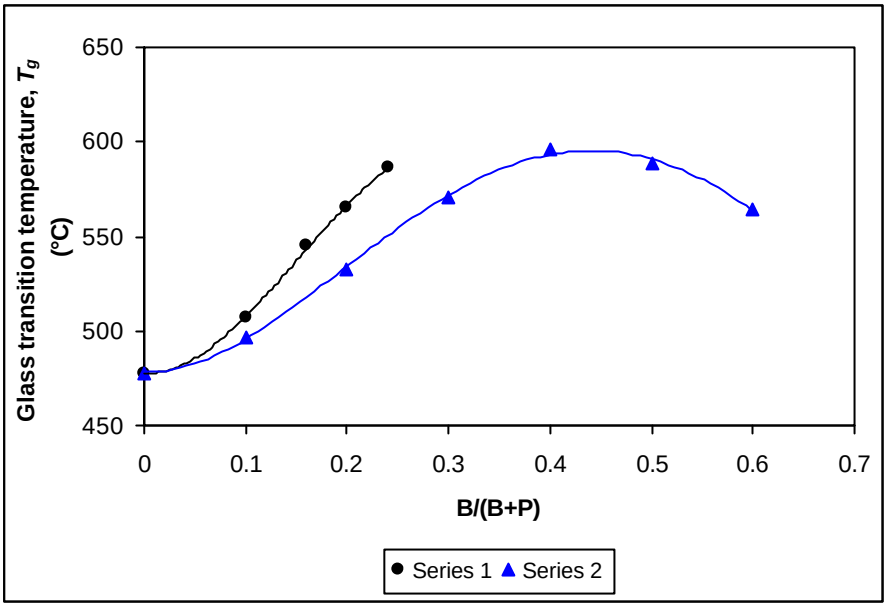

Figure 6.3a : Glass transition temperature (T_g) of BaBP glasses

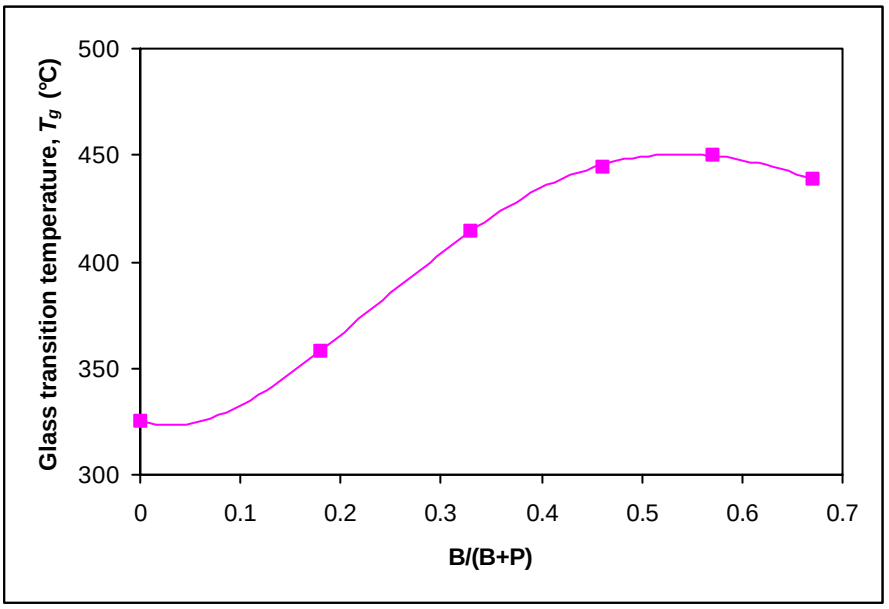

Figure 6.3b : Glass transition temperature (T_g) of NaBP glasses

The addition of B_2O_3 led to the formation of (B-O-P) bridging bonds that cross-linked the phosphate chains. These (B-O-P) bonds were associated with the B(4) units as these units dominated at low boron (phosphate-rich) compositions. The (B-O-P) bridging bonds polymerised the glass network and increased the packing density of atoms, creating a more compact borophosphate network. This led to increased density and the subsequent increase in *n*.

The increase in the boron content also increased the T_g of the glasses at compositions with low boron content. The T_g of a glass is dependent on the covalent cross link density and metal-oxygen cross link strength [9]. Therefore, the increase in T_g was due to the increase in the structural cross-linking density of the glass network, caused by the (B-O-P) bridging bonds. For the BaBP series 2 and NaBP glasses, in addition to the polymerisation effect of boron on the glass network, the substitution of B_2O_3 for either BaO or NaO resulted in the replacement of stronger covalent (B-O-P) bonds for the ionic (Ba-O-P) or (Na-O-P) bonds, thus increasing the structural strength of the glass. This was because B^{3+} has a higher field strength than Ba^{2+} and Na^{+} [12].

Both n and T_g of the BaBP series 2 and NaBP glasses exhibited a maximum before decreasing as more boron was added. Such behaviour generally corresponded to a structural network change in terms of bonding. As the concentrations of boron increased further, B(3) units became the preferred coordination in borate-rich compositions, compared to the preferred B(4) units in phosphate-rich compositions. This resulted in a structural change from a disordered borophosphate network to a borate network and also a reduction in the (B-O-P) bridging bonds as the boron content increased. This decreased the density of the glass as well as the cross-linking density and hence weakened the glass network. Therefore, both n and T_g decreased with the addition of boron at borate-rich compositions. The crossover point for this structural change from a borophosphate network to a borate network is indicated by the maximum point observed at B/(B+P) = 0.4 for the BaBP series 2 glasses and B/(B+P) = 0.6 for the NaBP glasses.

6.4.2 Thermal Expansion Coefficient and Thermo-optic Coefficient

α and dn/dT of the BaBP and NaBP glasses are shown in Figures 6.4a and 6.4b. There seemed to be no evidence of any maximum or minimum point throughout the range of BaBP and NaBP glasses examined, in contrast to the maximum peak observed for both n and T_g when the glass network crossed from a rigid borophosphate structure to a borate network.

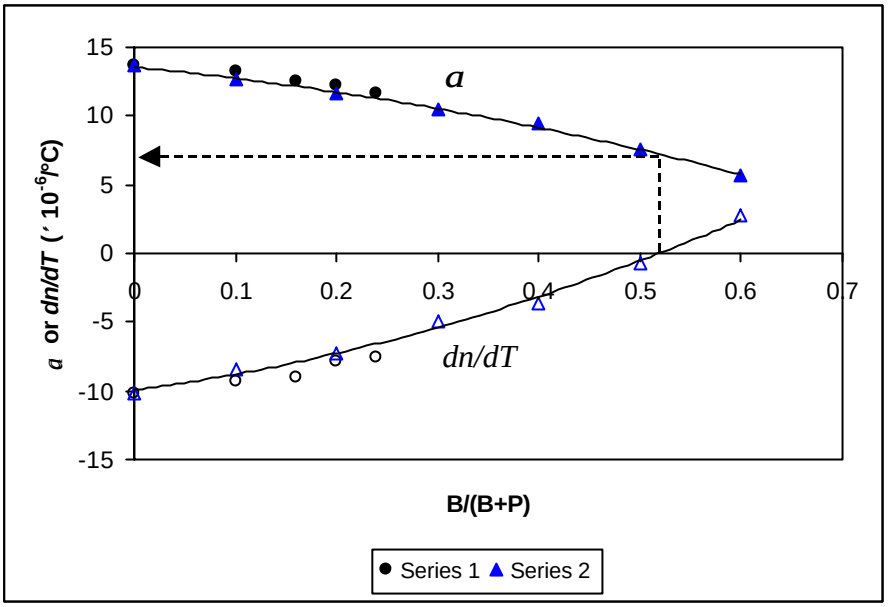

Figure 6.4a : α and *dn/dT* of BaBP glasses as a function of B/(B+P) ratio (α measured over 50 - 120°C, *dn/dT* measured at λ = 632.8 nm over 20 – 100 °C)

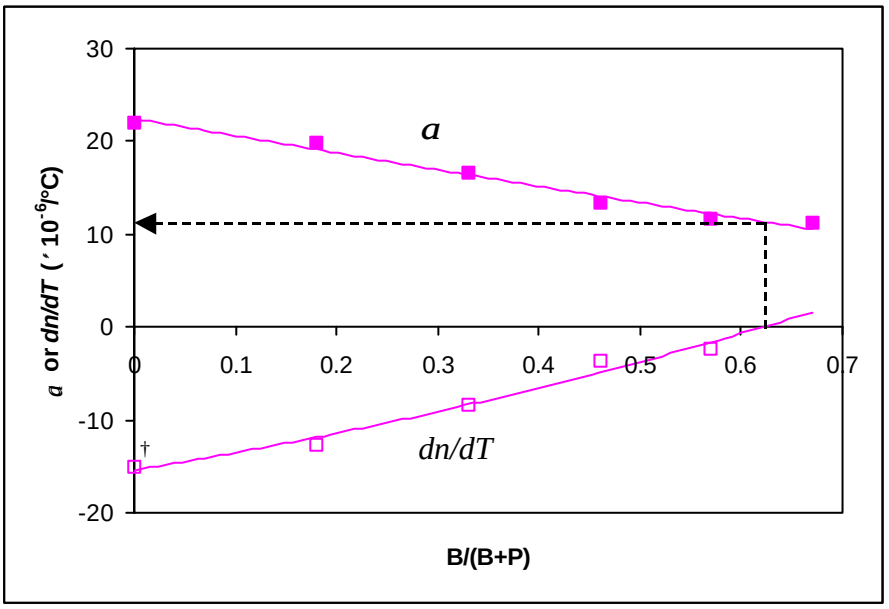

† [4]

Figure 6.4b : α and *dn/dT* of NaBP glasses as a function of B/(B+P) ratio (α measured over 50 - 120°C, *dn/dT* measured at λ = 632.8 nm over 20 – 100 °C)

The addition of boron made the glass network highly cross-linked and hence led to a decrease in the α of the glasses. At the same time, the *dn/dT* of the glasses changed to positive values, as shown in Figure 6.4a and 6.4b. Comparison of the results for BaBP and NaBP glasses showed that BaBP glasses had smaller α values compared to NaBP. This was due to the higher field

strength of Ba^{2+} compared to Na^{+}, thus, Ba^{2+} cations formed stronger bonds with the NBOs.

The results for *dn/dT* can be explained in terms of α via equation (1.15), which can be derived from the Lorentz-Lorenz equation, as described in Section 1.4.

$$\frac{dn}{dT} = A\left[\frac{d(\ln P_e)}{dT} - 3\alpha\right] \tag{1.15}$$

where $A = [(n^2-1)(n^2+2)/6n]$. As stated earlier, the addition of boron decreases α, and as α decreases, $d(\ln P_e)/dT$ will become more dominant such that $d(\ln P_e)/dT > 3\alpha$, resulting in positive *dn/dT*. Figures 6.4a and 6.4b also show that in order to obtain negative *dn/dT*, BaBP glasses must exhibit $\alpha > 7.5\times10^{-6}$/°C while NaBP glasses must exhibit $\alpha > 11.5\times10^{-6}$/°C.

dn/dT values of the BaBP and NaBP glasses have been estimated from the β_i of each glass component (Table 2.4) and equation (2.5), as discussed in Section 2.2. The data were compared against the experimentally measured *dn/dT*, as shown in Figure 6.5. There were offsets between the measured and estimated *dn/dT* results, although both sets of data showed a similar trend where *dn/dT* of the glasses changed to positive values as the B/(B+P) ratio increased. The differences could be due to the limitations associated with using such methods to estimate *dn/dT*, as discussed in Section 2.2. Also, the β_i value for boron has been estimated without considering the change of the coordination number of B^{3+} with glass composition.

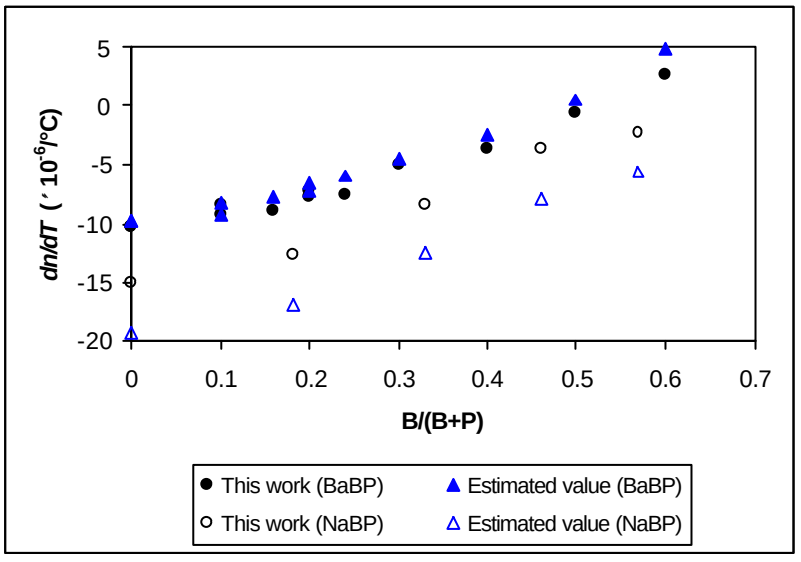

Figure 6.5 : Comparison of measured and estimated *dn/dT* of BaBP and NaBP glasses

Figures 6.6a and 6.6b show the linear relationship between *dn/dT* and α for the BaBP and NaBP glasses, respectively. Based on these relationships, semi-empirical equations for *dn/dT* can be obtained, enabling the estimation of the *dn/dT* of any BaBP glasses within $1.585 \leq n \leq 1.610$ and $5.68\times10^{-6}/°C \leq \alpha \leq 13.67\times10^{-6}/°C$ and any NaBP glasses within $1.484 \leq n \leq 1.512$ and $11.20\times10^{-6}/°C \leq \alpha \leq 22.03\times10^{-6}/°C$. The values for *n* were quoted for λ = 589.3 nm, the values for α were quoted over 50 - 120°C and *dn/dT* values were measured at λ = 632.8 nm over 20 - 100°C.

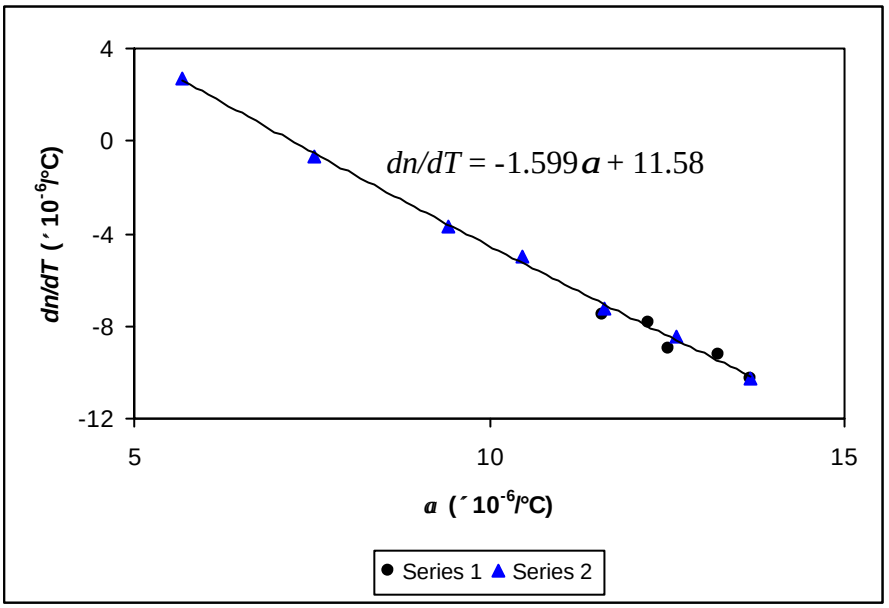

Figure 6.6a : *dn/dT* of BaBP glasses as a function of α

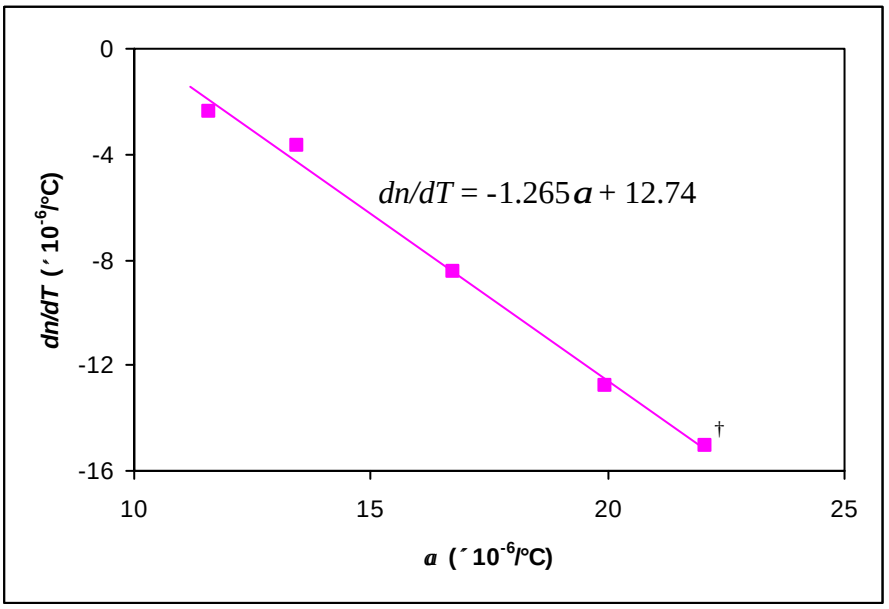

† *dn/dT* from ref [4]

Figure 6.6b : *dn/dT* of NaBP glasses as a function of α

Equation (1.15) can also be represented in another form, as described in Section 1.4. This new expression is shown as equation (1.16).

$$\frac{dn}{dT} = A(g - 3)\alpha \qquad (1.16)$$

In order to obtain negative *dn/dT*, g must be less than 3. The g values for the BaBP and NaBP glasses are plotted in Figure 6.7, and found to be $1.95 \leq g \leq 3.67$ for the BaBP glasses and $1.80 \leq g \leq 2.66$ for the NaBP glasses. The results showed that in order to obtain negative *dn/dT*, the BaBP glasses must have a B/(B+P) ratio of less than 0.52 (equivalent to 52 mol% B_2O_3) while NaBP glasses must have a B/(B+P) ratio of less than 0.66 (equivalent to ~ 49 mol% B_2O_3).

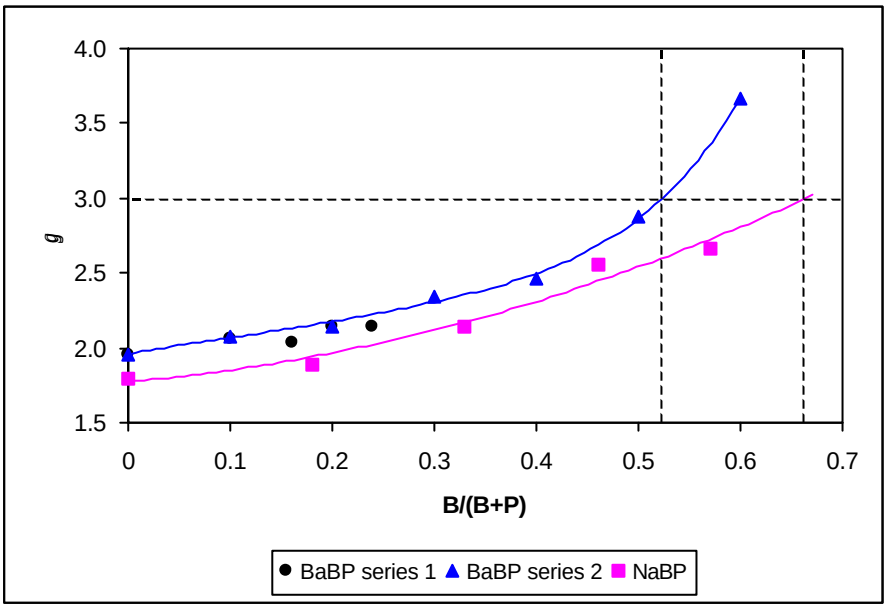

Figure 6.7 : *g* of BaBP and NaBP glasses as a function of B/(B+P) ratio

6.4.3 OH Content and UV Spectrum

The relative OH content of the BaBP and NaBP glasses are given in Table 6.3. From the results for the BaBP series 1 glasses, it can be seen that the addition of B_2O_3 reduced the relative OH content. This was due to the fact that the B^{3+} ions formed bridging bonds that cross-linked the phosphate chains, improving the chemical durability of the glass [13].

For the BaBP series 2 and NaBP glasses, the relative OH content of the glasses decreased upon the initial addition of boron until it reached a minimum before increasing with further boron addition. The minimum point observed for the relative OH content coincided with the maximum points observed for both n and T_g. As stated earlier, B(4) units dominated at phosphate-rich compositions, forming (B-O-P) bridging bonds, while B(3) units dominated at borate-rich compositions. The formation of (B-O-P) bonds reduced the number of phosphate NBOs, thus minimising the formation of (P-OH) bonds. Hence the relative OH content of the glasses decreased. However, as the amount of B_2O_3 increased, the glass network changed from a borophosphate network to a borate network. The number of (B-O-P) bonds between phosphate chains was reduced and the network became less resistant to hydrolysis. This accounted for the increase in the relative OH content at high boron content. Figure 6.8 shows the IR transmission spectra through the BaBP series 2 glasses with different B_2O_3 content.

Generally NaBP glasses had higher relative OH content compared to the BaBP glasses with similar boron content. This was due to the lower field strength of Na^+, compared to Ba^{2+} [12].

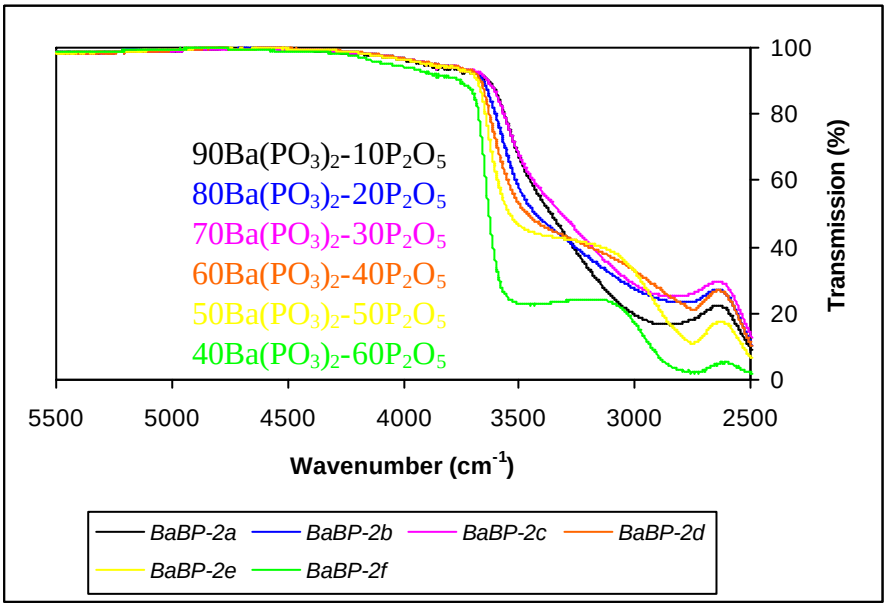

Figure 6.8 : Infrared transmission spectra through (100-x)$Ba(PO_3)_2$-xB_2O_3 glasses. The spectra are normalised for a 1 mm thick sample and corrected for Fresnel loss.

Figures 6.9 and 6.10 show the UV transmission and UV absorption, respectively, of some BaBP series 2 glasses. The UV edge of a glass depends on the electronic band gap transitions, which are influenced by the structure and bonding in the glass network [14,15]. From the inset shown in Figure 6.9, it can be seen that the UV edge shifted towards lower wavelengths before shifting again towards higher wavelength as the boron content increased. Bartholomew [16] found that as the number of NBOs decreases, the UV edge shifted to a lower wavelength. At low boron content, the addition of boron shifted the UV edge to lower wavelengths due to the higher degree of cross-linking and BO bonds in the glass network, through the formation of (B-O-P) bridging bonds. As the boron content increased further, B(3) units replaced B(4) units and the number of (B-O-P) bridging bonds decreased. Hence, the number of NBOs increased, shifting the UV edge to higher wavelengths. Such observation has also been noted in the literature [7,17].

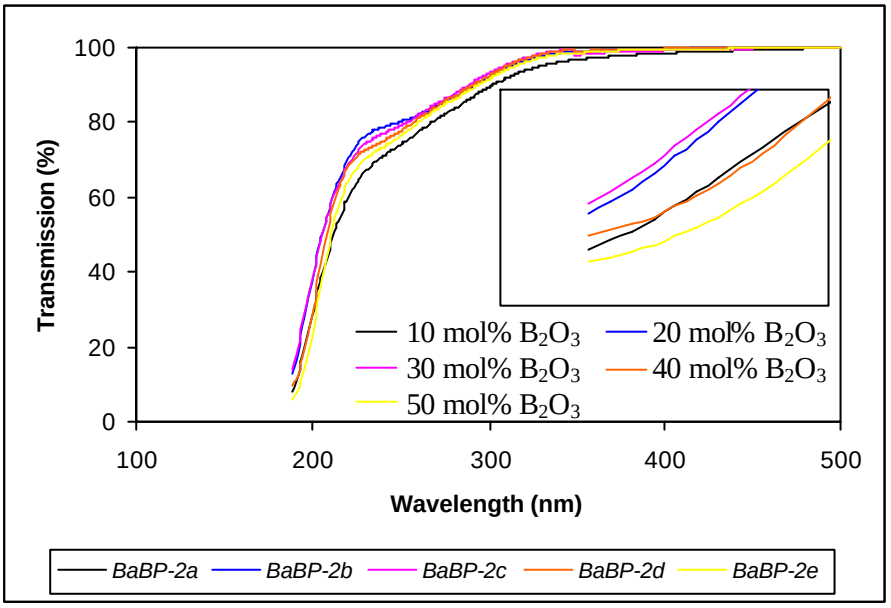

Figure 6.9 : Ultraviolet transmission spectra through (100-*x*)$Ba(PO_3)_2$-*x*B_2O_3 glasses. The spectra are normalised for a 1 mm thick sample and corrected for Fresnel loss. Inset : Transmission spectra near 190 nm.

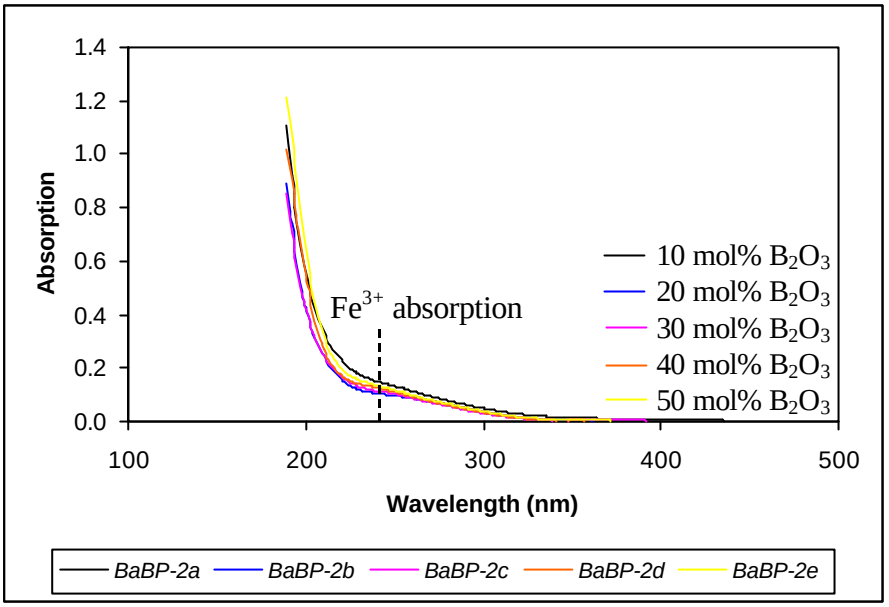

Figure 6.10 : Ultraviolet absorption spectra through (100-*x*)$Ba(PO_3)_2$-*x*B_2O_3 glasses. The spectra are normalised for a 1 mm thick sample and corrected for Fresnel loss.

6.4.4 Athermalisation

The athermalisation principle set out in Section 1.3 shows that glasses must exhibit negative *dn/dT* in order to satisfy the athermal condition of equation (1.3), due to the positive α value. The athermalisation parameters for the BaBP and NaBP glasses are given in Table 6.4, which shows most of the glasses investigated exhibited negative *dn/dT*. Therefore, these borophosphate glasses have application potential in athermalisation work.

Sample	**Composition (mol%)**			***dn/dT*** **(´ 10^{-6}/°C)**	***nα*** **(´ 10^{-6}/°C)**	***(1/L)(dS/dT)*** **(´ 10^{-6}/°C)**
	BaO	**B_2O_3**	**P_2O_5**			
BaBP-1a	50	5	45	-9.27	21.18	11.91
BaBP-1b	50	8	42	-8.97	20.08	11.11
BaBP-1c	50	10	40	-7.82	19.64	11.82
BaBP-1d	50	12	38	-7.52	18.66	11.13
BaBP-1e	50	15	35	Phase-separated sample		
BaBP-1f	50	20	30	Phase-separated sample		
Sample	**$Ba(PO_3)_2$**	**B_2O_3**		***dn/dT*** **(´ 10^{-6}/°C)**	***nα*** **(´ 10^{-6}/°C)**	***(1/L)(dS/dT)*** **(´ 10^{-6}/°C)**
BaBP-2a	90	10		-8.45	20.09	11.65
BaBP-2b	80	20		-7.26	18.53	11.27
BaBP-2c	70	30		-5.01	16.70	11.69
BaBP-2d	60	40		-3.68	15.03	11.35
BaBP-2e	50	50		-0.69	11.99	11.30
BaBP-2f	40	60		+2.72	9.00	11.72
Sample	**$NaPO_3$**	**B_2O_3**		***dn/dT*** **(´ 10^{-6}/°C)**	***nα*** **(´ 10^{-6}/°C)**	***(1/L)(dS/dT)*** **(´ 10^{-6}/°C)**
NaBP-1a	90	10		-12.75	29.67	16.92
NaBP-1b	80	20		-8.43	25.07	16.64
NaBP-1c	70	30		-3.61	20.29	16.68
NaBP-1d	60	40		-2.36	17.49	15.13
NaBP-1e	50	50		nm	16.92	-
Silica [4]				+10.40	0.80	11.20

Table 6.4 : Athermalisation parameters of BaBP and NaBP glasses

However, Table 6.4 shows that the bulk glasses were not athermal on their own as their 1/*L(dS/dT)* values were not zero. From the results, there are four highlighted samples that showed comparable 1/*L(dS/dT)* values to that of silica. As the bulk glasses were not athermal, two or more glasses must be used together to obtain the required properties for the fabrication of athermal devices. The way this method works has been previously described in Section 4.4.5.

6.5 Device Fabrication

This section describes the fabrication of planar devices and fibres using the borophosphate glasses developed. As described in Section 5.5, the combination of core and clad glasses used must be such that the combined core and clad dn/dT produces $dn_{eff}/dT < 0$ and the α of the fibre cladding glass or planar device substrate is low. These conditions reduce the temperature sensitivity of the device.

Assuming $V = 2.405$ (single-mode operation), $\lambda_{cut\text{-}off} = 1000$ nm and $\lambda_B = 1040$ nm, the possible combinations of borophosphate glasses for fibre fabrication are presented in Table 6.5. The parameters were determined using the analysis for FBGs set out in Section 1.3.3. The choice of λ_B was decided by the refractive index of the glasses, the availability of the appropriate grating phase mask and the available source.

Core	Clad	NA	n_{eff}	dn_{eff}/dT (´ 10^{-6}/°C)	$(T_g)_{co} - (T_g)_{cl}$ (°C)	$\alpha_{co} - \alpha_{cl}$ (´ 10^{-6}/°C)	$d\lambda_B/dT$ (pm/°C)
BaBP-1a	*KAP-1d*	0.526	1.557	-6.73	-36	4.52	4.56
BaBP-1b	*KAP-1d*	0.538	1.559	-6.50	2	3.81	4.72
	KAP-1e	0.516	1.563	-6.22	-76	4.85	3.84
	BaBP-2c	0.175	1.599	-8.18	-26	2.04	5.58
	BaBP2d	0.161	1.600	-7.94	-51	3.10	4.63
BaBP-1c	*KAP-1e*	0.523	1.564	-5.26	-56	4.56	4.48
BaBP-1d	*BaBP-2e*	0.244	1.602	-6.15	-3	4.05	3.84

Table 6.5 : Combination of core and clad glasses using KAP and BaBP glasses

During the previous extrusion trial involving the combination of *BaP-1c* and *KAP-1d* in Section 5.5.1.2, the process was unsuccessful because of crystallisation in the core glass. This occurred due to the mismatch of T_g and T_s between the core and clad glasses, where the difference between the T_g of the core and clad, ($T_{g,co}$ - $T_{g,cl}$), was -65°C. As for the planar waveguide fabrication, detailed in Section 5.5.2, there were cracks in the spin-coated core and overclad layers because of the large (α_{co} - α_{cl}), which was approximately 5×10^{-6}/°C.

Hence, for this part of the work, an attempt was made to match both the T_g and α of the core and clad glasses as close as possible without compromising the temperature sensitivity of the Bragg wavelength too much. From Table 6.5, the combination of *BaBP-1b* and *BaBP-2c* was chosen, which should produce $d\lambda_B/dT$ ~ 5.6 pm/°C (7.4 pm/°C at λ_B = 1.3 μm and 9.2 pm/°C at λ_B = 1.55 μm). This combination offered ($T_{g,co}$ - $T_{g,cl}$) = -26°C and (α_{co} - α_{cl}) ~ 2×10^{-6}/°C, which were favourable conditions for preventing cracks as well as crystallisation in either glass at the extrusion temperature (equivalent to T_s). Furthermore, the fibre was ideal for single mode operation as its NA was about 0.18. It should be noted that all $d\lambda_B/dT$ values were calculated based on the measured results of n at λ = 589.3 nm, α over 50 – 120 °C and dn/dT at λ = 632.8 nm over 20 – 100 °C. Figure 6.11 shows the transmission spectra for the *BaBP-1b* (core) and *BaBP-2c* (clad) glasses, collected using a UV/Vis/NIR spectrophotometer in the 190 – 3300 nm range.

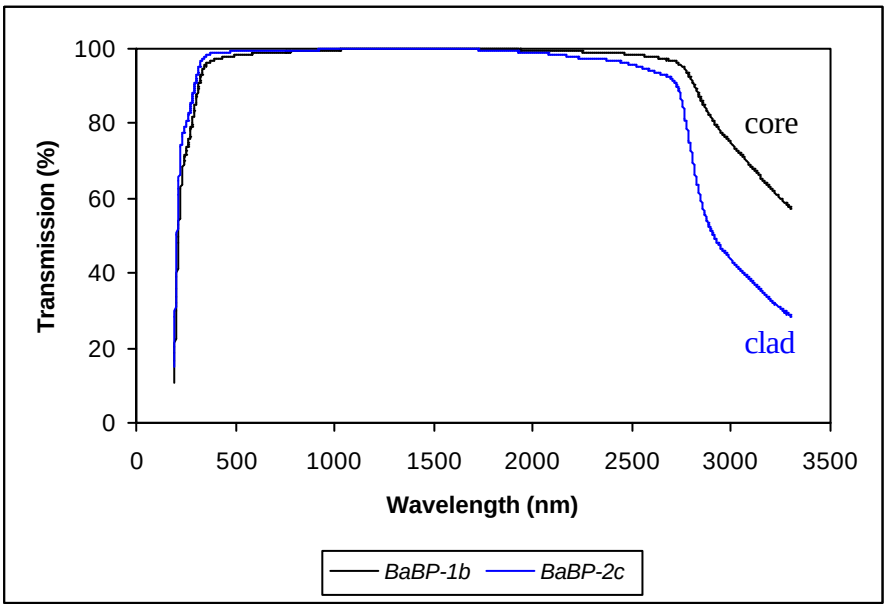

Figure 6.11 : Transmission spectra through *BaBP-1b* (core) and *BaBP-2c* (clad) glasses. The spectra are normalised for a 1 mm thick sample and corrected for Fresnel loss

6.5.1 Fibre Fabrication

This section describes the extrusion work and the fibre drawing process involving the chosen combination of *BaBP-1b* (core) and *BaBP-2c* (clad) glasses.

6.5.1.1 Extrusion

The *BaBP-1b* glass had the composition $50BaO\text{-}8B_2O_3\text{-}42P_2O_5$ with properties of $n_{co} = 1.604$, $\alpha_{co} = 12.52\times10^{-6}/°C$ and $dn/dT_{co} = -8.97\times10^{-6}/°C$, while the *BaBP-2c* glass had the composition $70Ba(PO_3)_2\text{-}30B_2O_3$ with properties of $n_{cl} = 1.594$, $\alpha_{cl} = 10.48\times10^{-6}/°C$ and $dn/dT_{cl} = -5.01\times10^{-6}/°C$. The optical and thermal conditions for fibre fabrication were previously discussed in Section 5.5.1.1. Based on the properties of the core and clad glasses, it can be seen that $n_{co} > n_{cl}$, $\alpha_{co} > \alpha_{cl}$ and $(\alpha_{co} - \alpha_{cl}) = 2.04\times10^{-6}/°C$, thus satisfying all the conditions.

Figure 6.12 shows the DTA plots for both *BaBP-1b* (core) and *BaBP-2c* (clad) glasses. As discussed earlier in Section 5.5.1.2, the core and clad T_s can be estimated using equation (5.4) to determine the extrusion temperature. The T_s for the core and clad glasses were estimated to be 607°C and 648°C, respectively. T_f is the fibre drawing temperature, which will be discussed later and can be estimated from equation (6.1).

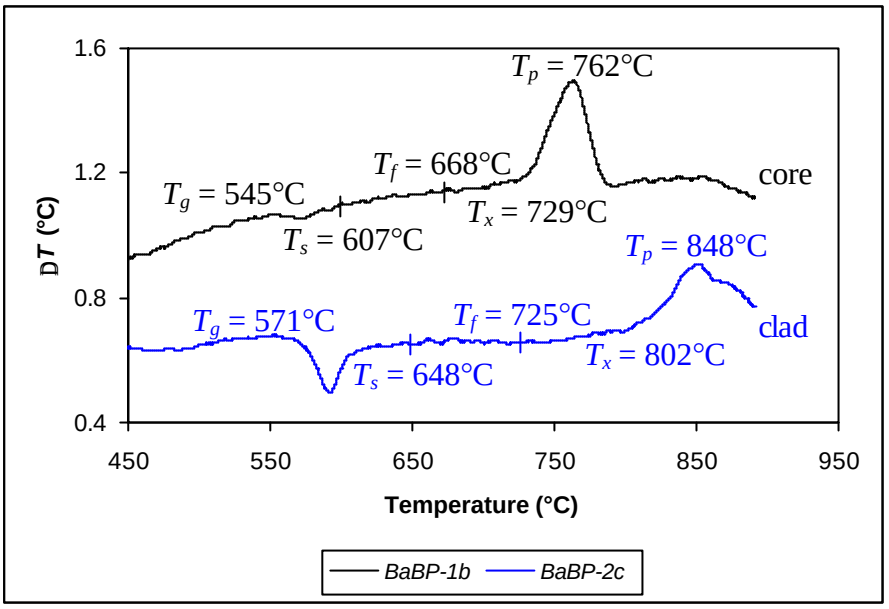

Figure 6.12 : DTA plots for *BaBP-1b* (core) and *BaBP-2c* (clad) glasses

(The curves have been displaced to fit the same D*T* range)

For the extrusion of a cane, the core (*BaBP-1b*) and clad (*BaBP-2c*) glasses were first prepared using the 2-step melting process detailed in Section 3.1.1. The dimensions were :

- core glass of h = 7 mm and f = 29 mm, core die with a hole f of 2 mm
- clad glass of h = 9 mm and f = 29 mm, clad die with a hole f of 2 mm

The extrusion body assembly followed the procedures discussed in Sections 3.5.1 and 5.5.1.2.

The extrusion rig furnace was first heated to the clad glass T_s of 650°C. Pressure, P, was then applied, with an increment of 10 bar (1 MPa) every 2 minutes, up to 75 bar (7.5 MPa). At this point, the extrusion rate was ~ 0.017 mm/min. The furnace temperature was then increased by 5°C and the extrusion rate increased to 0.033 mm/min. As the extrusion process progressed, the extrusion rate suddenly increased to 0.085 mm/min and cracks began to appear in the cane. At this point, the extrusion process was stopped.

Figure 6.13 shows the extruded cane obtained at the end of the extrusion process, which shows a large core within the cane. The large core size, coupled with the fact that there was a $\Delta\alpha$ between

the core and clad glasses, probably explained the cracks in the cane.

At the beginning of the extrusion process, the clad glass was first extruded while the core glass began to flow into the clad glass. During the course of the process, the core glass, which was softer than the clad glass, started to flow straight through the clad glass and be extruded, preventing much of the clad glass from flowing through the clad die. This accounted for the large core size obtained, producing a cane with a (core/clad) ratio up to ~ 0.8. However, it was suggested that the trend would eventually reverse, with the (core/clad) ratio decreasing, as the supply of the core glass was depleted. A second cane extrusion trial was carried out to verify this.

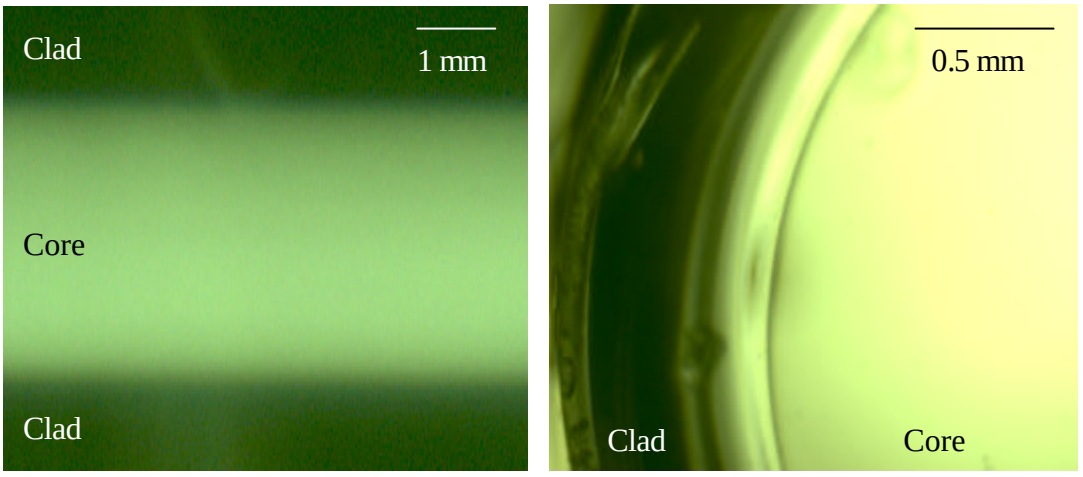

(a) (b)

Figure 6.13 : *BaBP-1b* : *BaBP-2c* extruded cane : (a) side view and (b) cross-section

For the second extrusion trial, the dimensions of the glasses used were:

- core glass of h = 5 mm and f = 29 mm, core die with a hole f of 4 mm
- clad glass of h = 12 mm and f = 29 mm, clad die with a hole f of 2 mm

The reason for the smaller amount of core glass and the larger core die hole compared to the previous trial was to allow the soft core to flow out quicker, leaving the majority of the clad and residual core glasses intact. Similar extrusion conditions as in the first trial were applied. At the beginning of the process, the extrusion rate was around 0.02 – 0.04 mm/min. As the core glass began to flow through, the extrusion rate increased to 0.10 mm/min and as the process continued

further, the extrusion rate decreased and remained at 0.03 mm/min. A final yield of ~ 1.8 m was obtained. The extruded cane was then analysed under the optical microscope to determine the (core/clad) ratio along the length of the cane and the results are shown in Figure 6.14. The diameter of the cane during the final part of the extrusion process was about 2.2 mm.

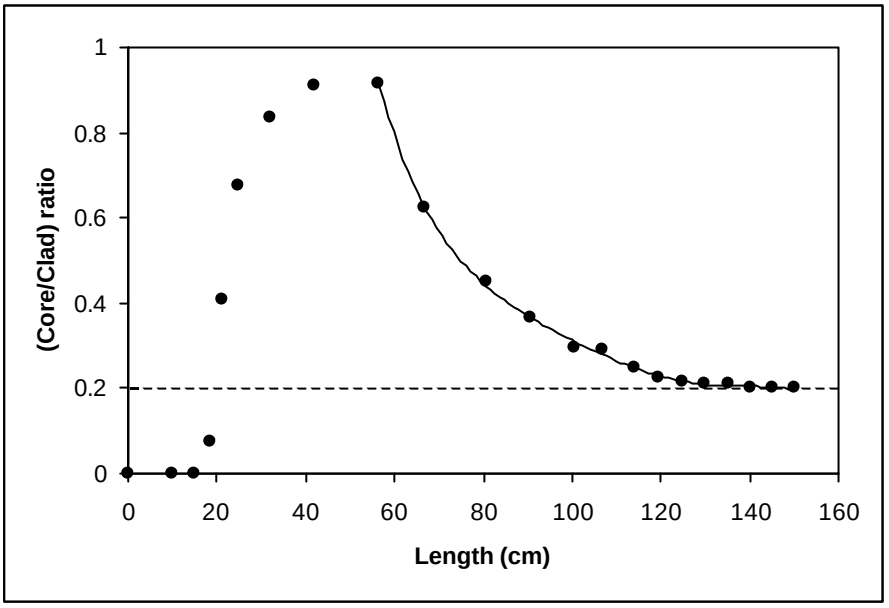

Figure 6.14 : (Core/clad) ratio at different cane lengths

In order to obtain the preform for fibre drawing, a tube of clad glass was also extruded, into which the cane can be inserted to further reduce the (core/clad) ratio. A clad glass of h = 27 mm and f = 29 mm was prepared. The clad die used was designed to produce a tube with an ID of 2.5 mm and an OD of 10 mm. Extrusion of the tube was carried out at T = 650°C (clad glass T_s) and P = 8 bar (0.8 MPa). The extrusion rate at the start of the process was 0.18 mm/min but the rate decreased to 0.10 mm/min as the clad glass was depleted. A tube of ~ 150 mm long was obtained.

Photograph 6.1 shows the extruded cane and tube, which formed the preform for fibre drawing. The extruded cane of diameter 2.2 mm with a (core/clad) ratio of 0.2 would be inserted into the extruded tube of diameter 10 mm to produce a (core/clad) ratio of 0.044. The stresses induced can be calculated based on the analysis in Section 5.5.1.2, and found to be ~ 3.5 MPa and ~ 0.015 MPa for the cane and the expected fibre, respectively.

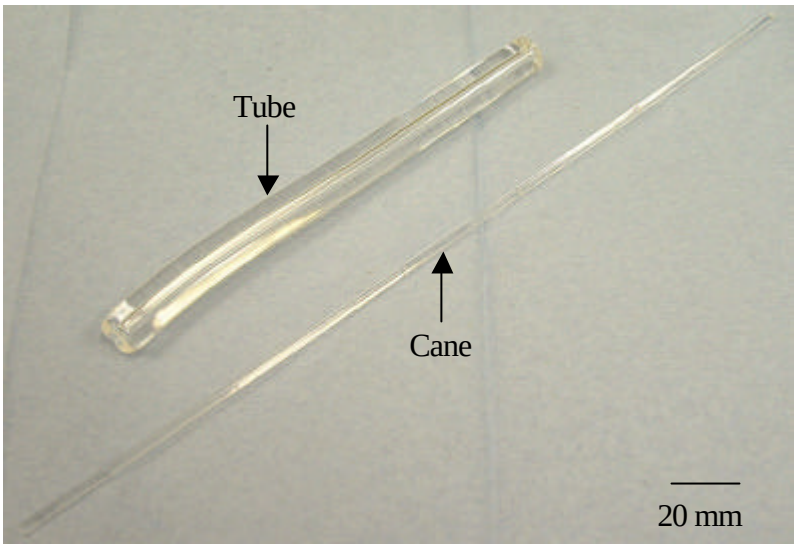

Photograph 6.1 : *BaBP-1b* : *BaBP-2c* preform

6.5.1.2 Fibre Drawing

Fibre drawing was carried out using the extruded cane and tube described in Section 6.5.1.1. An overview of the fibre drawing process has been described in Section 3.5.2. For the preform, a cane with length, L = 140 mm, OD = 2.2 mm and (core/clad) ratio = 0.2 was inserted into a tube with L = 130 mm, ID = 2.5 mm and OD = 9.8 mm.

Fibre drawing is generally carried out at a viscosity of ~ 10^4 – 10^6 poise (1 Poise = 0.1 Pa s). Using Figure 5.15 as the basis, the fibre drawing temperature, T_f (°C), of the core and clad glasses can be estimated from equation (6.1).

$$T_f \sim \frac{2(T_x - T_g)}{3} + T_g \qquad (6.1)$$

The core and clad T_f are estimated to be 668°C and 725°C, respectively.

Experimentally, the furnace in the fibre pulling tower was set to ~ 850°C (corresponding to ~ 700°C in real temperature). When the temperature was reached, the preform began to neck

down and dropped under its own weight. The preform was fed into the furnace at a rate of 300 rpm (~ 2.5 mm/min) and the end of the fibre was attached to a spooling drum to collect the fibres. The drum rate was set at 240 – 280 rpm (~ 9.1 – 10.6 m/min) in order to obtain 125 – 150 μm OD fibres. Figure 6.15 shows the cross-section of the 150 μm fibres pulled.

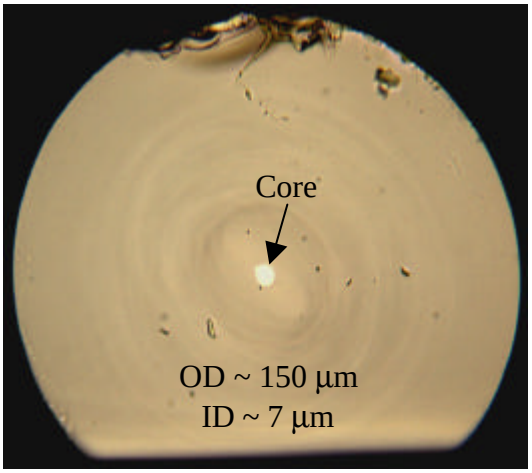

Figure 6.15 : Cross-section of 150 mm OD *BaBP-1b* : *BaBP-2c* fibre

6.5.1.3 Fibre Characterisation

Fibre attenuation measurement was performed using the cut-back method with the set-up as shown in Figure 6.16. Light from the source was focused into the single-mode silica fibre, which coupled into the fibre under test. The output of the light was then collected using a multi-mode silica fibre connected to an optical spectrum analyser (OSA), which recorded the transmitted power at different wavelengths.

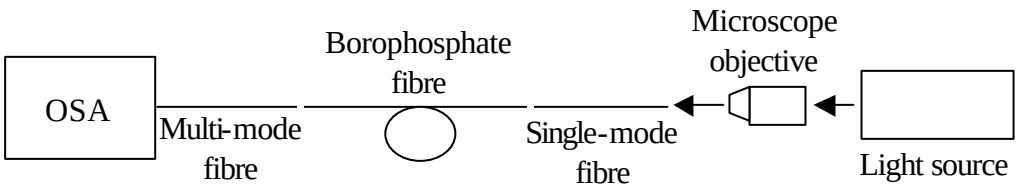

Figure 6.16 : Loss measurement set-up

For cladding loss estimation, a white light source was used for the measurement over a wavelength range of 500 – 1600 nm. A transmission spectrum was first obtained for an initial

length of the borophosphate fibre. A specified length was then cut from the fibre and a second transmission spectrum was obtained. Comparison between the spectra before and after the cut-back against the length cut would give an estimate of the loss, α_{loss}, in dB/m. Figure 6.17 shows the cladding loss for the *BaBP-1b* : *BaBP-2c* 150 μm fibre at different wavelengths. The average cladding loss for the fibre was approximately 5 dB/m for the wavelength range of 600 – 1400 nm with significant losses at 1400 – 1600 nm due to OH absorption.

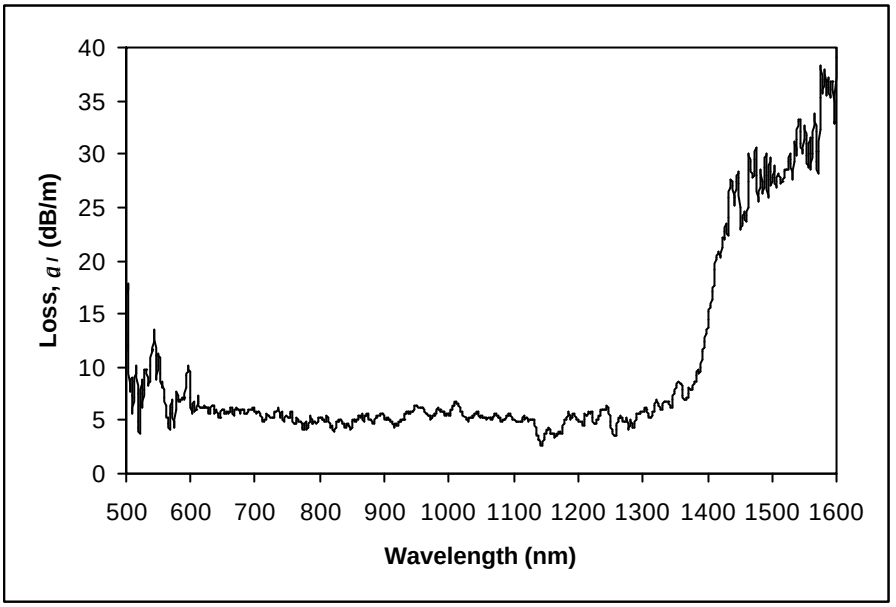

Figure 6.17 : *BaBP-1b* : *BaBP-2c* fibre cladding loss

For core loss estimation, a He-Ne laser was used for the measurement. A white light source was unable to provide a substantial power after transmission through the borophosphate fibre. In order to obtain the transmission spectrum of the core only, an index matching fluid (n_D = 1.620) was applied to the fibre, in addition to bends being introduced into the fibre, to strip the cladding modes. The procedures for measurements were the same as that of the cladding loss measurements. Figure 6.18 shows the core loss for the borophosphate 150 μm fibre.

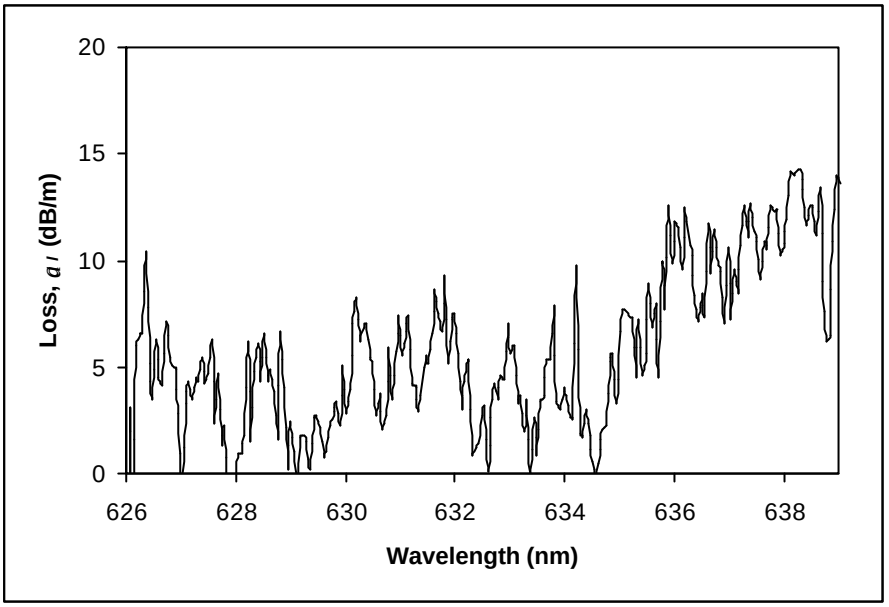

Figure 6.18 : *BaBP-1b* : *BaBP-2c* fibre core loss

Fibre NA measurement was performed using the set-up shown in Figure 5.22, where the borophosphate fibre replaced the glass sample in the figure. The objective lens and CCD camera were mounted on a translation stage where the distance from the fibre end can be varied via the micro-gauge. When the focus on the fibre was reached, the micro-gauge was set to zero. Profiles were then taken at distances of 0, 20, 40 and 60 μm and the fibre NA was estimated to be ~ 0.14. This was lower than the expected value of 0.18, based on the calculation using equation (5.2). The difference can be attributed to experimental error in the measurement of the refractive index as well as differences in the glass compositions of the samples used for the refractive index measurement and the extrusion process due to evaporation during the melting process and experimental error during the weighing of the raw materials. Based on the NA of 0.14, the fabricated fibre had a single-mode cut-off wavelength, $\lambda_{cut\text{-}off}$, of 1.28 μm.

6.5.2 Planar Waveguide Fabrication

The spin-coating process was used to fabricate planar devices using the borophosphate glasses. A 3-layer planar sample had previously been fabricated, as described in Section 5.5.2. The principles of the process are in Section 3.6.1.

For this work, the substrate used was the *BaBP-2c* glass while the core was the *BaBP-1b* glass. A substrate with dimensions of h = 2 mm and f = 32 mm was first prepared and optically polished on one surface and flat polished on the other surface. For the spin-coating process, the substrate was attached and held by vacuum in the spin-coating rig upper furnace and heated to ~ 570°C (substrate T_g). The core glass was melted in a platinum crucible in a separate furnace at 1250°C and transferred to the spin-coating rig lower furnace. The crucible with the molten core glass was then raised to the upper furnace to be dipped by the substrate. The crucible was then lowered and spinning of the substrate began. The sample was annealed for 60 minutes and then ramped down to room temperature at a rate of 1°C/min. Inspection of the deposited core layer whilst inside the spin-coating rig showed a successful deposition without any cracks. However, when the vacuum was released to drop the sample from the vacuum chuck, the sample did not drop as it appeared that the annealing temperature had been higher than necessary, causing the substrate to soften and be partly sucked into the holes of the vacuum chuck. The annealing temperature is critical in this respect and was noted for future experiments. Attempts to save the sample proved unsuccessful and in the end, the sample had to be broken into pieces. A second attempt to repeat the process but adjusting the annealing temperature was unsuccessful, as the spinning assembly of the rig had developed some mechanical problems. The spin coating rig had since been taken out of operation and no further fabrication could be done.

6.6 Channel Definition

As with Section 5.6, direct UV writing and femtosecond writing were carried out on the borophosphate bulk glasses to define some channel waveguides.

6.6.1 UV Writing

The direct UV writing technique has been described in Section 3.6.2. Similar writing conditions to that used for the glasses in Section 5.6.1 were applied to the bulk glasses in this work : a UV spot size of ~ 6.5 μm, writing powers of 50mW and 100 mW, scan speeds of 5 – 500 mm/min and channel separation of 200 μm. Bulk glasses of *BaBP-1a*, *BaBP-1b* and *BaBP-2c* were used.

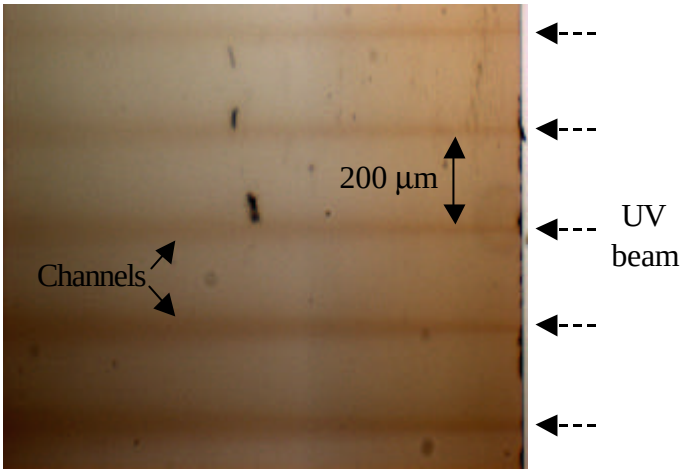

Figure 6.19 : Cross-section of UV written channels in *BaBP-1b* bulk glass

Figure 6.19 shows the written channels in the *BaBP-1b* glass. It can be seen that direct UV writing resulted in slab channels. A check using He-Ne laser showed that the channels were not guiding. These observations were similar to the results in Section 5.6.1.

6.6.2 Femtosecond Writing

The direct femtosecond writing technique has been described in Section 3.6.3. For this part of the work, 10X and 50X microscope objectives were used to focus the laser spot. The writing conditions were : powers of 20 - 260 mW, scan speeds of 20 - 100 µm/s and channel separation of 50 - 100 µm. The *BaBP-1b* bulk glass was used for this work. Figure 6.20 shows the waveguides written at 20 mW at speeds of 60, 80 and 100 µm/s using different microscope objectives.

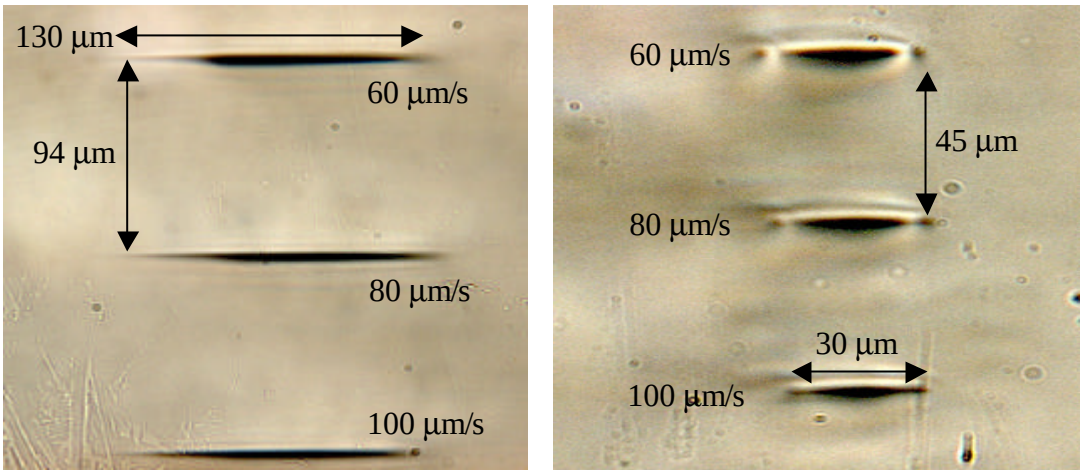

(a) (b)

Figure 6.20 : Cross-section of femtosecond written channels at 20 mW in *BaBP-1b* bulk glass with a (a) 10X objective and (b) 50X objective

As with Figure 5.21 in Section 5.6.2, the waveguides written had an ellipsoidal shape. This was due to the asymmetric beam profile of the laser beam along and perpendicular to the beam propagation direction. The femtosecond channels written with a 10X objective had a longer shape than that written with a 50X objective due to its larger confocal parameter, caused by the bigger beam spot size [18].

The set-up shown in Figure 5.22 was used to measure the NA of the waveguides. The procedures were exactly the same as those used in Section 5.6.2 for the NA measurement of the *KAP-1d* sample. Profiles were taken at distances of 0 - 400 µm at every 100 µm interval. Characterisation of the waveguide written with a 50X microscope objective at a writing power of 150 mW and a scan speed of 40 µm/s showed an NA of 0.08 ($\Delta n \sim 2.0\times10^{-3}$) along the beam propagation direction and an NA of 0.02 ($\Delta n \sim 1.25\times10^{-4}$) in the direction perpendicular to the beam propagation.

6.7 Summary

The properties of different compositions of barium borophosphate and sodium borophosphate glasses have been studied. Results in the literature revealed that tetrahedral boron units were incorporated into the glass network at low boron content while trigonal boron units were present at high boron content. This change in the glass structural network caused a maximum peak in the refractive index and the glass transition temperature. Tetrahedral boron units formed (B-O-P) bridges between phosphate chains and this led to an increase in the compactness, density of covalent cross links and strength of the glass structure. Consequently, the refractive index and the glass transition temperature increased. At high boron content, trigonal boron units dominated and a borate network replaced the rigid borophosphate network, leading to a decrease in the structural density and strength of the glasses. Consequently, the refractive index and the glass transition temperature decreased. The change of the glass structure from a borophosphate network to a borate network coincided with the maximum point observed in these properties. The structural change, however, did not appear to affect the measured thermal expansion and thermo-optic coefficient of the glasses. The systematic addition of boron led to the decrease of the thermal expansion coefficient and the subsequent progress towards positive thermo-optic coefficient values.

Glasses with negative dn/dT have been achieved, where the corresponding thermal expansion must exceed 7.5×10^{-6}/°C for barium borophosphate glasses and 11.5×10^{-6}/°C for sodium borophosphate glasses. For the barium borophosphate glasses, the semi-empirical equation of $dn/dT = -1.599\alpha + 11.58$ was defined for the composition range within $1.585 \leq n \leq 1.610$ and 5.68×10^{-6}/°C $\leq \alpha \leq 13.67\times10^{-6}$/°C. For the sodium borophosphate glasses, the semi-empirical equation of $dn/dT = -1.265\alpha + 12.74$ was defined for the composition range within $1.484 \leq n \leq 1.512$ and 11.20×10^{-6}/°C $\leq \alpha \leq 22.03\times10^{-6}$/°C.

The *BaBP-1b* glass and *BaBP-2c* glass were used as the core and clad glasses, respectively, for device fabrication due to their matched optical and thermal properties. The extrusion process managed to produce the preform required and fibre pulling was successfully performed. 125 µm and 150 µm fibres were drawn and characterisation of the 150 µm fibres showed an average cladding loss of ~ 5 dB/m over 600 – 1400 nm, an average core loss of 5 dB/m at the He-Ne

wavelength and an NA of 0.14.

Direct UV writing at 244 nm and direct femtosecond writing at 798 nm at different powers and writing speeds were investigated on some borophosphate bulk glasses. However, the UV written channels were not guiding because of the small, if any, refractive index change induced, due to the weak absorption of borophosphate glasses at 244 nm. The femtosecond technique was able to write some waveguides in the *BaBP-1b* sample and an NA of 0.08 ($\Delta n \sim 2.0\times10^{-3}$) was estimated for the waveguide written with a 50X microscope objective at a writing power of 150 mW and a scan speed of 40 μm/s. Hence, femtosecond writing is a potentially good technique for producing a positive refractive index change in barium borophosphate glasses. This can be exploited to write channel waveguides and/or gratings.

REFERENCES

1. K. Shima, K. Himeno, T. Sakai, S. Okude and A. Wada, *"A novel temperature-insensitive long-period fiber grating using a boron-codoped-germanosilicate-core fiber"*, in: Conference on Optical Fiber Communication, paper FB2, OFC 1997.

2. K. Kintaka, J. Nishii, H. Nishiyama, Y. Kawamoto and A. Sakamoto, *"Athermalization of a silica-based waveguide with a UV-induced Bragg grating on a crystallized glass substrate"*, Journal of Lightwave Technology 21 (3), pp 831-836 (2003).

3. T. Enomoto, M. Harumoto, M. Shigehara, S. Ishikawa and H. Kanamori, *"Temperature-insensitive long-period fiber gratings written in P_2O_5 co-doped GeO_2-SiO_2 core optical fibers"*, in : Topical Meeting on Bragg Gratings, Photosensitivity and Poling, paper ThE9, BGPP 1999, Florida, US, September 1999.

4. W. Vogel, *"Optical properties of oxide glasses"*, Optical Properties of Glass, D.R. Uhlmann and N.J. Kreidl (Eds), The American Ceramic Society Inc., OH, (1991).

5. M. Born and E. Wolf, Principles of Optics, Chapter 2, Pergamon Press, Oxford, (1984).

6. D. Ehrt, P. Ebeling and U. Natura, *"UV transmission and radiation-induced defects in phosphate and fluoride-phosphate glasses"*, Journal of Non-Crystalline Solids 263&264, pp 240-250 (2002).

7. N. Hadj Youssef, M.S. Belkhiria, J.J. Videau and M.B. Amara, *"Investigation of the physico-chemical properties of calcium borophopshate glasses. Effect of the substitution of sodium for calcium"*, Materials Letters 44, pp 269-274 (2000).

8. H. Yun and P.J. Bray, *"Nuclear magnetic resonance studies of the glasses in the system K_2O-B_2O_3- P_2O_5"*, Journal of Non-Crystalline Solids 30, pp 45-60 (1978).

9. N.H. Ray, *"A study of the coordination of boron in potassium borophosphate glasses by Raman spectroscopy"*, Physics and Chemistry of Glasses 16, pp 75-80 (1975).

10. R.K. Brow, *"An XPS study of oxygen bonding in zinc phosphate and zinc borophosphate glasses"*, Journal of Non-Crystalline Solids 194, pp 267-273 (1996).

11. R.K. Brow and D.R. Tallant, *"Structural design of sealing glasses"*, Journal of Non-Crystalline Solids 222, pp 396-406 (1997).

12. W. Vogel, Glass Chemistry, Chapters 8 and 9, Springer-Verlag, Berlin, (1994).

13. N.H. Ray, Inorganic polymers, pp 79, Academic Press, London, (1978).

14. D. Ehrt and W. Seeber, *"Glass for high performance optics and laser technology"*, Journal of Non-Crystalline Solids 129, pp 19-30 (1991).

15. J.A. Duffy, *"Charge transfer spectra of metal ions in glass"*, Physics and Chemistry of Glasses 38 (6), pp 289 (1997).

16. R.F. Bartholomew, *"Structure and properties of silver phosphate glasses – Infrared and visible spectra"*, Journal of Non-Crystalline Solids 7, pp 221-235 (1972).

17. J.F. Ducel and J.J. Videau, *"Physical and chemical characterisations of sodium borophosphate glasses"*, Material Letters 13, pp 271-274 (1992).

18. R. Osellame, S. Taccheo, M. Marangoni, R. Ramponi, P. Laporta, D. Polli, S. De Silvestri and G. Cerullo, *"Femtosecond writing of active optical waveguides with astigmatically shaped beams"*, Journal of the Optical Society of America B 20 (7), pp 1559-1567 (2003).

CHAPTER 7

CONCLUSIONS

7.1 Conclusions

The central wavelength of lightwave devices, such as the resonance wavelength of a grating, is sensitive to changes in temperature and this compromises the performance of these devices. This is due to the temperature dependence of the optical path lengths. Therefore, the concept of athermalisation is essential in correcting this problem. This was where the research project came in; to study various phosphate glass systems as possible athermal glasses, by utilising their negative refractive index change with temperature to counter the effect of thermal expansion. Figure 7.1 briefly summarises the stages involved in this research in the order they were carried out.

It was important to be able to measure the various properties of glasses that characterise and define an athermal material. Refractive indices, n, glass transition temperatures, T_g, and thermal expansion coefficients, α, were measured using commercial equipment. However, there was no available set-up to measure the thermo-optic coefficient, *dn/dT*. Hence an interferometer was set up as part of this research work to measure the *dn/dT* of glasses. The set-up was tested by measuring the *dn/dT* of some commercial glasses (silica, N-FK51 and N-PK51) with known *dn/dT* as well as the *dn/dT* of a barium metaphosphate glass sample at different sample thickness. The experimental and literature *dn/dT* values were comparable, confirming the accurate measurement of *dn/dT* with this interferometer set-up. The estimated error in the measured value was $\pm 0.3\times10^{-6}$/°C.

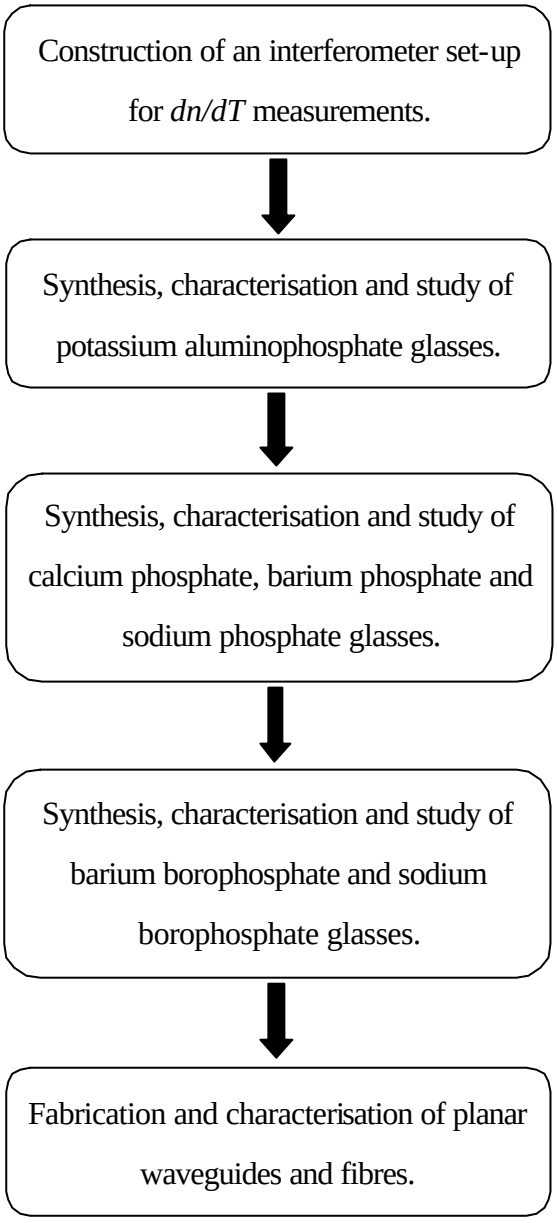

Figure 7.1 : Flow diagram summarising the main stages in the research

Phosphate glasses were the subject of this research because they exhibit negative *dn/dT* [1]. Discussions in earlier chapters showed that negative *dn/dT* is necessary to counter the positive thermal expansion of most glasses, in order to produce athermal glasses. Several phosphate glass families were prepared and studied in this work, namely the aluminophosphate, the binary phosphate and the borophosphate families. The modifiers incorporated into each family consisted of low field strength cations, such as Na^+, K^+, Ca^{2+} and Ba^{2+}, which also exhibit negative *dn/dT*. The borophosphates are particularly interesting as both boron oxide and phosphorus oxide are glass formers with negative *dn/dT*. This research work represented the first extensive

measurement of *dn/dT* in phosphate glasses.

The refractive index, the thermo-optic coefficient and thermal properties such as the glass transition temperature and thermal expansion coefficient of all the glasses formulated were measured. The data gathered were consistent with the structural changes associated with the addition of modifiers.

The first of the family of glasses synthesised were the ternary potassium aluminophosphate glasses (K_2O-Al_2O_3-P_2O_5). The properties of the glasses were investigated, and found to be strongly influenced by the effect of Al^{3+} on the glass structural network. Al^{3+} forms (P-O-Al) bridging bonds [2] between phosphate chains, increasing the structural polymerisation of the glass network and packing density of the atoms and hence resulting in a more compact network. This strengthening effect of Al^{3+} led to increased densities and refractive indices, increased glass transition temperatures, lower thermal expansion coefficients and consequently positive thermo-optic coefficients. However, this trend was reversed when a low field strength modifier, such as K^+, was incorporated. This was because the cation depolymerised the network and formed weak ionic bonds with the phosphate non-bridging oxygens. The monotonic changes in the glass properties as the compositions changed from ultraphosphate to polyphosphate compositions suggested a gradual change in the structural network as modifiers were added.

Binary calcium phosphate, barium phosphate and sodium phosphate glasses were also studied in the ultraphosphate and metaphosphate compositions. Generally, the structural network of binary phosphate glasses depends on the glass compositions : whether the number of terminal oxygens available is sufficient to meet the coordination requirement of each modifying cation [3]. If there are sufficient terminal oxygens available, the modifiers can exist at isolated sites. The addition of the modifiers causes the network to expand to accommodate these modifiers, which at the same time depolymerises the network. This results in decreased density, refractive index and glass transition temperature. However, when there are insufficient terminal oxygens available, the modifiers begin to share oxygens and in the process, form clusters of modifiers. This creates a more compact network and increases the cross-linking density of the network, leading to increased density, refractive index and glass transition temperature. The point at which this structural transition occurs coincides with the minima observed in the refractive index and glass

transition temperature results. However, the systematic addition of modifiers led to the increase of the thermal expansion coefficient and the subsequent progress towards negative thermo-optic coefficient. The OH content in the glasses must be minimised as water has a depolymerising effect due to the formation of (P-OH) bonds. This can affect the glass properties, as observed in the refractive index of the barium phosphate glasses.

The borophosphate glass families were also examined in this research. B_2O_3, like P_2O_5, also exhibits negative *dn/dT*. The properties of different barium borophosphate and sodium borophosphate compositions were assessed and can be explained based on the incorporation of tetrahedral and trigonal boron units in the glass structural network [4,5]. Tetrahedral boron units dominate at phosphate-rich compositions and forms (B-O-P) bridging bonds between phosphate chains. This increases the compactness, density of covalent cross-links and strength of the glass structure, resulting in increased refractive index and glass transition temperature. At borate-rich compositions, trigonal boron units dominate and a borate network replaces the rigid borophosphate network. This decreases the structural density and strength of the glasses, resulting in decreased refractive index and glass transition temperature. This network transition coincides with the maxima observed in the refractive index and glass transition temperature results. The systematic addition of boron decreased the thermal expansion and changed the thermo-optic coefficient to positive values.

dn/dT of the glasses had been found to be strongly linked to α. There was a specific minimum α value for each glass family, beyond which α would overcome the effect of polarisability change with temperature so that the glasses would exhibit negative *dn/dT*. Semi-empirical equations relating *dn/dT* and α had been defined for each glass family, allowing the estimation of *dn/dT* of any glass in the same family within a certain range. These results are summarised in Table 7.1.

Glasses	α_{min} (´ 10^{-6}/°C)	***dn/dT* equation**	**Valid range : *n*, α (´ 10^{-6}/°C)**
Potassium aluminophosphate	9.5	$dn/dT = -1.514\alpha + 14.82$	$1.469 \le n \le 1.519$ $6.84 \le \alpha \le 21.25$
Calcium phosphate	9.0	$dn/dT = -2.088\alpha + 18.50$	$1.526 \le n \le 1.551$ $8.60 \le \alpha \le 10.22$
Barium phosphate	9.0	$dn/dT = -2.104\alpha + 18.90$	$1.547 \le n \le 1.585$ $11.62 \le \alpha \le 13.67$
Barium borophosphate	7.5	$dn/dT = -1.599\alpha + 11.58$	$1.585 \le n \le 1.610$ $5.68 \le \alpha \le 13.67$
Sodium borophosphate	11.5	$dn/dT = -1.265\alpha + 12.74$	$1.484 \le n \le 1.512$ $11.20 \le \alpha \le 22.03$

Table 7.1 : *dn/dT* semi-empirical equations

The *dn/dT* semi-empirical equations for calcium phosphate and barium phosphate were approximately similar and this implied that the change of polarisability with temperature was dominated by the phosphate matrix, irregardless of the cations. Based on this assumption, the semi-empirical equation could be generalised for any calcium phosphate and barium phosphate and perhaps any alkaline earth phosphate glasses within 8.60×10^{-6}/°C $\le \alpha \le 13.67\times10^{-6}$/°C.

Glasses with negative *dn/dT* had been achieved in all the families of glasses investigated and this suggests that phosphate glasses are promising candidates for athermal waveguide development. To my knowledge, the *dn/dT* results for the potassium aluminophosphate, calcium phosphate, barium borophosphate and sodium borophosphate glasses are the first reported data. *dn/dT* values for barium phosphate are available in the literature [6], and are in agreement with the measured results of this research work.

This project started off with the aim of developing bulk phosphate glasses that are athermal so that optical devices can be directly fabricated on these glasses without the need for extra processing steps. However, the study and analysis of the glasses prepared in this research (Tables

4.4, 5.4 and 6.4) as well as Schott commercial glasses [7] (Appendix D) showed that there was not a single bulk glass that was athermal on its own. Therefore, in order to fabricate athermal devices, a multi-layer system approach has to be used so that the properties of the different glass layers can be utilised to compensate each other. To achieve athermalisation, the combination of glasses used must be such that the overall device exhibits $dn_{eff}/dT < 0$ and also the α of the fibre cladding glass or planar device substrate must be low.

Fibres were fabricated using the phosphate glasses studied in this research. The extrusion process was used to extrude a cane and a tube of borophosphate glasses, which formed the preform for fibre drawing. The extrusion process applied in this work showed that the technique can handle dissimilar glasses in terms of their softening temperatures, where the difference between the core and clad glasses was 40°C, with the core softer than the clad. To my knowledge, this was the first work to apply the two-die assembly to overcome this difference in the softening temperatures. The attenuation of the 150 µm fibres, with a 7 µm core, was assessed and an average cladding loss of ~ 5 dB/m over 600 – 1400 nm and an average core loss of 5 dB/m at the He-Ne wavelength were reported. The NA of the fibres was estimated to be ~ 0.14. The successful extrusion of the cane, where the core glass was significantly softer than the clad glass at the extrusion temperature, showed that the process can be used to extrude a combination of glasses in which their thermal properties are dissimilar.

The process of spin-coating was used to produce planar samples by spinning and depositing core and overclad layers onto glass substrates. A 3-layer planar sample based on potasium aluminophosphate and barium phosphate glasses was successfully fabricated. The spin-coating process also demonstrated the ability to deposit glass layers free of crystals. The process can also be used for glasses with dissimilar thermal properties.

The techniques of direct UV writing and direct femtosecond writing were investigated as a means of producing waveguides in the phosphate glasses. It was found that the UV beam wrote straight through the bulk glasses, due to the weak absorption of the phosphate glasses at 244 nm, which produced slab channels. UV exposure turned the transparent ‘oxidised’ glass to its ‘reduced’ pink coloration. Assessment of the channels at the He-Ne wavelength showed no waveguiding effect, implying a small or no induced refractive index change in the glasses. However, the

femtosecond writing produced some waveguides in the phosphate glasses, with an estimated NA of ~ 0.08 ($\Delta n \sim 2.0\times10^{-3}$). Further characterisation of the waveguides will be performed by Erica Bricchi (a PhD student in the ORC) and reported in her thesis.

The successful fabrication of fibres and planar samples as well as waveguides via femtosecond writing offers the possibility of utilising these processes in producing phosphate-based devices. For fibres, direct femtosecond writing can be used to focus and write gratings into the fibre core. For planar samples, the technique can be used to define waveguides as well as gratings in the core of a 2-layer planar sample.

Hitherto, the development and fabrication of multi-layer athermal devices have focused on silica [8-12]. However, as silica exhibits positive α and *dn/dT*, silica has to be combined with other materials which exhibit negative *dn/dT* or mounted on suitable substrates, to achieve athermalisation. The use of substrates can be an obstacle to the broad use of WDM systems from the viewpoint of cost, device size and reliability. Also, the use of silica restricts the choices of materials that can be used in combination with silica, as their α values must be matched closely to the low α of silica. The athermal condition specifies that both α and *dn/dT* are essential in determining the temperature insensitivity of the device. Hence, alternatively, we can control the *dn/dT*, in conjunction with the α of the glasses, where this method offers flexibility in choosing the combination of glasses for athermal devices. The phosphate glass family offers the possibility of achieving athermalisation by making use of its negative *dn/dT*. Manipulation of the glass compositions allows simultaneous modification of both α and *dn/dT*, without any restriction. This means that combinations of glasses with any α can be used potentially for athermalisation purposes, provided there is a corresponding negative *dn/dT*. By understanding the effect of modifiers and the glass structural network on the glass properties, we can vary the glass compositions to meet the required optical and thermal properties and fabricate athermal devices using a combination of similarly matched glasses from the same family.

Finally, phosphate-based glasses, being softer glasses compared to silica, can make use of the extrusion and spin-coating processes for device fabrication, which are considerably easy, fast and efficient processes. Together with new studies and techniques for realising positive change in refractive index with direct irradiation such as femtosecond laser writing, devices can be realised.

7.2 Future Work

Ultimately, the vision of this research topic should propagate beyond the study of phosphate glass systems and the fabrication of phosphate-based devices established in this work. The study of *dn/dT* of these glasses will be beneficial in expanding the database of glass properties. *dn/dT* semi-empirical equations can also be established for different glass systems, allowing fast and easy estimation of *dn/dT* of different glasses. Overall, these studies will provide a better understanding of the modifier effect and the structural effect on the properties of glasses.

The similarity of the *dn/dT* semi-empirical equations obtained for the calcium phosphate and barium phosphate glasses in different ranges of α suggested that the equation can be generalised for any glasses within the two glass systems over the whole range of α established in the study. The generalisation of the equation over a glass system having two different modifiers separately offers the possibility that it can be applied to any binary alkaline phosphate glasses within the same α range. Hence, other alkaline earth phosphate glasses should be studied to establish their corresponding semi-empirical equations for comparison with that of the calcium phosphate and barium phosphate glasses.

Another possible area for future work is the fabrication of planar samples. At this point, no athermal planar samples had been fabricated as the spin-coating rig had been taken out of operation. However, it had already been demonstrated that the spin-coating process was able to deposit core and overclad layers on phosphate glass substrates.

Despite the successful drawing of the borophosphate fibres, further fibre fabrication can be carried out using a different combination of glasses to improve the athermalisation of the fibres. Also, the performances of the fibres can be improved by using higher purity raw materials and improving the quality of the extruded preform.

Further investigation of femtosecond writing on the phosphate glasses should be performed. A comprehensive study of the different writing conditions can be carried out to identify the optimum writing conditions to write waveguides in these glasses. The study of femtosecond writing on these glasses can also provide to the femtosecond enthusiasts, a better understanding of the phenomena

that occur in the immediate surrounding area of the beam focus. Eventually, this technique can be applied to the definition of waveguides and gratings in the core of a 2-layer spin-coated sample.

Eventually, one of the future aims is to write gratings into the fabricated phosphate fibres. One method of doing this is by direct femtosecond writing where the beam can be focused into the core of the fibres to write the gratings. This method had been successfully demonstrated for the fabrication of gratings inside soda-lime glasses [13]. An alternative method is the use of a 193 nm ArF excimer laser to expose the fibres through the appropriate masks to form the gratings [14]. Although both the core and cladding are exposed, the refractive index difference between the core and cladding means that light that propagates in the fibre is still confined in the core. Another area that can be explored is the addition of dopants, such as Eu^{2+}, Ce^{3+} and Tb^{3+}, to increase the photosensitivity of the glasses for direct UV writing [15]. An understanding of the effects of these dopants on the structure and properties of the phosphate glasses has to be established, in order to tailor the glass compositions to meet the required optical and thermal requirements for athermalisation.

Ultimately, the fabricated athermal planar samples and fibres should be characterised. The resonance wavelength change of the grating with temperature should be measured to verify the temperature insensitivity of the devices and compared against the theoretical values.

REFERENCES

1. W. Vogel, *"Optical properties of oxide glasses"*, Optical Properties of Glass, D.R. Uhlmann and N.J. Kreidl (Eds), The American Ceramic Society Inc., OH, (1991).

2. N.J. Kreidl and W.A. Weyl, *"Phosphates in ceramic ware : IV, Phosphate glasses"*, Journal of The American Ceramic Society 24 (11), pp 372-378 (1941).

3. U. Hoppe, *"A structural model for phosphate glasses"*, Journal of Non-Crystalline Solids 195, pp 138-147 (1996).

4. H. Yun and P.J. Bray, *"Nuclear magnetic resonance studies of the glasses in the system K_2O-B_2O_3- P_2O_5"*, Journal of Non-Crystalline Solids 30, pp 45-60 (1978).

5. R.K. Brow, *"An XPS study of oxygen bonding in zinc phosphate and zinc borophosphate glasses"*, Journal of Non-Crystalline Solids 194, pp 267-273 (1996).

6. O.S. Shchavelev and V.A. Babkina, *"Properties of glasses of the systems P_2O_5-SrO and P_2O_5-BaO"*, Neorg. Mater. 6 (12), pp 2183-2186 (1970).

7. Schott glass catalogue – Product range 2000 (1998).

8. Y. Kokubun, N. Funato and M. Takizawa, *"Athermal waveguides for temperature-independent lightwave devices*", IEEE Photonics Technology Letters 5 (11), pp 1297-1300 (1993).

9. Y. Kokubun, S. Yoneda and H. Tanaka, *"Temperature-independent narrowband optical filter at 1.3mm wavelength by an athermal waveguide*", Electronics Letters 32 (21), pp 1998-2000 (1996).

10. Y. Kokubun, S. Yoneda and S. Matsuura, *"Temperature-independent optical filter at 1.55mm wavelength using a silica-based athermal waveguide*", Electronics Letters 34 (4), pp 367-369 (1998).

11. D. Bosc, B. Loisel, M. Moisan, N. Devoldère, F. Legall and A. Rolland, *"Temperature and polarisation insensitive Bragg gratings realised on silica waveguide on silicon"*, Electronics Letters 33 (2), pp 134-136 (1997).

12. K. Kintaka, J. Nishii, H. Nishiyama, Y. Kawamoto and A. Sakamoto, *"Athermalization of a silica-based waveguide with a UV-induced Bragg grating on a crystallized glass substrate"*, Journal of Lightwave Technology 21 (3), pp 831-836 (2003).

13. Y. Li, W. Watanabe, K. Yamada, T. Shinagawa, K. Itoh, J. Nishii and Y. Jiang, *"Holographic fabrication of multiple layers of grating inside soda-lime glass with femtosecond laser pulses"*, Applied Physics Letters 80 (9), pp 1508-1510 (2002).

14. L. Dong, L. Reekie, J.L. Cruz and D.N. Payne, *"Grating formation in a phosphorus-doped germanosilicate fibre"*, in: Conference on Optical Fiber Communication, paper TuO2, OFC 1996, San Jose, California (US), 1996.

15. H. Ebendorff-Heidepriem, C. Riziotis and E.R. Taylor, *"Novel photosensitive glasses"*, in : Glass Odyssey : 6th ESG Conference, Montpellier, France, June 2002.

APPENDICES

APPENDIX A

Derivation of *dn/dT* from Lorentz-Lorenz equation

The thermo-optic coefficient, *dn/dT*, can be derived from the definition of refractive index, *n*, via the Lorentz-Lorenz equation. The Lorentz- Lorenz equation is defined as below.

$$\frac{\left(n^2-1\right)V_m}{n^2+2}=\frac{4\pi}{3}N_A P_e$$

where n = refractive index

V_m = molar volume

P_e = polarisability

N_A = Avogadro's number

let $\frac{4\pi}{3}N_A = C$ = constant,

$$\frac{\left(n^2-1\right)V_m}{\left(n^2+2\right)}=CP_e,$$

Taking the natural logarithm on both sides,

$$ln\left[\frac{\left(n^2-1\right)V_m}{\left(n^2+2\right)}\right]=ln\left(CP_e\right)$$

$$ln\left(n^2-1\right)-ln\left(n^2+2\right)+ln\,V_m=ln\,C+ln\,P_e,$$

By differentiating both sides with respect to temperature, T,

$$\left[\frac{2n}{\left(n^2-1\right)}\cdot\frac{dn}{dT}\right]-\left[\frac{2n}{\left(n^2+2\right)}\cdot\frac{dn}{dT}\right]+\frac{d\left(\ln V_m\right)}{dT}=\frac{d\left(\ln P_e\right)}{dT}+\frac{d\left(\ln C\right)}{dT}$$

where $\frac{d\left(\ln C\right)}{dT}=0$

$$\therefore\frac{dn}{dT}\left[\frac{2n}{\left(n^2-1\right)}-\frac{2n}{n^2+2}\right]+\frac{d\left(\ln V_m\right)}{dT}=\frac{d\left(\ln P_e\right)}{dT}$$

$$\frac{dn}{dT}\left[\frac{2n\left(n^2+2\right)-2n\left(n^2-1\right)}{\left(n^2-1\right)\left(n^2+2\right)}\right]=\frac{d\left(\ln P_e\right)}{dT}-\frac{d\left(\ln V_m\right)}{dT}$$

$$\frac{dn}{dT}\left[\frac{6n}{\left(n^2-1\right)\left(n^2+2\right)}\right]=\frac{d\left(\ln P_e\right)}{dT}-\frac{d\left(\ln V_m\right)}{dT}$$

$$\frac{dn}{dT}=\frac{\left(n^2-1\right)\left(n^2+2\right)}{6n}\left[\frac{d\left(\ln P_e\right)}{dT}-\frac{d\left(\ln V_m\right)}{dT}\right]$$

$$\underline{\underline{\frac{dn}{dT}=A\left[\frac{d\left(\ln P_e\right)}{dT}-\frac{d\left(\ln V_m\right)}{dT}\right]}}\qquad\text{where } A=\frac{\left(n^2-1\right)\left(n^2+2\right)}{6n}$$

$\frac{d\left(\ln V_m\right)}{dT}$ can also be expressed as $3\boldsymbol{a}$ as shown below,

$$\text{Let}V_m=l^3\qquad\text{where } l=length$$

Taking the natural logarithm on both sides,

$$\ln V_m=3\ln(l)$$

Differentiating with respect to T,

$$\frac{d(\ln V_m)}{dT} = 3\left(\frac{1}{l}\right)\left(\frac{dl}{dT}\right)$$

as $\frac{1}{l}\frac{dl}{dT} = \boldsymbol{a}$,

$$\underline{\underline{\frac{d(\ln V_m)}{dT} = 3\boldsymbol{a}}}$$

APPENDIX B

Raw Material Calculation for Glass Synthesis

1. Potassium aluminophosphate

$K_2O + P_2O_5 = 2K(PO_3)$, $Al_2O_3 + 3P_2O_5 = 2Al(PO_3)_3$

To melt,

20 mol% K_2O, 15 mol% Al_2O_3, 65 mol% P_2O_5

which produces :

40 mol $K(PO_3)$ and 30 mol $Al(PO_3)_3$

being equivalent to :

57.14 mol% $K(PO_3)$ and 42.86 mol% $Al(PO_3)_3$

To calculate the weight of the raw material required for each glass component,

$$w_i = \frac{x_i M_i}{\sum x_i M_i}$$ w = weight, x = mol%, M = molar mass

$M(K_2O) = 94.2$, $M(Al_2O_3) = 101.96$, $M(P_2O_5) = 141.94$

Therefore, the weight% (wt%) required for the components are 14.906 wt% K_2O, 12.10 wt% Al_2O_3, and 72.994 wt% P_2O_5.

As K_2CO_3 was used as the starting material, the weight% for K_2O has to be converted to that for K_2CO_3,

$$m_{K_2CO_3} = m_{K_2O} \frac{M_{K_2CO_3}}{M_{K_2O}}$$ m = mass in g, M = molar mass

$M(K_2CO_3)$ = 138.21

Hence, a 100 g glass requires 21.87 g K_2CO_3

As $Al(OH)_3$ was used as the starting material, the weight% for Al_2O_3 has to be converted to that for $Al(OH)_3$,

$Al_2O_3 + 3H_2O = 2Al(OH)_3$,

$$m_{Al(OH)_3} = m_{Al_2O_3} \frac{2M_{Al(OH)_3}}{M_{Al_2O_3}}$$

$M(Al(OH)_3)$ = 78.004,

Hence, a 100 g glass requires 18.514 g $Al(OH)_3$

Therefore, a 100 g piece of glass requires

21.87 g K_2CO_3, 18.514 g $Al(OH)_3$, 72.994 g P_2O_5

2. <u>Calcium phosphate</u>

$CaO + P_2O_5 = Ca(PO_3)_2$

To melt,

30 mol% CaO, 70 mol% P_2O_5

which produces :

30 mol $Ca(PO_3)_2$ and 40 mol P_2O_5

being equivalent to :

42.86 mol% $Ca(PO_3)_2$ and 57.14 mol% P_2O_5

To calculate the weight of the raw material required for each glass component,

$$w_i = \frac{x_i M_i}{\sum x_i M_i}$$ w = weight, x = mol%, M = molar mass

M(CaO) = 56.08, M(P_2O_5) = 141.94, M($CaCO_3$) = 100.09, M($Ca(PO_3)_2$) = 198.02

Therefore, the weight% required for the components are 51.13 wt% $Ca(PO_3)_2$, 48.87 wt% P_2O_5.

The starting material of $CaCO_3$ and P_2O_5 required to form 51.13 wt% $Ca(PO_3)_2$ can be obtained using the following equations.

$$m_{CaCO_3} = m_{Ca(PO_3)_2} \frac{M_{CaCO_3}}{M_{Ca(PO_3)_2}}$$ m = mass in g, M = molar mass

$$m_{P_2O_5} = m_{Ca(PO_3)_2} \frac{M_{P_2O_5}}{M_{Ca(PO_3)_2}}$$

Therefore, a 100 g piece of glass requires

25.84 g $CaCO_3$ and 85.52 g P_2O_5

3. <u>Sodium borophosphate</u>

$0.8NaPO_3 – 0.2B_2O_3$

To melt,

80 mol% $NaPO_3$, 20 mol% B_2O_3

To calculate the weight of the raw material required for each glass component,

$$w_i = \frac{x_i M_i}{\sum x_i M_i}$$ w = weight, x = mol%, M = molar mass

$M(Na_2O)$ = 61.98, $M(P_2O_5)$ = 141.94, $M(Na_2CO_3)$ = 105.99, $M(NaPO_3)$ = 101.96, $M(B_2O_3)$ = 69.62

Therefore, the weight% required for the components are 85.42 wt% $NaPO_3$, 14.58 wt% B_2O_3.

The starting material of Na_2CO_3 and P_2O_5 required to form 85.42 wt% $NaPO_3$ can be obtained using the following equations.

$$m_{Na_2CO_3} = m_{NaPO_3} \frac{M_{Na_2CO_3}}{2M_{NaPO_3}}$$ m = mass in g, M = molar mass

$$m_{P_2O_5} = m_{NaPO_3} \frac{M_{P_2O_5}}{2M_{NaPO_3}}$$

Therefore, a 100 g piece of glass requires

44.40 g Na_2CO_3, 14.58 g B_2O_3, 59.46 g P_2O_5

APPENDIX C

EDAX Analysis of Glasses

EDAX analysis was carried out on some of the glasses in order to compare the nominal compositions and the analysed composition as well as the level of SiO_2 contamination. Analysis was carried out on three separate spots for each sample. The analysed compositions are shown below and have an error of ±3% due to changes in experimental conditions over time during the analysis. The SiO_2 contamination originated from the melting procedure discussed in Section 3.1.1. It is possible that the presence of SiO_2 may affect the measured value of *dn/dT* for these glasses, however, as the results showed consistency within the different glass systems, these levels of contamination may not be a major cause of concern.

1. *KAP-4b* ($15K_2O$-$15Al_2O_3$-$70P_2O_5$)

Glass component	Analysed compositions (mol%)		
	1	2	3
K_2O	12.4	12.3	12.3
Al_2O_3	13.9	14.4	14.2
P_2O_5	73.4	73.2	73.4
SiO_2	0.3	0.1	0.1

2. *CaP-1a* ($50CaO$-$50P_2O_5$)

Glass component	Analysed compositions		
	1	2	3
CaO	52.8	52.4	53.0
P_2O_5	46.3	46.7	46.2
SiO_2	0.9	0.9	0.8

3. *BaP-1c* (50BaO-50P_2O_5)

Glass component	Analysed compositions		
	1	**2**	**3**
BaO	53.1	52.6	52.9
P_2O_5	45.9	46.5	46.1
SiO_2	1.0	0.9	1.0

4. *BaP-1e* (40BaO-60P_2O_5)

Glass component	Analysed compositions		
	1	**2**	**3**
BaO	42.1	43.4	42.4
P_2O_5	57.1	55.8	56.6
SiO_2	0.8	0.8	1.0

APPENDIX D

Commercial Schott Glasses

The table below shows the properties of commercial Schott glasses. It gives a rough estimate of the temperature dependence of the optical path length, *dS/dT*, for each glass, calculated using equation (1.2), which was defined earlier in Section 1.3.1. Calculations were made based on the data supplied in the Schott glass catalogue – Product range 2000 (1998).

$$\frac{1}{L}\left(\frac{dS}{dT}\right) = n\alpha + \frac{dn}{dT} \tag{1.2}$$

The first column shows the designation of each glass. Columns two to four show the refractive index at λ = 589.3 nm, thermal expansion coefficient for the range of -30°C to 70°C and the relative thermo-optic coefficient at λ = 546.1 nm for the range of 20°C to 40°C, respectively. Column five lists the calculated result of 1/*L*. *dS/dT* for each glass.

Glass	n_D	α ($\times 10^{-6}$/°C)	*dn/dT* ($\times 10^{-6}$/°C)	*1/L(dS/dT)* ($\times 10^{-6}$/°C)
BASF51	1.72356	5.40	10.10	*19.41*
F2	1.61989	8.20	4.40	*17.68*
F5	1.60328	8.00	4.60	*17.43*
K10	1.50129	6.50	4.20	*13.96*
LaFN7	1.74931	5.30	8.30	*17.57*
LF5	1.58132	9.10	2.00	*16.39*
LLF1	1.54803	8.10	2.90	*15.44*
N-BAF10	1.6699	6.20	4.90	*15.25*
N-BAF3	1.58261	7.20	3.40	*14.79*
N-BAF4	1.60556	7.20	3.30	*14.86*
N-BAF51	1.65211	8.40	2.90	*16.78*
N-BAF52	1.60852	6.90	3.30	*14.40*
N-BAK1	1.57241	7.60	2.30	*14.25*
N-BAK2	1.53988	8.00	1.70	*14.02*
N-BAK4	1.56874	7.00	3.90	*14.88*
N-BAK50	1.556	4.60	5.60	*12.76*

Glass	n_D	α (´10^{-6}/°C)	*dn/dT* (´10^{-6}/°C)	*1/L(dS/dT)* (´10^{-6}/°C)
N-BALF4	1.57946	6.50	5.10	*15.37*
N-BALF5	1.5473	7.30	2.90	*14.20*
N-BASF2	1.6643	7.10	4.40	*16.22*
N-BASF64	1.70384	7.30	4.30	*16.74*
N-BK10	1.49775	5.80	3.50	*12.19*
N-BK7	1.51673	7.10	3.00	*13.77*
N-F2	1.6199	7.80	3.50	*16.14*
N-FK5	1.48743	9.20	-1.00	*12.68*
N-FK51	1.48651	13.30	-5.70	*14.07*
N-K5	1.52241	8.20	2.10	*14.58*
N-KF9	1.52337	8.60	1.80	*14.90*
N-KZFS2	1.55827	4.40	5.30	*12.16*
N-KZFS4	1.61324	7.30	3.70	*15.48*
N-LAF2	1.74383	8.10	1.00	*15.13*
N-LAF21	1.78785	6.20	4.90	*15.98*
N-LAF28	1.773	5.80	5.40	*15.68*
N-LAF3	1.71687	7.60	1.60	*14.65*
N-LAF32	1.79441	5.90	5.60	*16.19*
N-LAF33	1.78567	5.60	8.50	*18.50*
N-LAF34	1.77236	5.80	5.40	*15.68*
N-LAF7	1.74931	7.30	4.20	*16.97*
N-LAK10	1.7199	5.70	5.10	*14.90*
N-LAK12	1.67779	7.60	-0.40	*12.35*
N-LAK21	1.6404	6.80	1.00	*12.15*
N-LAK22	1.65103	6.60	3.10	*14.00*
N-LAK33	1.75385	6.00	4.40	*14.92*
N-LAK8	1.71289	5.60	5.00	*14.59*
N-LAK9	1.69089	6.30	3.70	*14.35*
N-LASF30	1.80303	6.20	5.30	*16.48*
N-LASF31	1.88048	6.80	5.20	*17.99*
N-LASF36	1.79692	7.30	5.60	*18.72*
N-LASF40	1.83385	5.80	9.30	*19.94*
N-LASF41	1.83484	6.20	5.40	*16.78*
N-LASF43	1.80593	5.60	6.50	*16.61*
N-LASF44	1.80405	6.20	5.30	*16.49*
N-LF5	1.58132	8.00	3.00	*15.65*
N-LLF1	1.54803	8.00	1.70	*14.08*
N-LLF6	1.53159	7.70	3.60	*15.39*
N-PK51	1.52849	12.70	-6.70	*12.71*
N-PSK3	1.55224	6.20	3.00	*12.62*
N-PSK53	1.62005	9.40	-2.30	*12.93*
N-SF1	1.71715	9.10	1.80	*17.43*
N-SF10	1.72806	9.40	1.50	*17.74*

Glass	n_D	***α*** ***(´10^{-6}/°C)***	***dn/dT*** ***(´10^{-6}/°C)***	***1/L(dS/dT)*** ***(´10^{-6}/°C)***
N-SF15	1.69872	8.00	3.40	*16.99*
N-SF4	1.75489	9.50	1.40	*18.07*
N-SF5	1.67253	7.90	3.40	*16.61*
N-SF56	1.78444	8.70	2.00	*17.52*
N-SF6	1.80491	9.00	1.50	*17.74*
N-SF64	1.70571	8.50	2.70	*17.20*
N-SF8	1.68874	8.60	2.60	*17.12*
N-SK15	1.62286	6.70	2.70	*13.57*
N-SK16	1.62032	6.30	2.30	*12.51*
N-SK2	1.60729	6.00	4.50	*14.14*
N-SK4	1.61262	6.50	2.80	*13.28*
N-SK5	1.58904	5.50	3.70	*12.44*
N-SSK2	1.62219	5.80	5.20	*14.61*
N-SSK5	1.65833	6.80	3.20	*14.48*
N-SSK8	1.61762	7.20	2.90	*14.55*
N-ZK7	1.5084	4.50	7.00	*13.79*
PK50	1.52047	8.80	0.20	*13.58*
SF1	1.71715	8.10	7.90	*21.81*
SF10	1.72803	7.50	8.10	*21.06*
SF11	1.78446	6.10	12.90	*23.79*
SF14	1.76157	6.60	11.00	*22.63*
SF15	1.69875	7.90	6.10	*19.52*
SF2	1.64752	8.40	4.60	*18.44*
SF4	1.75496	8.00	9.20	*23.24*
SF5	1.67252	8.20	5.80	*19.51*
SF56A	1.78444	7.90	10.00	*24.10*
SF57	1.84636	8.30	12.50	*27.82*
SF6	1.80491	8.10	11.10	*25.72*
SFL57	1.84635	8.70	2.90	*18.96*
SK51	1.62081	8.90	-0.50	*13.93*

APPENDIX E

Bismuthate Glass

In order to increase the capacity in wavelength division multiplexing (WDM) systems, optical amplifiers with a wide and flat gain spectrum are needed. Also, a compact amplifier is required to meet the low spatial and cost effective demand for metro use, where erbium-doped planar waveguide amplifiers have been proposed.

Bi_2O_3-based glasses have been developed and can accept up to 13000 ppm of Er with broadband emission and negligible concentration quenching [1,2]. Bi_2O_3-based Er-doped fibres had previously been reported to exhibit a net gain of 18 dB at 1560 nm and > 9 dB in C + L bands [3,4]. Hence, an Er-doped Bi_2O_3-based planar waveguide amplifier is a possible candidate for a compact amplifier.

This section contains details on the study of photolithography and ion beam milling (IBM) as a technique for fabricating channel waveguides in bismuthate glasses, which I carried out during the course of my PhD. The materials included here are taken from the final report presented to ASAHI Glass Company Ltd, which funded the work.

REFERENCES

1. S. Tanabe, N. Sugimoto, S. Ito and T. Hanada, *"Broad-band 1.5 mm emission of Er^{3+} ions in bismuth-based oxide glasses for potential WDM amplifier"*, Journal of Luminescence 87-89, pp 670-672 (2000).

2. N. Sugimoto, *"Ultrafast optical switches and wavelength division multiplexing (WDM) amplifiers based on bismuth oxide glasses"*, Journal of The American Ceramic Society 85 (5), pp 1083-1088 (2002).

3. N. Sugimoto, Y. Kuroiwa, K. Ochiai, S. Ohara, Y. Fukasawa, S. Ito, S. Tanabe and T. Hanada, *"Novel short-length EDF for C+L band amplification"*, in : Optical Amplifiers and their Applications, OAA 2000, Quebec City, Canada, 2000.

4. Y. Kuroiwa, N. Sugimoto, K. Ochiai, S. Ohara, Y. Fukasawa, S. Ito, S. Tanabe and T. Hanada, *"Fusion spliceable and high efficient Bi_2O_3-based EDF for short-length and broadband application pumped at 1480 nm"*, in : Optical Fibre Communication, OFC 2001, Anaheim, California (US), March 2001.

Project Title: **Erbium-doped waveguide amplifiers in AGC bismuth glass**

Final Report 26/01/2004

Optoelectronics Research Centre
University of Southampton (UK)

Contract Start: 01/02/2002
Contract Termination: 31/01/2004

Authors: A. Favre (ORC), E.R. Taylor (ORC), E. Lee (ORC)

Project funded by Asahi Glass Company (Japan)

Chapter II: Hot-dip spin-coating and photolithography technology followed by Ion Beam Milling

Introduction

Numerous techniques for the fabrication of planar and channel waveguides can be found in the literature. Traditional techniques are ion exchange, plasma enhanced chemical vapour deposition (PECVD), flame hydrolysis deposition (FHD), radio frequency magnetron sputtering, pulsed laser deposition (PLD). Most of these techniques are well developed for silicate glasses, but difficulties still exist in reproducing the stoichiometry of multi-component glasses in planar waveguide form and in the optical quality of these films, which leads to high waveguide losses. Planar and channel Er^{3+}-doped Bi_2O_3-based glass waveguides were fabricated using RF magnetron sputtering followed by photolithography technology and reactive ion beam etching [2.1]. The total loss of the channel waveguide at 1620 nm was around 13 dB due to the poor quality of the sputtered core and clad glass layers and interfaces. Spectroscopic properties of Er^{3+} ions were also affected. The lifetime of the Er^{3+} ions excited at 980 nm was measured to be half of that measured in an Er^{3+}-doped Bi_2O_3-based fibre, which accounted for non-radiative decay.

Hot-dip spin-coating offers an alternative to problems associated with fabrication. The process involves dipping a glass substrate into a molten glass followed by spinning. Since the waveguides are processed directly from the molten phase of the glass, the composition and hence spectroscopy of the glass is preserved. This is essential as most glass development for optical devices are formulated specifically for tailoring their optical properties for the intended application. In particular, in bismuthate glass and in this work the broadness of the Er^{3+} ion emission must be preserved to realise gain in the L-band. This chapter presents the fabrication of planar waveguides in the Bi_2O_3-based glass using hot-dip spin-coating. A three-layered slab waveguide consisting of a substrate, core and overclad Bi_2O_3-based glass films have been fabricated.

After spin-coating, it is then necessary to define the channel waveguides in the slab. In this work, channel waveguides or lateral confinement was fabricated using conventional photolithography technology and ion-beam milling. While the technique is conventional, the photolithography process itself had to be studied to allow the fabrication of channel

waveguides from the spin-coated films. The modification to the technique is presented here.

I. Fabrication of planar waveguides by hot-dip spin-coating

1. Bibliography

Theoretically, the idea of spin coating molten glass dates from the 1950s [2.2]. Practically, the technique has been developed only recently at the ORC [2.3]. With the help of numerical simulation of the process [2.4], it has been successfully applied to fabricate low-loss optical planar waveguides in fluoroaluminate (AlF) glasses [2.5]. The glass with a viscosity of 0.1 poise at 1000 °C was spin coated into a waveguide geometry directly from its liquid phase at this temperature. Waveguides with thickness ranging from 2 to 10 μm were obtained with an excellent thickness uniformity (0.1 μm/mm) in the central area of the substrate. Optical losses as low as 0.1 dB/cm at 1048 nm were measured.

2. Experimental

Planar 3-layered glass samples (clad/core/overclad) were prepared by a two-stage hot-dip spin-coating process. The clad or substrate and overclad were from the same glass composition with a refractive index of 2.01 while the core was Er^{3+}-doped with a refractive index of 2.03. The expansion coefficient were matched, both core and clad glasses having the same thermal expansion coefficient of 8.5×10^{-6}/°C. The glasses required for this procedure were:

(1) substrate glass disk with diameter 25 - 35 mm and thickness 2 - 2.3 mm,
(2) 200 g core glass (Er^{3+}-doped) melt in platinum crucible,
(3) 200 g clad glass melt in platinum crucible for the overclad.

The apparatus used is shown in FIG. II.1. It consisted of two furnaces where the top furnace will hold the substrate and the lower furnace will hold the glass melts. A polished Bi_2O_3-based glass substrate, was preheated to a furnace of 595°C in the upper annealing furnace. The core glass for the core film was heated up to 1250°C in a separate furnace and then transferred into the lower furnace, which had been preheated to 700°C. The use of a separate furnace was needed because the current lower furnace can only go up to 1000°C.

When the melt was in the lower furnace, an Aerotech ATS0200 positioning system was used to immediately transfer the molten glass between furnaces. Accurate control of the melt position resulted in the surface of the substrate being dipped a fraction of millimetre into the molten glass. The dip time was less than a second. The computer was used to synchronise the melt withdrawal and spinning of the substrate. After spinning, the melt crucible was withdrawn back to its original position in the lower furnace. The result was a slab waveguide consisting of a clad glass substrate and a spin-coated core film. This waveguide was maintained at the preset upper furnace temperature for the next process. The next process was to deposit an overclad. For this, the process of dip and spin as for the core, but replacing the core melt with the clad melt, was repeated to deposit spin-coated overclad film. The deposited three-layer slab waveguides were then annealed in the upper furnace at 595°C for one hour, followed by a slow ramp down to room temperature at 1 °C/min.

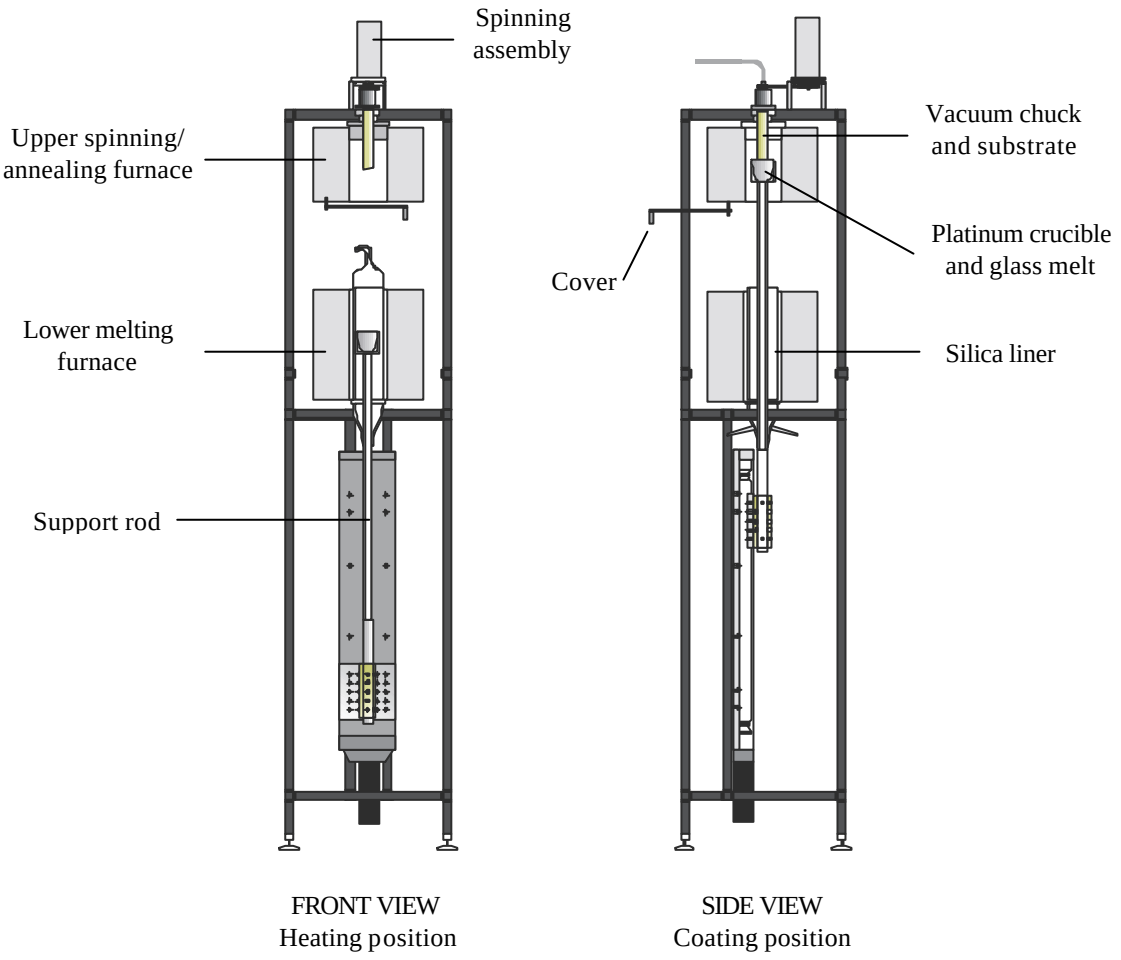

FIG. II.1: Apparatus for hot-dip spin-coating of waveguides using molten glass.

Crucible preparation

The core and clad glasses to be spun were melted in two different platinum crucibles. The same melt was used several times. When the glass composition was changed, the remaining glass in the crucible was melted at 1250 ºC for 30 minutes under oxygen and cast on a brass mould. The crucible was then placed in nitric acid 70 % for etching for 48 hours or more to be cleaned, rinsed and dried.

Substrate preparation

The substrate was prepared by AGC with both flat faces optically polished. Before each spin-coating, the sample was cleaned with methanol and dried with nitrogen. The sample was held in the upper furnace by a vacuum chuck consisting of a small section of boron nitride and the rest was made up of stainless steel. The sample was in direct contact with the boron nitride impregnated with holes to hold the sample in vacuum. After several furnace temperature and substrate thickness trials with dip and spin, the best results were for an upper substrate furnace temperature of 595°C and substrate thickness of 2 to 2.3 mm.

A list of all the samples prepared by hot-dip spin-coating is provided in ANNEX II.1 with the detailed experimental conditions.

In order to determine the glass films thickness, some of the 3-layered glass samples fabricated by hot-dip spin-coating were cut at two edges and the cross-sections were polished. Optical microscopy was used to examine the cross-section of the films. The thickness of the core and clad films are summarized in ANNEX II.1.

3. Results

From first principles, the film thickness h from a single spin is determined by the density ρ (kg/m^3) and the viscosity η (Pa.s), of the fluid, and external parameters such as the angular velocity ω (s^{-1}), and the spin time, t (s) [2.6]:

$$h = (1/\omega)\times\sqrt{(3\eta/4\rho t)}$$

Thus, from the variable experimental parameters, the faster the spin rate (w), the thinner the film; the more viscous the melt (h) the thicker the film; and the longer the spin time (t), the thinner the film. The glass melts were melted at a temperature as high as possible before any appreciable loss of material via evaporation can be observed. This temperature was close to liquidus (log h=0) temperature based on a typical bismuthate viscosity curve provided by AGC and reproduced here as FIG. II.2.

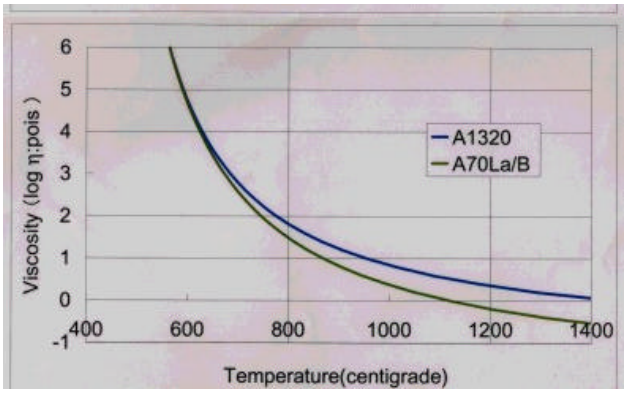

FIG. II.2: Viscosity curve of Bi_2O_3-based glass.

Harwood et al. had studied the effect of the experimental parameters on the final waveguide in AlF glasses [2.4]. In agreement with the earlier work on AlF glasses, in this study, the thickness of the spun bismuthate film was determined by the temperature of the substrate and glass melt (viscosity) and the spinning speed and time.

FIG. II-3 is a photograph of a spin-coated bismuthate glass. The crown around it was the quenched residue of the melt that spun out. For a first step, the substrate was coated with the core. The desired film thickness at this first dip was around 15 micron. A cross-section core-coated substrate from the first dip is shown in FIG II.4. The first deposited glass film underwent a re-flow during the second spin-coating stage, when the overclad was deposited, thus reducing the core dimensions. This was first observed for AlF glass and the theory for the process has been presented [2.4].

During the dip, the heat was transferred from the deposited core melt to the substrate, thus the substrate temperature increased. A temperature gradient was established as illustrated below:

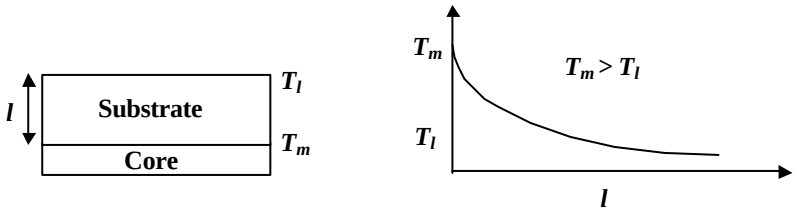

where T_m is the melt temperature and T_l is the final temperature at the back end. Heat was conducted away from the substrate via the vacuum chuck materials. The theory had been developed in reference [2.6]. It was important that $T_l < T_s$, the softening point of the glass, otherwise the substrate glass will be sucked into the vacuum. This was one reason why the substrate thickness and temperature were important. The other reason for control of substrate temperature and thickness is illustrated in Fig II.5. The final thickness of the two layers was very sensitive to the substrate temperature because of the fast quenching after dipping. FIG. II.5 shows an optical microscope picture of the cross-section of two 3-layered glass samples. Sample a) was prepared with a substrate temperature of 580 °C and sample b) with a substrate temperature of 595 °C in order to thin down the final core film thickness. A 5 µm core film thickness was achieved, which suggested a practical potential for single mode operation in the channel guides. The waveguides exhibited very good thickness uniformity over the central area, with only minor curvature of the surface observed at the border of the disc (FIG. II.3). The higher substrate temperature retained the deposited melt temperature at a higher temperature during the spinning process, allowing thinner deposited films as seen in the core and overclad layers of Fig II.5.

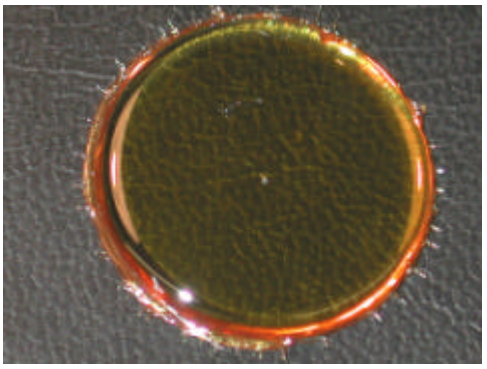

FIG. II.3: Photograph of a spin-coated Bi_2O_3-based glass waveguide.

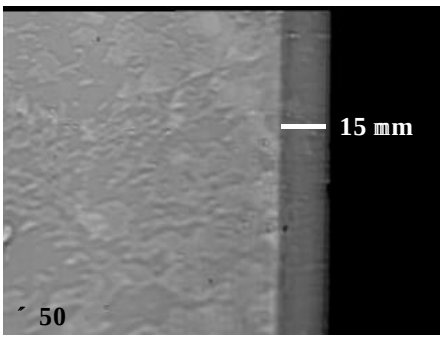

FIG.II.4: Cross-sectional optical microscope picture of a core single layer spin-coated sample.

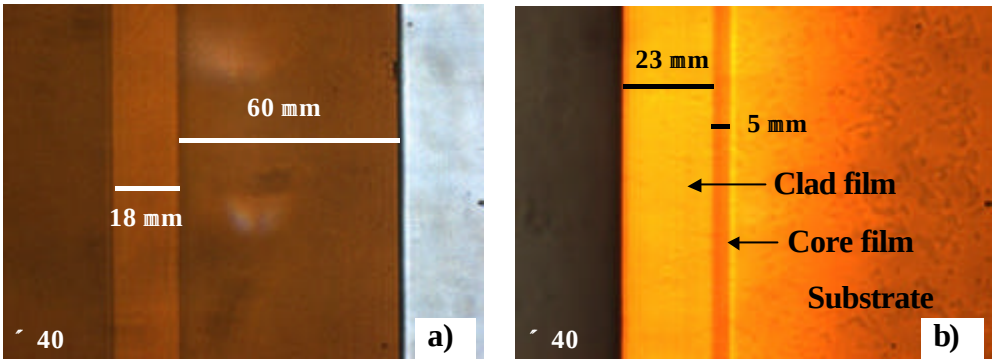

FIG. II.5: Cross-sectional optical microscope pictures of two spin-coated Bi_2O_3-based glass waveguide prepared with a substrate temperature of: a) 580 °C, b) 595 °C.

4. Conclusion

We have shown in this work that fabrication of a three-layered film using hot dip spin coating of bismuthate glass can be reproduced repeatedly. The desired core thickness of 5 micron can be achieved. This is the first demonstration of hot dip spin coating in a bismuthate glass. The deposition of layers using this process is efficient.

III. Fabrication of channel waveguides by photolithography and dry etching

The hot dip spin-coat technique applied to bismuthate glass gave a slab waveguide of dimensions typically shown in FIG. II.5b: overclad = 20-25 µm, core = 5-6 µm, substrate = 2.0-2.3 µm. This overclad was thicker than traditional overcladding prepared by Chemical Vapour Deposition or sputtering techniques, which is nominally a few microns. The challenge in this work was how to fabricate lateral confinement through such a thick overclad layer. Ion beam milling (IBM) was our instrument of choice. As with spin coating of bismuthate glass, IBM in this glass was pioneering work.

The principle for producing channel waveguides by photolithography technology and ion beam milling is described in FIG. II.10. A thin film of a polymer photoresist is deposited onto the substrate by spinning. The photoresist-coated sample is then exposed to UV light through a patterned mask to imprint the specific pattern onto the sample, then developed to wash away the UV-exposed photoresist, leaving only the imprinted pattern. The as-prepared sample is then etched by ion beam milling where both photoresist and glass

unprotected by the photoresist are etched by ion bombardment. The excess photoresist is then washed off creating the desired channel waveguides.

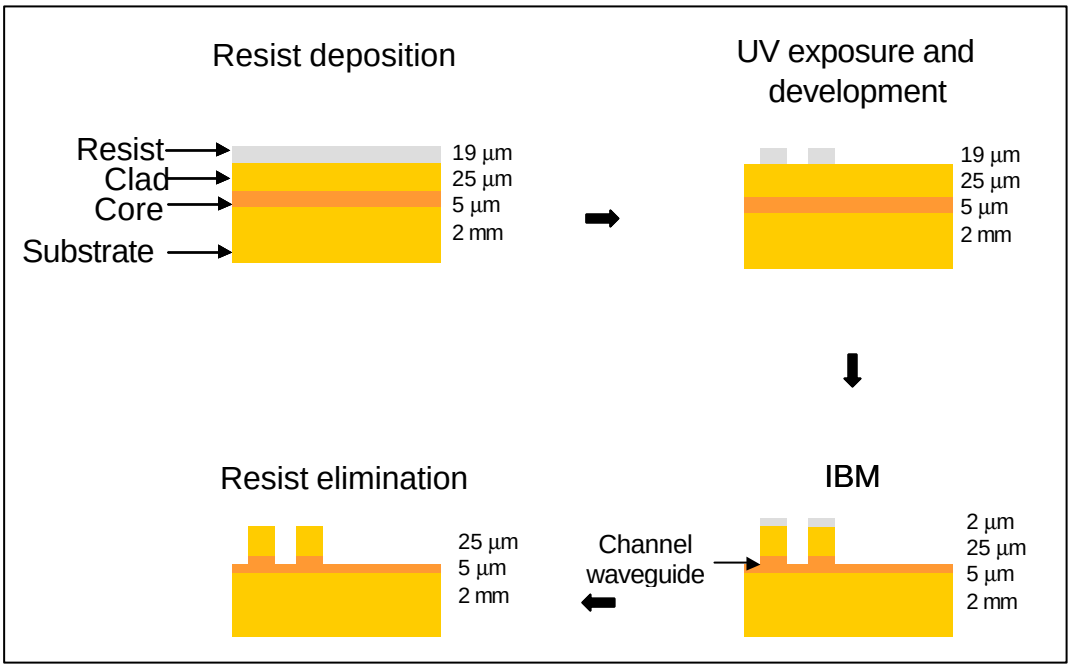

FIG. II.10: Photolithography and reactive etching.

The desired waveguide geometry that will support singlemode operation at both pump (980 nm) and signal (1535 nm) wavelengths is shown in FIG. II.11.

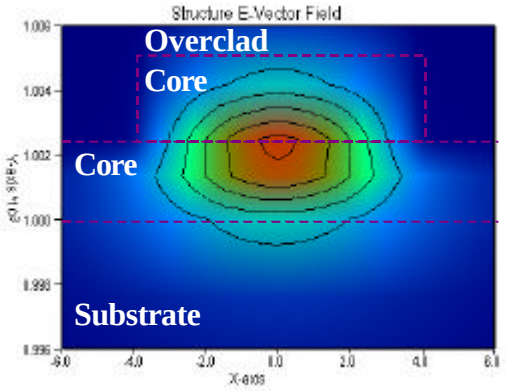

FIG. II.11: Singlemode waveguide geometry, 8µm ridge width, N_{eff}=2.024622.

1. Experimental

Photolithography process

The first step in the photolithography process was to identify a suitable photoresist. Ideally the photoresist should be more resistant to the etch than the glass. The photoresist SU8-10

was identified as a suitable resist. The resist was supplied by Microchem (www. Microchem.com). It is a negative resist.

Using bulk substrate glass, the photolithography process was studied. The substrate was cleaned with acetone followed by isopropanol, then rinsed with de-ionised water, blown dry with nitrogen and placed in a 120°C oven for 24 hours to dry.

The processing steps are:

(1) Deposition of the photoresist - When the resist was applied to the bismuthate substrate and spun, a thin uniform layer of resist appeared on the substrate. The final resist thickness was determined by the spinning speed. We have achieved film thickness > 20 micron, comparable to the overclad thickness. The spinning speed reached 500 rpm in 5 seconds and was held for 5 seconds. The final speed 1300 rpm was reached in 5 seconds and held for 45 seconds.

(2) Prebaking the photoresist film - Adherence of the film was achieved by pre-baking in a hotplate using the following process:
   - Hold at room temperature for 1 min
   - Ramp from room temperature to 35 °C and hold for 3 min
   - Ramp from 35 °C to 55 °C and hold for 3 min
   - Ramp from 55 °C to 75 °C and hold for 3 min
   - Ramp from 75 °C to 95 °C and hold for 20 min
   - The film was cooled down from 95 °C to room temperature in 30-60 minutes

(3) Masking - Channels were created in the photoresist film by exposing the film through a metallic mask under a UV lamp at around 300 mJ/cm^2.

(4) Post-baking following masking - Final adherence of the photoresist patterns on the glass substrate was obtained by post-baking on a hotplate, following the process:
   - Hold at room temperature for 1 min
   - Ramp from room temperature to 35 °C and hold for 3 min
   - Ramp from 35 °C to 55 °C and hold for 3 min
   - Ramp from 55 °C to 75 °C and hold for 3 min
   - Ramp from 75 °C to 95 °C and hold for 20 min
   - The film was cooled down from 95 °C to room temperature in 30-60 minutes

(5) Hard-baking – This was an optional step continuing from the standard post-baking procedure above. It improved the resistance of the photoresist to the argon ion beam during IBM. Following from above:

- Ramp from 75 °C to 95 °C and hold for 20 min
- This is the hard-bake process. Ramp from 95 °C to 150°C in increments of 10°C and holding for a minute at each increment
- The film was cooled down from 150 °C to room temperature in 30-60 minutes

(6) Getting the pattern - The part of the photoresist film that has not been exposed under UV (undeveloped resist) was removed by washing it off with Microprosit EC-solvent for 5 minutes. The sample was then cleaned with isopropanol and deionised water and blown dry with nitrogen, and then dried in an oven.

The quality of the imprinted patterns was characterised by optical microscopy, SEM (LEO 430) and surface profilometry (Tencor Instruments Alpha-Step 200).

Ion beam milling

The ion beam milling experiments were performed with a reactive ion beam etcher (Oxford Instruments) (FIG. II.12). The experimental parameters were the following:

	Current (mA)	**Voltage (V)**
Beam	125	500
Accelerator	10	500
Discharge	1500	50
Cathode filament	15	-
Beam neutralizer:		
- **Filament I**	1700	-
- **Emission I**	25	-

- Argon volume in the gun: 6 mL/min
- Argon volume in the beam neutraliser: 5 mL/min
- Argon pressure: $< 3 \times 10^{-6}$ mB

The samples were placed at an angle θ of 0°, 20° and 40° and etched for times ranging from 4 to 20 hours.

The argon beam size was 150 mm and the sample was rotating to ensure a good homogeneity of the final etched sample.

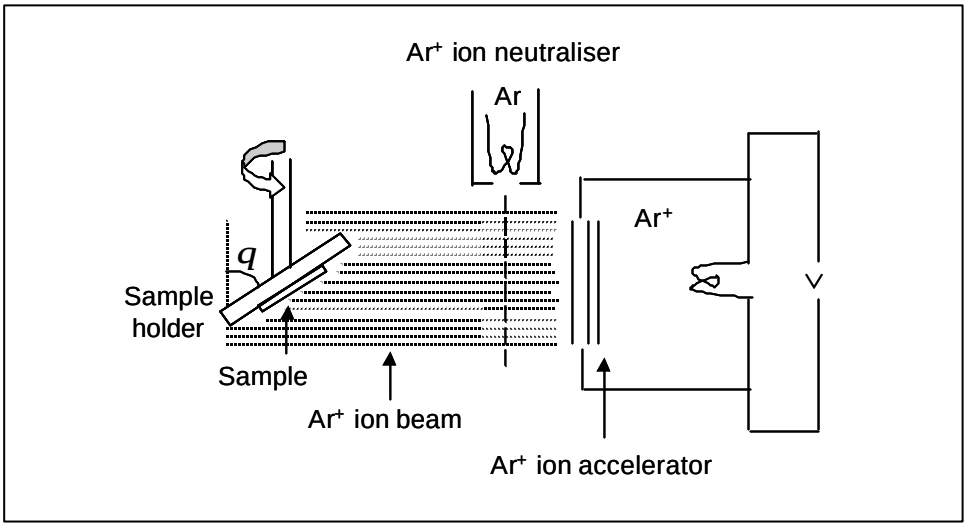

FIG. II.12: Apparatus for ion beam milling.

2. Results

2.1 Photoresist SU8-10

Photolithography

A preliminary study of the photolithography process using SU8-10 applied to a bulk Bi_2O_3-based glass sample revealed that straight parallel ridges with vertical sidewalls could be obtained. This is illustrated in the SEM pictures of Fig II.13. The photoresist thickness was 20 microns. The mask used to design the lines allows to pattern ridges of widths ranging from 2 to 16 µm. We repeatedly observed that ridges having a width below 4 µm systematically adopted a wavy profile (FIG. II.14), possibly due to a difference in expansion coefficient between the SU8-10 and the glass; the stress flexure was higher for smaller dimensions. Under standard SU8-10 photolithographic processing, SU8-10 was unsuitable for optical devices requiring channels $\leq$ 4 micron.

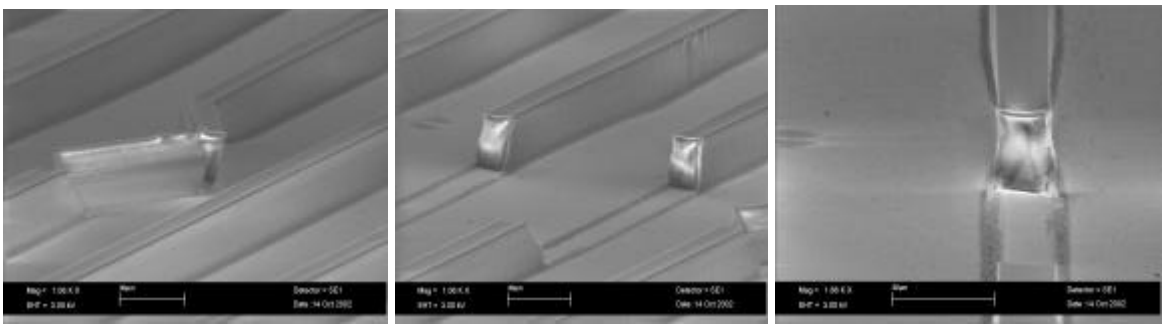

FIG. II.13: SEM pictures of SU8-10 ridges.

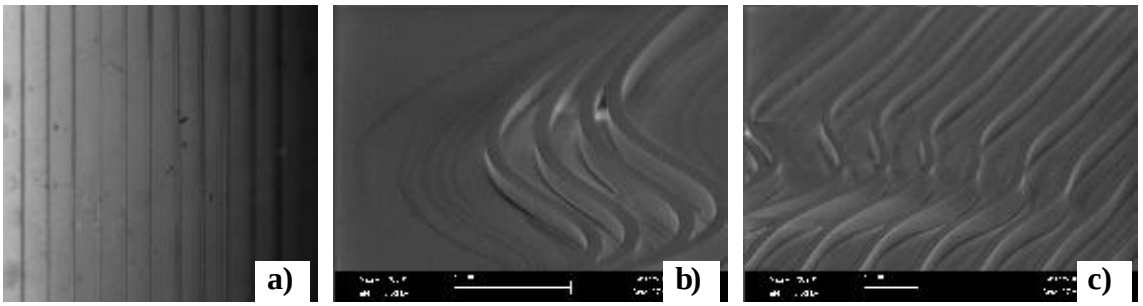

FIG. II.14: a) Optical microscope picture showing ridges of width > 4 μm, b) and c) SEM pictures showing ridges of width < 4 μm.

Ion beam milling

The ion beam milling etch rates of a bulk Bi_2O_3-based glass sample and of the SU8-10 photoresist, after deposition of a film on a glass substrate, were determined for different angles θ of the argon ion beam on the sample. The values are reported in TABLE II.2.

TABLE II.2: Etch rate of Bi_2O_3-based glass and SU8-10 resist.

Sample	Etch rate @ θ = 20 ° (nm/min)	Etch rate @ θ = 40 ° (nm/min)
Bi_2O_3 glass	28 - 30	36 - 37
SU8-10 photoresist		25

The etch rate of the Bi_2O_3-based glass was slightly higher than the etch rate of the photoresist, which meant that if a photoresist of thickness similar to the overclad was deposited, then the overclad will etch out before the resist was totally etched away. The etch rate at an angle θ of 40°, was greater than at 20°. This has been generally observed for other materials.

The resistance of the resist towards the argon ion beam was evaluated for the standard process and after the added hard-baked process. FIG. II.15 shows the SEM picture after ion beam milling of two samples with resist ridges prepared with the standard photolithography process and etched for 10 hours with an angle θ of 0° (FIG. II.15a), and with the added hard-baked process with an angle θ of 40° (FIG. II.15b).

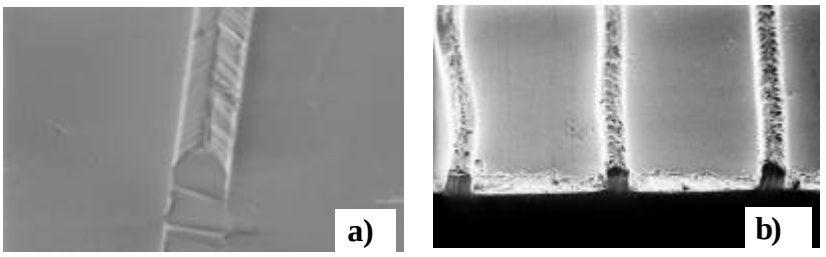

FIG. II.15: SEM picture of resist ridges after IBM for 10 hours with a) standard (θ = 0°) and b) hard-baked (θ = 40°) processes.

Under the Ar^+ beam, the resist ridges prepared with the standard process adopted a pyramidal profile while the ridges prepared with the hard-baked procedure showed better resistance.

2.2 Bismuthate glass

In a preliminary experiment, a bulk Bi_2O_3 substrate disk (B2bSC) was exposed to the argon ion beam after performing the photolithography process with SU8-10. The photoresist thickness was 20 µm. The sample was processed for ion beam milling for 8 hours with an angle θ of 40°. After processing, the sample was placed in an acetone filled dish in an ultrasonic bath for 24 hours in order to dissolve the remaining photoresist.

The glass ridges appeared with vertical sidewalls at the top, but the bottom was slightly curved, as illustrated in FIG. II.16. The total height was approximately 16 µm with good vertical definition in the region of 10 µm.

There was difficulty in removing any remaining resist after the ion beam milling process if it was carried out for several hours. But the presence of the resist on the waveguides should not affect the optical characterizations.

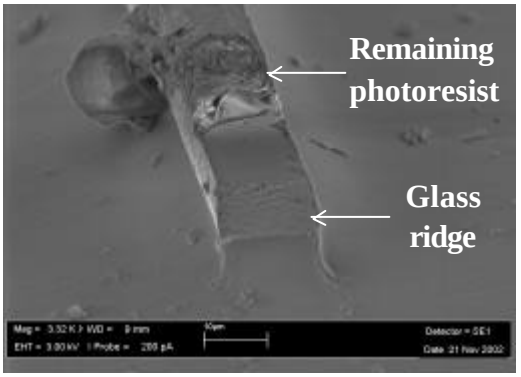

FIG. II.16: SEM pictures of a Bi_2O_3-based glass ridge (θ = 40°).

Spin-coated samples B3aSC-25b, B3aSC-27b and B3aSC-28b were prepared by photolithography. FIG. II.17 show the results for sample B3aSC-27b. The resist was 20 µm thick.

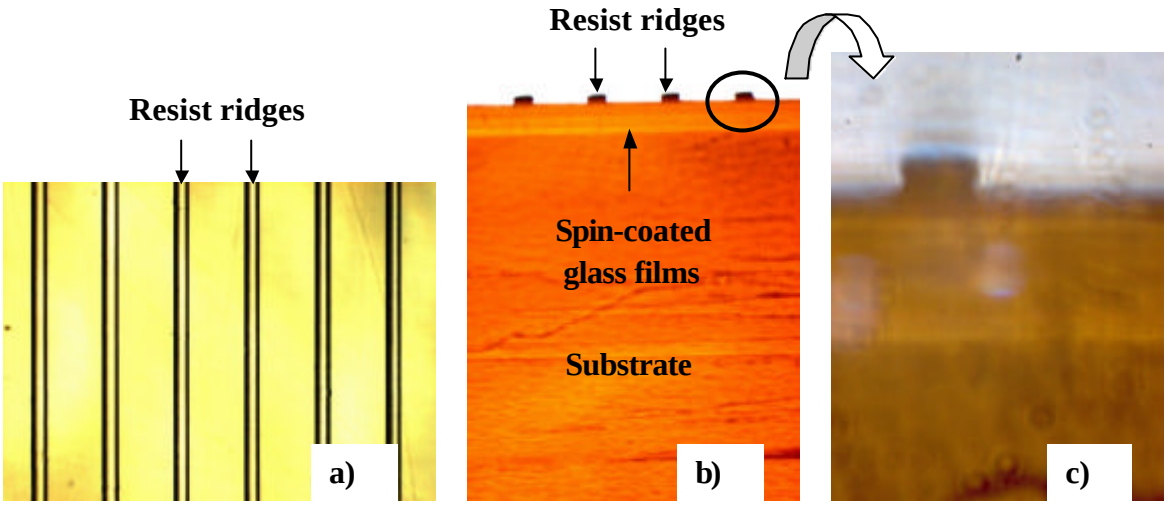

FIG. II.17: Optical microscope pictures of B3aSC-27b after photolithography process: a) Surface, b) and c) Cross-section.

After photolithography, the samples were exposed to the argon ion beam under the following conditions:

- Sample B3aSC-25b was etched for 18 hours with an angle $q = 40$ °
- Sample B3aSC-27b was etched for 10 hours with an angle $q = 20$ °
- Sample B3aSC-28b was etched for 14 hours with an angle $q = 40$ °

FIG. II.18 represents the surface of the three samples after etching. The surface of B3aSC-25b looks very rough compared to B3aSC-27b and B3aSC-28b, also seen on the SEM pictures (FIG. II.19). It is unclear to us why this is the case.

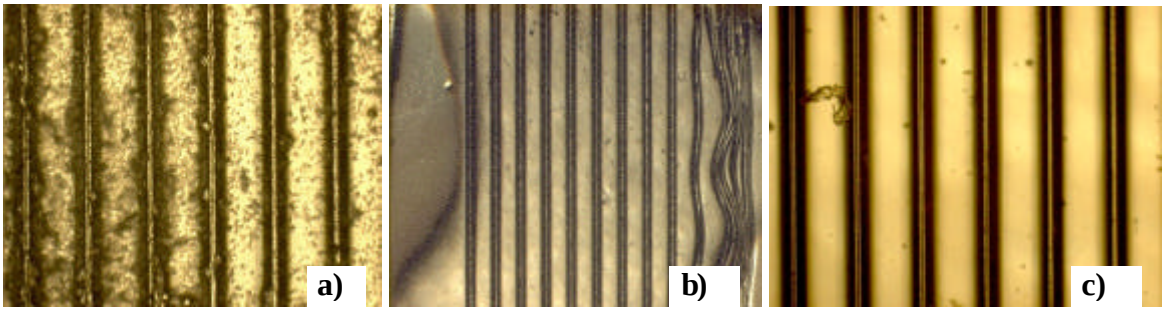

FIG. II.18: Optical microscope picture of the samples surface after etching: a) B3aSC-25b (18 hours), b) B3aSC-27b (10 hours) and c) B3aSC-28b (14 hours).

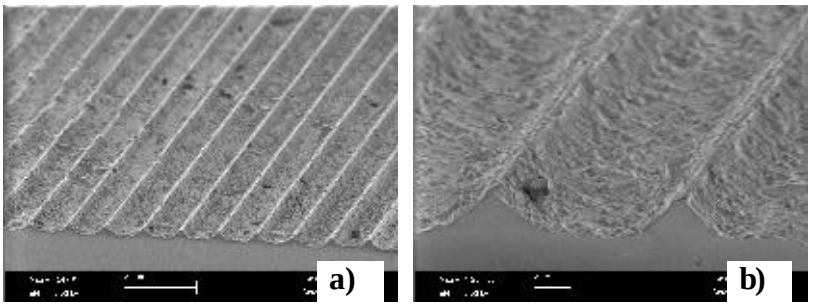

FIG. II.19: SEM photographs of B3aSC-25b surface.

For all three samples, after several hours of ion etching, the glass ridges adopted a pyramidal shape instead of the expected vertical side walls (FIG. II.20).

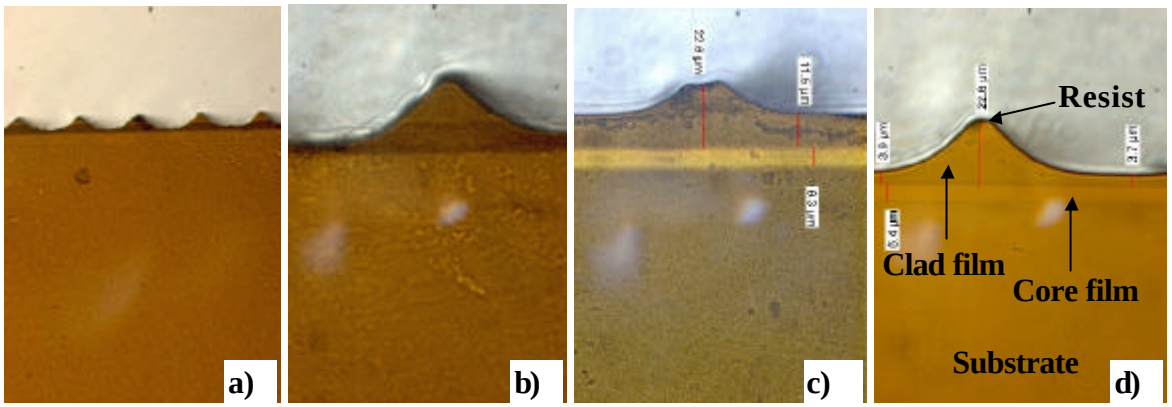

FIG. II.20: Optical microscope picture of the cross-section of: a-b) B3aSC-25b, c) B3aSC-27b and d) B3aSC-28b.

In addition, for samples 25b and 28b etched at sample angle of 40°, the profiles were more wedged than for sample 27b etched at 20°. The etch rate of the glass was smaller at 20° than at 40° and sample 27b was also etched for a shorter time, thus the amount of glass etched in sample 27b was less than in samples 25b and 28b. This was evident in the remaining overclad in the area unprotected by the resist in samples 27b and 28b, 11.5 and 3.7 µm respectively. Sample 27b was not as wedged since not as much had been etched out.

Half of the Bi_2O_3 sputtered sample provided by AGC was used to pattern ridges by photolithography and IBM. A photoresist film was applied on the surface and IBM was performed for 2-3 hours in order to etch about 2-3 micron of the Bi_2O_3 glass layer. Fifteen ridges with a width ranging from 2 to 16 µm were obtained. The cross-section of the sample after IBM showing a glass ridge is represented in FIG. II.21. All the glass ridges revealed a wedged profile.

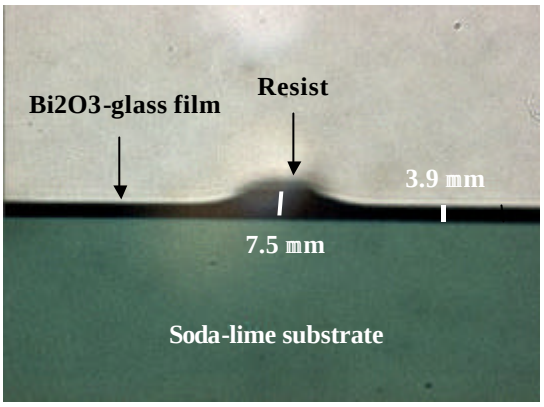

FIG. II.21: Optical microscope picture of the cross-section of the sputtered sample after IBM.

The photoresist thickness in the samples before etching was ~ 25 µm. We knew that the photoresist had vertical walls before ion-beam milling. We then had to find out what happened to the thick photoresist layer after long etching time, greater than 8 hours. A review of the result of Fig II.14 shows that for an initial photoresist layer of 20 µm and 8 hours of processing, vertical walls can be achieved for glass heights of 10 - 12 µm.

The experiment was carried out using a bulk bismuthate glass to which a 20 µm photoresist pattern had been imprinted. It was placed in the IBM at sample angle of 0° to avoid any contribution from overshadowing effects which may be present at angles > 0°. Our results show that after 10 hours, the photoresist profile itself was wedged as shown in FIG. II.15. It therefore implied that the wedge ridges obtained in samples 25b - 28b derived from the fact that the photoresist took this shape during the processing and imparted the shape on the final ridge, as might be expected. We are unclear as to why the sides of the photoresist should etch more efficiently than the centre. It may be that for thick ridges, there may be an interplay between the beam coming in and the materials coming out. It is therefore important not to expose the photoresist to long etch times.

An attempt to use reactive ion etching (RIE) with CHF_3 as the reactant gas was tried to thin down the overclad layer. Using the same processing conditions in the (RIE) as normally used to etch 10 nm/min of silica, a bismuthate glass sample was processed for 10 hours. No evidence of etching was noticed and there was also no adverse effect on the surface of the glass.

Therefore the approach to fabricating the desired waveguide geometry is:

a. Taking a 3 layer spin coated sample with overclad of 22 - 30 µm, and etch the surface overclad down to 5 µm. At an angle of 40° and etch rate of 35 nm/min, the process should take ~ 7 hours.
b. We will need to etch out 5 µm of the overclad and 2 µm into the core, a total of 7 µm for the desired waveguide geometry and thus an etch time of at least 3.3 hours.
c. As the photoresist etch rate is 25 nm/min, a thickness of SU8-10 > 5 µm will be sufficient.
d. A SU8-10 will be applied to the sample from step (1) using photolithography.
e. The sample will be exposed to ion beam etching for 3.5 hours.
f. Finally, the remaining photoresist will be removed.

In order to avoid the shadowing effect, the procedure described above was applied to the 3-layer spin-coated sample B1SC-10b. It was initially etched by IBM and the overclad thickness was reduced from 22 to about 7 µm. The photolithography process was then applied and IBM was performed again (with q = 40 °) to produce the glass ridges. FIG.II.22 shows the cross-section of the sample after this process with wedged glass ridges.

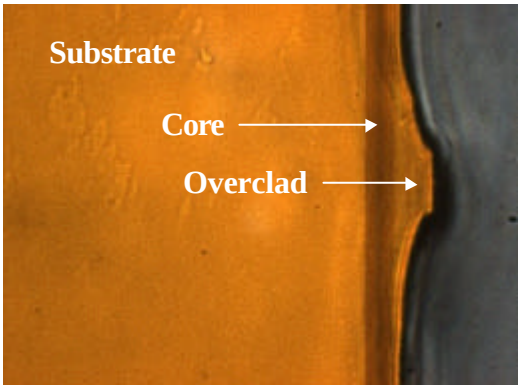

.FIG. II.22: Optical microscope picture of the cross-section of sample B1SC-10b after IBM.

Optical characterisations

The guidance property at 633 nm of the wedged channel waveguides obtained by photolithography and IBM were evaluated using helium-neon laser. Light was launched by coupling with a microscope objective lens into a standard single mode fibre, which was butt-coupled to one end-face of the waveguide. FIG. II.23 represents the output of three waveguides obtained from glass ridges of different width for sample B3aSC-25b.

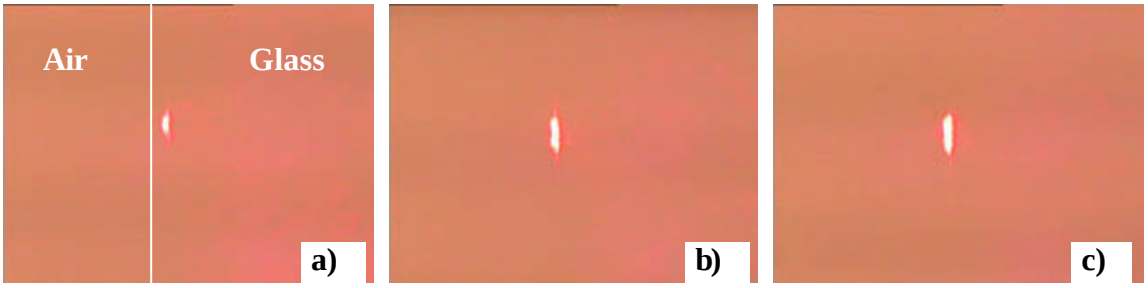

FIG. II.23: Modal output of three waveguides with ridges of width: a) 4.5 µm, b) 6.5 µm, c) 11 µm.

3. Conclusion

We have investigated photolithography using SU8-10 photoresist and ion beam milling (IBM) as techniques to define channel waveguides in a spin-coated bismuthate glass. The process can be equally applicable to slab waveguides prepared by other processes other than spin-coating such as sputtering. The optimum etch time observed on a Bi_2O_3-based glass bulk sample in the IBM was 8 hours to ensure good vertical definition. This was equal to etching out 12 µm of the photoresist. At longer etch times or when more photoresist was removed, the verticality was compromised as the photoresist walls were etched more efficiently imparting a wedged ridge profile. The effect was observed for sample angle positions in the IBM of 0°, 20° and 40°. Unfortunately, on the spin-coated samples, wedged ridges were observed even after a 2-3 hours IBM etch time. An added hard-bake treatment of the photoresist before IBM can increase the resistance of the photoresist and allow longer etch times.

References

[2.1] Y. Kondo et al., Fabrication of Bi_2O_3-based Er-doped waveguide for integrated optical amplifiers, Optical Fiber Communication, 17-22 March 2002, Anaheim, California, USA.

[2.2] A.G. Emslie, F.T. Bonner and L.G. Peck, J. Appl. Phys. 29 (1958) 858.

[2.3] D.W.J.Harwood, E.R.Taylor, C.T.A.Brown, D.P.Shepherd, D.N.Payne, Novel fabrication technique for planar glass waveguides, ECOC '98, Madrid, Spain, 20-24 Sep 1998 WdA34.

[2.4] D.W.J.Harwood, E.R.Taylor, Y.Rubin, G.Deflandre, Numerical simulation of the hot dip spin coating process for the fabrication of glass optical waveguides, Glass Technol. 43(C) (2002) 170-3. Proceedings of XIX International Congress on Glass, Edinburgh, 1-6 Jul 2001.

[2.5] D.W.Harwood, E.Taylor, R.Moore, D.N.Payne, Fabrication of uoride glass planar waveguides by hot dip spin coating, J. Non-Cryst. Solids 332 (2003)190-98.

[2.6] D.W.Harwood, Towards a 1.3 μm planar neodymium doped fluoride glass waveguide amplifier, Thesis, University of Southampton, 2000.

PUBLICATIONS

Papers

1. E.T.Y. Lee and E.R.M. Taylor, *"Thermo-optic coefficients of potassium alumino-metaphosphate glasses"*, Journal of Physics and Chemistry of Solids, Vol. 65, No. 6, pp 1187-1192 (2004).

2. E.T.Y. Lee and E.R.M. Taylor, *"Compositional effects on the thermo-optic coefficients of potassium aluminophosphate glasses"*, Optical Materials – Accepted for publication.

3. E.T.Y. Lee and E.R.M. Taylor, *"Compositional effects on the thermo-optic coefficients of barium borophosphate glasses"*, Proceedings of SPIE Photonics West 2004, Paper 5350-24, San Jose (California, US).

4. E.T.Y. Lee and E.R.M. Taylor, *"Compositional effects on the optical and thermal properties of sodium borophosphate glasses"*, Journal of Physics and Chemistry of Solids – Accepted for publication.

5. E.T.Y. Lee and E.R.M. Taylor, *"Optical and thermal properties of binary barium phosphate and calcium phosphate glasses"*, Submitted to Optical Materials.

6. A. Favre, E. Lee, V. Apostolopoulos, C.B.E. Gawith, C.Y. Tai, E. Taylor, Y. Kondo and F. Koizumi, *"Fabrication and characterisation of planar and channel waveguides in bismuth-based oxide glasses"*, Proceedings of SPIE Photonics West 2003, paper 4990-21, San Jose (California, US).

7. A. Favre, E. Lee, V. Apostolopoulos, C.B.E. Gawith, C.Y. Tai, E. Taylor, Y. Kondo and F. Koizumi, *"UV-written channel waveguides in Er^{3+}-doped Bi_2O_3-based glass"*, Physica Status Solidi (c), Vol. 1, No. 2, pp 295-298 (2004).

8. A. Favre, E. Lee, V. Apostolopoulos, C.B.E. Gawith, C.Y. Tai, E. Taylor, Y. Kondo and F. Koizumi, *"Fabrication and characterization of UV-written channel waveguides in Bi_2O_3-based glass"*, Optical Materials – Article in Press.

Conference Presentations

1. E.T.Y. Lee and E.R.M. Taylor, *"Compositional effects on the thermo-optic coefficients of potassium aluminophosphate glasses"*, Presented at the American Ceramic Society 'Glass & Optical Materials Division Fall 2003 Meeting', 12-15 October 2003, Corning, US.

2. E.T.Y. Lee and E.R.M. Taylor, *"Compositional effects on the thermo-optic coefficients of barium borophosphate glasses"*, Presented at 'Photonics West 2004', 24-29 January 2004, San Jose, US.

3. A. Favre, E. Lee, V. Apostolopoulos, C.B.E. Gawith, C.Y. Tai, E. Taylor, Y. Kondo and F. Koizumi, *"Fabrication and characterization of planar and channel waveguides in bismuth-based oxide glasses"*, Presented at 'Photonics West 2003', 25-31 January 2003, San Jose, US.

4. A. Favre, E. Lee, V. Apostolopoulos, C.B.E. Gawith, C.Y. Tai, E. Taylor, Y. Kondo and F. Koizumi, *"UV-written channel waveguides in Er^{3+}-doped Bi_2O_3-based glass"*, Presented at the 'European Materials Research Society Fall Meeting', 15-19 September 2003, Warsaw, Poland.